UNIVERSIDAD NACIONAL AUTÓNOMA DE MEXICO

PROGRAMA DE MAESTRÍA Y DOCTORADO EN CIENCIAS QUÍMICAS

REDES METAL-ORGÁNICAS CON METALES DIAMAGNÉTICOS d^{10}. ESTUDIOS ESTRUCTURALES Y DETECCIÓN ESPECTROSCÓPICA DE ANIONES.

TESIS

PARA OPTAR POR EL GRADO DE

DOCTOR EN CIENCIAS

PRESENTA

M. en C. Luis David Rosales Vázquez

Dr. Alejandro Dorazco González

Instituto de Química, UNAM

CIUDAD DE MÉXICO, NOVIEMBRE, 2022

UNIVERSIDAD NACIONAL AUTÓNOMA DE MÉXICO

PROGRAMA DE MAESTRÍA Y DOCTORADO EN CIENCIAS QUÍMICAS

REDES METAL-ORGÁNICAS CON METALES DIAMAGNÉTICOS d^{10}. ESTUDIOS ESTRUCTURALES Y DETECCIÓN ESPECTROSCÓPICA DE ANIONES.

T E S I S

PARA OPTAR POR EL GRADO DE

DOCTOR EN CIENCIAS

P R E S E N T A

M. en C. Luis David Rosales Vázquez

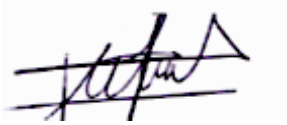

Dr. Alejandro Dorazco González

Instituto de Química, UNAM

Ciudad de México, Noviembre, 2022.

Agradecimientos

A mi mamá y a mi hermano Ale por tanto apoyo, con cariño.

Al Dr. Alejandro Dorazco González, la Dra. Silvia Elena Castillo Blum y el Dr. Víctor Sánchez Mendieta por su mentoría en la realización del trabajo y apoyo brindado.

A los académicos que contribuyeron como colaboradores en la publicaciones: Dr. Antonio Téllez López, Dr. Jonathan Jaramillo García, Dr. Roberto Escudero, Dr. Francisco Morales, Dr. Juan M. Germán Acacio, el Dr. José C. Páez Franco, el Dr. Alfredo Rafael Vilchis Nestor, el Dr. Joaquin Barroso Flores, Dr. José de Jesús Cázares Marinero M en C. Josue Valdes García y Dr. Iván Bazany Rodríguez.

A los técnicos académicos. Q. María A. Peña González, Q. María de la Paz Orta Pérez, M en C. Elizabeth Huerta Salazar, M. en C. Lucia del Carmen Márquez Alonso, Dra. Adriana Romo Pérez, Dra. Beatriz Quiroz-García, Dr. Diego Martínez Otero, M. en C. Alejandra Núñez cuya ayuda en las técnicas de caracterización ha sido invaluable

A la UNAM como institución y por el “Programa de apoyo a proyectos de investigación e innovación tecnológica PAPIIT-UNAM 2020-2023, IN216220”

Al Instituto de Química de la UNAM por todos los servicios y apoyos brindados durante el trabajo.

Al CONACyT por el programa “Ciencia de frontera 2019, proyecto 160671”, así como por la beca brindada al CVU 713164

Índice

Resumen **1**

Lista de abreviaturas **4**

Lista de figuras **5**

Lista de tablas **9**

Capítulo I: Marco teórico **10**

1.1 PCs y MOFs 10

1.2 Diseño de PCs y MOFs. 10

1.2.1 Centro metálico 10

1.2.2 Ligantes 12

1.2.2.1 Diseño estructural 12

1.2.2.2 Diseño orientado a aplicaciones 14

1.2.2.3 Construcción de PCs y MOFs luminiscentes 17

1.2.2.4 Aplicaciones de PCs y MOFs luminiscentes en el sensado 21

1.2.3 Antecedentes I: Estructurales 25

1.2.3.1 Redes metal-orgánicas con derivados alquílicos de 2,2'-bipiridina y el ligante puente el ácido 1,4-ciclohexendicarboxílico 25

1.2.3.2 Redes metal-orgánicas con el ligante tptc y el ion Zn(II) 26

1.2.4 Antecedentes II: Detección fluorescente de aniones por redes metal orgánicas luminiscentes 29

1.2.4.1 Redes metal-orgánicas capaces de detectar al ion cianuro 29

1.2.4.2 Redes metal-orgánicas capaces de detectar atorvastatina 33

1.3 Justificación 34

1.4 Objetivo general 36

1.4.1 Objetivos particulares para el sistema I 36

1.4.1 Objetivos particulares para el sistema II 37

Capítulo II: Resultados **38**

2.1 Sistema I: "Polímeros de coordinación con el ligante puente 1,4-chdc y ligantes auxiliares luminiscentes derivados de la 2,2'-bpy aplicados en la detección fluorescente de aniones"…38

2.1.2 Análisis estructural 39

2.1.2.1 Polímero $[Zn(4,4\text{-dmbp})(e,a\text{-}cis\text{-}1,4\text{-chdc})(H_2O)\cdot 2(H_2O)]_n$ (1) 40

2.1.2.2 Polímero $[Zn(5,5\text{-dmbp})(e,a\text{-}cis\text{-}1,4\text{-chdc})(H_2O)]_n$ (2) 44

2.1.2.3 Polímero $[Zn_2(4,4\text{-dtbp})_2(e,a\text{-}cis\text{-}1,4\text{-chdc})_2(H_2O)_2\cdot 7(H_2O)]_n$ (3) 47

2.1.1.4 Comparación estructural e influencia de las sustituciones de los grupos alquilo en los PCs (1), (2) y (3) 51

2.1.2 Estudios de las propiedades luminiscentes aplicadas al sensado de aniones y análisis espectroscópicos. 53

2.1.3 Caracterización complementaria 64
2.1.3.1 Difracción de rayos X de polvos 64
2.1.3.2 Análisis termogravimétrico 65
2.1.3.3 Fluorescencia del estado sólido 66
2.1.4 Conclusiones del Sistema I 67
2.2 Sistema II: "MOF de Zn(II) y el ligante ácido terfenil-3,3",5,5" tetracarboxílico aplicado en la detección de aniones farmacéuticos de la familia de las estatinas." 70
2.2.1 Análisis estructural 71
2.2.1.1 MOF $\{[Zn_3(Htptc)_2]\cdot(H_2O)_{1.3}\cdot(CH_3CH_2OH)_{3.1}\}_n$ (4) 72
2.2.2 Estudios de las propiedades luminiscentes aplicadas al sensado de aniones y análisis espectroscópicos. 74
3.4.3 Aplicación del MOF (4) en la detección fluorescente de atorvastatina en tabletas comerciales 88
2.2.3 Conclusiones del sistema II 91
Capítulo III: Desarrollo experimental 93
3.1 Disolventes y reactivos: 93
3.2 Instrumentación. 93
3.3 Cristalografía de rayos X de monocristal. 94
3.4 Síntesis de los compuestos. 94
[Zn(4,4-dmbp)(e,a-cis-1,4-chdc)(H_2O)·2(H_2O)]n (1). 94
[Zn(5,5-dmbp)(*e,a-cis*-1,4-chdc)(H_2O)]*n* (2). 95
[Zn_2(4,4-dtbp)$_2$(*e,a-cis*-1,4-chdc)$_2$·5(H_2O)]*n* (3) 95
[Zn_2(4,4-dtbp)$_2$(*e,a-cis*-1,4-chdc)$_2$·5(H_2O)]*n* (4) 95
Capítulo IV: Anexos 96
4.1 Reconocimientos y constancias de eventos de divulgación científica 96
4.2 Publicaciones en revistas indexadas 104

Resumen

El presente trabajo se centra en la síntesis de redes metal orgánicas cristalinas, su caracterización estructural por análisis de rayos X, la caracterización espectroscopia, el análisis térmicos y su aplicación en la detección fluorescente de aniones inorgánicos y orgánicos farmacéuticos. El capítulo I aborda los aspectos generales de las redes metal orgánicas funcionales a la detección luminiscente. En el capítulo II se incluyen los resultados de dos diferentes tipos de redes metal orgánicas contemplando su síntesis química, análisis estructural, espectroscópico y su aplicación en la detección de aniones.

El primer sistema describe la obtención de tres nuevos polímeros de coordinación luminiscentes de Zn(II) unidimensionales con los ligantes di-alquil-2,2´-bipiridinas y el ácido 1,4-ciclohexanodicarboxílico. Los estudios estructurales por difracción de rayos-X muestran que los compuestos tienen las fórmulas generales: $[Zn(4,4\text{-dmbp})(e,a\text{-}cis\text{-}1,4\text{-chdc})(H_2O)\cdot 2(H_2O)]_n$ (1), $[Zn(5,5\text{-dmbp})(e,a\text{-}cis\text{-}1,4\text{-chdc})(H_2O)]_n$ (**2**), y $[Zn_2(4,4\text{-dtbp})_2(e,a\text{-}cis\text{-}1,4\text{-chdc})_2(H_2O)_2\cdot 7(H_2O)]_n$ **(3)** (*e,a-cis*-1,4-chdc = ecuatorial,axial-cis-ácido 1,4-ciclohexanodicarboxílico, 4,4′-dtmb = 4,4′-dimetil-2,2′-bipiridina, 5,5′-dtmb = 5,5′-dimetil-2,2′-bipiridina, 4,4′-dtbb = 4,4′-ditert-butil-2,2′-bipiridina). Estos polímeros de Zn(II) fueron estudiados como quimiosensores de oxianiones, halogenuros y pseudohalogenuros en medio acuoso por múltiples técnicas espectroscópicas.

El polímero (**3**) exhibe una selectividad por el ion cianuro a través de un mecanismo de apagamiento de la luminiscencia con una constante de Stern-Volmer = 9.7×10^4 M^{-1} y con un límite de detección de 0.9 μmol L^{-1}. De acuerdo a la literatura, $\{[Zn_2(H_2O)_2(e,a\text{-cis-}1,4\text{-chdc})_2(4,4'\text{-dtbb})_2]\cdot 7H_2O\}n$, es de los pocas redes metal orgánicas existentes capaces de detectar al ion cianuro, permaneciendo como una temática de interés poco explorada y sustentada en la conocida toxicidad exhibida por tal ion.

El segundo sistema se enfoca en la síntesis del MOF luminiscente poroso $\{[Zn_3(Htptc)_2]\cdot(H_2O)_{1.3}\cdot(CH_3CH_2OH)_{3.1}\}n$ (**4**) con el ligante ácido terfenil-3,3”,5,5” tetracarboxílico (H_4tptc) y su uso como quimiosensor para una serie de estatinas y diferentes aniones orgánicos e inorgánicos.

El MOF (**4**) posee un arreglo tridimensional con una serie de canales porosos los cuales representan más del 30% de espacio disponible de su estructura cristalina. Sus propiedades luminiscentes se aplicaron en el análisis de analitos de importancia biológica, entre ellos: oxianiones, dicarboxilatos, citrato, adenosina 5´-trifosfato y fármacos de la familia de las estatinas cuya composición química la integran grupos carboxilatos y anillos aromáticos deficientes de electrones.

Una notable disminución de la fluorescencia por parte del quimiosensor, ocurre selectivamente para la Atorvastatina en un sistema etanol-agua. Su constante de Stern-Volmer es igual a 1.40×10^5 M^{-1}, con un límite de detección de 4.2 μmol L^{-1}. Interesantemente, la selectividad por el fármaco persiste aún

en la presencia de especies coexistentes en la orina y sangre. La aplicación del MOF para la detección de atorvastina se extendió al sensado en tabletas comerciales de atorvastatina de 20 mg (Eturión® y Sortis®) con resultados consistentes y verificados por cromatografía HPLC. Dada la importancia de las estatinas como uno de los principales fármacos mundialmente utilizados para el tratamiento de la hipertensión y alto colesterol, siendo estos padecimientos una problemática recurrente en la sociedad mexicana, $\{[Zn_3(Htptc)_2]\cdot(H_2O)_{1.3}\cdot(CH_3CH_2OH)_{3.1}\}_n$ constituye el primer MOF capaz de detectar atorvastatina, en un área de aplicación ascendente por parte de estos materiales porosos en el sensado de fármacos.

Los aspectos experimentales a detalle de ambos sistemas, así como la instrumentación requerida en sus estudios es cubierta en el capítulo III.

Finalmente, en el capítulo IV se integran los productos de publicación en revistas indexadas y de difusión científica.

De forma general, los resultados de los sistemas de los polímeros de coordinación **(1-3)** y del MOF **(4)** resaltan la utilidad de las redes metal orgánicas luminiscentes como potenciales herramientas analíticas para la detección directa de especies aniónicas en fase acuosa.

Redes metal orgánicas sintetizadas en el presente trabajo

Sistema I

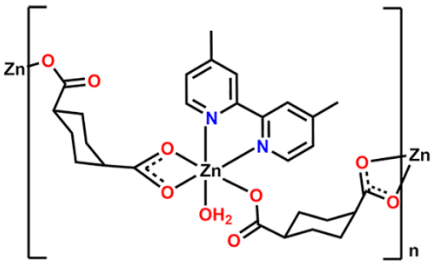

$[Zn(4,4\text{-dmbp})(e,a\text{-}cis\text{-}1,4\text{-chdc})(H_2O)\cdot 2(H_2O)]_n$
(1)

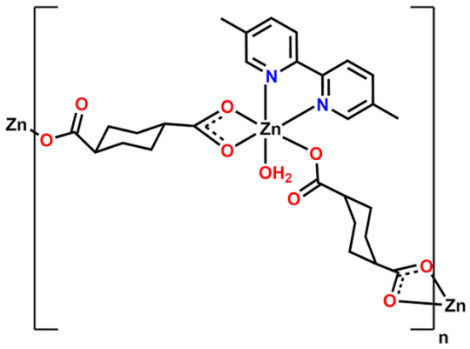

$[Zn(5,5\text{-dmbp})(e,a\text{-}cis\text{-}1,4\text{-chdc})(H_2O)\cdot]_n$
(2)

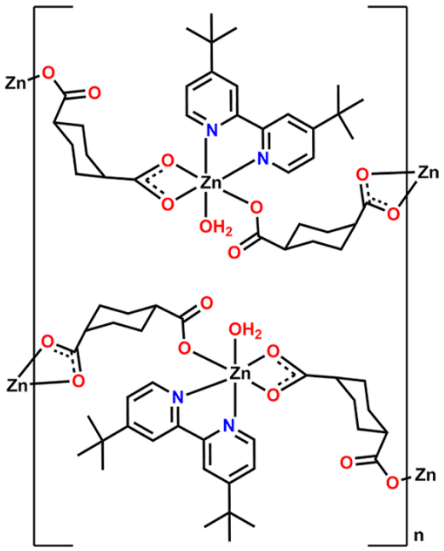

$[Zn(4,4\text{-dtbp})(e,a\text{-}cis\text{-}1,4\text{-chdc})(H_2O)_2\cdot 7(H_2O)]_n$
(3)

Sistema II

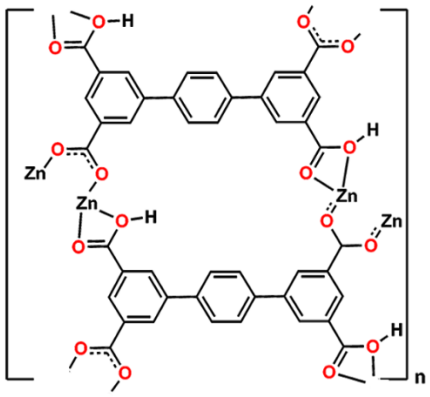

$[Zn_3(Htptc)_2]\cdot(H_2O)_{1.3}\cdot(EtOH)_{3.1}]_n$
(4)

Lista de abreviaturas

1,4-chdc	Ácido 1,4-ciclohexendicarboxilíco
4,4-dmbp	4,4-dimetil-2,2'-bipiridina
4,4-dtbp	4,4-diterbutil-2,2'-bipiridina
5,5-dmbp	5,5-dimetil-2,2'-bipiridina
ATV	Atorvastatina
BDC	Ácido tereftálico
bpy	2,2'-bipiridina
°C	Grados Celsius
cm	Centímetros
CPMAS	Cross Polarization Magic Angle Spinning
DCM	Diclorometano
DFT	Density functional theory
DMA	N,N-dimetilacetamida
DMF	N,N-dimetilformamida
DMSO	Dimetilsulfóxido
EDS	Energy Dispersive Scattering
EtOH	Etanol
eq	Equivalente
FT-IR	Fourier-transform infrared spectroscopy
FV	Fluvovastatina
h	hora
HOMO	Highest occupied molecular orbital
HPLC	High-perfomance liquid chromatography
H_3BTB	4,4´,4´´-bencen-1,3,5-triyl-tris(ácido benzoico)
Htptc	Ácido terfenil-3,3",5,5" tetracarboxílico
I_0/I	Parámetro relativo de extinción de la fluorescencia
IR	Infrarrojo
L	Ligante
LDD	Límite de detección
LUMO	Lowest unoccupied molecular orbital
M	Molaridad/Molar
MeCN	Acetonitrilo
MeOH	Metanol
min	minuto
mM	Milimolar
MOFs	Metal organic framework
NP	Nanopartículas
nM	Nanomolar
PCs	Polímeros de coordinación
PET	Photoinduced electron transfer
ppm	Partes por millón
PRV	Pravastatina
RMN	Resonancia magnética nuclear
RSV	Rosuvastatina
s	Segundo
S_0	Estado electrónico basal
S_1	Estado electrónico singulete
SEM	Scanning Electron Microscopy
t	Tiempo
τ	Tiempo de vida
t.a.	Temperatura ambiente
TCLM	Transferencia de carga Ligante Metal
TCML	Transferencia de carga Metal Ligante
TGA	Termogravimetric analysis
THF	Tetrahidrofurano
u.a.	Unidades arbitrarias
USC	Unidad secundaria de construcción
UV-Vis	Ultravioleta visible
ZIF	Zeolitic Inorganic Framework

Lista de figuras

Figura 1. a) Representación poliedral del MOF-2. b) USC “rueda de paleta” que conecta a cuatro ligantes en una geometría defina por un cuadrado. 11

Figura 2. a) Representación poliedral del HKUST-1-Cu-Zn tras su preparación in situ.[14] b) Representación poliedral de UiO-66 y UiO-66(Ti al 44%). I) Intercambio post-sintético del centro metálico Zr(IV) por Ti(IV).[15] 11

Figura 3. Ligante ácido terfenil-3,3”,5,5” tetracarboxílico 12

Figura 4. Ligantes con la misma topicidad que exhiben una diferente orientación espacial de conectividad por la magnitud del ángulo entre sus grupos carboxilo. 13

Figura 5. Imagen modificada de la referencia 15 donde cada inciso corresponde a una modificación del ligante manteniendo la red isoreticular para cada derivado del MOF-177 a) = H_3BTB; b) H_3BTB-NH_2, c) H_3BTB-NO_2, d) H_3BTB-OCH_3, e) H_3BTB-OC_7H_7, f) H_3BTB-F_2, g) H_3BTB-C_4H_4, h) H_3BTB-F[11] 13

Figura 6. a) USC común para los MOFs NU-903, NU-904 y NU-1008. b) Representación poliedral del NU-903 con el ligante TCPB en una red scu. c) Representación poliedral del NU-904 con el ligante TCPB-NO_2 en una red shp. d) Representación poliedral del NU-1008 con el ligante TCPB-Br en una red csq.[26] 14

Figura 7. Diagrama de Jablonski 15

Figura 8. Mecanismo PET reductivo y PET oxidativo.[44] 17

Figura 9. Mecanismo FRET ilustrado en un espectro de luminiscencia.[48] 17

Figura 10. a) Mecanismo TCML. b) Mecanismo TCLM.[38] 19

Figura 11. Mecanismos que dan origen a la luminiscencia en los PCs y MOFs. 20

Figura 12. Cualidades deseadas en una red metal orgánica para su uso como sensor luminiscente. 21

Figura 13. a) USC del $\{[Zn_2(\mu_2\text{-BDC})_2(iQ)_2]\}_n$. b) Estructura laminar del MOF. c) Espectro de fluorescencia del MOF en presencia de diferentes solventes.[69] 22

Figura 14. Graphical abstract de “Efficient chemosensors for toxic pollutants based on photoluminescent Zn(II) and Cd(II) metal–organic networks”. 23

Figura 15. Ligantes derivados de la 2,2'-bipiridina 25

Figura 16. Representación poliedral de los polímeros de coordinación de Cd(II) con el ligante puente 1,4-chdc y los ligantes auxiliares luminiscentes a) 4,4-dmbp b) 5,5-dmbp y 4,4-dmbp 26

Figura 17. Representación poliedral del MOF A1, con la USC tetraédrica que constituye la arquitectura 3D con canales triangulares 27

Figura 18. Representación poliedral del MOF A2, con la USC tetraédrica constructora de la red rectangular. 28

Figura 19. Representación poliedral del MOF A3 (a) isoreticular al MOF NOTT-101 (b). 29

Figura 20. a) Representación poliedral del bio-MOF-1. I) Intercambio del catión dimetilamonio por el 3,6-diaminoacridinio II) Adición del ion cianuro reaccionando con ion 3,6-diaminoacridinio, reemplazándolo en la red el catión tetrabutilamonio. b) Mecanismo de reacción del ataque nucleofílico del ion cianuro al catión 3,6-diaminoacridinio 30

Figura 21. a) Representación poliedral del ZIF-90 b) Topologia simplificada de la red *sod*. c) Representación 2D de las caras de la red *sod* en el ZIF-90. I) ZIF-90 tras la reacción de condensación

aldólica de malonotrilio con el grupo aldehído. II) ZIF-90 modificado posterior a la reacción Knoevenagel en el grupo dicianovinilo.....31

Figura 22. a) Representación poliedral del UiO-66 emulando el arreglo esperado de los MOFs con sus respectivas sustituciones en el ligante TDC para A4, y 1,4-BDC-NH-$COCF_3$ para UiO-66-NH-$COCF_3$. b) Topología simplificada de la red *bcu*. c) Representación 2D de las caras de la red *bcu* en el A4. I) A4 tras el intercambio de ligante con el CPAA II) Apagamiento de la fluorescencia en el A4 modificado posterior a la adición del ion cianuro. d) Representación 2D de las caras de la red *bcu* en UiO-66-NH-$COCF_3$. I) Formación de enlaces de hidrógeno en UiO-66-NH-$COCF_3$ tras la adición del ion cianuro generando fluorescencia en el MOF. 33

Figura 23. a) Representación poliedral del ZIF-8. b) ZIF-8 y las nanopartículas de F_3O_4 (F_3O_4 NP) dispuestos en el óxido de grafeno (OG) para constituir el material híbrido que absorbe atorvastatina.[38] 34

Figura 24. Ligantes utilizados en el Capítulo II para su estudio estructural en polímeros de coordinación de Zn(II) y su aplicación en el sensado de aniones inorgánicos.....35

Figura 25. a) Ligante base del Capítulo III en la síntesis de un nuevo MOF aplicado a la detección fluorescente de estatinas. b) Grupo de estatinas estudiadas 36

Figura 26. Resumen gráfico del sistema I 38

Figura 27. Reacción general para la obtención de los PCs (1-3). I = Metanol-H_2O, t.a. 2eq. NaOH...38

Figura 28. Representación elipsoidal al 50% del polímero [Zn(4,4-dmbp)(e,a-cis-1,4-chdc)(H_2O)·2(H_2O)] (1).....40

Figura 29. Representación poliedral de (1) mostrando su estructura polimérica de cadena zigzag 1D. 41

Figura 30. Interacciones π – π del tipo cara – cara entre los anillos aromáticos presentes en la estructura polimérica, indicados en amarillo. 42

Figura 31. Designaciones de los graph set descriptors: D = Patrón finito de conectividad, C = cadena, S = enlace de hidrógeno intramolecular y R = anillo.[137].....43

Figura 32. Enlaces de hidrógeno exhibidos en (1) bajo una representación poliedral 43

Figura 33. Representación elipsoidal al 50% del polímero [Zn(5,5-dmbp)(e,a-cis-1,4-chdc)(H_2O)]$_n$ (1) 44

Figura 34. Representación poliedral de la cadena polimérica en zigzag de (2).....45

Figura 35. Empaquetamiento cristalino de (2) omitiendo los átomos de hidrógeno por claridad en una representación poliedral.....46

Figura 36. a) Enlaces de hidrógeno de (2) y b) Arreglo laminar bidimensional derivado de los enlaces de hidrógeno. Ambos incisos son una representación poliedral 47

Figura 37. Representación elipsoidal al 50% del polímero [Zn_2(4,4-dtbp)$_2$(*e,a-cis*-1,4-chdc)$_2$(H_2O)$_2$·7(H_2O)]$_n$ (3) (se omiten los átomos de hidrógeno del ligante por claridad). 47

Figura 38 Representación poliedral de las cadena polimérica en (3) 49

Figura 39. Enlaces de hidrógeno exhibidos en (3) bajo una representación poliedral. 50

Figura 40. Comparación de las estructuras supramoleculares de los PCs a) (1). b) (2). c) (3) en representación poliedral.....53

Figura 41. Emisión fluorescente de los CPs (1-3) en agua.....54

Figura 42. Comparación de la respuesta de apagamiento de la fluorescencia en los PCs (1-3) 55

Figura 43. Titulación fluorimétrica del CP (3) en presencia del ion CN^-. b) Perfil de titulación y cálculo de la constante K_{sv} = 9.8 x 10^4 M^{-1} a 434 nm 56

Figura 44. Estudio de la competitividad a través de los perfiles de titulación de (3); ante la presencia únicamente del anión cianuro (color negro) y en coexistencia de varios aniones inorgánicos (color rojo) 57

Figura 45. Perfiles de la titulación de (3) con el ion CN^- a diferentes condiciones de pH.....58

Figura 46. Espectro de ^{13}C por la técnica CPMAS del polímero (3).....59

Figura 47. Espectro de infrarrojo del CP (3).....61

Figura 48. Propuesta del mecanismo de interacción del ion cianuro con el CP (3). 61

Figura 49. Micrografías tomadas por SEM de a) cristal de (3) y b) residuo sólido de la reacción de (3) con NaCN 62

Figura 50. Mapeo por EPS de a) cristal de (3) y b) residuo sólido de la reacción de (3) con NaCN ...63

Figura 51. Espectro de infrarrojo del residuo de la reacción de (3) con NaCN 63

Figura 52. Espectro de ^{13}C CPMAS del sólido insoluble en agua atribuido al ligante 4,4'-dtbp 64

Figura 53. Difractograma de rayos X de polvos de (3) a) Experimental. b) Simulado.....65

Figura 54. Análisis termogravimétrico de (3).....66

Figura 55. a) Espectro de fluorescencia de los compuestos (1-3) en estado sólido. b) Fotografía de (3) bajo la lámpara de UV (254nm) 67

Figura 56. Tiempo de vida de la fluorescencia de (3).....67

Figura 57. Resumen gráfico del sistema II 70

Figura 58. Reacción general para la obtención del MOF (4) 70

Figura 59. Representación elipsoidal al 50% del MOF $\{[Zn_3(Htptc)_2]\cdot(H_2O)_{1.3}\cdot(CH_3CH_2OH)_{3.1}$ (4).....72

Figura 60. Representación simplificada de la conectividad del cluster del MOF(4) 73

Figura 61. USC y construcción de red del MOF (4).....74

Figura 62. Representación "spacefill" de (4) en el eje cristalográfico *b*. b) Representación de volumen disponible en (4) en color mostaza 74

Figura 63. Mediciones de fluorescencia de (4) en el medio 8:2 etanol agua durante 10 horas.....75

Figura 64. Difractograma del MOF (4) en: a) Tras permanecer en agitación constante en el sistema etanol-agua 8:2. b) Experimental. c) Simulado, con las respectivas asignaciones de los índices de Miller de los picos más intensos. 76

Figura 65. Espectros de infrarrojo de (4). a) Recién sintetizado. b) Tras 24h en el sistema etanol:agua (8:2). 77

Figura 66. a) Espectro de fluorescencia de (4) y posterior a la adición de estatinas y oxoaniones. b) Emisión relativa de (4) tras la adición de los analitos sensados. 78

Figura 67. Curva de titulación fluorimétrica de (4) con ATV 78

Figura 68. Perfil de titulación de ATV por el MOF (4) en el rango de 0 a 16mM. b) Perfil de titulación completo de ATV por el MOF (4). 79

Figura 69. a) Espectro de fluorescencia de (4) con la adición de cada bioanalito. b) Histograma de la respuesta de los bioanalitos en la fluorescencia de (4). c) Histograma de la respuesta de los bioanalitos en la fluorescencia de (4) antes y después de añadir atorvastatina al sistema. d) Fotografía de las emulsiones de (4) con cada bionalito bajo la lámpara de uv a 254nm.....81

Figura 70. Espectro de infrarrojo de a) 4 tras la adición de atorvastatina y b) 4 recién sintetizado.....82

Figura 71. Difractograma de a) 4 tras la adición de atorvastatina y b) 4 recién sintetizado 82

Figura 72. Espectro de ^{13}C por la técnica CPMAS del a) MOF 4, b) Atorvastatina y c) el MOF 4 con atorvastatina. 83

Figura 73. Micrografías tomadas por SEM con su respectivo mapeo por EDS de a) cristal del MOF 4) y b) muestra del MOF 4 tratado con atorvastatina 84

Figura 74. Tiempo de vida de la fluorescencia del MOF (4) y del MOF (4) tratado con atorvastatina.85

Figura 75. a) Espectro de UV-vis de la atorvastatina en presencia del MOF durante 7 horas. b) Relación de la concentración inicial de atorvastatina sobre la cuantificada a través del tiempo. 86

Figura 76. Propuesta de la interacción entre 4 (representación capped sticks) y la atorvastatina (representación ball sticks). 87

Figura 77. Representación en superficie de los orbitales HOMO y LUMO de la interacción MOF-atorvastatina. 87

Figura 78. Espectro de fluorescencia de (4) tras cada ciclo 88

Figura 79. Difractograma de rayos X de polvos de (4) tras cada ciclo.....89

Figura 80. Espectro de infrarrojo de la atorvastatina comercial.....90

Figura 81. Espectro de fluorescencia de (4), y tras las correspondientes mediciones de atorvastatina en tabletas comerciales 90

Lista de tablas

Tabla 1. Ejemplos selectos de redes metal orgánicas aplicas en la detección luminiscente de aniones 24
Tabla 2. Datos cristalográficos para los compuestos (1-3). 39
Tabla 3. Longitudes y ángulos de enlace selectos de la esfera de coordinación del ion Zn(II) en (1). 41
Tabla 4. Enlaces de hidrógeno del polímero (1) 44
Tabla 5. Longitudes y ángulos de enlace selectos de la esfera de coordinación del ion Zn(II) en (2). 45
Tabla 6. Enlaces de hidrógeno del polímero (2) 46
Tabla 7. Longitudes y ángulos de enlace selectos de la esfera de coordinación de los átomos de Zn en (3). 48
Tabla 8. Enlaces de hidrógeno del polímero (3) 50
Tabla 9. Redes metal-orgánicas aplicadas en la detección del ion CN^- en agua 56
Tabla 10. Relación de la Magnitud de Δ con el tipo de unión del carboxilato[140] 60
Tabla 11. Modo de coordinación de los carboxilo por análisis de infrarrojo 60
Tabla 12. Picos más representativos con sus respectivos índices de Miller de difractograma (3) 65
Tabla 14. Longitudes y ángulos de enlace selectos de la esfera de coordinación del ion Zn(II) en (4). 72
Tabla 15. Longitudes y ángulos de enlace selectos de la esfera de coordinación del ion Zn(II) en (4). 73
Tabla 16. Sensores capaces de detectar atorvastatina. 80
Tabla 17. Resultados de las mediciones de atorvastatina en tabletas comerciales 91

Capítulo I: Marco teórico

1.1 PCs y MOFs

La química reticular se encarga del estudio del ensamblaje molecular a través de enlaces fuertes encaminados a la obtención de compuestos cristalinos de dos y tres dimensiones, siendo principalmente estudiados los polímeros de coordinación (PCs).[1]

Los PCs son estructuras construidas por iones metálicos unidos entre sí por ligantes orgánicos mediante enlaces covalentes y/o de coordinación, extendiéndose en 1D, 2D y 3D.[2] Arreglos cristalinos bi- y tridimensionales con nodos basados en iones o cúmulos metálicos, enlazados por ligantes orgánicos que suelen presentar porosidad, han sido definidos como “metal-organic frameworks” (MOFs).[1] Por ende, arquitecturas de tipo cadena (1D) son referidas como PCs, mientras que estructuras laminares (2D) y arreglos 3D porosos son más comúnmente llamados MOFs en lugar de PCs.[3,4]

1.2 Diseño de PCs y MOFs.

Los pilares fundamentales en los que se basan el diseño de los PCs y MOFs radican en: 1) La elección del ión metálico, considerando las características intrínsecas al metal como su carga, número de oxidación, número de coordinación y geometría. 2) La elección del ligante, inicialmente contemplando su longitud, flexibilidad o rigidez, y su capacidad de conectar múltiples centros metálicos (ditópicos, tritópicos, etc.).[2] Sin embargo, a medida que estructuras cada vez más complejas se han logrado sintetizar, fue necesario profundizar en los pilares de las síntesis buscando su entendimiento y análisis lógico.

1.2.1 Centro metálico

Para el ion metálico, se observó que diversos conjuntos de distintos metales son capaces de formar cúmulos con estructuras similares en determinadas redes, y al establecer la conectividad de estos cúmulos hacia los ligantes en formas geométricas definidas, se desarrollaron las unidades secundarias de construcción “USC” para describir la topología de los MOFs.[5–7] Uno de los ejemplos más reconocidos de USC es la “rueda de paleta” en el MOF-2 (Figura 1) con el ion Zn(II) y en el HKUST-1 con el ion Cu(II), aunque esa misma USC ha sido encontrada en una gran cantidad de metales (Ni, Co, Re, Cr, Mn, W, Tc, Os, Cd, Bi, Al, Mg, In).[8]

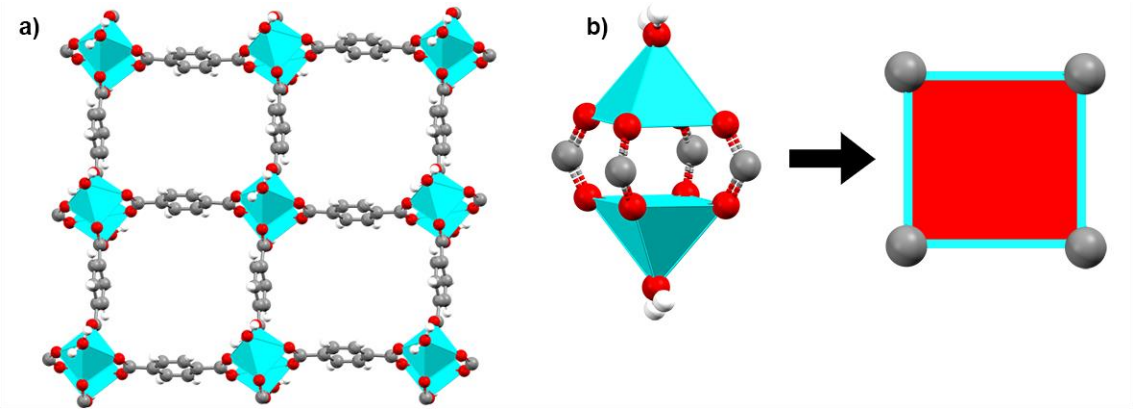

Figura 1. a) Representación poliedral del MOF-2 en los colores; Zn: azul cielo, C: gris, H: blanco, O: rojo. b) USC "rueda de paleta" que conecta a cuatro ligantes en una geometría defina por un cuadrado.[i]

Dado que una USC es una estructura común entre varios iones metálicos, el siguiente paso en la construcción de nuevos MOFs, desde la perspectiva puramente del ion metálico, fue el de utilizar dos o más iones metálicos que compartieran la misma USC,[9] en los denominados "MOFs de metales-mixtos".[10–13] Para ello existen dos metodologías posibles: colocar los múltiples iones metálicos *in situ* durante el ensamblado del MOF,[14] y en la segunda se intercambia parcialmente el ión metálico de origen por otro.[15] (Figura 2).

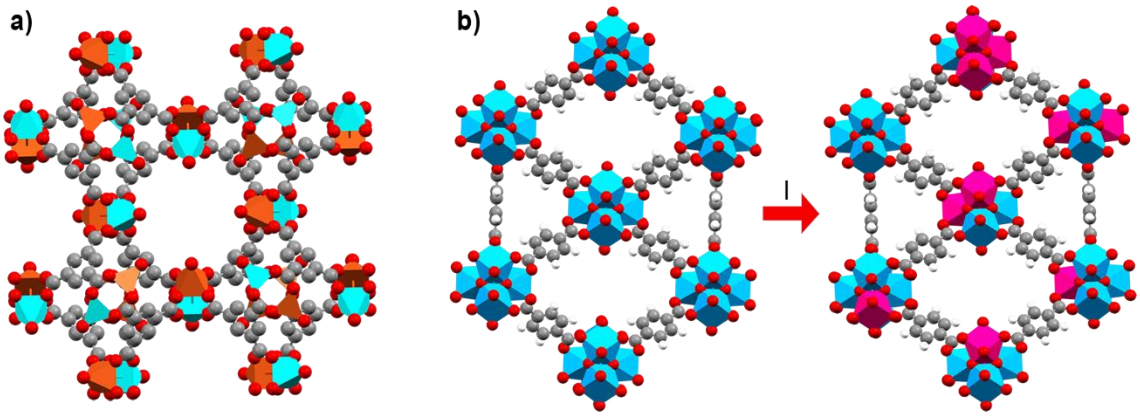

Figura 2. a) Representación poliedral del HKUST-1-Cu-Zn tras su preparación in situ en los colores; Cu: naranja, Zn: azul cielo, C: gris, H: blanco, O: rojo.[14] b) Representación poliedral de UiO-66 y UiO-66(Ti al 44%) en los colores; Zr: azul celeste, Ti: rosa, C: gris, H: blanco, O: rojo. I) Intercambio post-sintético del centro metálico Zr(IV) por Ti(IV).[15]

[i] La conectividad de las SBUs también es conocida como "punto de extensión".

Aun considerando la aproximación del diseño de un MOF por su USC, siempre existe el factor de las condiciones de síntesis, que independientemente de partir del mismo ligante e ion metálico, es posible obtener diferentes USC generando a su vez distintas estructuras.[16] Tal y como ocurre en la conversión del MOF-2 al MOF-5 modificando la temperatura,[17] o la síntesis del UHM-8 y el UHM-9 por el cambio de disolventes,[18] entre otros ejemplos.[16,19,20] Particularmente, en la sección de "Antecedentes" se describen redes metal-orgánicas con distintas USC basadas en los mismos constituyentes: el ligante ácido terfenil-3,3",5,5" tetracarboxílico (H_4tptc) (Figura 3) y el ion Zn(II), componentes del MOF protagonista del Capítulo III y cuyas distintas redes son resultado de la variaciones en las condiciones de síntesis.

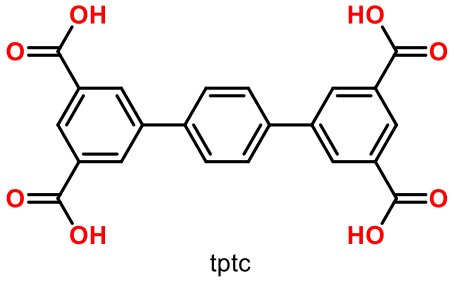

tptc

Figura 3. Ligante ácido terfenil-3,3",5,5" tetracarboxílico

Los parámetros de síntesis (temperatura, pH, disolventes, tiempo de reacción, etc.) actualmente no exhiben patrones característicos que permitan pronosticar la arquitectura de una red metal-orgánica como tiende a suceder con el centro metálico y el ligante. En su lugar, representan el conjunto de alternativas encaminadas a obtener el compuesto deseado o bien, un abanico de oportunidades para la preparación de nuevos PCs/MOFs. [16] Por ende, resulta conveniente enfocarse en los pilares del diseño sintético: el ligante y el centro metálico.

1.2.2 Ligantes

1.2.2.1 Diseño estructural

El diseño centrado en los ligantes ha sido trabajado bajo dos vertientes principales, la estructural y la funcionalización orientada a aplicaciones específicas. La estructural comprende esencialmente el desarrollo de ligantes nuevos, modificando su longitud, topicidad (el número de sitios de unión del ligante hacia el ion metálico/USC) o su orientación espacial de conectividad.[21] Esto último se encuentra relacionado a cambios en los ángulos con los que el ligante une a los nodos de la red, tal y como ocurre entre los ácidos isoftálico y el 2,5-tiofendicarboxilico de forma ejemplificativa (≈ 120° para el ácido isoftálico y ≈ 150° para el 2,5-tiofendicarboxilico ilustrado en la Figura 4).

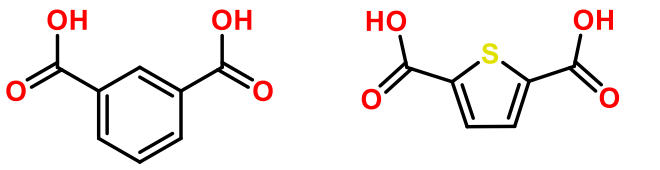

Ácido isoftálico Ácido 2,5-tiofendicarboxílico

Figura 4. Ligantes con la misma topicidad que exhiben una diferente orientación espacial de conectividad por la magnitud del ángulo entre sus grupos carboxilo.

Asimismo, existen modificaciones que pretenden mantener la misma topicidad y orientación espacial de conectividad, incorporando grupos alifáticos o aromáticos en el ligante, y/o grupos funcionales que no establezcan un enlace formal con el ion metálico.[22] Cuando los cambios en el ligante no afectan la USC ni la orientación espacial de conectividad, se mantiene la misma topología en el MOF y se les conoce como isoreticulares.[9,23] Consecuentemente, resulta interesante estudiar si las funcionalizaciones en el ligante tendrán un impacto en el arreglo arquitectónico de las redes metal-orgánicas ya que son comúnmente difíciles de predecir. Destacan particularmente, los casos de los derivados del MOF-177, con numerosos ejemplos de modificaciones en su ligante H_3BTB = 4,4´,4´´-bencen-1,3,5-triyl-tris(ácido benzoico), manteniéndose todos como MOFs isoreticulares (Figura 5).[11] Y en contraste, la serie NU-903 (también conocido como Zr-CAU-24),[24,25] 904 y 1008, donde sustituciones simples en el ligante por el grupo -NO_2 y -Br tuvieron un rol preponderante en la red a pesar de ser grupos que no extienden la conectividad de la red, ni interaccionan con los centros metálicos (Figura 6).[26]

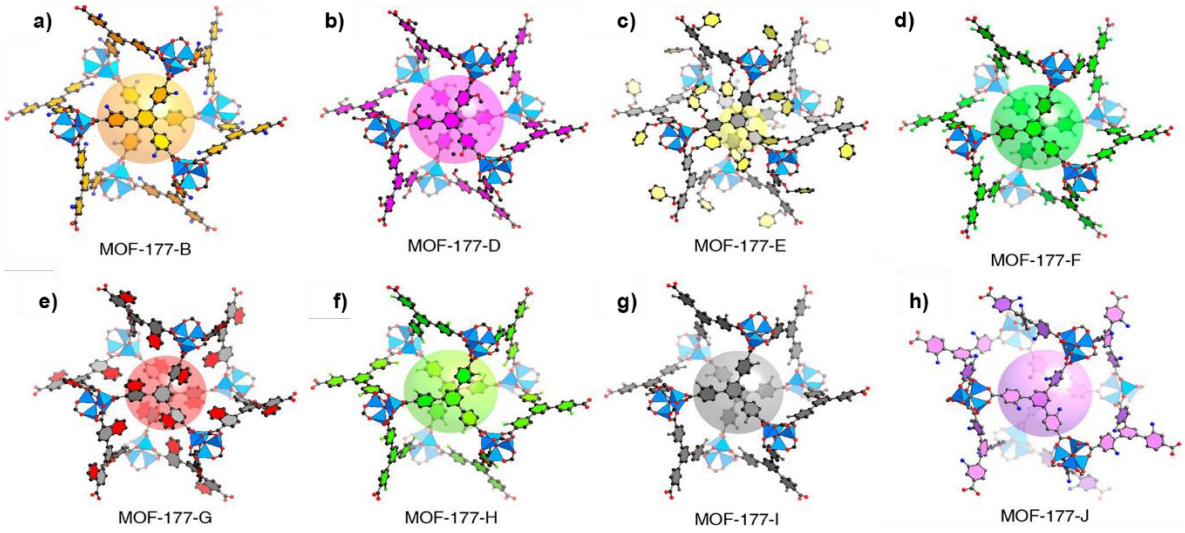

Figura 5. Imagen modificada de la referencia 15 donde cada inciso corresponde a una modificación del ligante manteniendo la red isoreticular para cada derivado del MOF-177 a) = H_3BTB; b) H_3BTB-NH_2, c) H_3BTB-NO_2, d) H_3BTB-OCH_3, e) H_3BTB-OC_7H_7, f) H_3BTB-F_2, g) H_3BTB-C_4H_4, h) H_3BTB-F[11]

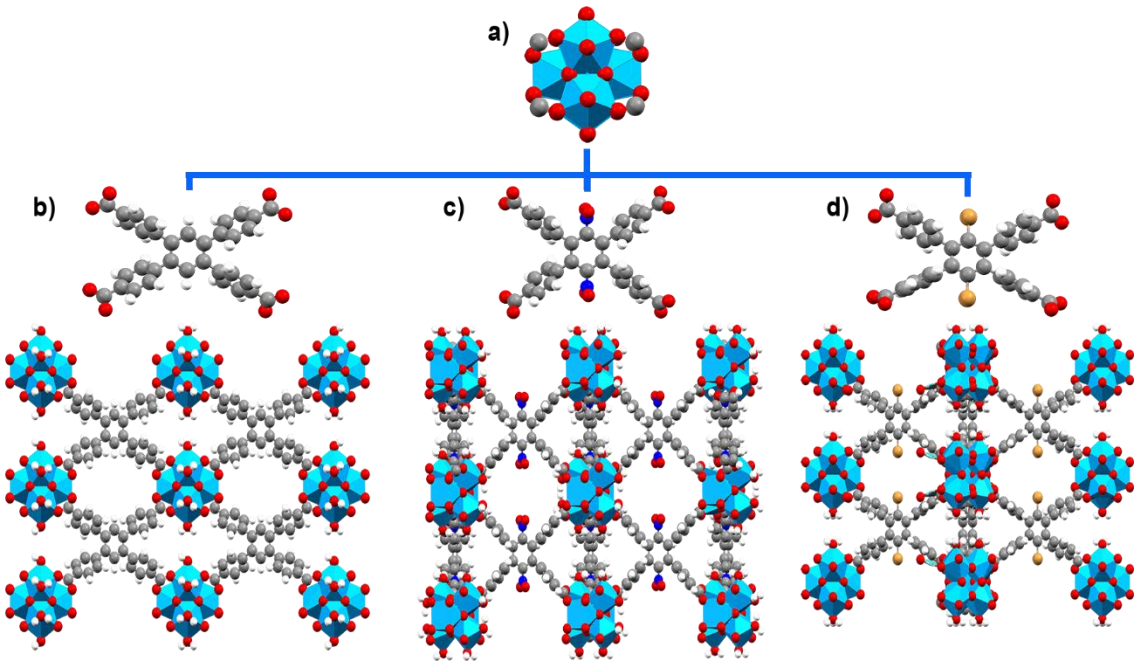

Figura 6. a) USC común para los MOFs NU-903, NU-904 y NU-1008. b) Representación poliedral del NU-903 con el ligante TCPB en una red scu. c) Representación poliedral del NU-904 con el ligante TCPB-NO_2 en una red shp. d) Representación poliedral del NU-1008 con el ligante TCPB-Br en una red csq. [ii] Los colores de las representaciones corresponden Zr: azul celeste, C: gris, N: azul marino, H: blanco, O: rojo, Br: café claro.[26]

1.2.2.2 Diseño orientado a aplicaciones

El basto conjunto de aplicaciones que han encontrado las redes metal orgánicas en los años recientes (adsorción de gases,[27,28] catálisis,[29,30] biomédicas,[31–33] ambientales[34,35] y la detección luminiscente[36–38]) ha permitido que el diseño de nuevos ligantes haya sido enfocado hacia la funcionalización selectiva acorde a sus aplicaciones.

En cada área de aplicación, se han establecido ciertas bases a tomar en cuenta en el diseño del ligante en la construcción de PCs y MOFs que mejoren su desempeño. Específicamente, en el sensado luminiscente, existen una serie de variables a considerar, tanto del ligante como del centro metálico, pero antes de profundizar en ellas, es necesario hacer una breve mención de los aspectos básicos de la luminiscencia, de tal forma que se facilite su comprensión hacia su diseño funcional.

[ii] La base de datos de los tipos redes puede ser consultada en http://rcsr.anu.edu.au/

1.2.2.2.1 Fundamentos de luminiscencia

La luminiscencia es el fenómeno mediante el cual se emite luz durante el proceso de relajación tras haber absorbido energía.[39] El mecanismo de la luminiscencia consiste en la absorción de energía para promover a un electrón del estado basal S_0 hacia el estado excitado.[38] Dependiendo de la naturaleza del estado excitado, la luminiscencia se clasifica en fluorescencia y fosforescencia[40] (ver Figura 7).

En la fluorescencia, la emisión de fotones proviene de estados de la misma multiplicidad de espín del electrón, desde nivel energético excitado S_1 al basal S_0 y, con una duración no mayor a los 10 nanosegundos.[38,39] En contraste, en la fosforescencia ocurre un cambio en la multiplicidad del espín y el proceso tiene una duración superior a los microsegundos. Adicionalmente, es posible la existencia de un nivel energético superior denominado S_2 a partir de cual, por "conversión interna", el electrón puede regresar al estado energético S_1 para relajarse por el proceso de fluorescencia, o bien, ocurrirá un "cruce intersistemas" donde la multiplicidad de espín del electrón cambiará y llegará al nivel energético T_1, mismo que dará origen a la fosforescencia.[38,39,41] De forma gráfica, ambos procesos son ilustrados en el diagrama de Jablonksi (Figura 7), el cual incluye a su vez, los niveles de relajación vibracionales.

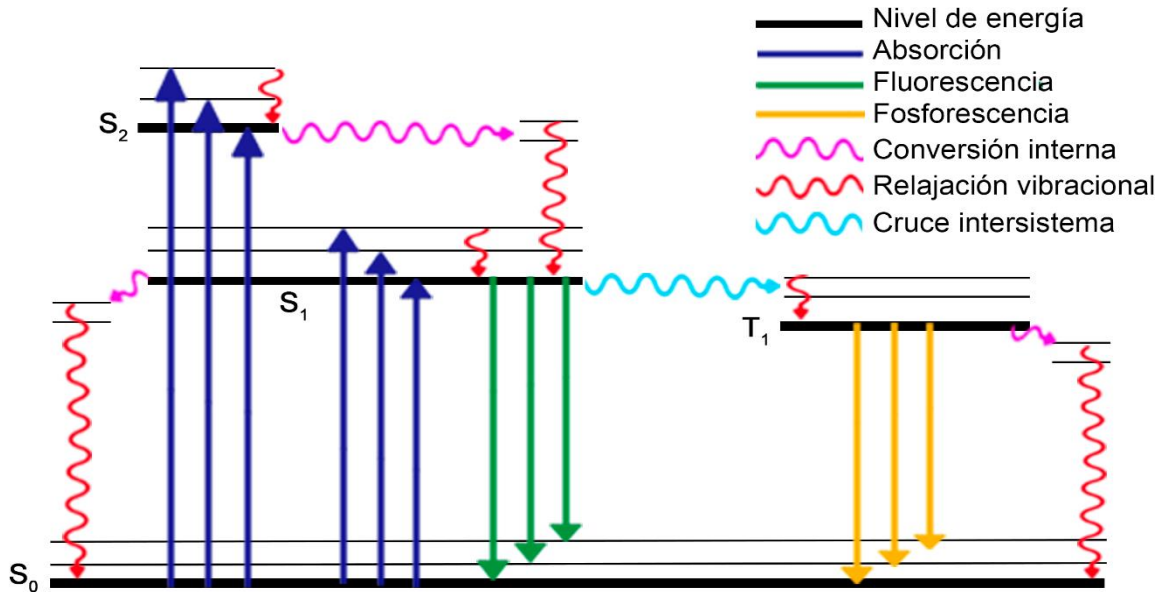

Figura 7. Diagrama de Jablonski

Las propiedades luminiscentes son caracterizadas por tres parámetros: 1) el espectro de luminiscencia, graficando la intensidad de emisión en función de la longitud de onda, 2) el rendimiento cuántico (*Q*), que describe la eficiencia del proceso de emisión como el cociente del número de fotones emitidos con

respecto a los fotones absorbidos, y 3) el tiempo de vida (T), que consiste en el tiempo promedio en el cual la molécula pasa del estado excitado al estado basal antes de emitir fotones y, que es inversamente proporcional a la suma de sus constantes de relajación radiativas (emisión de fotones, denominada por k_r) y no radiativas (vibracionales y térmicas, k_{nr}) mostradas en la ecuación (1).[39,42]

$$T = \frac{1}{k_r + k_{nr}} \qquad \text{Ecuación (1)}$$

Dichos parámetros permiten el uso de la luminiscencia como una herramienta rápida, repetible y suficientemente sensible para la detección de analitos.[42] Por consiguiente, cambios ocurridos en cualquiera de ellos, ofrecen información útil sobre la interacción del analito con el sensor, su selectividad y/o sensibilidad.[43] Comúnmente, los PCs y MOFs ven afectados los parámetros de sus propiedades luminiscentes a través de uno o la combinación de 2 mecanismos principales: la transferencia electrónica fotoinducida (PET: photoinduced electron transfer) y la transferencia de energía de resonancia Förster (FRET: Förster resonance energy transfer) .[41]

1.2.2.2.1.1 Transferencia electrónica fotoinducida

El mecanismo PET involucra proceso redox interno entre los estados excitados del fluoróforo y otra molécula que acepta o dona electrones provocando en ambos casos la disminución de la luminiscencia o apagamiento.[38]

Se considera una transferencia electrónica reductiva cuando los orbitales HOMO (highest occupied molecular orbital) y LUMO (lowest unoccupied molecular orbital) del fluoróforo excitado son de menor energía que los del agente apagador con la que entran en contacto, de tal forma que se promueve el electrón del HOMO del agente apagador hacia el orbital LUMO del fluoróforo.[44] En la transferencia electrónica oxidativa, el fluoróforo excitado actúa como donador del electrón, debido a que sus orbitales HOMO y LUMO son energéticamente superiores al del agente apagador, promoviendo el electrón del LUMO del fluoróforo excitado al LUMO del agente apagador.[44] Ambas representaciones del mecanismo PET se exponen en la Figura 8.

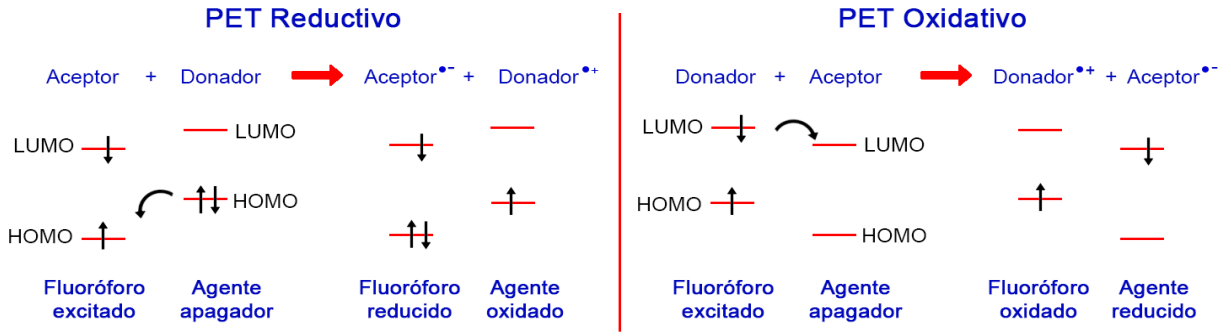

Figura 8. Mecanismo PET reductivo y PET oxidativo.[44]

Los PCs y MOFs luminiscentes actúan como aceptores de electrones al interactuar con analitos con grupos ricos de electrones en un mecanismo PET reductivo, mientras que su rol se invierte al ser los donadores de electrones ante moléculas deficientes de densidad electrónica a través del mecanismo PET oxidativo.[38,44]

1.2.2.2.1.2 Transferencia de energía de resonancia Förster

Tras la absorción de energía por parte del fluoróforo (donador), su banda de emisión puede coincidir con la banda de absorción de un analito (aceptor), ese traslape de bandas derivan en el apagamiento de la luminiscencia y se denomina mecanismo FRET (ver Figura 9).[44,45] Particularmente, es frecuente encontrar ese mecanismo en MOFs luminiscentes porosos con la capacidad de almacenar o interaccionar con iones y/o moléculas apagadoras de la luminiscencia.[46,47]

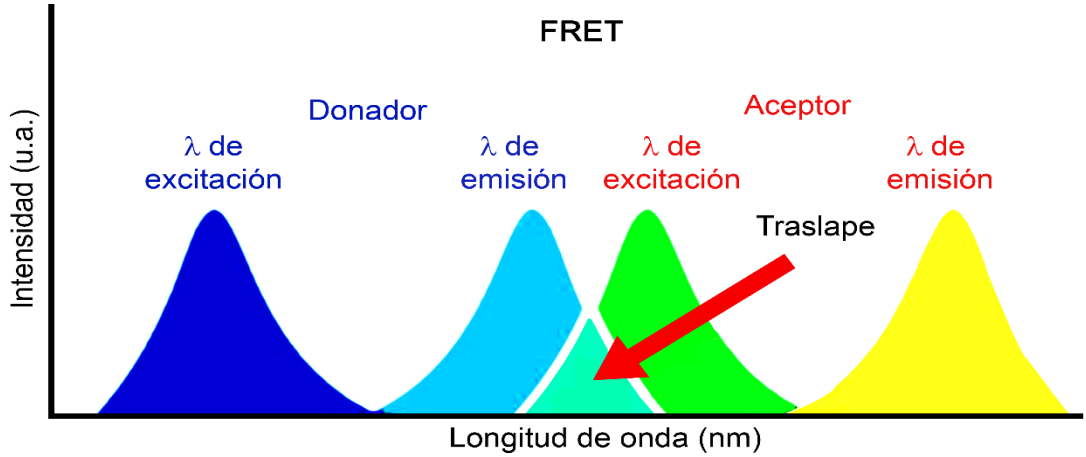

Figura 9. Mecanismo FRET ilustrado en un espectro de luminiscencia.[48]

1.2.2.3 Construcción de PCs y MOFs luminiscentes

La mayoría de los PCs y MOFs luminiscentes, absorben energía a través de un haz de luz incidente, siendo la principal causa de que sean considerados fotoluminiscentes.[38–41] Sus procesos de emisión ya sea por fluorescencia o fosforescencia, dependen principalmente de la elección de sus componentes y

del posible arreglo estructural que limita los procesos de relajación vibracionales.[38–41,43] Asimismo, en algunos casos, también se ven afectados por su capacidad de fungir como anfitriones de moléculas huéspedes con cualidades luminiscentes propias.[49,50] En los siguientes apartados se profundiza en el estudio detallado de los constituyentes desde la perspectiva del diseño de redes metal orgánicas luminiscentes buscando la comprensión de sus propiedades fotofísicas, puntualizando en los mecanismos que le dan origen, según sea el caso correspondiente.

1.2.2.3.1 Centro metálico

Nodos con iones metálicos de capa cerrada o diamagnéticos son candidatos a tener emisiones considerables, tal es el caso de los metales alcalino, alcalino térreos, metales del bloque d con configuración d^{10} o d^{0}, y algunos cationes metálicos provenientes del bloque p como In^{+3} y Pb^{2+}.[43] Los metales paramagnéticos tienen poca emisión o carecen de ella, debido a que al recibir energía, exhiben transiciones electrónicas de entre sus orbitales semi llenos evitando que el proceso de relajación al estado basal ocurra en fuentes no radiativas, a diferencia de como sucede en la mayoría de los metales diamagnéticos.[39,40]

Los iones lantánidos por sí mismos, no son muy aptos para absorber luz eficientemente debido a transiciones electrónicas prohibidas entre los orbitales ***f*** dadas las reglas de selección de Laporte,[36,40] no obstante, pueden presentar fuerte emisión al unirse a ligantes capaces de absorber energía y transferir esa energía al lantánido en un fenómeno denominado como efecto antena.[36,39,43]

Al mecanismo que da origen de la luminiscencia únicamente por el centro metálico, se le conoce como “centrada en el metal “ (CM) aunque no es frecuentemente encontrado ya que la mayoría de los PCs y MOFs suelen utilizar ligantes que contribuyen a las propiedades luminiscentes.[41] La simbiosis que ejercen los centros metálicos con sus ligantes para emitir fotones, sucede mediante los mecanismos de transferencia de carga metal-ligante (TCML) o ligante-metal (TCLM). La elección del mecanismo por TCML o TCLM, está asociada al menor nivel energético del estado excitado de la red metal-orgánica. Si el menor nivel energético del estado excitado del ligante es inferior a la del metal, la transferencia de carga irá del metal al ligante para la emisión de luz (TCML), situación contraria que ocurre en TCLM y que se aprecia en la Figura 10.[38] El mecanismo TCLM se ve favorecido en iones metálicos diamagnéticos y en los lantánidos, mientras que en los paramagnéticos del bloque *d*, suele ser por TCML, recayendo más la tarea de la emisión por parte del ligante.[41]

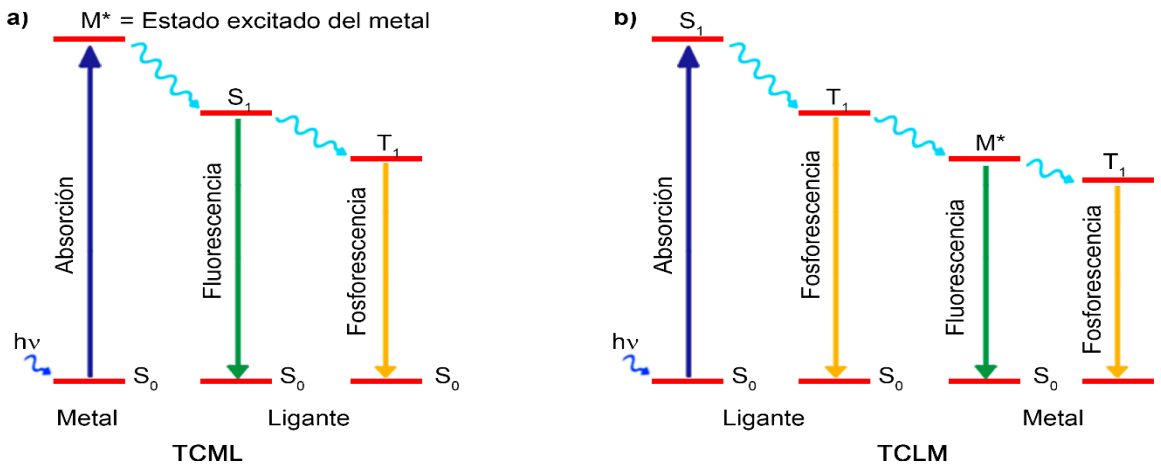

Figura 10. a) Mecanismo TCML. b) Mecanismo TCLM.[38]

1.2.2.3.2 Ligante

Una de las aproximaciones más comunes para propiciar la luminiscencia en ligantes orgánicos, es la de utilizar aquellos que presenten sistemas π-conjugados, debido a que suelen exhibir altas absorciones y emisiones de fotones, ocasionadas por sus transiciones electrónicas.[36] Otra estrategia recurrente, tiende a utilizar ligantes rígidos, mismos que limitan el grado de libertad de movimiento de la estructura del CP/MOF, atenuando con ello los procesos de relajación vibracionales, e incrementando su emisión. [43]

Notablemente, ambos enfoques convergen en el uso de ligantes aromáticos, cuya conjugación y rigidez innata, los hace buenos candidatos para favorecer las propiedades luminiscentes. Dentro del uso de ligantes aromáticos, varias alternativas en su funcionalización incorporan la fusión con otros anillos aromáticos capaces de extender la conjugación π y a la sustitución de átomos de hidrógeno por otros átomos o grupos funcionales con la misma finalidad o bien, que estén orientados a la disminución del relajamiento por procesos no radiativos.[43] Entre los numerosos ejemplos de ligantes que cumplen la primera de estas características destacan el ligante ácido terfenil-3,3”,5,5” tetracarboxílico cuyos MOFs luminiscentes son detallados en la sección de antecedentes. Por su parte, la disminución de los procesos vibracionales en el apagamiento de la fluorescencia de redes metal-orgánicas, puede verse favorecida por la sustitución de átomos de hidrógeno por grupos alquilo como se plantea en el uso de derivados de 2,2’-bipiridina ligantes base del capítulo II, y cuyos ejemplos pueden consultarse en la sección de antecedentes.

Independientemente de las modificaciones que contemple el ligante para mejorar sus propiedades luminiscentes, la emisión del CP/MOF únicamente causada por el ligante (“centrada en el ligante” (CL)) es poco frecuente ya que el planteamiento sintético pretende brindar las mejores ventajas posibles en

la combinación del sistema metal-ligante,[41] remitiendo nuevamente al origen de la luminiscencia por los mecanismos TCLM y TCLM.

En la Figura 11 se exponen la totalidad de los mecanismos descritos con respecto al diseño del CP/MOF luminiscente basado en la elección del metal y del ligante.

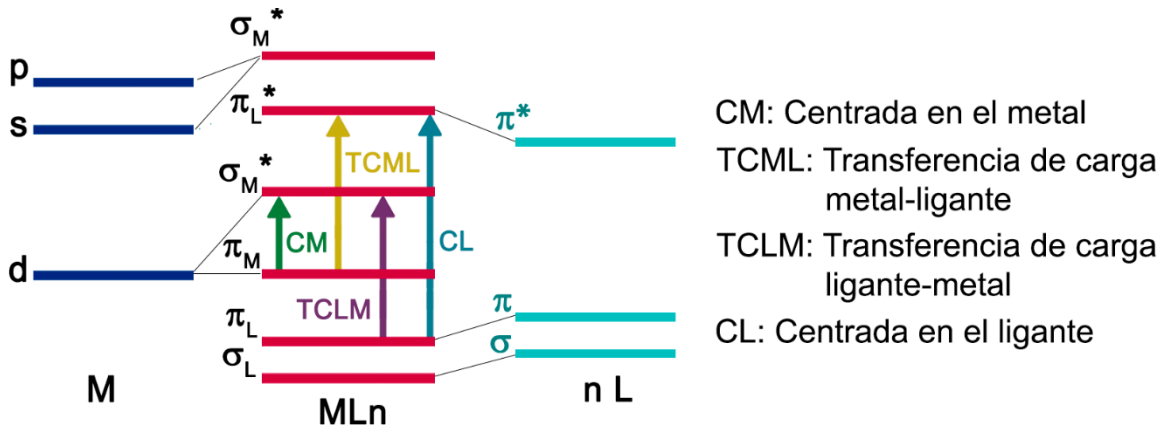

Figura 11. Mecanismos que dan origen a la luminiscencia en los PCs y MOFs.

Es de mencionar que existen agentes externos a los constituyentes del CP/MOF, los cuales poseen propiedades luminiscentes intrínsecas y pueden potenciar la emisión del sensor. Fluoróforos orgánicos como los colorantes,[49,51] iones lantánidos[52,53] y nanopartículas de ciertos metales como Ag[54] y Au,[55] destacan entre las principales opciones de iones y moléculas huéspedes que propician la emisión. La importancia de adicionar esos agentes externos con luminiscencia inherente se justifica en la mejora de dichas cualidades, al disminuir el apagamiento por aglomeración tras encontrarse localizados en una matriz (como lo es el CP/MOF) y en esa misma restricción de movimiento, se promueve el proceso de relajación radiativo.[55,56]

De forma general, el uso de PCs/MOFs como sensores luminiscentes debe de conllevar 1) su estabilidad química, específicamente para las condiciones en las que se realiza el sensado, 2) una respuesta óptica de luminiscencia estable y reproducible, de forma que sus determinaciones puedan ser validadas, y 3) sitios específicos de reconocimiento donde exista la interacción con el analito objetivo a sensar, generando el cambio medible en la respuesta óptica, parámetros que son representados en la Figura 12.

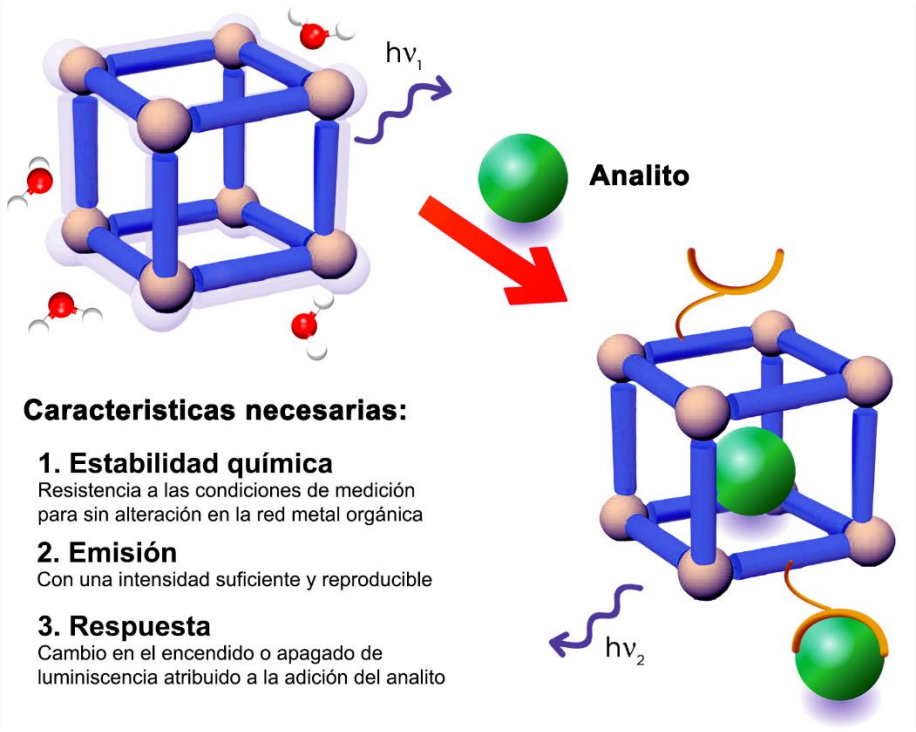

Figura 12. Cualidades deseadas en una red metal orgánica para su uso como sensor luminiscente

En conjunto, el comprender las bases del diseño en la construcción de PCs y MOFs luminiscentes, permite dar el siguiente paso hacia sus aplicaciones en el sensado de diversos analitos.

1.2.2.4 Aplicaciones de PCs y MOFs luminiscentes en el sensado

Existen numerosos analitos a los que están dirigidos la detección luminiscente por parte de MOF y PCs, principalmente agentes contaminantes del medio ambiente. Entre ellos se puede mencionar a los solventes como: MeCN,[57] THF,[58] acetona,[59,60] DMF,[61] DCM,[62] piridina,[63] anilina,[64] entre otros.[65–68] Importantemente, algunos de ellos como el $\{[Zn_2(\mu_2\text{-BDC})_2(i\text{Q})_2]\}_n$ (BDC = ácido tereftálico , *i*Q = isoquinolina) un derivado del MOF-2 que incorpora a su diseño la isoquinolina como ligante fluorescente, es aplicado al sensado de isómeros de xilenos, por un incremento selectivo en la fluorescencia para el isómero -*para* con respecto a los -*orto* y -*meta* (Figura 13).[69]

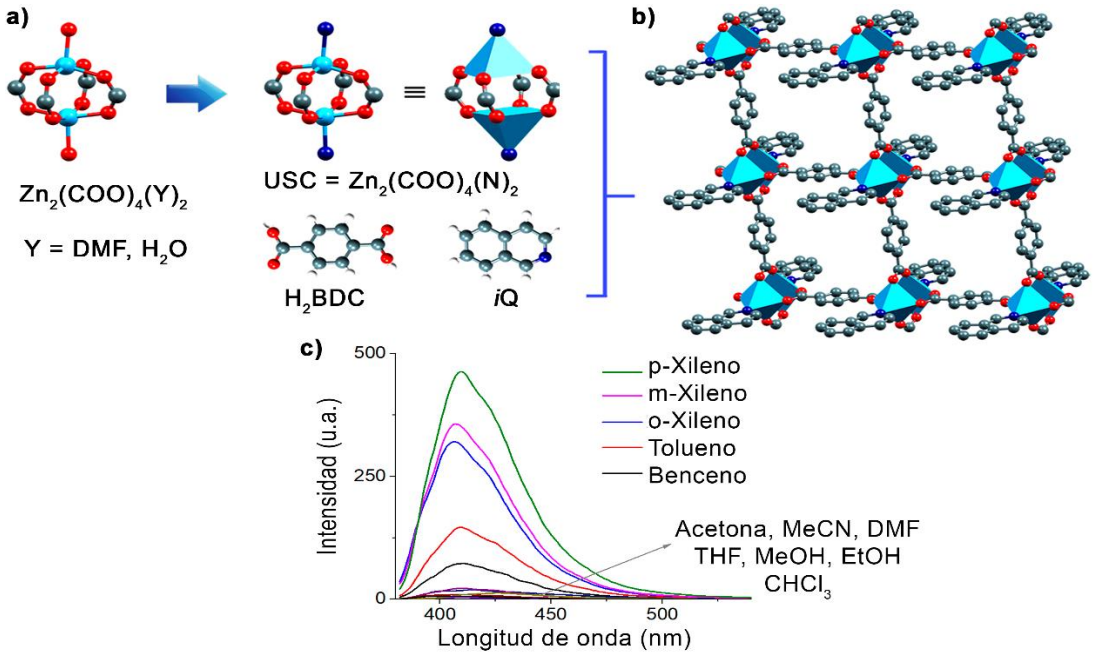

Figura 13. a) USC del {[$Zn_2(\mu_2\text{-}BDC)_2(iQ)_2$]}*n*. en los colores; Zn: azul cielo, C: gris, H: blanco, O: rojo. b) Estructura laminar del MOF. c) Espectro de fluorescencia del MOF en presencia de diferentes solventes.[69]

Otro contaminante común son los nitrocompuestos, que si bien pueden ser utilizados algunos como disolventes,[70,71] la detección fluorescente por parte de estos materiales metal-orgánicos, se ha aplicado principalmente en explosivos[72–74] y pesticidas.[75–82] Como se ha discutido en la sección anterior, moléculas con el grupo nitro suelen ser apagadoras de la fluorescencia por lo que son buenos candidatos a sensar. Por ende, en la literatura es común encontrar varios reviews acerca de la detección fluorescente de explosivos[73,83,84] y, recientemente, han empezado a emerger aquellos que discuten los centrados en pesticidas[85,86] como el *frontier "Efficient chemosensors for toxic pollutants based on photoluminescent Zn(II) and Cd(II) metal–organic networks"* que incluye aspectos de los mecanismos de sensado y un compendio de PCs y MOFs basados en los iones Zn(II) y Cd(II) utilizados en el monitoreo de herbicidas y pesticidas (Figura 14).

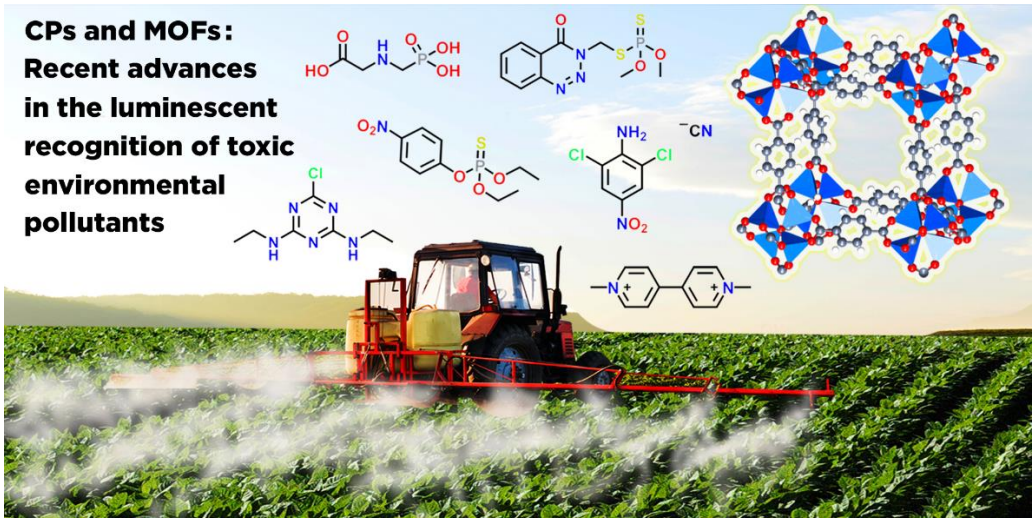

Figura 14. Graphical abstract de "Efficient chemosensors for toxic pollutants based on photoluminescent Zn(II) and Cd(II) metal–organic networks".

Los cationes metálicos también son considerados una fuente importante de contaminación, sobre todo aquellos metales pesados que suelen ser considerablemente tóxicos para el ser humano, por lo que su detección a través de PCs y MOFs ha sido abordada hacia cationes como Hg(II),[61,87] Cd(II),[58] Pb(II).[64,88] Mientras que también se han dirigido su atención a cationes metálicos con interés biológico, tal es el caso de Ca(II),[89] Fe(II/III),[98,100,101] Cu(II)[88] y Zn(II).[41,92]

Por su parte, en el desarrollo industrial en la producción reactivos, moléculas de interés farmacéuticos y catalizadores, generan la producción extensiva de aniones inorgánicos cuya deposición en suelos y cuerpos de agua representan una amenaza ambiental considerable.[65] La mayor parte de las redes metal orgánicas luminiscentes empleadas como sensores, se han limitado a la detección de los aniones CrO_4^{2-}, $Cr_2O_7^{2}$, MnO_4^{-} y en menor proporción a algunos otros aniones como halogenuros, arseniatos y fosfatos.[35,66,90,93,94] Dentro de esta misma búsqueda, resalta el ion cianuro, quien, pese a su alta toxicidad, solo existen contados ejemplos de PCs y MOFs que sean capaces de detectarlo, mismos que son abordados a detalle en la sección de antecedentes. En la Tabla 1 se realiza un recopilatorio de redes metal orgánicas aplicadas a la detección de aniones.

Tabla 1. Ejemplos selectos de redes metal orgánicas aplicas en la detección luminiscente de aniones

Red	Anión	Límite de detección	Referencia
$\{[Zn_2(tpeb)_2(2,3\text{-}ndc)_2]\cdot H_2O\}_n$	$Cr_2O_7^{2-}$	8.58×10^{-9}	95
	CrO_4^{2-}	7.23×10^{-9}	95
$\{[Zn(ATA)(L_1)]\cdot H_2O\}_n$	$Cr_2O_7^{2-}$	4.30×10^{-7}	95
	CrO_4^{2-}	2.50×10^{-7}	95
$[Zn_2(mtrb)_2(btec)].H_2O\}_n$	$Cr_2O_7^{2-}$	3.05×10^{-7}	96
	CrO_4^{2-}	5.72×10^{-7}	96
$[Zn_2(BDC)_{1.5}(L_2)(DMF)]\cdot 1.5DMF$	MnO_4^-	3.00×10^{-8}	97
	$Cr_2O_7^{2-}$	3.00×10^{-8}	97
	CrO_4^{2-}	3.00×10^{-8}	97
$[Zn(2\text{-}bpeb)(BDC)]_n$	$Cr_2O_7^{2-}$	1.44×10^{-3}	98
	MnO_4^-	2.70×10^{-5}	98
$[Zn_4Eu_2(imdc)_4(SO_4)(H_2O)8] \cdot 4H_2O\}_n$	I^-	---	99
$\{[Cd(IPA)(L_7)]\}_n$	$Cr_2O_7^{2-}$	1.20×10^{-5}	100
	CrO_4^{2-}	1.83×10^{-5}	100
$\{[Cd(ATA)(L_1)]\cdot 2H_2O\}_n$	$Cr_2O_7^{2-}$	$1.90. \times 10^{-7}$	95
	CrO_4^{2-}	1.80×10^{-7}	95
$[Cd(2\text{-}bpeb)_{0.5}(CNA)(H_2O)]_n$	MnO_4^-	7.79×10^{-5}	101
	$Cr_2O_7^{2-}$	3.70×10^{-4}	101
$[Cd(2\text{-}bpeb)_{0.5}(NDC)]_n$	MnO_4^-	1.31×10^{-4}	101
	$Cr_2O_7^{2-}$	9.20×10^{-5}	101
$Cd(bbi)H_2L_3$	Ceftriaxona de sodio	9.25×10^{-5}	102
$[Cd_{2.5}(PDA)(trz)_3]_n$	I^-	6.30×10^{-7}	103
NH_2-MIL-101(Al)	F^-	5.26×10^{-5}	104

tpeb = 1,3,5-tri-4- piridil-1,2-etilenilbenceno, ndc = ácido naftalendicarboxilico, ATA = ácido 2-amino-1,4-bencendicarboxilico, L_1 = 4-piridil carboxaldehido isonicotinoilhidrazona, mtrb = 1,3-bis(1,2,4-triazol-4-ilmetil)benceno, btec = ácido 1,2,4,5-bencentetracarboxílico, BDC ácido tereftálico, L_2 = ácido piridin 4-carboxílico, 2-bpeb = 2-(4-((E)-2-(piridin-2-il)vinil)stiril)- piridina, imdc = ácido imidazol-4,5-dicarboxilico, IPA = ácido isoftálico, CNA = ácido 4-carboxilcinamico, NDC = ácido 2,6-naftalendicarboxilico, bbi = 1,4-bis(2- metil-imidazol-1-il)butano and L_3 = ácido 1,2-fenilendiacetico, PDA = ácido 1,4-fenilendiacetico, tz = 1,2,4-triazol.

Finalmente, la gama de los fármacos ha tomado mayor relevancia como moléculas objetivo a detectar dentro del ámbito de los materiales híbridos metal-orgánicos cristalinos, ya sea por aspectos contaminantes dada su difícil degradación y los metabolitos subsecuentes que tienden a terminar en

cuerpos de agua tras la excreción de su uso; así como por su interés clínico. Entre ellos es común el sensado de antibióticos que tengan en su estructura al grupo nitro,[79,81,105] como derivados de la familia de la nitrofurazona[106] y fármacos como ceftriaxona,[107] tretraciclina,[108] sulfametazina[109,110] y ciprofloxacino,[111] entre otros.[112] En lo concerniente a fármacos del tipo iónico, solo existen limitados ejemplos en la literatura para los cationes farmacéuticos palmatina y berberina. Mientras la ceftriaxona de sodio pertenece al único caso de un fármaco aniónico sensados por una red metal-orgánica. Ante esta oportunidad, en lo que constituye una corriente creciente de analitos objetivo, el presente trabajo busca extender en el sensado de aniones farmacéuticos con derivados de la familia de las estatinas. Las estatinas son medicamentos comúnmente recetados contra la hipertensión e hipercolesterolemia, enfermedades recurrentes en la población mexicana, y una red metal orgánica pudiese ser una alternativa en su monitoreo antes de que puedan ser considerados como contaminantes emergentes.

1.2.3 Antecedentes I: Estructurales

1.2.3.1 Redes metal-orgánicas con derivados alquílicos de 2,2'-bipiridina y el ligante puente el ácido 1,4-ciclohexendicarboxílico

El uso de ligantes derivados de 2,2´-bipiridina con grupos alquilo y el ácido 1,4-ciclohexendicarboxílico han sido empleados en redes metal-orgánicas luminiscentes de Cd(II). El estudio contempla la síntesis de cuatro polímeros de coordinación con los ligantes: 1,10-fenantrolina, 4,4-dimetil-2,2'-bipiridina (4,4-dmbp), 5,5-dimetil-2,2'-bipiridina (5,5-dmbp) y 4,4-diterbutil-2,2'-bipiridina (4,4-dtbp) (Figura 15). De los resultados obtenidos, aquellos CPs con sustituciones del átomos de hidrógeno en las posiciones 4,4- y 5,5- en la bipiridina son los que exhiben mayor intensidad fluorescente. Aunado a ello se analizó que la incorporación de un grupo metilo a la 2,2´-bipiridina no ejerce de una influencia estructural relevante ya que se mantiene la misma topología de red para los PCs basados en los ligantes 4,4-dmbp y 5,5-dmbp. En cambio, el uso de 4,4-dtbp como ligante auxiliar generó un polímero de una topología de red inédita 2D modificando por completo la estructura polimérica exhibida por sus similares (Figura 16). El conjunto de polímeros bidimensionales con ligantes derivados de 2,2´-bipiridina también fue estudiado por sus propiedades de luminiscencia, resaltando el CP con el ligante 4,4-dtbp en su aplicación en el sensado de acetonitrilo.

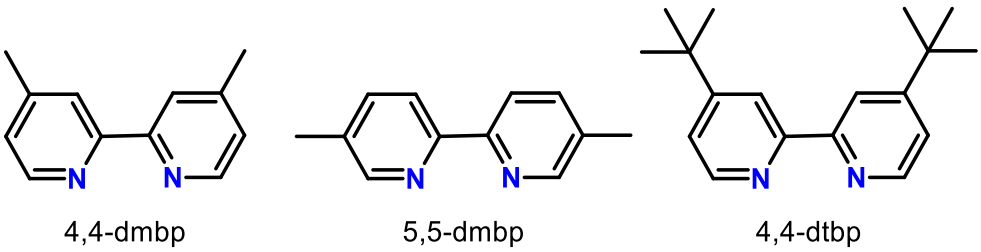

Figura 15. Ligantes derivados de la 2,2'-bipiridina

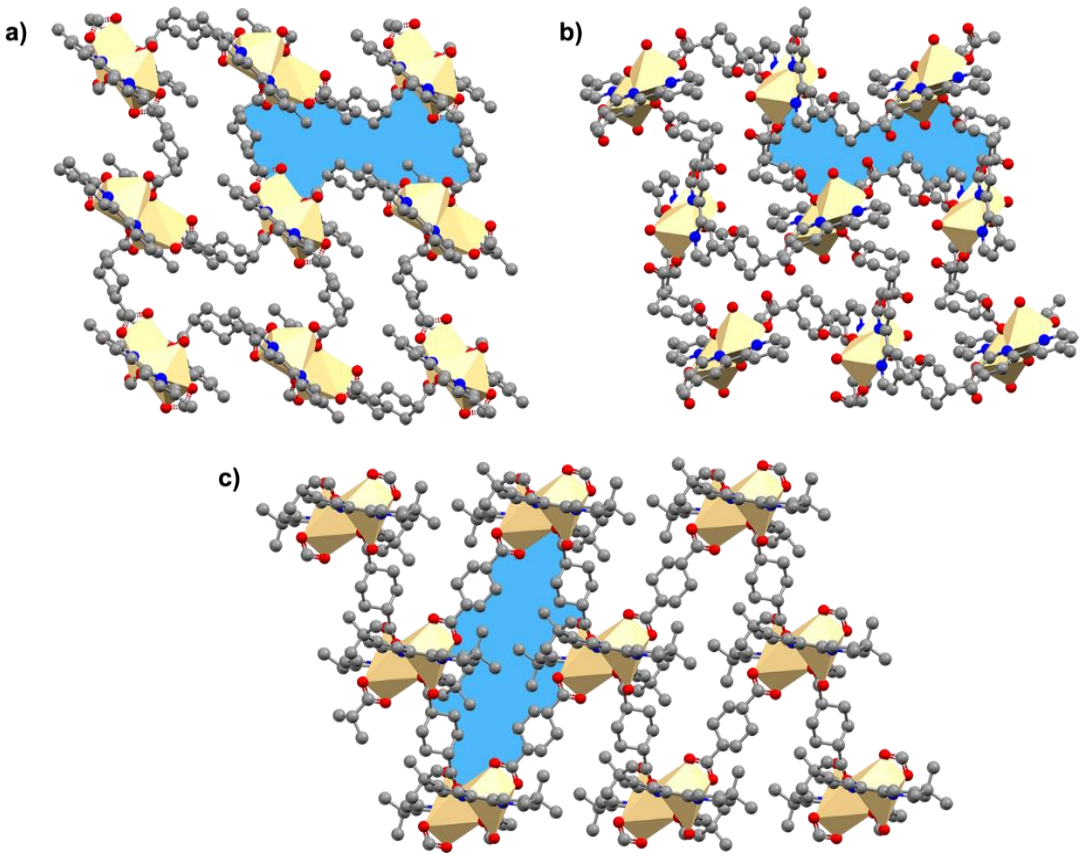

Figura 16. Representación poliedral de los polímeros de coordinación de Cd(II) con el ligante puente 1,4-chdc y los ligantes auxiliares luminiscentes a) 4,4-dmbp b) 5,5-dmbp y 4,4-dmbp en los colores Cd: beige, C: gris, H: blanco, O: rojo, N: azul marino. En color azul se rellenado los ciclos de la red denotando la misma topología para a) y b).

No existe otro antecedente directo que combine ambos ligantes en una red metal orgánica y que sea empleado en la detección luminiscente de algún analito.

1.2.3.2 Redes metal-orgánicas con el ligante tptc y el ion Zn(II)

El ligante tptc (Figura 3) es uno de los constituyentes frecuentemente empleados en la familia de MOFs de la Universidad de Nottingham (NOTT-MOFs) con el ion central Cu(II).[113–116] En lo que respecta a su uso con nodos centrales con base a átomos de Zn(II), existen tres diferentes MOFs, cada uno de ellos con una USC distinta y que fue obtenida al variar el uso de diferentes disolventes.[117]

Al emplear DMA (N,N-dimetilacetamida) como disolvente, se obtiene el MOF $[Zn_2(tptc)(DMA)(H_2O)]\cdot 2.5H_2O\cdot 3.5DMF$ **(A1)** (Figura 17). Las moléculas de agua presentes en el MOF

provienen del uso de la sal $Zn(NO_3)_2 \cdot 6H_2O$. Su USC está integrada por dos átomos de Zn(II) cristalográficamente independientes penta-coordinados, que unen a cuatro carboxilatos del ligante tptc a través de una unión tipo enlace μ_2-η^1:η^1 ($Zn_2(COO)_4$), estableciendo una conectividad de la USC definida por un tetrahedro.[117] Además, quedan en la USC puntos terminales de red (moléculas que no extienden la conectividad de la red) por la coordinación de las moléculas de disolvente DMA y H_2O. Cada ligante conecta a cuatro USCs, generando una arquitectura 3D con canales triangulares a lo largo del eje cristalográfico *a* en una red tipo ***lon.***[iii]

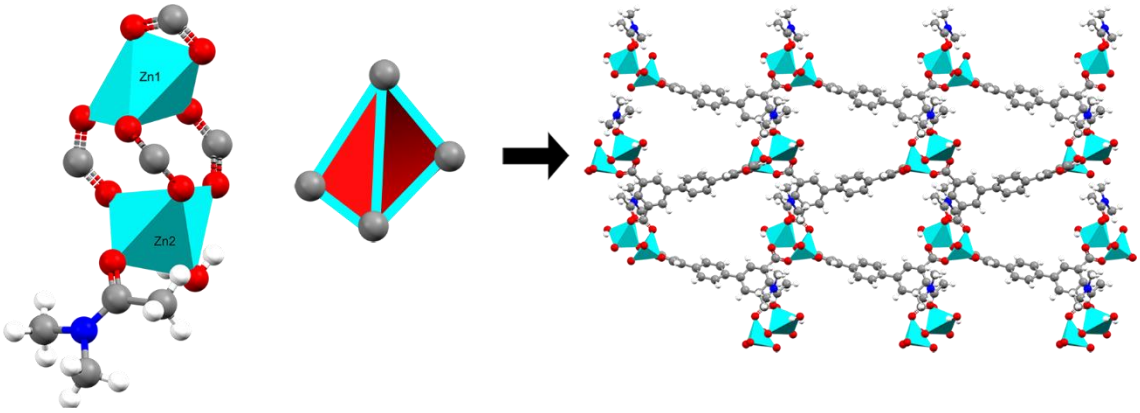

Figura 17. Representación poliedral del MOF A1, con la USC tetraédrica que constituye la arquitectura 3D con canales triangulares, en los colores; Zn: azul cielo, C: gris, H: blanco, O: rojo, N: azul marino.

Cuando se hace uso de DMF en lugar de DMA, el resultado es el MOF $[Zn_2(tptc)(DMF)_3] \cdot 4H_2O \cdot 5.5DMF$ **(A2)** (Figura 18). El MOF posee una USC constituida por dos centros metálicos de Zn(II) hexacoordinados, y al igual que en **(A1)**, son cristalográficamente distintos. La USC ($Zn_2(COO)_4$), conecta a cuatro ligantes tptc en tres diferentes modos de unión de los grupos carboxilo: μ_1-η^1: η^1, μ_2-η^2: η^1 y μ_2-η^1: η^1 y adicionalmente, posee tres moléculas de DMF como punto de extensión terminales. Como resultado, la representación geométrica de la USC también resulta en un tetraedro. La red 4-conectada construye un arreglo 3D con canales rectangulares en una topología tipo ***dia***.[117] Notablemente, el mismo MOF ha sido reportado por Jin con diferentes proporciones de disolventes de cristalización en la celda unitaria.[118]

[iii] La base de datos con los tipos de redes puede ser consultada en http://rcsr.anu.edu.au/

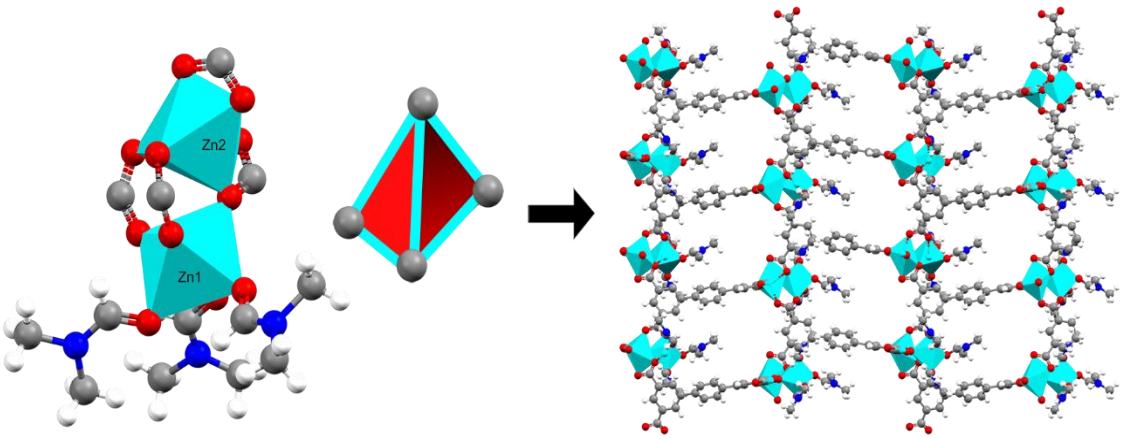

Figura 18. Representación poliedral del MOF A2, con la USC tetraédrica constructora de la red rectangular, en los colores; Zn: azul cielo, C: gris, H: blanco, O: rojo, N: azul marino.

Finalmente, la combinación de disolventes DMA:DMF en una proporción 1:1 en volumen, convergen en la síntesis del MOF $[Zn(tptc)_{0.5}(H_2O)]\cdot DMA\cdot DMF$ **(A3)** (Figura 19). Los nodos de la red compuestos por la USC paddle-wheel (ver Figura 1b), conllevan a la construcción de un MOF isoreticular al NOTT-101 (NOTT-101 con el centro metálico de Cu(II) y con Zn(II)) con una topología cúbica ***nbo*.**[119] Interesantemente, se han sintetizado MOFs idénticos a **(A3)** bajo diferentes combinaciones de disolventes: DMF:H_2O,[120] DMA:1,4-dioxano:H_2O,[121] DMF-1,4-dioxano[122] que son reportados como ”nuevos” al únicamente cambiar las moléculas de disolventes ocluidas en el cristal. Con ello queda explícito, que las condiciones de síntesis son un parámetro difícil de contemplar hacia la planificación de una estructura de una red metal-orgánica, sino que se encuentran encaminadas a ser el conjunto de alternativas para construir nuevas USC y, por ende, nuevos MOFs.

Otros particularidades importantes de los MOFs ensamblados con el ion Zn(II) y el ligante tptc, es que todos ellos son fotoluminiscentes y se han aplicado al sensado de disolventes,[117] hidrocarburos aromáticos,[120] cationes y explosivos.[118]

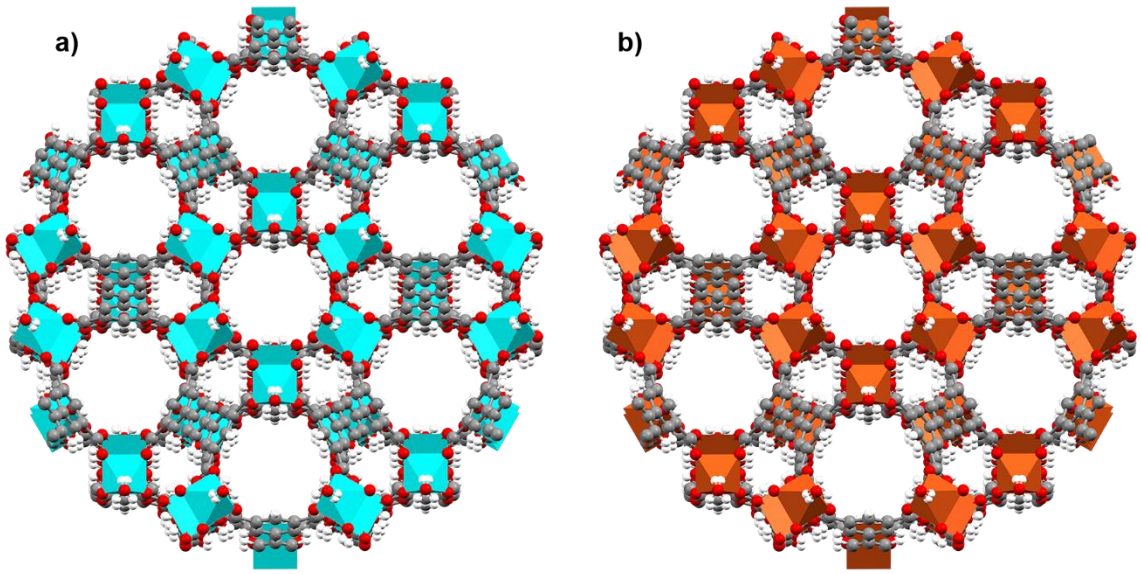

Figura 19. Representación poliedral del MOF A3 (a) isoreticular al MOF NOTT-101 (b), en los colores; Zn: azul cielo, Cu: naranja C: gris, H: blanco, O: rojo, N: azul marino.

1.2.4 Antecedentes II: Detección fluorescente de aniones por redes metal orgánicas luminiscentes

1.2.4.1 Redes metal-orgánicas capaces de detectar al ion cianuro

Actualmente, existen algunos pocos PCs/MOFs capaces de detectar al ion cianuro, entre ellos el bio-MOF-1[123] ($Zn_8(ad)_4(BPDC)_6O•2Me_2NH_2,8DMF,11H_2O$), el cual está constituido por los ligantes adenina (ad) y el ácido bifenil-4,4-dicarboxílico (BPDC) en una estructura 3D aniónica balanceada por el catión dimetilamonio. Su USC está conformada por el cluster Zn_4O ordenados en forma de octaedros para generar una red cúbica del tipo ***pcu***. Karmakar[124] utiliza la red aniónica del bio-MOF-1 para realizar dos sustituciones de su contraión, en el sensado del ion cianuro. La primera de ellas es el reemplazo del catión dimetilamonio por el colorante catiónico 3,6-diaminoacridinio, sin embargo, hasta esta instancia el MOF no exhibe fluorescencia. El cambio en la respuesta óptica viene dado por la adición de cianuro de tetrabutilamonio al MOF, donde ocurre un ataque nucleofílico del ion cianuro a la posición 8 del catión 3,6-diaminoacridinio, dejándolo con carga neutra desplazando el colorante por el catión tetrabutilamonio en el MOF. El colorante con carga neutra, se convierte en el responsable de la emisión fluorescente (Figura 20).[124] Las mediciones de la fluorescencia fueron efectuadas en medio acuoso, con un límite de detección calculado a 1.9×10^{-8} M.[124]

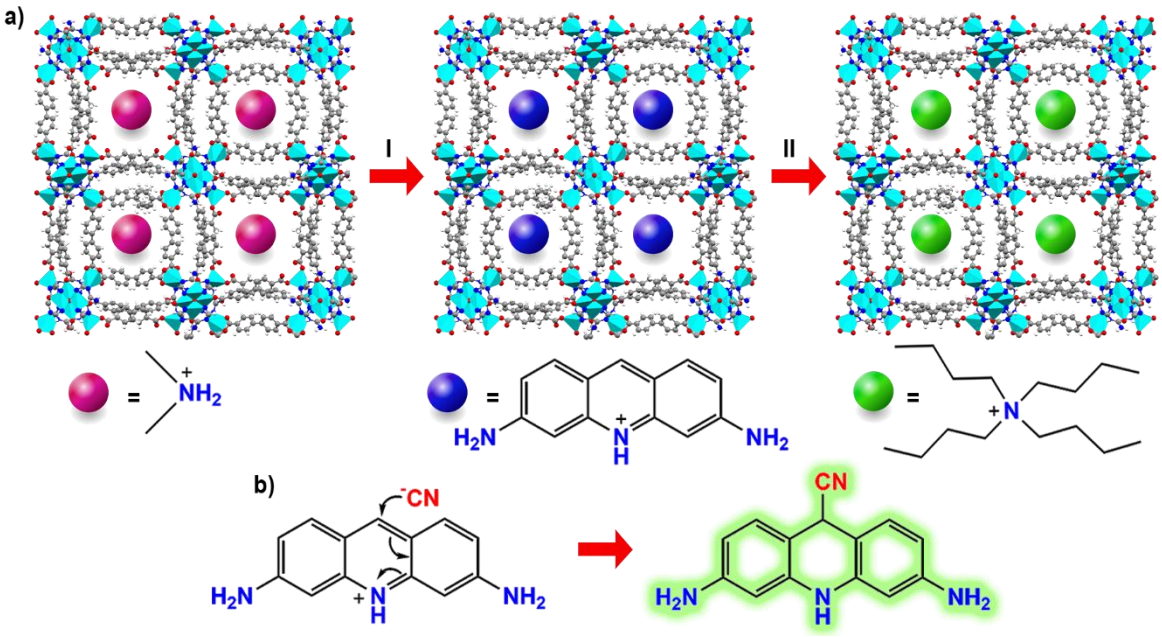

Figura 20. a) Representación poliedral del bio-MOF-1 en los colores; Zn: azul cielo, C: gris, H: blanco, O: rojo. I) Intercambio del catión dimetilamonio por el 3,6-diaminoacridinio II) Adición del ion cianuro reaccionando con ion 3,6-diaminoacridinio, reemplazándolo en la red el catión tetrabutilamonio. b) Mecanismo de reacción del ataque nucleofílico del ion cianuro al catión 3,6-diaminoacridinio, tras quedar neutro, el colorante emite a 510nm.

Posteriormente, nuevamente Karmaka, utiliza el ZIF-90 para el mismo propósito de sensado.[125] El ZIF-90 constituido por el ion Zn(II) y el imidazol-2-caboxaldehído (Figura 21a) , con nodos tetraédricos originarios del ion metálico, genera una red 3D del tipo sod (similar al mineral sodalita) (Figura 21b).[126] Aprovechando la reactividad de los grupos aldehídos presentes en el MOF, realiza una reacción de condensación aldólica con malononitrilo, obteniendo una red metal-orgánica fluorescente. El sistema α,β-instaurado del ZIF, se coloca en presencia del ion cianuro, ocurriendo una condensación de Knoevenagel tras el ataque nucleofílico del ion cianuro sobre el doble enlace del grupo dicianovinilo (Figura 21c). La intensidad fluorescente (determinada en un sistema 1:1 vol. H_2O:DMSO), se ve atenuada por dicha reacción. El sensor posee un límite de detección de 2 x 10^{-6} M.[125] Ambos sistemas, el bio-MOF-1 y ZIF-90 modificados, son selectivos para el ion cianuro en competencia de otros aniones.[124,125]

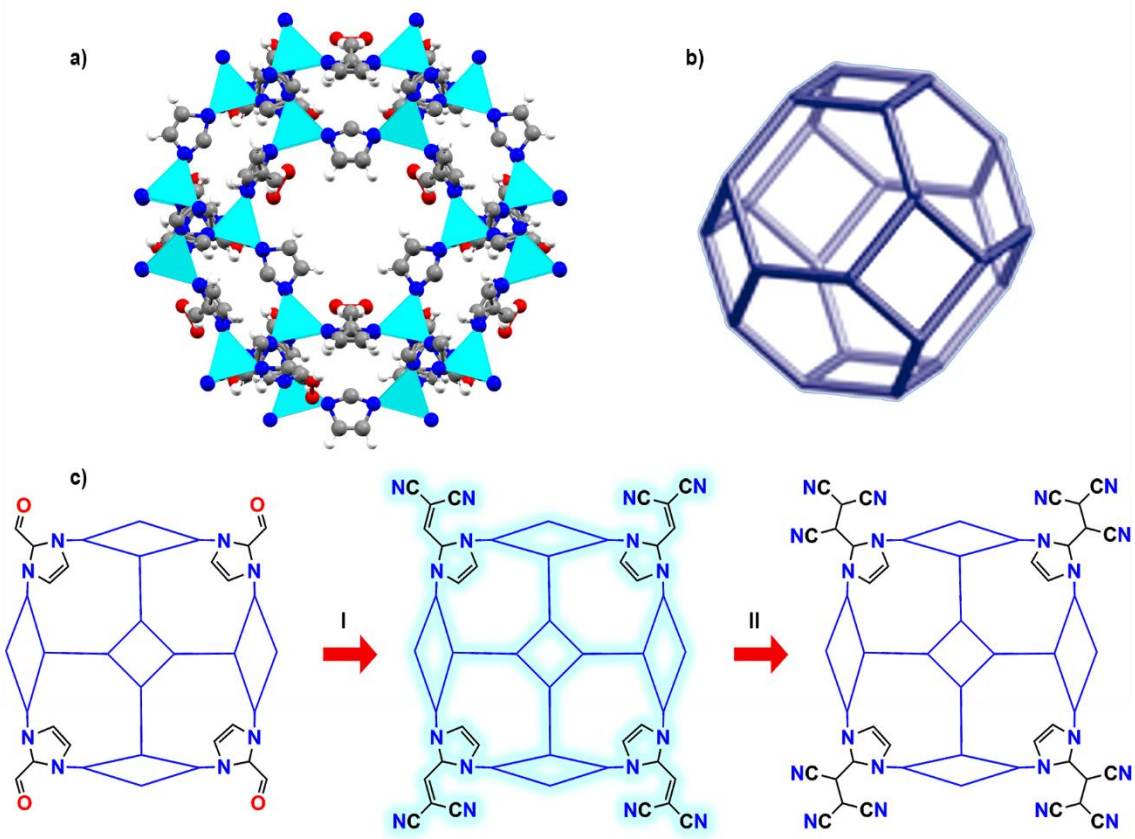

Figura 21. a) Representación poliedral del ZIF-90 en los colores; Zn: azul cielo, C: gris, N: azul marino, H: blanco, O: rojo. b) Topologia simplificada de la red *sod*. c) Representación 2D de las caras de la red *sod* en el ZIF-90. I) ZIF-90 tras la reacción de condensación aldólica de malonotrilio con el grupo aldehído. II) ZIF-90 modificado posterior a la reacción Knoevenagel en el grupo dicianovinilo.

La estrategia del ataque nucleofílico a un grupo cianovinilo, ha sido utilizada igualmente por Dalapti en la detección del ion cianuro en agua.[127] El autor parte de los principios de la química reticular,[6–8] basándose en el UiO-66, MOF con una red ***bcu*** que ha demostrado ser isoreticular[128,129] para construir su análogo con la misma USC, empleando Hf(IV) en lugar de Zr(IV) (ver Figura 22a) y utilizando al ligante el ácido tieno[2,3-b]tiofeno-2,5-dicarboxilico (H_2TDC) en reemplazo del ácido tereftálico (1,4-BDC), construyendo así, una red octaédrica como se exhibe en la Figura 22b. Al MOF resultante $[Hf_6O_4(OH)_4(C_8H_2O_4S_2)_6]\cdot 9H_2O\cdot 2DMF$ (también denominado **A4**[iv]); se le causan defectos de conectividad[130] a través de la reacción con el ácido 2-ciano-3-(pyren-1-yl) acrílico (CPAA) en un intercambio de ligantes que busca beneficiar sus propiedades de fluorescencia (Figura 22c). La red luminiscente es capaz de sensar el ion cianuro, cuando éste ataca al grupo cianovinilo, disminuyendo

[iv] A6 carece de un archivo CIF, su estructura fue determinada por la técnica de rayos X de polvos.

la fluorescencia de la red. El sensor exhibe selectividad al ion cianuro aún en la presencia de otros aniones, y su límite de detección está estimado en 3.5 x 10^{-7} M.[127]

UiO-66 también ha sido objeto de otras modificaciones en su ligante con el propósito de ser empleado como sensor fluorescente del ion cianuro. Rana[131] sustituye el 1,4-BDC por el ligante ácido (2,2,2-trifluoroacetamido)tereftálico (1,4-BDC-NH-$COCF_3$), y el ion Zr(IV) por Hf(V). Al compartir la misma USC y linealidad en el ligante en un MOF isoreticular (sin extender la longitud del ligante de forma considerable),[6–8] obtiene el UiO-66-NH-$COCF_3$[v] con la misma topología de red que se aprecia en la Figura 22a y 22b. Su mecanismo de detección del ion cianuro es completamente distinto al propuesto por Dalapti en el **(A4)**, ya que UiO-66-NH-$COCF_3$ utiliza el grupo amida presente en el ligante, para establecer enlaces de hidrógeno (pudiendo llegar hasta a la desprotonación)[132] $R_2NH \cdots {}^-CN$ encendiendo la fluorescencia del MOF (Figura 22d). Las mediciones de sus propiedades luminiscentes se realizaron en medio acuoso, y en competencia de otros aniones, demostrando su selectividad hacia el ion cianuro, con un límite de detección de 2.8 x 10^{-7} M.[131]

En un trabajo muy similar, la propuesta del mecanismo de interacción por enlaces de hidrógeno $R_2NH \cdots {}^-CN$ en el grupo 2,2,2-trifluoroacetamido por parte del UiO-66-NH-$COCF_3$, fue retomada por Gogoi en el DUT-52-NH-$COCF_3$.[132] La única diferencia entre el UiO-66-NH-$COCF_3$ y el DUT-52-NH-$COCF_3$,[vi] es que el ligante parte de un anillo de benceno en el primero y con el ion Hf(IV), mientras que el DUT hace lo propio con un ligante basado en naftaleno y el ion Zr(IV), por lo que ilustrado en la Figura 22a, b y d, cumple con el mismo propósito para el DUT-52-NH-$COCF_3$. El límite de detección para el ion cianuro fue calculado a 2.3 x 10^{-7} M, valor muy cercano al reportado por el UiO-66-NH-$COCF_3$.[132]

[v] UiO-66-NH-$COCF_3$ carece de un archivo CIF, su estructura fue determinada por la técnica de rayos X de polvos.
[vi] DUT-52-NH-$COCF_3$ carece de un archivo CIF, su estructura fue determinada por la técnica de rayos X de polvos.

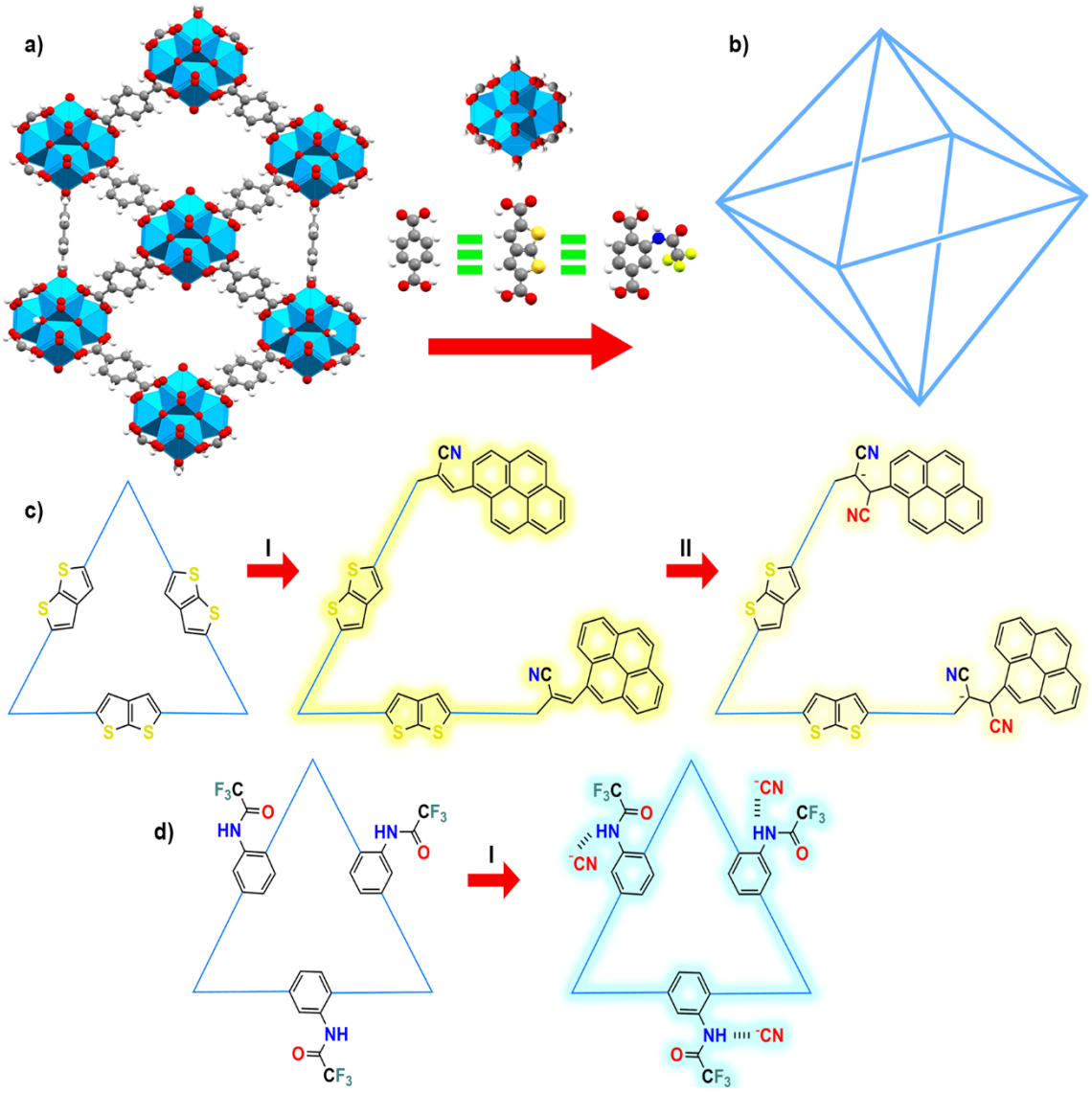

Figura 22. a) Representación poliedral del UiO-66 emulando el arreglo esperado de los MOFs con sus respectivas sustituciones en el ligante TDC para A4, y 1,4-BDC-NH-COCF$_3$ para UiO-66-NH-COCF$_3$, en los colores; Zr: azul celeste, C: gris, N: azul marino, H: blanco, O: rojo. b) Topología simplificada de la red *bcu*. c) Representación 2D de las caras de la red *bcu* en el A6. I) A4 tras el intercambio de ligante con el CPAA II) Apagamiento de la fluorescencia en el A6 modificado posterior a la adición del ion cianuro. d) Representación 2D de las caras de la red *bcu* en UiO-66-NH-COCF$_3$. I) Formación de enlaces de hidrógeno en UiO-66-NH-COCF$_3$ tras la adición del ion cianuro generando fluorescencia en el MOF.

1.2.4.2 Redes metal-orgánicas capaces de detectar atorvastatina

No existe ninguna red metal-orgánica que sea capaz de detectar el fármaco atorvastatina, sin embargo, se ha aplicado el ZIF-8 en un material híbrido de óxido de grafeno y nano partículas de Fe_3O_4 en la adsorción de atorvastatina en orina.[38]

El ZIF-8 (Figura 23a) posee la misma topología de red que el ZIF-90 (Figura 21b) y tiene como ligante constituyente al 2-metil-imidazol. En el material híbrido, la red metal-orgánica es dispuesta en las láminas de óxido de grafeno para fungir como el agente adsorbente del fármaco, así mismo, se adicionan nanopartículas al material para hacerlo magnético y con ello facilitar su separación (Figura 23b). El material es capaz de adsorber entre un 87-94% de la atorvastatina presente en la muestra y también fue puesto a prueba con otro fármaco de la familia las estatinas, la simvastatina, con resultados similares (84-95% de adsorción del fármaco en muestras enriquecidas).[38] Más allá del ejemplo aislado, no se encontró otra red metal-orgánica que tuviera relación alguna con la atorvastatina.

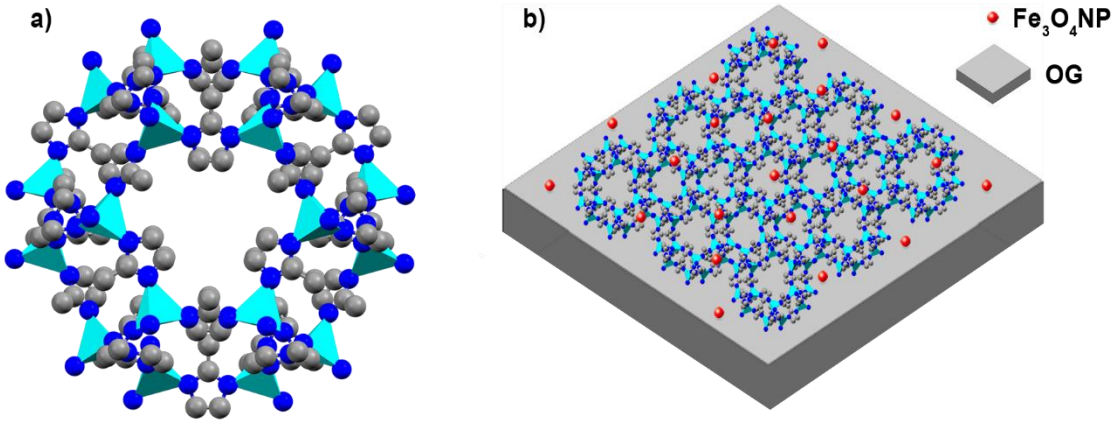

Figura 23. a) Representación poliedral del ZIF-8 en los colores; Zn: azul cielo, C: gris, N: azul marino, H: blanco. b) ZIF-8 y las nanopartículas de F_3O_4 (F_3O_4 NP) dispuestos en el óxido de grafeno (OG) para constituir el material híbrido que absorbe atorvastatina.[38]

1.3 Justificación

Se plantea la justificación específica para cada uno de los dos proyectos principales:

“Polímeros de coordinación con el ligante puente 1,4-chdc y ligantes auxiliares luminiscentes derivados de la 2,2’-bpy aplicados en la detección fluorescente de aniones”.

Se utilizan ligantes derivados de la 2,2´-bipiridina para la generación de nuevos polímeros coordinación con el ion diamagnético Zn(II) (Figura 24). Estructuralmente se pretende estudiar si las sustituciones en las posiciones 4,4 y 5,5 en el ligante auxiliar fluorescente, inducen un cambio en la arquitectura de los PCs. Adicionalmente, al emplear los ligantes π-conjugados, se espera que los respectivos PCs obtenidos sean fluorescentes y que las sustituciones por grupos alquilo en los ligantes derivados de la 2,2´-bipiridina ejerzan un efecto positivo en la emisión fluorescente, mismo que será correlacionado con el análisis estructural y con las potenciales propiedades de emisión de los nuevos polímeros.

Los PCs son aplicados en la detección fluorescente de aniones que presentan un riesgo en la calidad del agua potable, determinando su sensibilidad, selectividad y mecanismo de detección hacia un anión específico, ofreciendo una alternativa para su cuantificación por un nuevo sensor práctico y de fácil preparación.

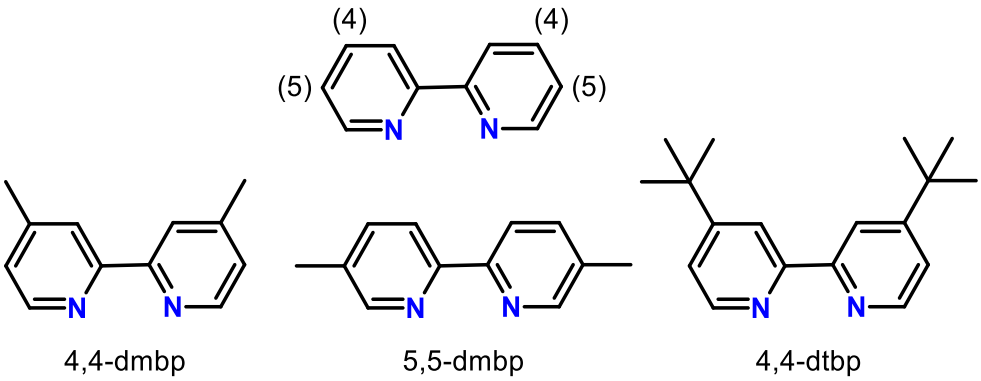

Figura 24. Ligantes utilizados en el Capítulo II para su estudio estructural en polímeros de coordinación de Zn(II) y su aplicación en el sensado de aniones inorgánicos.

"MOF de Zn(II) y el ligante ácido terfenil-3,3",5,5" tetracarboxílico aplicado en la detección fluorescente de aniones farmacéuticos de la familia de las estatinas"

Considerando los antecedentes de la obtención de nuevos MOFs a partir ligante aromático ácido terfenil-3,3",5,5" tetracarboxílico y el ion Zn(II), se plantea que en diferentes condiciones sintéticas, es posible obtener un nuevo MOF luminiscente poroso gracias a la característica rigidez, longitud y emisión del ligante. El nuevo MOF está encaminado a su aplicación en la detección luminiscente de aniones farmacéuticos de la familia de las estatinas (Figura 25).

La elección de las estatinas como analito objetivo de estudio, se fundamenta en que son fármacos frecuentemente recetados contra la hipertensión y colesterol alto. Desde 2012, México ha pasado de ocupar el lugar 20vo, ascendiendo año con año hasta el 15vo en 2018, en el ranking mundial del promedio por habitante en colesterol de baja densidad, mismo que se acumula en las arterias y conlleva problemas cardiacos[133]. Consecuentemente, el uso de estatinas como fármacos para regular enfermedades relacionadas, sigue en incremento y constituye una necesidad creciente su monitoreo en nuestro país.

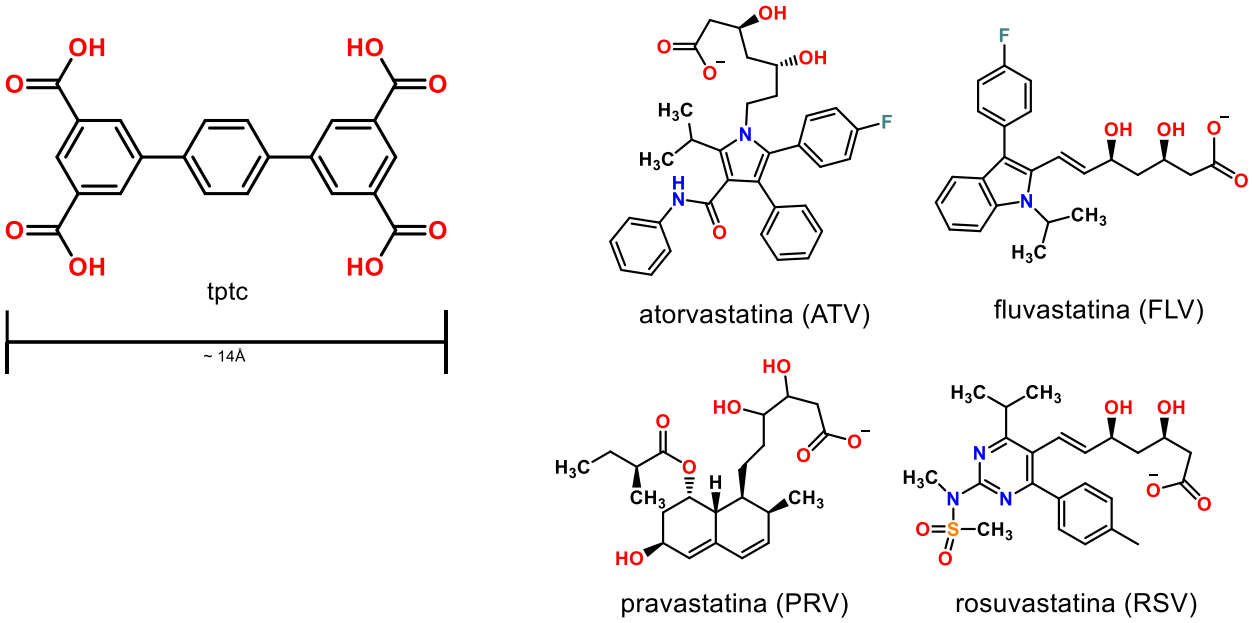

Figura 25. a) Ligante base del Capítulo III en la síntesis de un nuevo MOF aplicado a la detección fluorescente de estatinas. b) Grupo de estatinas estudiadas

1.4 Objetivo general

Sintetizar, estudiar estructural y espectroscópicamente nuevas redes metal orgánicas luminiscentes aplicadas en la detección de aniones.

1.4.1 Objetivos particulares para el sistema I

- Sintetizar los polímeros de coordinación de Zn(II) a base de los ligantes 1,4-chdc como ligante puente, y 4,4-dmbp, 5,5-dmbp y 4,4-dtbp como ligantes auxiliares luminiscentes.
- Caracterizar los polímeros de coordinación a través de difracción de rayos X de monocristal, análisis de infrarrojo, análisis termogravimétrico, análisis elemental, microscopia electrónica de barrido (SEM por sus siglas en ingles), resonancia magnética de sólidos por ángulo mágico.
- Determinar las propiedades luminiscentes de los polímeros de coordinación mediante emulsiones en distintos disolventes para seleccionar el medio en el cual se realizarán los estudios de detección fluorescente de aniones.
- Establecer si existe una correlación causada por las sustituciones de las posiciones 4,4- y 5,5- en el ligante 2,2´-bipiridina con sus propiedades luminiscentes en los polímeros.
- Para el polímero con la mayor intensidad fluorescente, se efectuarán curvas de titulación en la detección selectiva de un anión especifico, calculando su límite de detección tiempo de vida media de la fluorescencia.
- Identificar el mecanismo por el cual ocurre la detección fluorescente.

1.4.1 Objetivos particulares para el sistema II

- Sintetizar un nuevo MOF luminiscente con el ion Zn(II) y el ligante ácido terfenil-3,3”,5,5” tetracarboxílico.
- Caracterizar el MOF a través de estudios de difracción de rayos X de monocristal, difracción de rayos X de polvos, análisis de infrarrojo, análisis termogravimétrico, análisis elemental, microscopia electrónica de barrido (SEM por sus siglas en ingles), espectroscopía de energía dispersiva, resonancia magnética de sólidos por ángulo mágico.
- Determinar las propiedades luminiscentes del nuevo MOF a través de emulsiones en múltiples solventes para elegir el medio en el cual se realizarán los estudios de detección fluorescente de aniones farmacéuticos.
- Efectuar curvas de titulación en la detección selectiva de un anión farmacéutico, calculando su límite de detección y tiempo de vida de la fluorescencia.
- Identificar el mecanismo por el cual ocurre la detección fluorescente por medio de múltiples evidencias analíticas.
- Definir el tipo mecanismo de apagamiento e interpretarlo en las posibles interacciones o reacciones químicas del sistema huésped-anfitrión.
- Aplicar el nuevo sensor luminiscente en muestras reales acorde a los resultados de espectroscopia de fluorescencia

Capítulo II: Resultados

2.1 Sistema I: "Polímeros de coordinación con el ligante puente 1,4-chdc y ligantes auxiliares luminiscentes derivados de la 2,2'-bpy aplicados en la detección fluorescente de aniones".

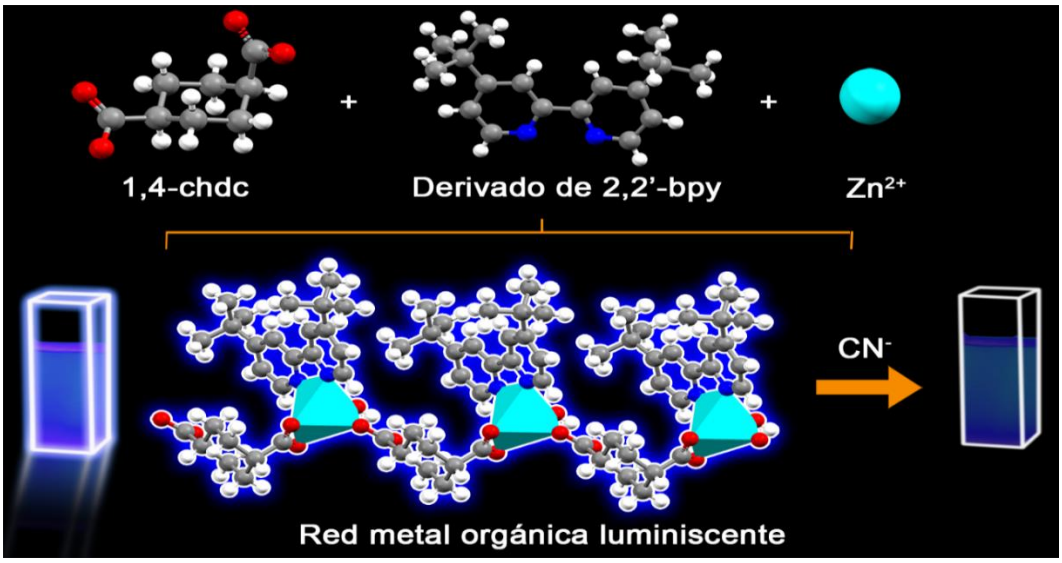

Figura 26. Resumen gráfico del sistema I

Para el sistema I se sintetizaron tres polímeros de coordinación unidimensionales con el ligante puente 1,4-ciclohexanodicarboxilato (1,4-chdc) y los ligantes luminiscentes auxiliares derivados de la 2,2´-bipiridina (4,4-dmbp, 5,5-dmbp y 4,4-dtbp): [Zn(4,4-dmbp)(*e,a-cis*-1,4-chdc)(H_2O)·2(H_2O)]*n* **(1)**, [Zn(5,5-dmbp)(*e,a-cis*-1,4-chdc)(H_2O)·3(H_2O)]*n* **(2)** y [Zn(4,4-dtbp)(*e,a-cis*-1,4-chdc)(H_2O)·7(H_2O)] **(3)**; mediante la siguiente reacción (Figura 27):

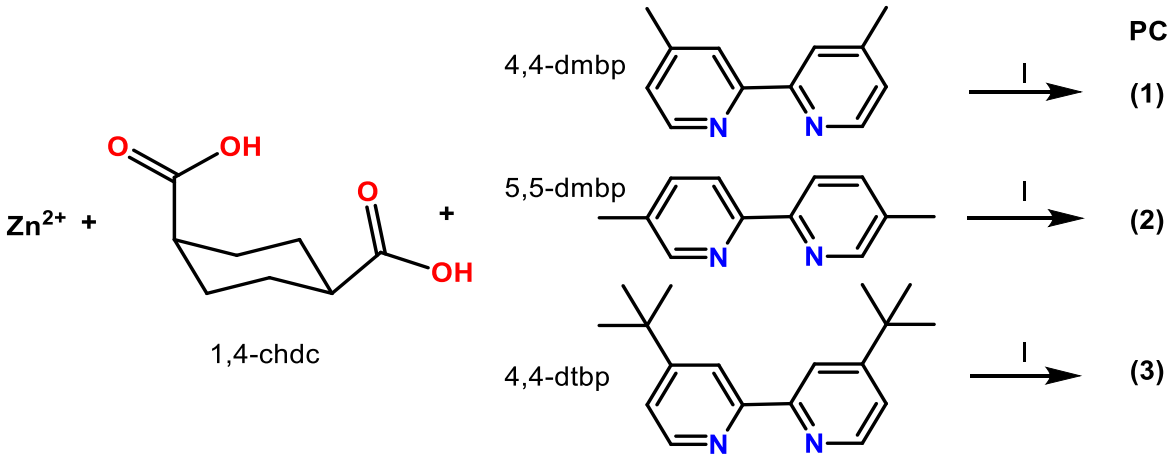

Figura 27. Reacción general para la obtención de los PCs (1-3). I = Metanol-H_2O, t.a. 2eq. NaOH

Los productos de reacción fueron obtenidos como cristales por lo que fue posible su resolución estructural mediante la técnica de rayos X de monocristal.

2.1.2 Análisis estructural

Los datos cristalográficos más relevantes de los tres PCs se enlistan en la Tabla 2. A continuación se realiza la descripción estructural de cada uno de los polímeros y una respectiva comparación de la arquitectura resultante tras variar los ligantes auxiliares luminiscentes.

Tabla 2. Datos cristalográficos para los compuestos (1-3).

Compuesto	1	2	3
Formula	$C_{20}H_{28}N_2O_7Zn$	$C_{20}H_{24}N_2O_5Zn$	$C_{52}H_{86}N_4O_{17}Zn_2$
Peso Molecular	473.81	437.78	1169.98
Temperatura K	100	293	100
Longitud de onda(Å)	0.71073	0.71073	1.54178
Sistema Cristalino	Monoclínico	Monoclínico	Monoclínico
Grupo Espacial	$P2_1/c$	$P2_1/c$	Pn
***a* (Å)**	8.8493(6)	10.0221(5)	9.2334(2)
***b* (Å)**	25.7425(15)	20.7033(9)	11.2034(3)
***c* (Å)**	9.7652(6)	10.1283(5)	27.9409(7)
***α* (grados)**	90	90	90
β (grados)	106.8621(12)	113.2768(10)	95.9508(13)
***γ* (grados)**	90	90	90
Volumen ($Å^3$)	2128.9(2)	1930.48(16)	2874.78(12)
Z	4	4	2
Coeficiente de absorción	1.198 mm^{-1}	1.307 mm^{-1}	1.612 mm^{-1}
F(000)	992	912	1244
Tamaño del cristal	0.454 x 0.168 x 0.112 mm^3	0.388 x 0.234 x 0.052 mm^3	0.362 x 0.069 x 0.044 mm^3
Rangos de los índices	-11<=h<=11 -28<=k<=33 -10<=l<=12	-12<=h<=12 -25<=k<=25 -12<=l<=12	-10<=h<=11 -13<=k<=13 -33<=l<=33
Reflexiones colectadas	23490	38671	24041
Final R índices [I>2sigma(I)]	R1 = 0.0291 wR2 = 0.0716	R1 = 0.0321 wR2 = 0.0862	R1 = 0.0299 wR2 = 0.0766
R índices (all data)	R1 = 0.0340 wR2 = 0.0741	R1 = 0.0343 wR2 = 0.0873	R1 = 0.0307 wR2 = 0.0773
Goodness-of-fit on F^2	1.027	1.125	1.032
Datos / Restricciones / Parámetros	4876/ 13 / 297	3944/ 3 / 261	8618/ 97 / 774

2.1.2.1 Polímero [Zn(4,4-dmbp)(*e,a-cis*-1,4-chdc)(H_2O)·2(H_2O)]$_n$ (1)

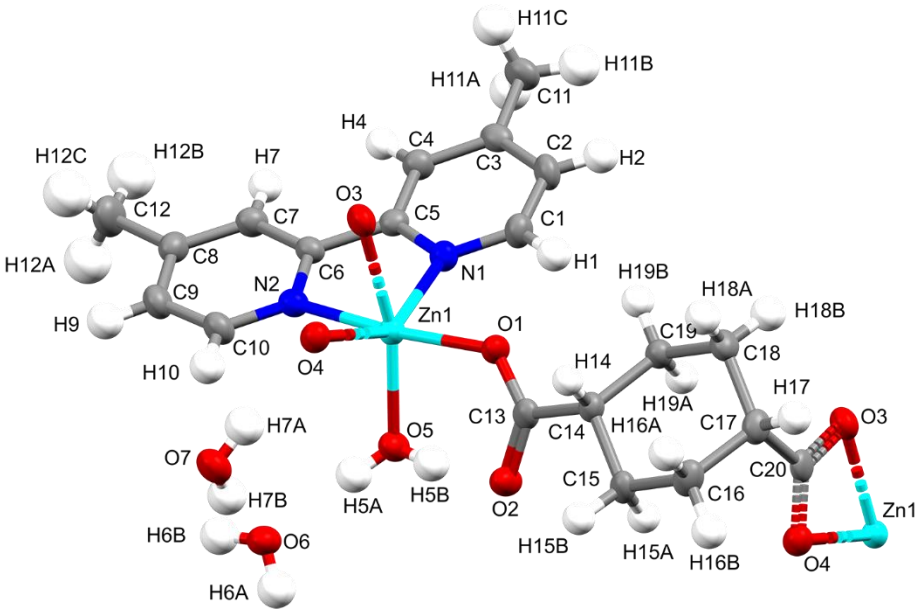

Figura 28. Representación elipsoidal al 50% del polímero [Zn(4,4-dmbp)(e,a-cis-1,4-chdc)(H_2O)·2(H_2O)] (1) en los colores; Zn: azul cielo, C: gris, N: azul marino, H: blanco, O: rojo.

El polímero de coordinación **(1)**, a base del ligante auxiliar luminiscente 4,4-dmbp, cristaliza en el sistema monoclínico, grupo espacial $P2_1/c$. La unidad asimétrica se encuentra conformada por el ion metálico Zn(II), el ligante puente 1,4-chdc^{-2}, el ligante 4,4-dmbp, una molécula de agua de coordinación y dos moléculas de agua de cristalización (Figura 28). El centro metálico presenta el número de coordinación seis y exhibe una geométrica de coordinación octaédrica distorsionada.

El átomo de zinc en el polímero **(1)** posee una esfera de coordinación integrada por el átomo O(5) de una molécula de agua, los átomos de nitrógeno N(1) y N(2) del ligante 4,4-dmbp y los átomos de oxígeno O(1), O(3) y O(4) provenientes del ligante puente 1,4-chdc^{-2}. La coordinación del ligante 1,4-chdc^{2-} al ion Zn(II), ocurre en dos formas distintas, una como quelato bidentado con los átomos de oxígeno O(3) y O(4) con un ángulo de mordida de 59.65°, mientras que con el átomo de oxígeno O(1) se coordina en forma monodentada. Por su parte, el ligante auxiliar luminiscente se une al centro metálico a través de un quelato bidentado con un ángulo de mordida de 77.14°. Ambas uniones quelato por parte de los ligantes, son responsables de la distorsión de la geometría octaédrica en el ion Zn(II). En la Tabla 3 se exponen los ángulos y distancias de enlace representativos de la esfera de coordinación del centro metálico. Las distancias y ángulos de enlace de la esfera de coordinación del átomo de Zn(II) son similares a las mostradas por otros PCs relacionados como aquel que utiliza como ligante auxiliar la 1,10-fenantrolina.[134]

Tabla 3. Longitudes y ángulos de enlace selectos de la esfera de coordinación del ion Zn(II) en (1).

Enlace	Longitud (Å)	Enlaces	Ángulo (°)
Zn(1)-O(1)	2.041(1)	O(1)-Zn(1)-N(2)	171.22(5)
Zn(1)-O(5)	2.079(1)	O(5)-Zn(1)-O(3)	163.52(5)
Zn(1)-N(1)	2.109(1)	N(1)-Zn(1)-O(4)	145.48(5)
Zn(1)-O(4)	2.142(1)	O(5)-Zn(1)-N(1)	108.24(6)
Zn(1)-N(2)	2.163(1)	O(5)-Zn(1)-O(4)	104.16(5)
Zn(1)-O(3)	2.256(1)	O(4)-Zn(1)-N(2)	91.22(5)
		N(2)-Zn(1)-O(3)	87.12(5)
		N(1)-Zn(1)-O(3)	87.07(5)
		N(1)-Zn(1)-N(2)	77.15(6)
		O(4)-Zn(1)-O(3)	59.65(5)

2.1.2.1.1 Estructura polimérica y supramolecular

El polímero **(1)** genera una cadena de zigzag 1D extendida a través del ligante puente 1,4-chdc^{2-} (Figura 29). Su topología es descrita como una red uninodal 2-coordinada. El ordenamiento de las cadenas en el cristal permite que exista una interacción π – π del tipo cara – cara entre los anillos aromáticos de la 4,4-dmbp con un ángulo entre centroides de 161.78° y una distancia de 3.813 (Figura 30).

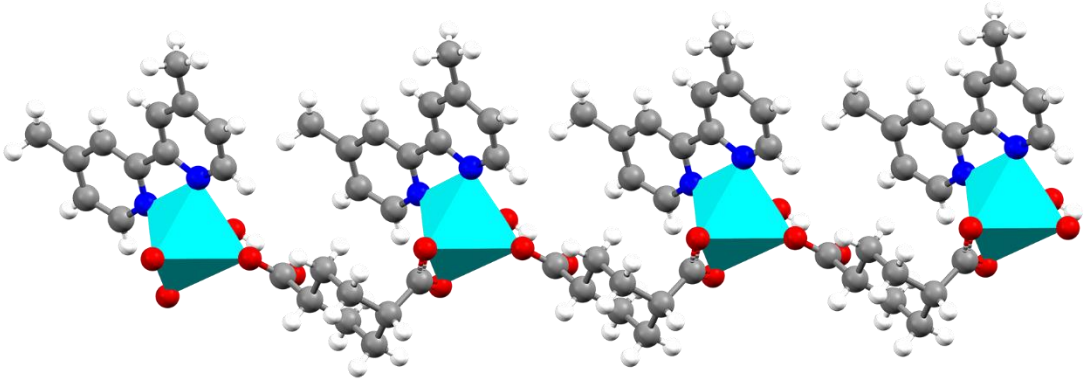

Figura 29. Representación poliedral de (1) mostrando su estructura polimérica de cadena zigzag 1D en los colores; Zn: azul cielo, C: gris, N: azul marino, H: blanco, O: rojo.

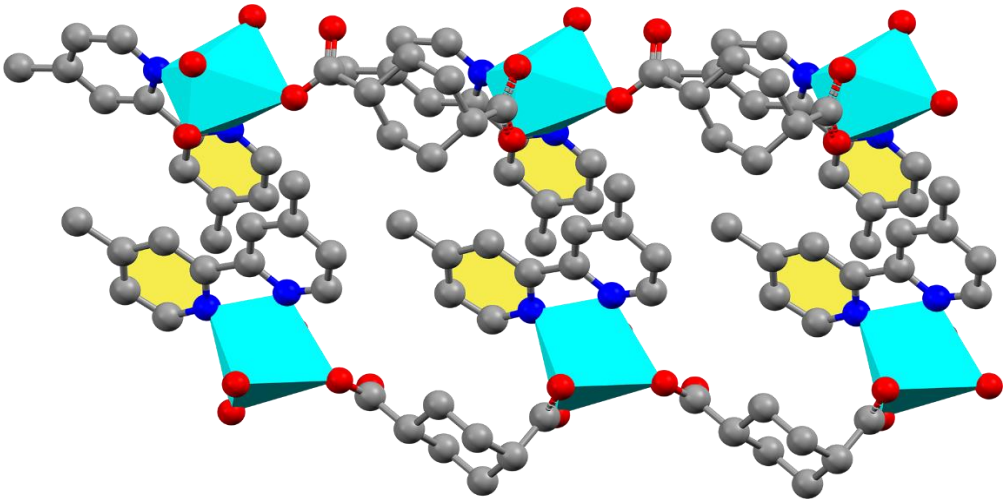

Figura 30. Interacciones π – π del tipo cara – cara entre los anillos aromáticos presentes en la estructura polimérica, indicados en amarillo.

La estructura cristalina de **(1)** muestra la presencia de enlaces de hidrógeno entre las moléculas de agua de cristalización y de coordinación conectando a dos cadenas poliméricas entre sí. El estudio descriptivo de los enlaces de hidrógeno procede a través de los "Graph set descriptors", el cual es un método que clasifica dichas interacciones en distintos motivos, identificando a las moléculas o átomos como nodos de una red, y a los enlaces de hidrógeno como las líneas de la red, de tal manera que patrones complejos de enlaces de hidrógeno puedan ser identificados de manera sistemática y consistente.[135–137]

El "graph set descriptor" se escribe como G_d,a(n). Donde G representa una de las 4 posibles designaciones (Figura 31), d es el número de enlaces de hidrógeno establecido por el átomo donador, a es el número de enlaces de hidrógeno establecido por el átomo aceptor y n es el número de átomos que conforman el patrón (también llamado "grado del patrón"). Cuando solo existe donador y un aceptor del enlace de hidrógeno, se omite escribir tanto a y d.[135–137]

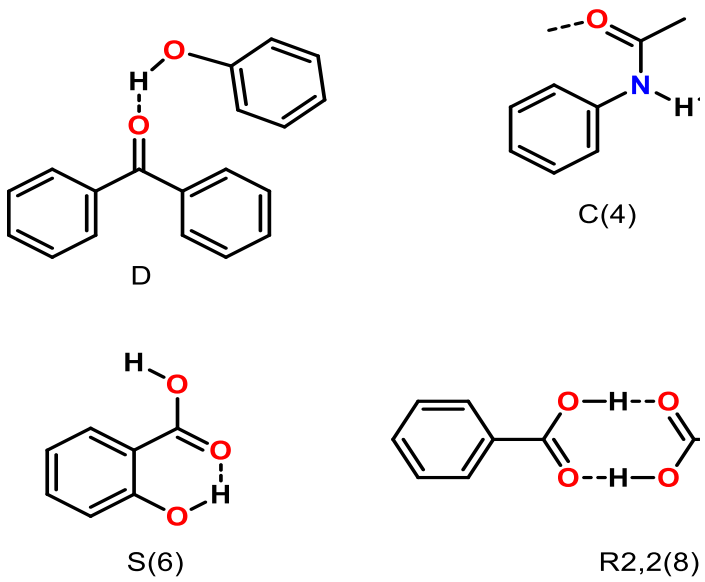

Figura 31. Designaciones de los graph set descriptors: D = Patrón finito de conectividad, C = cadena, S = enlace de hidrógeno intramolecular y R = anillo.[137]

Los patrones de la arquitectura supramolecular que forman los enlaces de hidrógeno pueden ser descritos por 2 principales grupos graph sets: R4,4(16) y R4,4(8). R4,4(16) describe el anillo de 16 miembros que, considerando sus vértices de forma simplificada, genera un hexágono, mientras que R4,4(8) hace lo propio para un cuadrado tal y como se muestra en la Figura 32. Ambos conjuntos de graph sets conllevan a la unión de las cadenas poliméricas en una estructura laminar 2D. La totalidad de enlaces de hidrógeno, así como su graph set de forma individual son presentados en la Tabla 4.

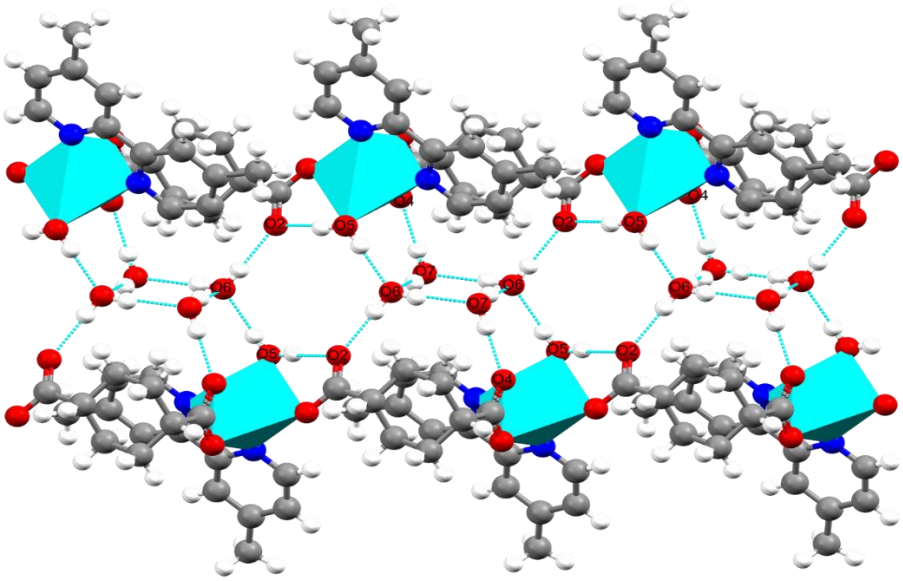

Figura 32. Enlaces de hidrógeno exhibidos en (1) bajo una representación poliedral en los colores Zn: azul cielo, C: gris, N: azul marino, H: blanco, O: rojo.

Tabla 4. Enlaces de hidrógeno del polímero (1)

D-H...A	d(D-H)	d(H...A)	d(D...A)	G_d,a(n)
O(5)-H(5A)...O(6)	0.827(15)	1.934(16)	2.7535(19)	D
O(5)-H(5B)...O(2)	0.834(15)	1.799(15)	2.6193(18)	S(6)
O(6)-H(6A)...O(2)	0.839(15)	1.922(15)	2.7567(18)	D
O(6)-H(6C)...O(7)	0.830(18)	1.917(18)	2.741(2)	D
O(7)-H(7A)...O(4)	0.850(15)	1.946(16)	2.7837(18)	D
O(7)-H(7B)...O(6)	0.848(18)	1.91(2)	2.741(2)	D

2.1.2.2 Polímero [Zn(5,5-dmbp)(*e,a-cis*-1,4-chdc)(H_2O)]$_n$ (2)

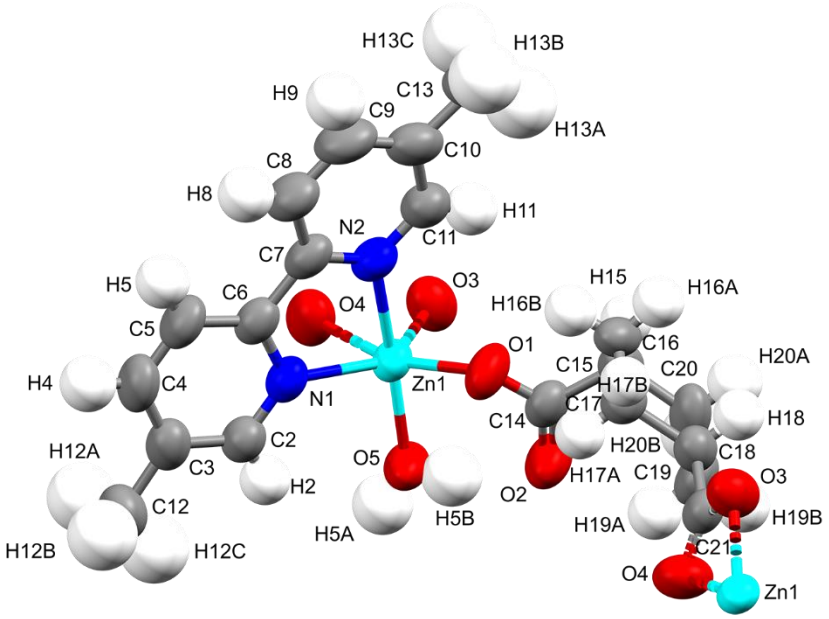

Figura 33. Representación elipsoidal al 50% del polímero [Zn(5,5-dmbp)(e,a-cis-1,4-chdc)(H_2O)]$_n$ (1) en los colores; Zn: azul cielo, C: gris, N: azul marino, H: blanco, O: rojo.

La síntesis del CP **(2)** es producto del uso del ligante 5,5-dmbp como ligante auxiliar luminiscente. Análogamente a **(1)**, el polímero **(2)** cristaliza en el grupo espacial $P2_1/c$ del sistema monoclínico. Su unidad asimétrica está integrada por el ion metálico Zn(II), los ligantes 1,4-chdc^{-2}, 5,5-dmbp y una molécula de agua de coordinación (Figura 33).

El centro metálico presenta un número de coordinación seis para una geometría octaédrica. La esfera de coordinación posee dos átomos de nitrógeno N(1) y N(2) derivados de la 5,5-dmbp unidos como quelato bidentado, tres átomos de oxígeno provenientes del ligante puente 1,4-chdc^{-2}, coordinados de forma monodentada y como quelato bidentado. Los ángulos de mordida de los quelatos son de 76.51° para el ligante derivado de 2,2´-bpy, y de 55.41° para el ligante 1,4-chdc^{-2}. Los valores de las distancias

de enlace, así como sus ángulos son comparables con los expuestos por **(1)** y otros polímeros relacionados.[134] Las distancias y ángulos de enlace más representativos son expuestos en la Tabla 5.

Tabla 5. Longitudes y ángulos de enlace selectos de la esfera de coordinación del ion Zn(II) en (2).

Enlace	Longitud (Å)	Enlaces	Ángulo (°)
Zn(1)-O(1)	1.988(2)	O(5)-Zn(1)-N(2)	169.49(9)
Zn(1)-O(3)	2.042(2)	O(4)-Zn(1)-O(1)	155.26(7)
Zn(1)-O(5)	2.050(2)	O(3)-Zn(1)-N(1)	136.61(8)
Zn(1)-N(1)	2.102(2)	O(1)-Zn(1)-N(1)	121.20(8)
Zn(1)-N(2)	2.172(2)	O(1)-Zn(1)-O(3)	99.86(8)
Zn(1)-O(4)	2.557(2)	O(5)-Zn(1)-N(1)	97.69(9)
		O(3)-Zn(1)-O(5)	95.36(10)
		O(3)-Zn(1)-N(2)	94.83(8)
		O(1)-Zn(1)-N(2)	85.48(8)
		N(1)-Zn(1)-N(2)	76.49(8)
		O(4)-Zn(1)-O(3)	55.40(7)

2.1.2.2.1 Estructura polimérica y supramolecular

Tal y como sucede en **(1)**, la estructura del polímero **(2)** genera una cadena de zigzag 1D conectando los centros metálicos a través del ligante puente 1,4-chdc^{2-} (Figura 33). Al exhibir nodos y conectividad espacial de ligantes idénticos al CP **(1)**, **(2)** también exhibe la topología de una red uninodal 2-coordinada. No obstante, a diferencia de **(1)** donde el ligante 4,4-dmbp se localiza en el mismo plano a lo largo de la cadena zigzagueante (Figura 29), en **(2)** el ligante es alternado 5,5-dmbp a través de la extensión de la cadena polimérica (Figura 34).

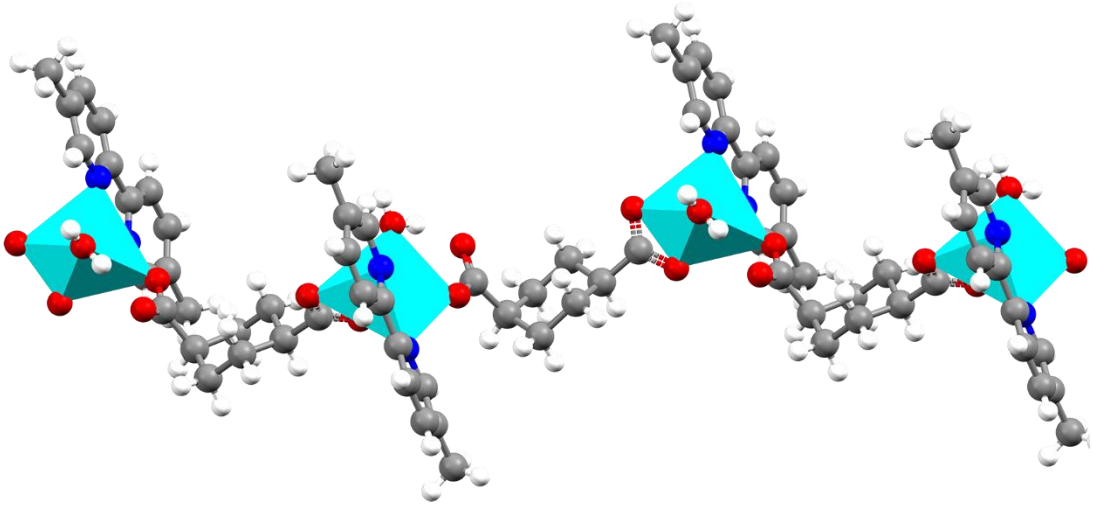

Figura 34. Representación poliedral de la cadena polimérica en zigzag de (2) en los colores; Zn: azul cielo, C: gris, N: azul marino, H: blanco, O: rojo.

El acomodo alternado del ligante 5,5-dmbp en las cadenas permite que se intercalen entre sí en el empaquetamiento cristalino (Figura 35), aunque carece de la presencia de interacciones π – π ya que difiere de los parámetros aceptables de para dicha interacción.[138] La distancia entre anillos aromáticos es de es 4.015 Å y el ángulo entre centroides es igual a 135.63°.

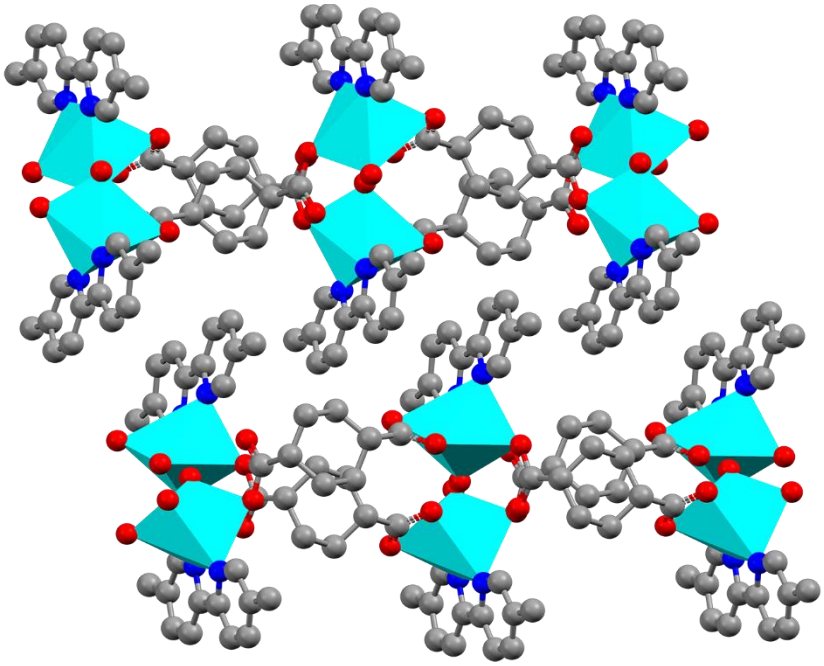

Figura 35. Empaquetamiento cristalino de (2) omitiendo los átomos de hidrógeno por claridad en una representación poliedral con los colores; Zn: azul cielo, C: gris, N: azul marino, O: rojo.

Únicamente existe una molécula de agua de coordinación en el polímero **(2)**, misma que actúa como donadora de dos enlaces de hidrógeno representado en la Figura 36a y Tabla 6. Considerando el conjunto de los enlaces de hidrógeno presentes en **(2)**, forman un anillo de 24 miembros descrito por el graph set R2,2(24) al conectar las cadenas poliméricas en una arreglo laminar 2D (Figura 36b).

Tabla 6. Enlaces de hidrógeno del polímero (2)

D-H...A	d(D-H)	d(H...A)	d(D...A)	G_d,a(n).
O(5)-H(5A)...O(3)	0.828(17)	1.830(18)	2.657(3)	C(11)
O(5)-H(5B)...O(2)	0.843(17)	1.811(18)	2.618(3)	S(6)

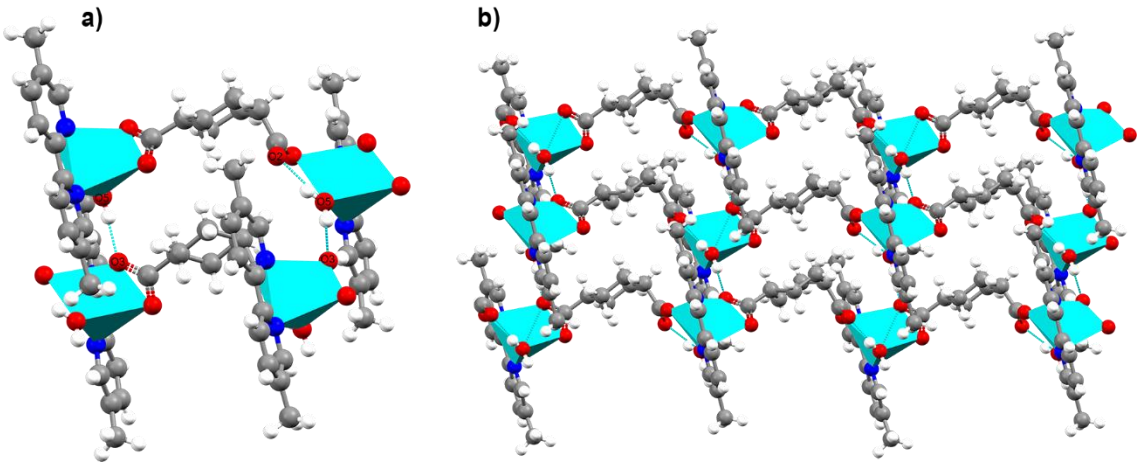

Figura 36. a) Enlaces de hidrógeno de (2) y b) Arreglo laminar bidimensional derivado de los enlaces de hidrógeno. Ambos incisos son una representación poliedral en los colores Zn: azul cielo, C: gris, N: azul marino, H: blanco, O: rojo.

2.1.2.3 Polímero $[Zn_2(4,4\text{-dtbp})_2(e,a\text{-}cis\text{-}1,4\text{-chdc})_2(H_2O)_2{\cdot}7(H_2O)]_n$ (3)

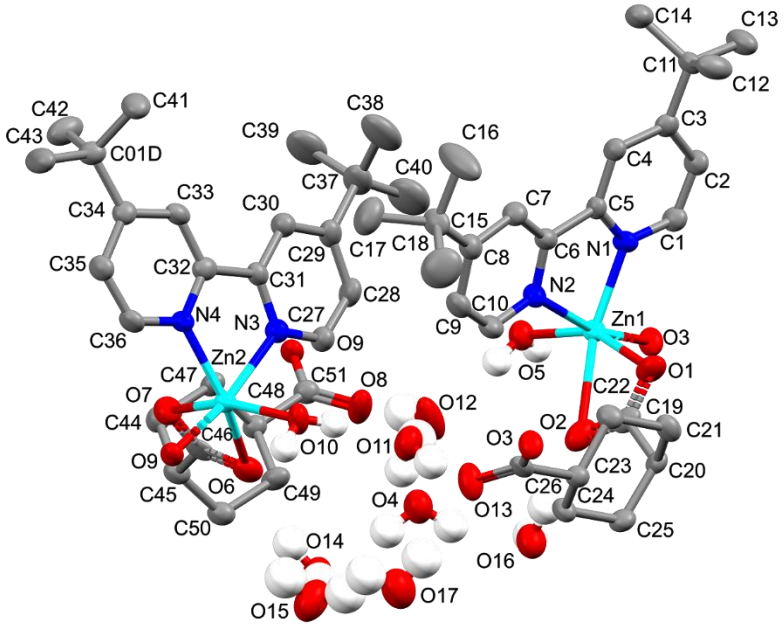

Figura 37. Representación elipsoidal al 50% del polímero $[Zn_2(4,4\text{-dtbp})_2(e,a\text{-}cis\text{-}1,4\text{-chdc})_2(H_2O)_2{\cdot}7(H_2O)]_n$ (3) en los colores; Zn: azul cielo, C: gris, N: azul marino, H: blanco, O: rojo (se omiten los átomos de hidrógeno del ligante por claridad).

Los resultados de análisis de difracción de rayos X de monocristal muestran que el polímero **(3)** posee dos iones Zn(II) cristalográficamente independientes que sirven como nodos de las cadenas

poliméricas, cada una de ellas extendiéndose mediante el ligante puente 1,4-chdc^{2-}. El compuesto **(3)** cristaliza en el sistema monoclínico, grupo espacial **Pn**. La unidad asimétrica la integran dos unidades del ligante auxiliar 4,4-dtbp, dos moléculas del ligante puente 1,4-chdc^{2-}, los centros metálicos Zn(1) y Zn(2), dos moléculas de agua de coordinación y siete moléculas de agua de cristalización (Figura 37).

A pesar de que ambos iones centrales son cristalográficamente independientes, comparten la misma conectividad de sus ligantes al presentar esferas de coordinación N_2O_4 idénticas, respetando la tendencia observada en los PCs **(1)** y **(2)**. Ambos iones centrales Zn(1) y Zn(2) poseen un número de coordinación de seis con una geometría de coordinación octaédrica distorsionada. El átomo de Zn(1) tiene como átomos donadores a los átomos N(1) y N(2) del ligante 4,4-tbbp, el átomo O(5) por parte de la molécula de agua y a los átomos de oxígeno O(1), O(2) y O(3) originarios del ligante puente 1,4-chdc^{2-}. En lo que respecta al átomo de Zn(2), su esfera de coordinación está conformada por los átomos de N(3) y N(4) del ligante auxiliar 4,4-tbbp, el átomo O(10) de una molécula de agua y los átomos de oxígeno O(6), O(7) y O(9) derivados del ligante puente 1,4-chdc^{2-}. Tal y como sucede para **(1)** y **(2)**, ambos nodos de **(3)** poseen los quelatos del ligante auxiliar luminiscente, y el correspondiente de ligante puente, además de una molécula de agua en su esfera primaria. La Tablas 7 resume los ángulos y distancias de enlace de las esferas de coordinación de los centros metálicos.

Tabla 7. Longitudes y ángulos de enlace selectos de la esfera de coordinación de los átomos de Zn en (3).

Enlace	Longitud (Å)	Enlaces	Ángulo (°)
Zn(1)-O(1)	2.031(3)	O(3)-Zn(1)-N(2)	165.29(11)
Zn(1)-O(5)	2.057(3)	O(1)-Zn(1)-O(5)	151.33(12)
Zn(1)-O(3)	2.070(3)	N(1)-Zn(1)-O(2)	148.82(10)
Zn(1)-N(1)	2.111(3)	O(5)-Zn(1)-N(1)	113.32(11)
Zn(1)-N(2)	2.151(3)	O(3)-Zn(1)-O(2)	103.59(10)
Zn(1)-O(2)	2.488(3)	O(1)-Zn(1)-N(2)	93.80(12)
		N(2)-Zn(1)-O(2)	91.05(11)
		O(5)-Zn(1)-N(2)	88.42(12)
		N(1)-Zn(1)-N(2)	76.28(12)
		O(1)-Zn(1)-O(2)	57.06(11)
Zn(2)-O(10)	2.040(3)	O(9)-Zn(2)-N(3)	166.24(10)
Zn(2)-O(9)	2.087(3)	O(10)-Zn(2)-O(7)	157.61(11)
Zn(2)-O(7)	2.096(3)	N(4)-Zn(2)-O(6)	148.67(10)
Zn(2)-N(4)	2.115(3)	O(10)-Zn(2)-N(4)	109.52(12)
Zn(2)-N(3)	2.173(3)	O(9)-Zn(2)-O(6)	102.48(10)
Zn(2)-O(6)	2.334(3)	O(9)-Zn(2)-O(7)	94.79(11)
		O(7)-Zn(2)-N(4)	92.28(11)
		O(10)-Zn(2)-N(3)	88.43(12)
		N(4)-Zn(2)-N(3)	75.90(12)
		O(7)-Zn(2)-O(6)	59.24(10)

2.1.2.3.1 Estructura polimérica y supramolecular

En **(3)**, la arquitectura de cada una de las cadenas poliméricas respeta el patrón mostrado en los PCs **(1)** y **(2)**, extendiéndose en una cadena zigzagueante unidimensional para una topología de red uninodal 2-coordinada (Figura 38). El acomodo del ligante 4,4-dtbp en **(3)** ocurre de forma similar a **(1)** a lo largo del plano correspondiente de cadena polimérica. En contraste con **(1)**, el compuesto **(3)** no exhibe no existe intercalamiento entre sus cadenas en la celda unitaria, por lo que carece de interacciones de tipo π – π.

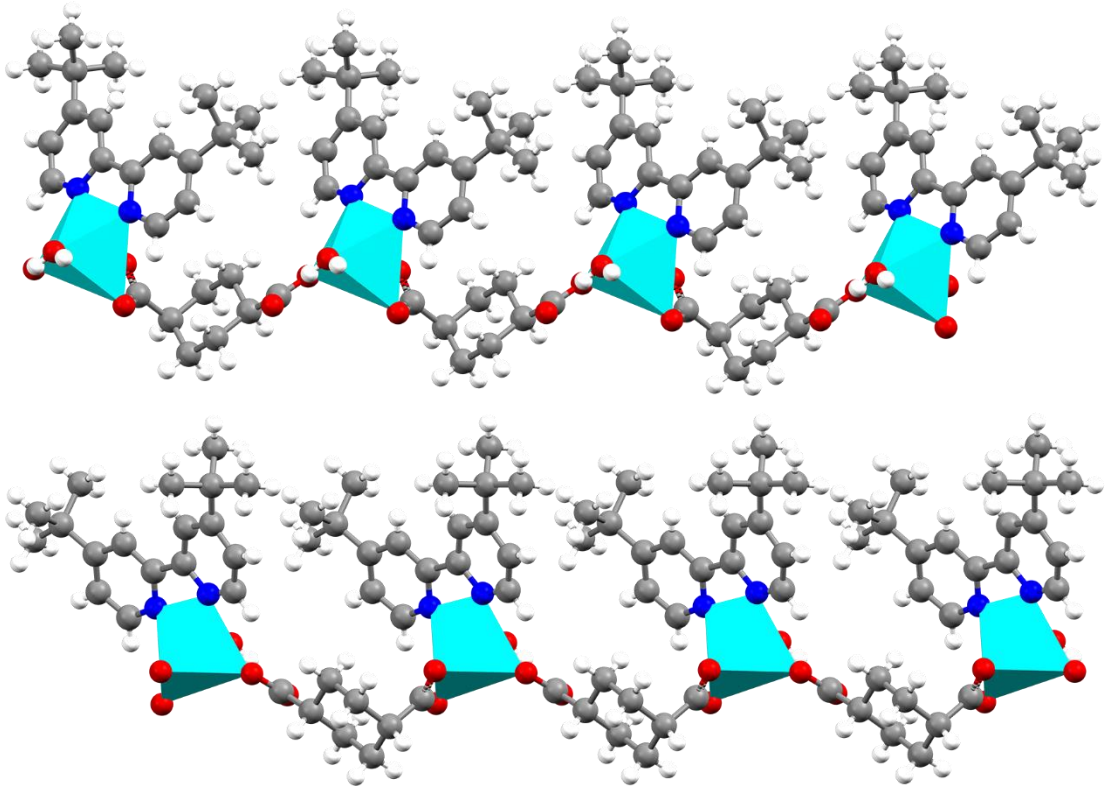

Figura 38 Representación poliedral de las cadena polimérica en (3) con los colores; Zn: azul cielo, C: gris, N: azul marino, H: blanco, O: rojo.

Ante la gran cantidad de moléculas de agua presentes en el polímero **(3)** se forman dieciocho distintos enlaces de hidrógeno en redes por sí mismas complejas cuya interacción permite unir ambas cadenas poliméricas. El graph set principal R6,6(16) está constituido por un anillo de dieciséis miembros y ocho vértices integrados de la siguiente forma: O(5) → O(4) → O(11) → O(13) → O(14) → O(15) → O(8) → O(12) → O(5) (Figura 39) el cual es el responsable de conectar ambas cadenas poliméricas. Otros dos graph set secundarios son generados en la arquitectura el R5,5(12) que constituye por sus vértices un anillo de seis miembros O(5) → O(4) → O(11) → O(10) → O(8) → O(12) → O(5) y el R4,4(8) en un

anillo de cuatro vértices O(5) → O(4) → O(17) → O(12) → O(5). El resto de los enlaces de hidrógeno se expone en la Tabla 8.

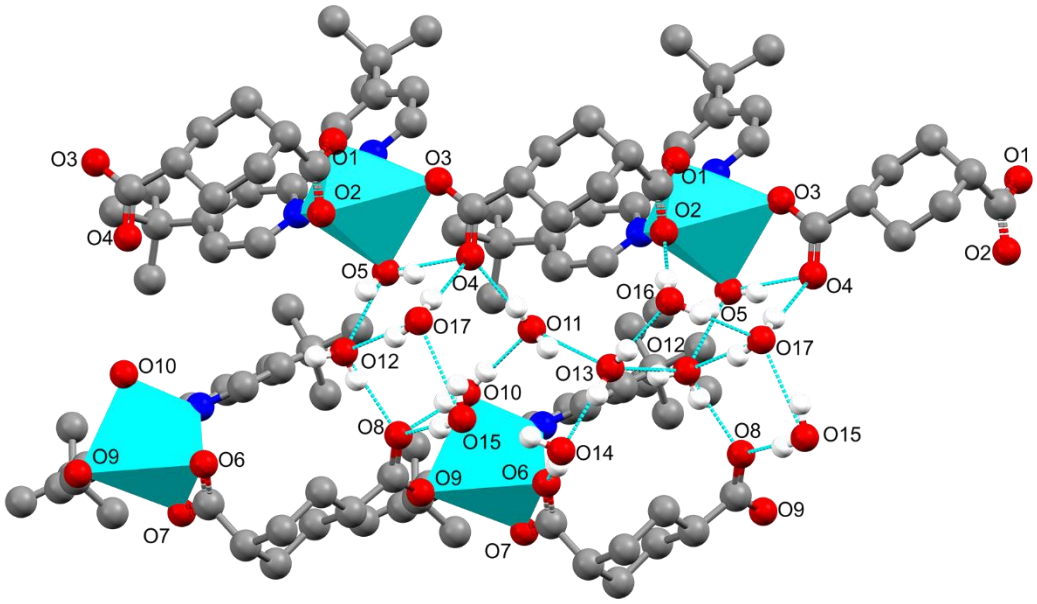

Figura 39. Enlaces de hidrógeno exhibidos en (3) bajo una representación poliedral en los colores Zn: azul cielo, C: gris, N: azul marino, H: blanco, O: rojo.

Tabla 8. Enlaces de hidrógeno del polímero (3)

D-H...A	d(D-H)	d(H...A)	d(D...A)	G_d,a(n).
O(5)-H(5A)...O(12)	0.84(2)	1.94(3)	2.732(4)	D
O(5)-H(5B)...O(4)	0.83(2)	1.84(3)	2.645(4)	R(11)
O(10)-H(10A)...O(11)	0.83(2)	1.85(2)	2.676(4)	D
O(10)-H(10B)...O(8)	0.83(2)	1.85(2)	2.673(4)	R(11)
O(11)-H(11A)...O(4)	0.88(2)	1.92(2)	2.765(4)	D
O(11)-H(11B)...O(13)	0.85(2)	1.97(3)	2.751(5)	D
O(12)-H(12D)...O(13)	0.84(2)	1.93(3)	2.709(5)	D
O(12)-H(12E)...O(8)	0.85(2)	1.88(3)	2.706(4)	D
O(13)-H(13D)...O(16)	0.87(2)	1.90(2)	2.737(5)	D
O(13)-H(13E)...O(14)	0.87(2)	1.85(2)	2.713(5)	D
O(14)-H(14D)...O(15)	0.92(2)	1.90(3)	2.818(5)	D
O(14)-H(14E)...O(6)	0.88(2)	1.90(3)	2.763(4)	D
O(15)-H(15A)...O(8)	0.90(2)	2.05(3)	2.939(5)	D
O(15)-H(15B)...O(17)	0.89(2)	2.00(3)	2.844(4)	D
O(16)-H(16D)...O(2)	0.88(2)	1.87(3)	2.748(4)	D
O(16)-H(16E)...O(17)	0.88(2)	2.08(3)	2.905(5)	D
O(17)-H(17D)...O(12)	0.89(2)	2.04(3)	2.901(5)	D
O(17)-H(17E)...O(4)	0.86(2)	2.06(3)	2.909(5)	D

2.1.1.4 Comparación estructural e influencia de las sustituciones de los grupos alquilo en los PCs (1), (2) y (3).

Todos los polímeros resultantes tienen en común una esfera de coordinación del centro metálico integrada por los mismos átomos de los ligantes; dos átomos de nitrógeno por parte del ligante derivado de la 2,2'-bipiridina, tres átomos de oxígeno del ligante puente, y un átomo de oxígeno de una molécula de agua, para una geometría de coordinación octaédrica distorsionada. El rango de distancias de enlace de los ligantes auxiliares luminiscentes hacia el respectivo ion metálico en cada uno de los PCs descritos es 2.10-2.17 Å, magnitudes congruentes con lo esperado para complejos de Zn con derivados de 2,2'-bipiridinas. El intervalo de las longitudes de enlace Zn-O en **(1)**, **(2)** y **(3)** (1.98-2.55 Å) también se encuentra en el rango observado para carboxilatos de Zn. Por su parte, los ángulos de mordida de cada quelato bidentado en su coordinación hacia el ion Zn(II) de cada CP, permanecen entre los valores promedios de 78(±4) para bipiridinas y 57(±4) para carboxilatos.

El modo de conectividad de los ligantes luminiscentes auxiliares es de quelato bidentado, mientras que en el ligante puente ocurre por una unión monodentada y un quelato bidentado. Sin embargo, existe una diferencia entre **(2)** y las cadenas de **(1)** y **(3)** que radica en la orientación del grupo carboxilo del ligante puente en su coordinación como quelato bidentado. Para los PCs **(1)** y **(3)**, el grupo carboxilo que une como μ^2- al ion Zn(II) se orienta en la posición axial del ciclohexano, en cambio para **(2)**, se encuentra en la posición ecuatorial. Destaca de esa diferencia, que los PCs **(1)** y **(3)** tienen sustituciones de grupos alquilo en las posiciones 4,4´-, mientras que en **(2)**, son las posiciones 5,5´- las modificadas. Con ello se observa a primera instancia, la influencia que ejerce en la estructura las sustituciones por grupos alquilo en el ligante auxiliar luminiscente.

El factor de la sustitución en las posiciones 5,5´- para **(2)**, además de repercutir en la orientación del quelato del ligante puente 1,4-chdc^{-2} también se vio reflejado en el ordenamiento alternado del ligante auxiliar luminiscente favoreciendo el empaquetamiento cristalino del CP y limitando la presencia de moléculas de cristalización. Concretamente, el ligante 5,5´-dmbp permite que las cadenas poliméricas se acomoden de forma más eficiente en la celda unitaria al alternar dicho ligante a lo largo de la estructura unidimensional, de tal forma que no requiere de la presencia de moléculas de disolvente ocluidas para llenar el posible vacío en la celda. A su vez, para el caso de los PCs **(1)** y **(3)** con ligantes auxiliares con grupos alquilo en las posiciones 4,4´-, numerosas moléculas de agua de cristalización fueron necesarias para que el acomodo de las cadenas poliméricas unidimensionales culminase en la obtención de cristales por su empaquetamiento cristalino.

Pareciese que también puede establecerse una correlación entre el número de moléculas de cristalización entre **(1)** y **(3)** derivada del mismo empaquetamiento cristalino. En el compuesto **(1)** al

tener grupos metilo como sustituyentes, genera un menor impedimento estérico en las cadenas dentro de la estructura del CP, a diferencia de los grupos ter-butilos mucho más voluminosos presentes en **(3)**. El mayor impedimento estérico en las cadenas del polímero **(3)**, evitan que éstas puedan intercalarse entre sí como sucede en **(1)**, dejando mayor espacio disponible en la celda cristalina que consecuentemente es ocupado por las moléculas de agua de cristalización. El intercalamiento de las cadenas en **(1)** solo permite que la presencia de dos moléculas de agua en la red, mientras que en **(3)** son requeridas de siete moléculas de agua de cristalización para evitar dejar huecos en la celda unitaria.

El rol de los enlaces de hidrógeno de las moléculas de agua tanto de coordinación como de cristalización en los tres PCs fue el de unir las cadenas entre sí, ya sea para construir estructuras laminares 2D en **(1)** y **(2)** o simplemente conectar pares de cadenas como sucede en **(3)**.

Notablemente, a pesar de las diferencias señaladas entre los PCs **(1)**, **(2)** y **(3)**, topológicamente siguen compartiendo la misma estructura de red, cadenas que se extienden en forma de zigzag prácticamente idénticas.

El conjunto de las observaciones entre las semejanzas y diferencias en **(1)**, **(2)** y **(3)**, permite establecer que: Estructuralmente, las sustituciones de grupos alquilo en las posiciones 4,4- y 5,5- de ligantes derivados de 2,2'-bpy no afecta a la topología de los polímeros de coordinación con el ligante puente 1,4-chdc^{-2} y el ion Zn (II) pero, si tiene un papel preponderante en la estructura supramolecular derivada de las interacciones secundarias en cada polímero (Figura 40).

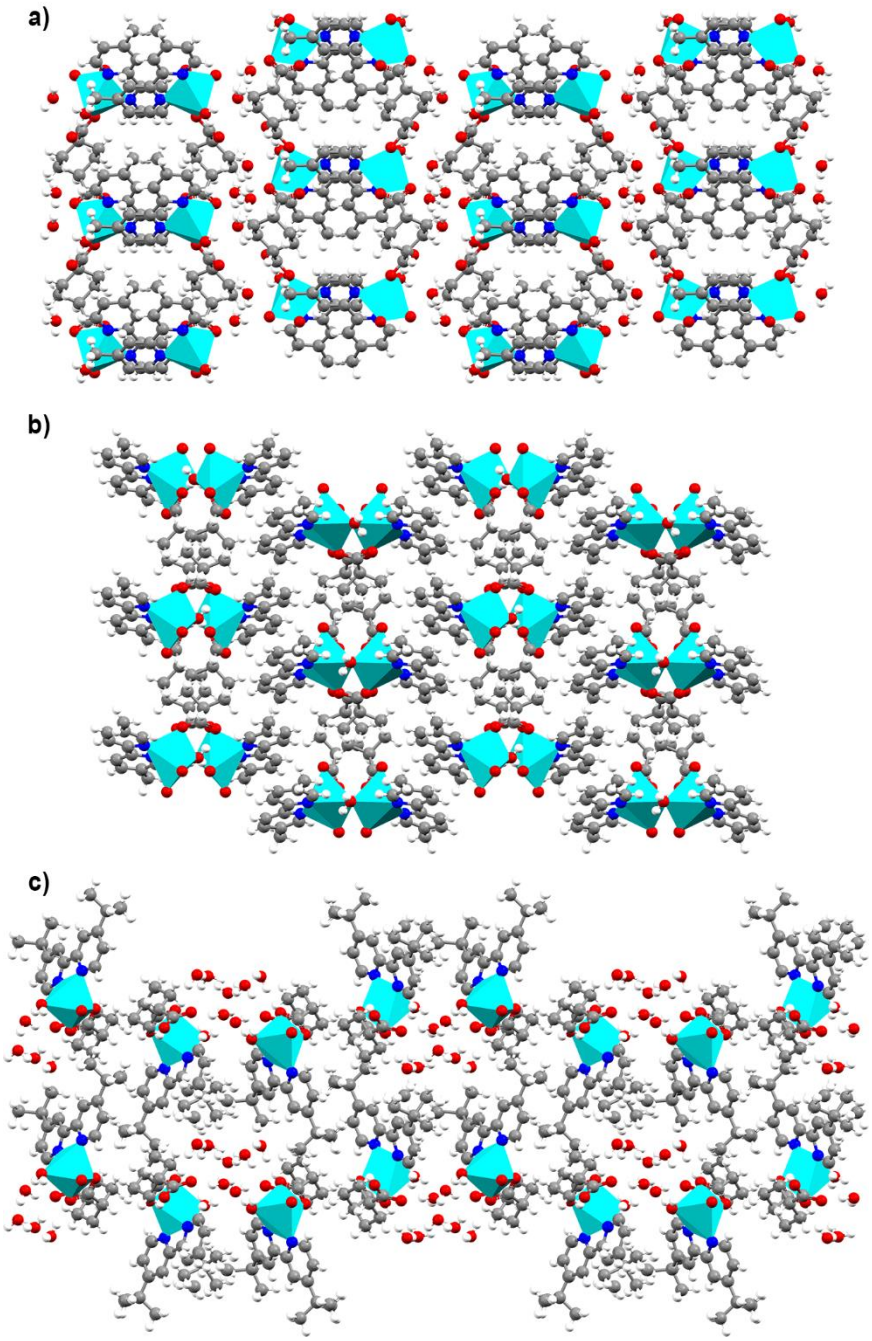

Figura 40. Comparación de las estructuras supramoleculares de los PCs a) (1). b) (2). c) (3) en representación poliedral con en los colores Zn: azul cielo, C: gris, N: azul marino, H: blanco, O: rojo.

2.1.2 Estudios de las propiedades luminiscentes aplicadas al sensado de aniones y análisis espectroscópicos.

Para los estudios de espectroscopia fluorescente se tomaron 3 mg de muestra de cada uno de los PCs en forma independiente y fueron trasvasados en 2500 µL de diversos disolventes, resultando en una emulsión que permanece en agitación constante para su determinación de la fluorescencia. La lista de

solventes estudiados fueron: acetona, acetato de etilo (AcOEt), butanol (BuOH), tetracloruro de carbono (CCl_4), diclorometano (DCM), N,N-dimetilformamida (DMF), etanol (EtOH), agua, isopropanol (i-PrOH), acetonitrilo (MeCN), y tetrahidrofurano (THF). El procedimiento se realizó con la finalidad de determinar cuál es el medio en el que exhiben su máxima emisión para cada polímero. De forma experimental, se buscó la longitud de onda de emisión en un intervalo de 240-350nm, debido a que el ligante auxiliar luminiscente respectivo derivado de la 2,2´-bpy, posee una banda de absorción máxima entre 240-290nm.

En la Figura 41 se presentan los espectros de emisión de **(1)**, **(2)** y **(3)** de los tres PCs en agua, disolvente en el cual exhiben la mayor intensidad fluorescente, y que es elegido como el medio en el que se realizan los estudios consecuentes de fluorescencia. A primera instancia, bajo las mismas condiciones de medición, **(3)** posee una mayor intensidad fluorescente que **(2)** y **(1)**

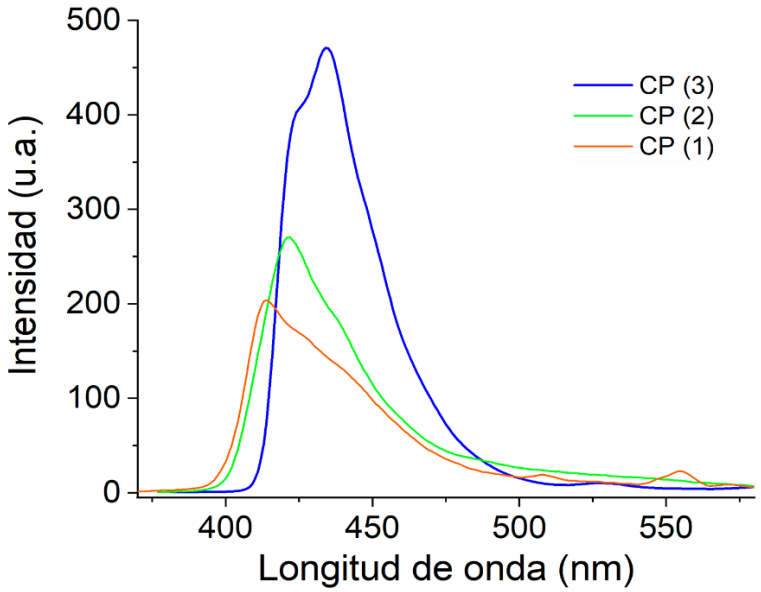

Figura 41. Emisión fluorescente de los CPs (1-3) en agua

Una vez determinado el medio adecuado de emisión en las emulsiones de los PCs, se procede a analizar el comportamiento fluorescente de los compuestos en presencia de diferentes aniones. Para ello se preparan soluciones 10mM de los siguientes aniones como sales de sodio: F^-, Cl^-, Br^-, I^-, CN^-, AcO^-, $H_2AsO_4^-$, HCO_3^-, $H_2PO_4^-$, $H_2P_2O_7^-$, NO_2^-, NO_3^- y SO_4^-. A la par, se prepara una solución con 1mg de polímero en 4 mL de agua, y se toma una alícuota de esa solución de 20 µL para llevarla a volumen total de 2500 µL en la celda. A continuación, se añaden 10 equivalentes por cada respectivo anión y se realizan las mediciones de fluorescencia graficándose en la figura 42 la relación de la intensidad inicial con respecto a la final tras la adición de cada anión.

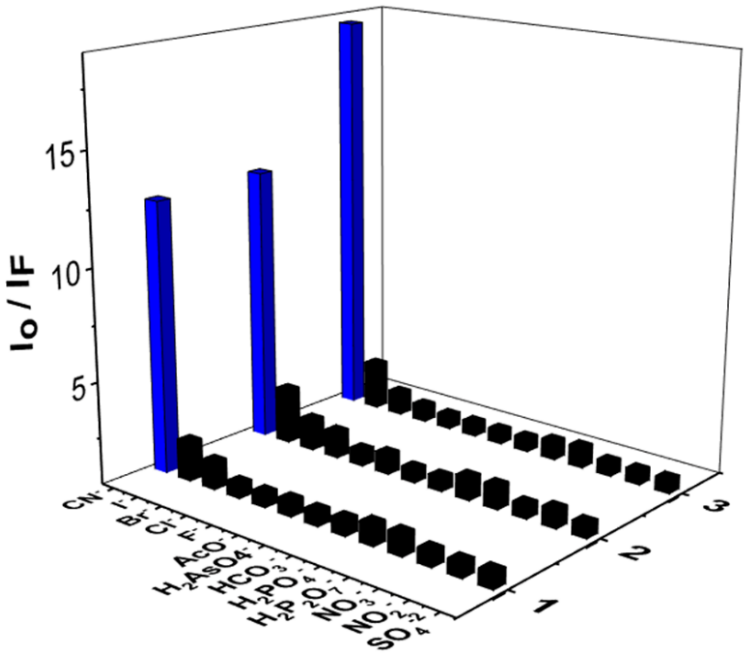

Figura 42. Comparación de la respuesta de apagamiento de la fluorescencia en los PCs (1-3)

Los tres polímeros presentan una respuesta similar ante el conjunto de aniones sensados, exhibiendo un apagamiento de la fluorescencia selectivo por el ion cianuro. No obstante, el mayor cambio óptico ocurre en polímero **(3)**. La posible explicación del por qué **(3)** exhibe mayor intensidad fluorescente que sus análogos **(1)** y **(2)**, puede ser abordada desde el punto de vista estructural. Si bien se ha descrito en la sección anterior como las redes poliméricas de los tres PCs forman la misma arquitectura y difieren en el acomodo supramolecular, se atribuye al factor de la sustitución de los átomos de hidrógeno por grupos alifáticos en el ligante auxiliar luminiscente, que exista una mejoría en la emisión del sensor, siendo menor el proceso de relajación vibracional que experimenta un grupo terbutilo en **(3),** a un grupo metilo en los PCs **(1** y **2)**, conllevando así a una mayor intensidad fluorescente por parte del polímero **(3)** bajo las mismas condiciones de medición. .

Basado en la intensidad de emisión y extinción de la fluorescencia en presencia de los diferentes aniones, se selecciona al compuesto **(3)** como sensor representativo al cual se le realiza una mayor caracterización espectroscópica, determinando su sensibilidad, tiempo de vida de la fluorescencia y se busca elucidar el mecanismo de apagamiento de fluorescencia correspondiente.

Para conocer su sensibilidad, se realiza la titulación fluorimétrica de **(3)** con el anión CN^- en agua a pH = 7 (Figura 43a). A partir de los datos aportados por la curva, se selecciona la longitud de onda donde se presenta la mayor emisión para graficar el perfil de la titulación en función del apagamiento vs la concentración del ion cianuro (Figura 43b). El perfil de la titulación fluorimétrica permite determinar su

constante de Stern-Volmer (K_{SV}) a partir de la pendiente, y, por métodos estadísticos se calcula la desviación estándar de las señales del blanco (σ). Ambos datos se emplean para determinar el límite de detección (LDD = 3σ/K_{SV}) de **(3)** hacia el anión CN^-, LDD = 0.90 μM. Notablemente, el límite de detección es considerablemente menor al que recomienda la OMS como concentración permisible en agua potable (2.7 mM) y se encuentra en el intervalo que otras redes metal orgánicas han exhibido (Tabla 9). Asimismo, el comportamiento lineal del perfil da indicios de que se trata de un apagamiento dinámico.

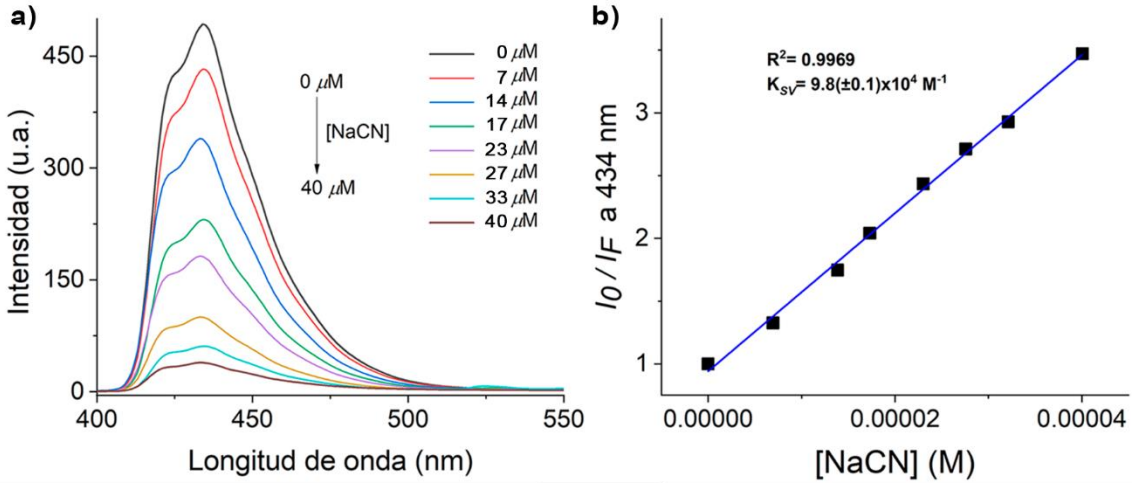

Figura 43. Titulación fluorimétrica del CP (3) en presencia del ion CN^-. b) Perfil de titulación y cálculo de la constante K_{sv} = 9.8 x 10^4 M^{-1} a 434 nm

Tabla 9. Redes metal-orgánicas aplicadas en la detección del ion CN^- en agua

Red	LDD	Año	Referencia
bio-MOF-1	1.9 x 10^{-8} M	2017	124
ZIF-90	2 x 10^{-6} M	2016	125
(3)	**9 x 10^{-7} M**	**2019**	139
$[Hf_6O_4(OH)_4(C_8H_2O_4S_2)_6]\cdot 9H_2O\cdot 2DMF$	3.5 x 10^{-7} M	2020	127
UiO-66-NH-$COCF_3$	2.8 x 10^{-7} M	2021	131
DUT-52-NH-$COCF_3$	2.3 x 10^{-7} M	2021	132

A fin de identificar el efecto de posibles aniones interferentes, se procedió a realizar una nueva titulación de CN^- pero en presencia de los aniones: F^-, Cl^-, Br^-, $H_2AsO_4^-$, HCO_3^-, $H_2PO_4^-$, NO_3^- y SO_4^- bajo las mismas condiciones a la que se efectúa la curva de la Figura 43a. Los resultados son presentados comparando los perfiles de titulación de la curva con CN^- y de CN^- con el resto de los aniones en la Figura 44. Como puede observarse, los perfiles mantienen su linealidad y son casi superponilbles, con dicha información, se establece que el polímero **(3)** posee alta selectividad hacia el ion CN^-.

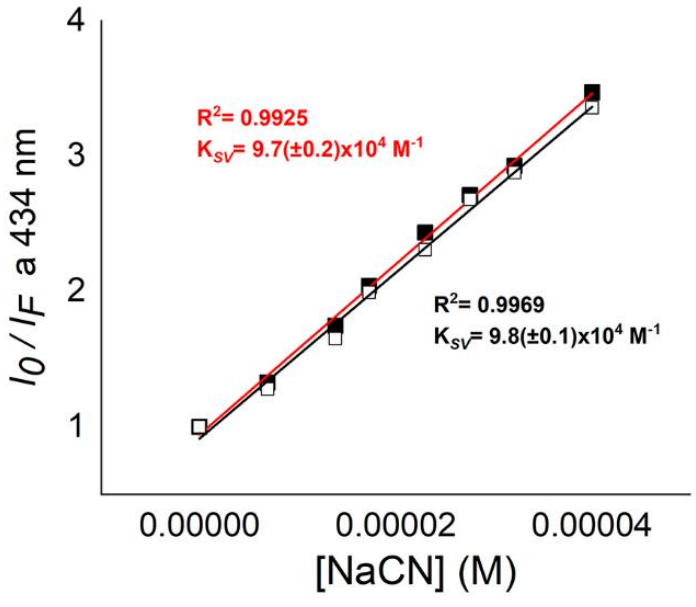

Figura 44. Estudio de la competitividad a través de los perfiles de titulación de (3); ante la presencia únicamente del anión cianuro (color negro) y en coexistencia de varios aniones inorgánicos (color rojo)

Al ser un sensor fácil de preparar, sensible y selectivo a la detección del ion cianuro en agua, tiene un alto potencial de aplicación en agua potable, por ende, fue de interés explorar su funcionabilidad a pH ácido y básico. Se realizaron entonces nuevas titulaciones del anión CN^- a pH = 5.5 y pH = 8.0. En la Figura 45 se muestran los perfiles de titulaciones resultantes. Tanto en pH ácido como básico, el apagamiento de la fluorescencia fue menor al que ocurre en un pH neutro. La explicación radica que en el pH = 5.5, el ion CN^- se encuentra más desplazado en el equilibrio hacia la especie HCN que hacia el anión CN^-,[vii] de tal forma que se limita la interacción del anión hacia el centro metálico, ya que se propone que el mecanismo de interacción ocurre por un ataque nucleofílico del ion cianuro al ion Zn(II), evidencia que se discute más adelante en el capítulo. Por su parte, en el medio básico al incrementar la concentración de grupos OH^-, puede justificarse el menor apagamiento de la fluorescencia por la formación de hidróxido de zinc y la competencia de entre los iones CN^- y OH^-.

[vii] El pKa del equilibrio es igual a 9.3 por lo que es un ácido débil

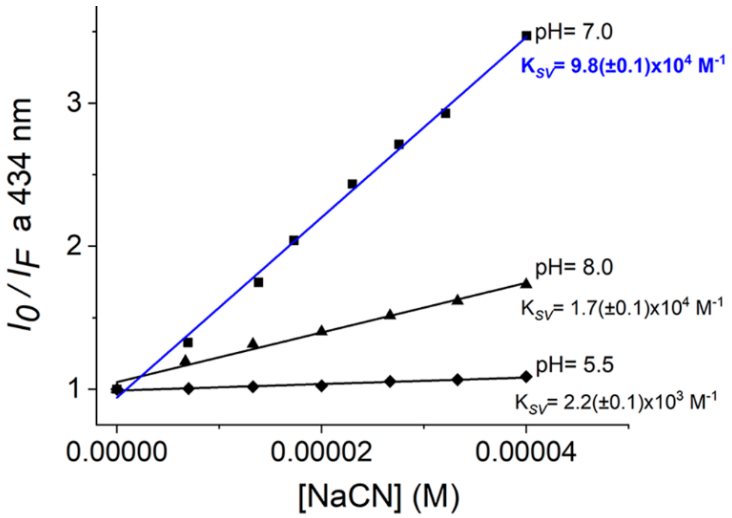

Figura 45. Perfiles de la titulación de (3) con el ion CN^- a diferentes condiciones de pH.

Con la intención de demostrar el mecanismo de sensado, se realizó primeramente una caracterización por resonancia magnética de sólidos de la técnica CPMAS (Cross Polarization Magic Angle Spinning) de ^{13}C y análisis de infrarrojo del polímero **(3)**.

En el espectro de ^{13}C CPMAS se identifican 20 señales provenientes de los dos ligantes, que a pesar de ser cristalográficamente independientes (Figura 46), mantienen sus desplazamientos respectivos en la técnica de resonancia utilizada. Las señales alifáticas del ligante puente 1,4-chdc se encuentran en el intervalo de los 25 a 32 ppm para los $^{13}CH_2$, mientras que en 38.3 y 47.1 ppm aparecen los picos correspondientes a los metinos ^{13}CH. Los carbonos cuaternarios de los grupos carboxilato se ubican a en dos señales a 183.7 y 184.7 ppm. En lo que concierne al ligante auxiliar luminiscente la 4,4-dtbp, posee dos tipos de señales dados sus carbonos del tipo sp^3, la de los grupos metilo $^{13}CH_3$ a 30ppm, y la del carbono cuaternario a 34.8 ppm. Los carbonos sp^2 de la 4,4-dtbp, se ubican en la región de 110 a 170 ppm.

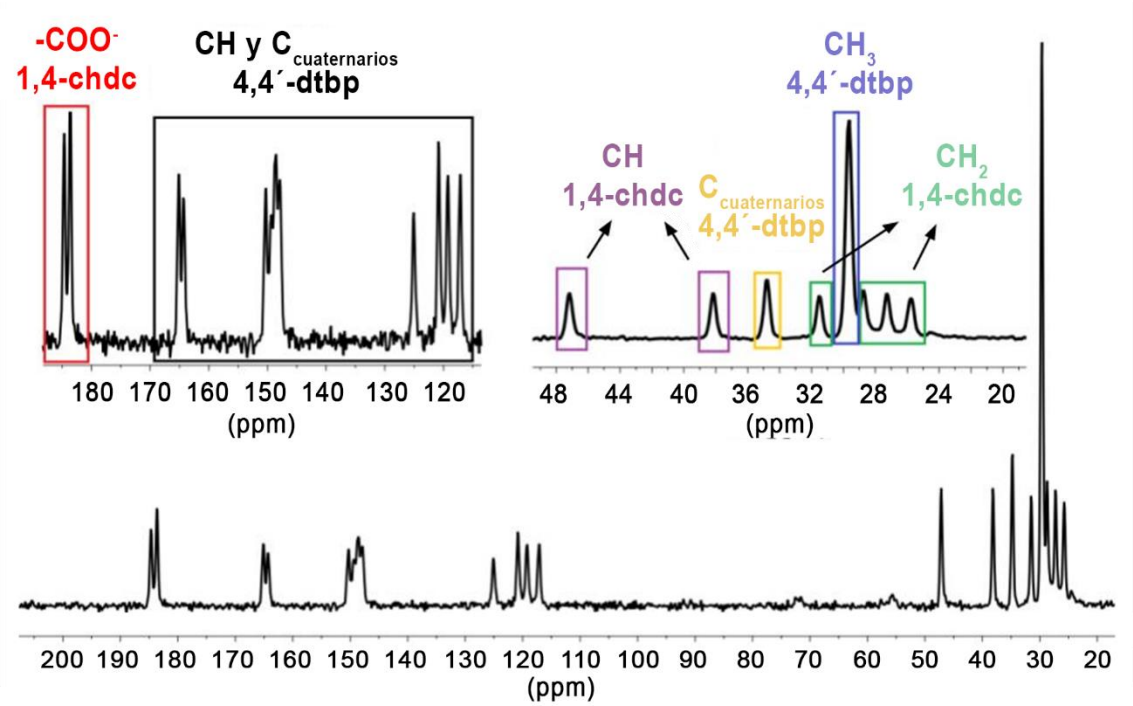

Figura 46. Espectro de ^{13}C por la técnica CPMAS del polímero (3)

Por su parte, la técnica de espectroscopia de infrarrojo permite estudiar los modos de coordinación de los grupos carboxilo al centro metálico a través del parámetro Δ. El parámetro Δ es la resta aritmética de las bandas de vibración asimétrica y simétrica de los carboxilatos $\Delta = \upsilon_{as}(COO^-) - \upsilon_s(COO^-)$. La magnitud de Δ obedece a la siguiente relación de acuerdo a lo propuesto por Zelenak:[140]

$$\Delta \text{ (quelato)} < \Delta\text{(enlace)} < \Delta\text{(ionico)} < \Delta\text{(monodentado)}$$

El valor Δ(iónico) es asignado a los acetatos en un intervalo de 160-170 cm^{-1}; mientras que en la unión monodentada implica el desplazamiento de $\upsilon_{as}(COO^-)$ a frecuencias superiores que las que exhiben los acetatos incrementando el valor de Δ. Cuando se trata de quelatos, la posición de la banda asimétrica se ubica a frecuencias menores.[140] En las uniones tipo enlace, la banda de vibración asimétrica se encuentra en una región muy cercana al que se exhibe en las uniones iónicas. Para distinguir entre ellas, se sugiere la realización de un estudio donde se compare el compuesto de coordinación a analizar (en este caso el nodo de la red) con la sal de acetato del metal utilizado bajo las bases dispuestas en la Tabla 10.

Tabla 10. Relación de la Magnitud de Δ con el tipo de unión del carboxilato[140]

Tipo de unión	Magnitud de Δ
Quelato bidentado	$(COO^-)_{complejo} << (COO^-)_{(AcO)_2Zn}$
Enlace bidentado	$(COO^-)_{complejo} \leq (COO^-)_{(AcO)_2Zn}$
Monodentado	$(COO^-)_{complejo} >> (COO^-)_{(AcO)_2Zn}$

Dado lo establecido con anterioridad, es posible tomar como referencia los valores de las bandas de vibración simétrica (1558 cm^{-1}) asimétrica (1445 cm^{-1})[141] del $Zn(CH_3CO_2)_2 \cdot 2H_2O$ teniendo un Δ(iónico) igual a 113, magnitud que sirve pauta en el análisis de los tipos de unión de los carboxilos al centro metálico en el estudio estructural del polímero **(3)**.

En el espectro de infrarrojo del polímero **(3)** (Figura 47), se observa una banda ancha en 3342 cm^{-1} originada por la vibración del enlace O-H, proveniente de las ocho moléculas de agua presentes en la estructura cristalina de **(3)**. En 3015 cm^{-1} se identifica la vibración del enlace C-H de los átomos de hidrógeno aromáticos del ligante 4,4-dtbp. En cuanto a la coordinación del grupo carboxilo, existe una banda amplia en la región de 1553 a 1547 cm^{-1} correspondiente a la vibración asimétrica COO^-, y otras dos bandas finas en 1445 cm^{-1} y 1408 cm^{-1} derivadas de la vibración simétrica COO^-. Considerando ambos grupos de bandas, es posible determinar el valor de Δ y establecer la asignación adecuada al tipo de conectividad del carboxilato al ion metálico partiendo de la referencia del parámetro Δ del $Zn(CH_3CO_2)_2 \cdot 2H_2O$, como es expuesto en la Tabla 11.

Tabla 11. Modo de coordinación de los carboxilo por análisis de infrarrojo

Bandas	Magnitud experimental de Δ	Tipo de unión
1553 cm^{-1} (υ_{as}) 1408 cm^{-1} (υ_s)	(COO^-)**(3)** >> $(COO^-)(AcO)_2Zn$ 145 cm^{-1} >> 113 cm^{-1}	Monodentado
1547 cm^{-1} (υ_{as}) 1445 cm^{-1} (υ_s)	(COO^-)**(3)** << $(COO^-)(AcO)_2Zn$ 102 cm^{-1} << 113 cm^{-1}	Quelato Bidentado

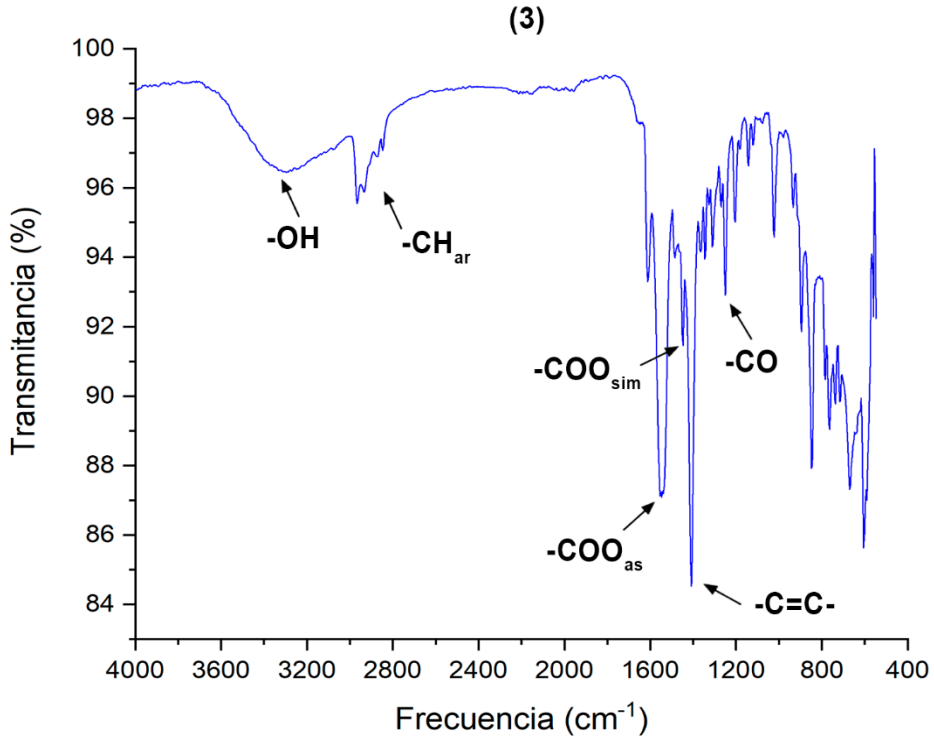

Figura 47. Espectro de infrarrojo del CP (3)

Los dos análisis espectroscópicos previamente descritos, sirven como parte de un conjunto de evidencias destinadas a la resolución del mecanismo de interacción del ion cianuro con el CP **(3)**. Como propuesta, se plantea que el mecanismo de apagamiento de la fluorescencia de la red metal-orgánica **(3)**, ocurra a consecuencia de un ataque nucleofílico al ion Zn(II), comprometiendo integridad estructural de las cadenas poliméricas para formar $Zn(CN)_2$ (Figura 48).

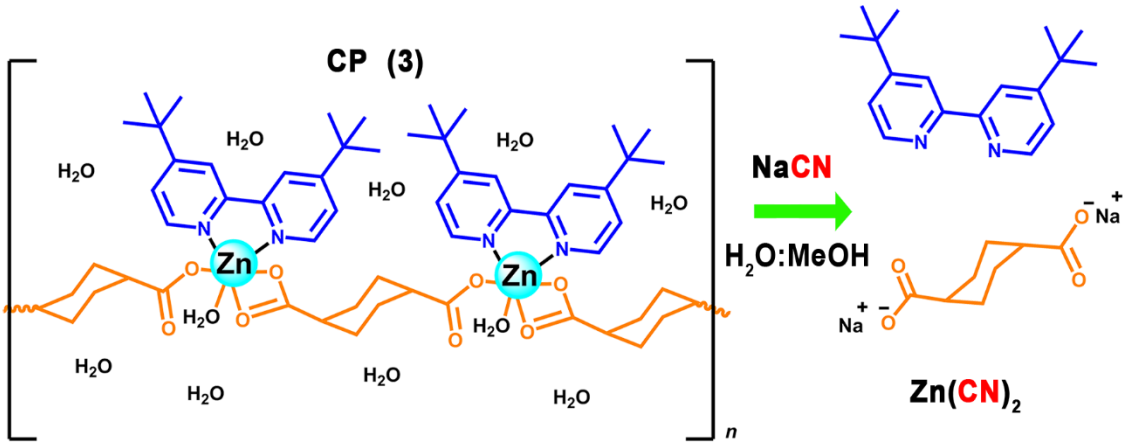

Figura 48. Propuesta del mecanismo de interacción del ion cianuro con el CP (3).

Para poner a prueba la conjetura, se procede a realizar un experimento en el cual se colocan los cristales del compuesto **(3)** en presencia de 3 equivalentes del ion CN^- (NaCN), en una solución acuosa a pH neutro, con agitación constante durante 24 horas. Transcurrido el tiempo, se filtra el sólido resultante y se lava con 50 mL de agua y metanol (1:1). De acuerdo a la propuesta del mecanismo de interacción, ocurre una reacción que lleva a la formación del producto $Zn(CN)_2$ como un sólido insoluble, y en las aguas madres se liberan los ligantes como 4,4-dtbp y Na_2(1,4-chdc).

Se empleó la técnica de microscopia de barrido electrónico (SEM scattering electronic microscopy) al observar que el residuo sólido resultante, pierde la cristalinidad que exhibía el CP **(3)** previo a la reacción con NaCN. En la técnica SEM se tomaron micrografías del cristal del polímero **(3)** y del nuevo sólido producto de la reacción (Figura 49). Adicionalmente, fue posible realizar un análisis de espectroscopia de energía dispersiva (EDS energy dispersive scattering) para la caracterización elemental en las micrografías tomadas por el microscopio electrónico, mapeando de colores los elementos presentes ambas muestras, ilustrado en la Figura 50.

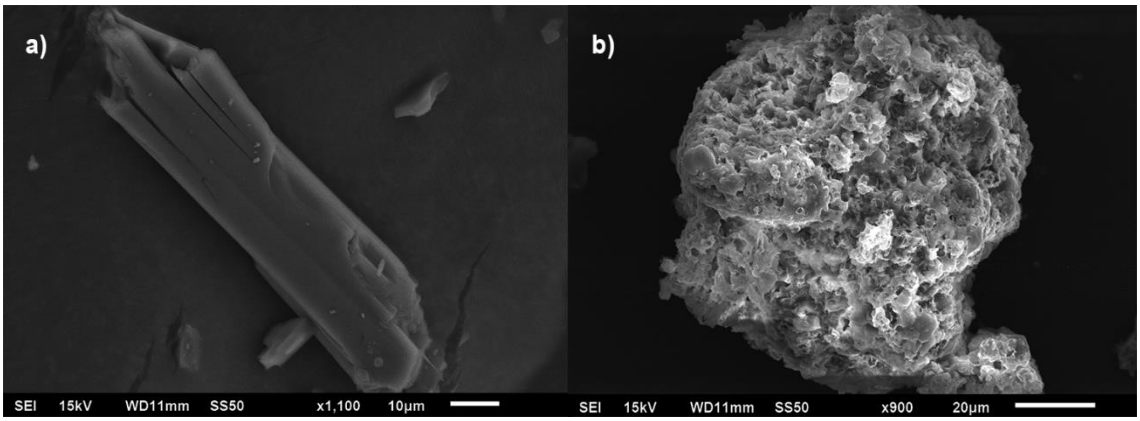

Figura 49. Micrografías tomadas por SEM de a) cristal de (3) y b) residuo sólido de la reacción de (3) con NaCN

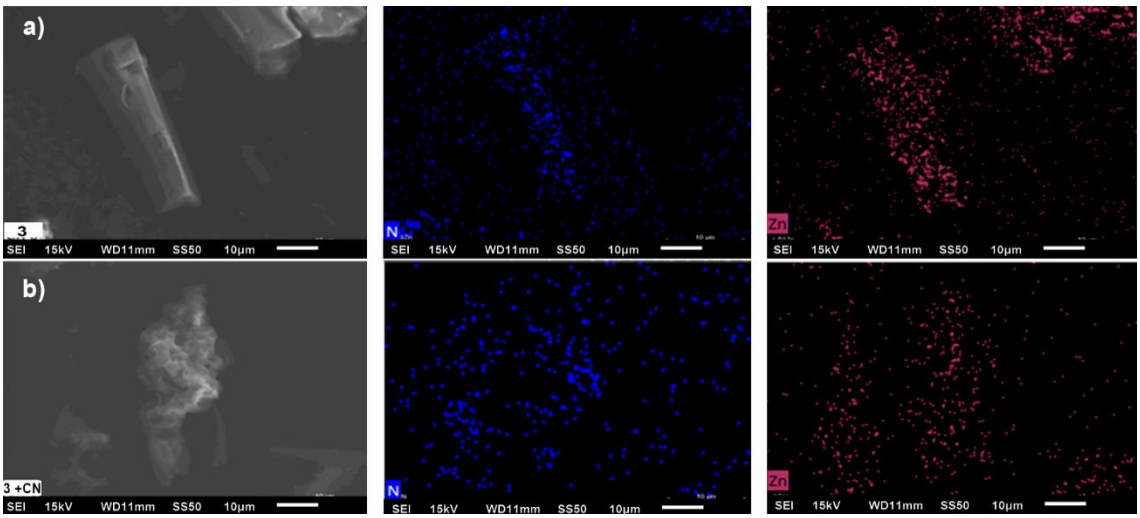

Figura 50. Mapeo por EPS de a) cristal de (3) y b) residuo sólido de la reacción de (3) con NaCN

La caracterización del sólido amorfo también fue respaldada por análisis de infrarrojo. El espectro obtenido (Figura 51), coincide con las bandas de identificación del $Zn(CN)_2$ tal y como son reportados en la literatura con la banda a 2217 cm^{-1} de la vibración de estiramiento C≡N, y una banda a 455 atribuida a vibraciones propias del acomodo del $Zn(CN)_2$ en su orientación en la celda unitaria dada su red cúbica.[142]

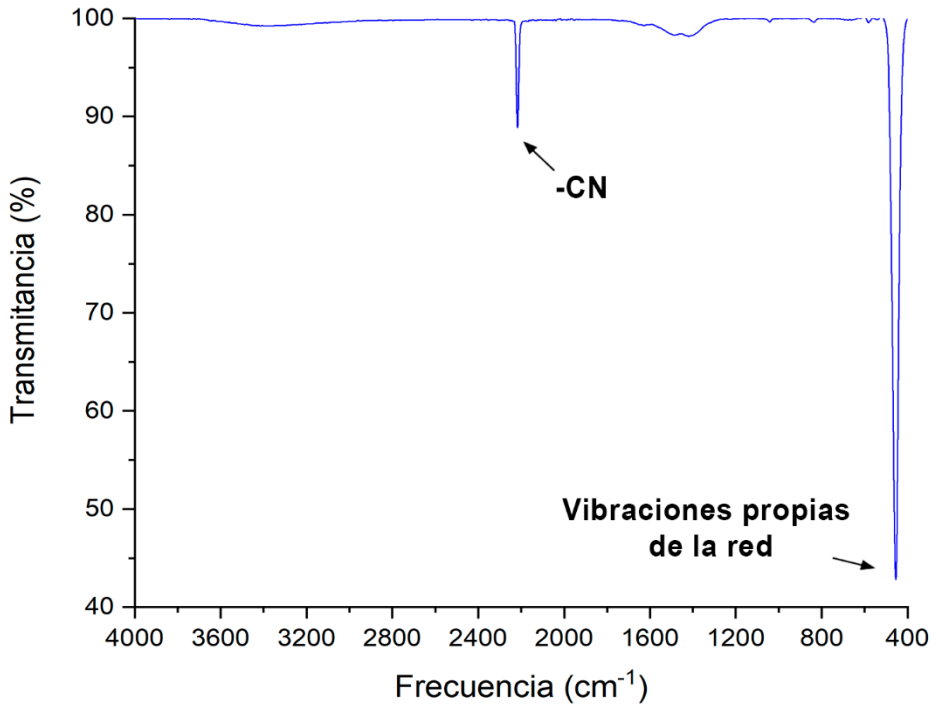

Figura 51. Espectro de infrarrojo del residuo de la reacción de (3) con NaCN

Conjuntamente, se analizaron las aguas madres mediante un tratamiento previo en el cual se llevan a sequedad en el rotavapor y se separan Na_2(1,4-chdc) de la 4,4-dtbp con la adición de agua y agitación.

La sal del carboxilato es soluble en agua, mientras que el ligante derivado de la 2,2´-bpy permanece insoluble. El sólido insoluble (4,4-dtbp) fue enviado ^{13}C CPMAS concordando con las señales esperadas (Figura 52).

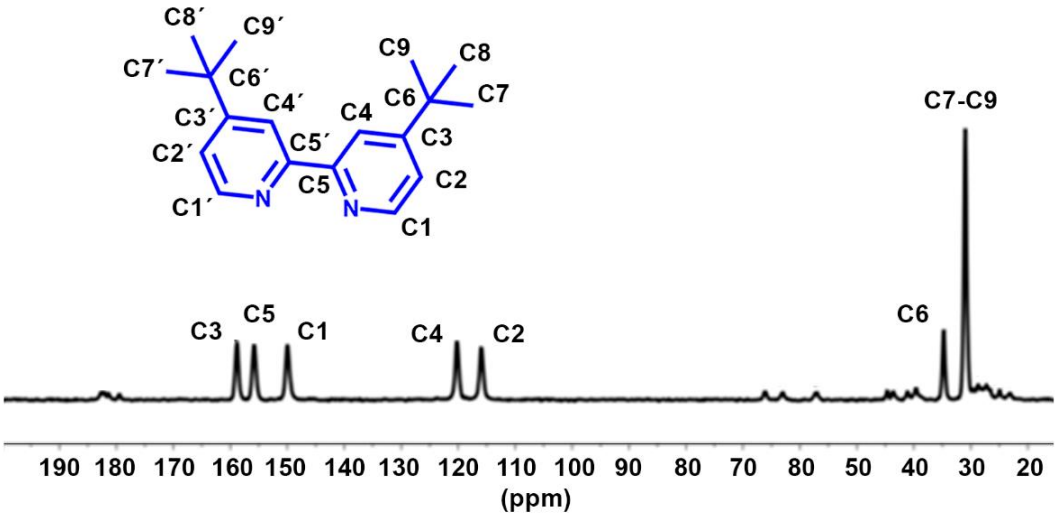

Figura 52. Espectro de ^{13}C CPMAS del sólido insoluble en agua atribuido al ligante 4,4'-dtbp

La totalidad de las pruebas analíticas respalda el enunciado que el ion CN^- realiza un ataque nucleofílico al centro metálico afectando la integridad estructural del CP **(3)** siendo el causante del apagado de la fluorescencia.

Además de la caracterización realizada, se consideró adecuado efectuar otros estudios recurrentes en el área de la química reticular como la difracción de rayos X de polvos y el análisis termogravimétrico. De igual manera, dada la facilidad sintética y económica para realizar grandes cantidades de muestra, fue posible estudiar la fluorescencia del estado sólido de los PCs y determinar el tiempo de vida de la fluorescencia.

2.1.3 Caracterización complementaria

2.1.3.1 Difracción de rayos X de polvos

El difractograma del polímero **(3)** (Figura 53) muestra una gran cantidad de picos, lo que es señal en una muestra cristalina, que su cristalización ocurre en un grupo espacial de baja simetría fenómeno que efectivamente sucede para el polímero **(3)**. Al cristalizar en el grupo espacial **Pn** del sistema monoclínico, queda indicado que las dos unidades asimétricas presentes en la celda (Z=2) pueden ser simétricamente repetibles entre sí, únicamente al realizar la operación de simetría de un plano *n.* La operación consiste en aplicar un plano espejo a la mitad del eje cristalográfico ***b*** de la unidad asimétrica y posteriormente desplazarla ½ a lo largo del eje cristalográfico ***a***. Otro aspecto visible en el

difractograma es que presenta señales muy finas, acordes a una muestra microcristalina y que ajusta tanto en la intensidad de los picos, como en su desplazamiento en el eje 2θ con el difractograma simulado (Figura 53b). Ambos factores son señal de pureza de la muestra, y que el cristal elegido en el estudio para difracción de rayos X de monocristal, es representativo de la totalidad de la muestra, es decir, que únicamente existe esa fase cristalina en el producto de síntesis. Las cuatro señales más intensas en el difractograma son puestas en la tabla, así como sus índices de Miller correspondientes de cada pico.

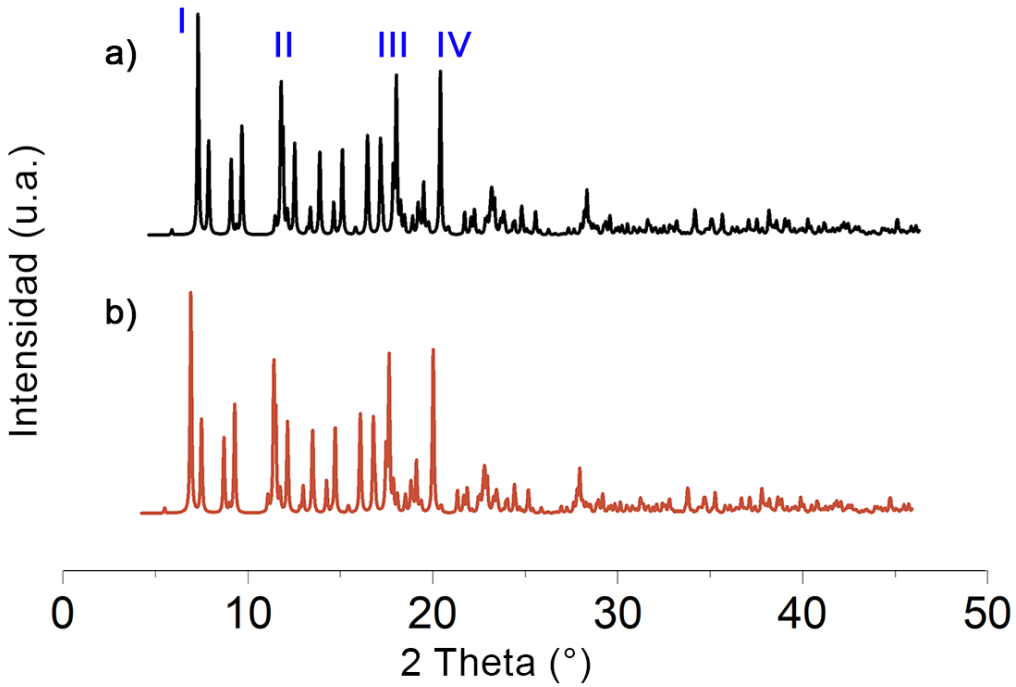

Figura 53. Difractograma de rayos X de polvos de (3) a) Experimental. b) Simulado.

Tabla 12. Picos más representativos con sus respectivos índices de Miller de difractograma (3)

Pico	2θ	h,k,l
I	7.89	0,1,0
II	12.71	1,0,-3
III	19.45	-2,0,-2
IV	22.03	2,0,-4

2.1.3.2 Análisis termogravimétrico

La Figura 54 muestra el termograma resultante del CP **(3)**. En él se aprecian tres regiones de pérdidas de peso importantes. La primera etapa ubicada entre 69.42°-154.73° pertenece a la pérdida de las nueve moléculas de agua existentes en la red, cuyo valor teórico esperado es de 13.85%, siendo el experimental de 12.59%. La siguiente pérdida sucede en el intervalo de temperatura de 154.74°-

419.39° y es atribuida a la descomposición de ligante auxiliar luminiscente con 4,4-dtbp con un porcentaje de peso de 45.83%. La magnitud porcentual experimental, coincide con la teórica esperada para dos moléculas del ligante 4,4-dtbp (45.83% experimental vs 45.88% teórica). Por último, en el intervalo de 419.39°-690.55° acontece la pérdida de las dos moléculas del ligante puente 1,4-chdc con un valor del 25.11% (29.09% teórico) dejando la muestra como óxidos de zinc.

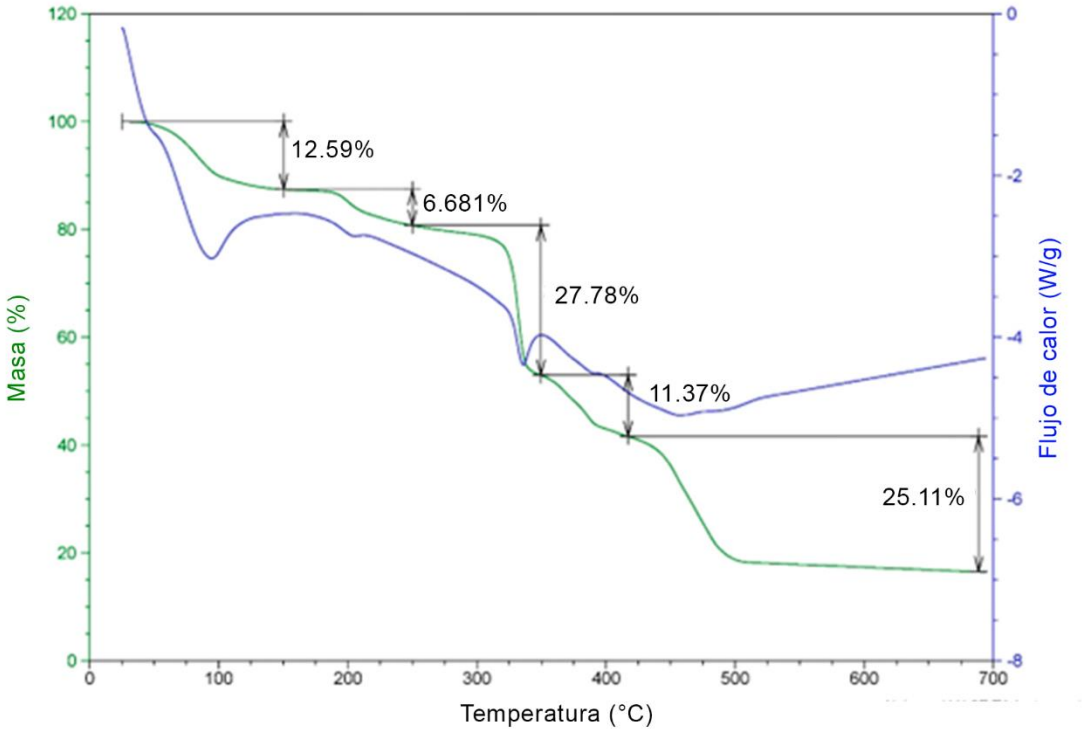

Figura 54. Análisis termogravimétrico de (3)

2.1.3.3 Fluorescencia del estado sólido

Al llenar la celda de medición de fluorescencia con muestra, fue posible efectuar el análisis fluorimétrico de los tres PCs (Figura 55). El espectro de fluorescencia en estado sólido de los compuestos **(1)**, **(2)** y **(3)**, es muy similar al que exhiben en emulsión, teniendo un ligero desplazamiento batocrómico de sus máximos de emisión (Figura 41). Para finalizar, se muestra una fotografía de los cristales luminiscentes de **(3)** bajo la lámpara de UV (254nm) (Figura 55b) y su tiempo de vida de la fluorescencia (Figura 56), el cual ocurre por un decaimiento bi-exponencial (τ_1 = 12.26 ns vs τ_2 = 2.14 ns).

.

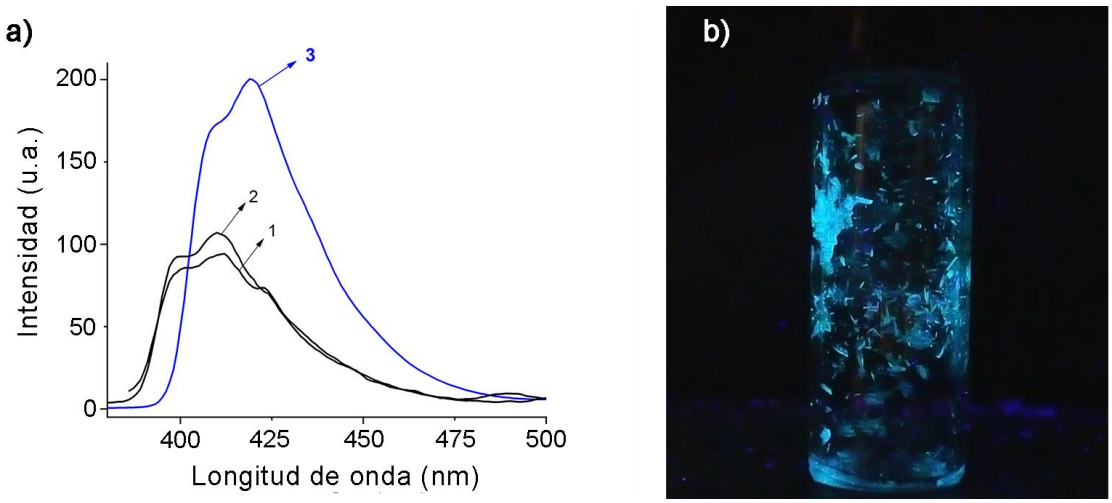

Figura 55. a) Espectro de fluorescencia de los compuestos (1-3) en estado sólido. b) Fotografía de (3) bajo la lámpara de UV (254nm)

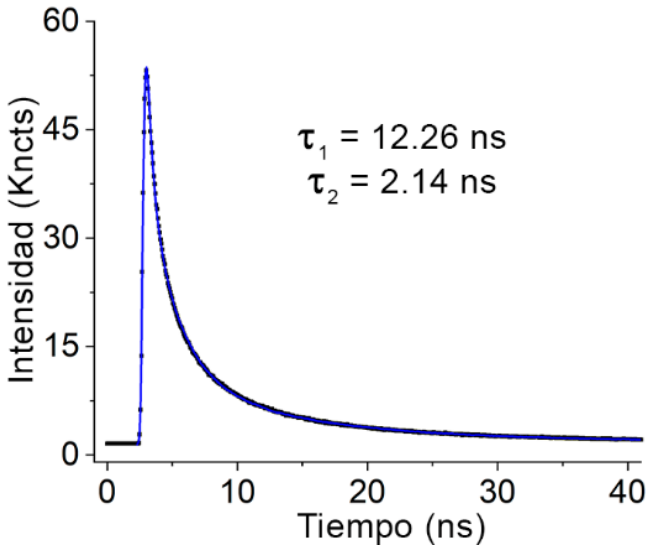

Figura 56. Tiempo de vida de la fluorescencia de (3).

2.1.4 Conclusiones del Sistema I

Se sintetizaron con éxito monocristales de tres nuevas redes metal-orgánicas luminiscentes con el centro metálico de Zn(II) y los ligantes 1,4-chdc como ligante puente, y los ligantes derivados de la 2,2-bipiridina como ligantes auxiliares luminiscentes.

A partir de los estudios de difracción de rayos X de monocristal, fue posible llevar a cabo el análisis estructural de los nuevos PCs, comparando la influencia de las sustituciones de grupo alquilo en los ligantes auxiliares en la arquitectura de los polímeros estableciendo lo siguiente: “Estructuralmente, las

sustituciones de grupos alquilo en las posiciones 4,4- y 5,5- de ligantes derivados de 2,2'-bpy no afectan a la topología de los polímeros de coordinación con el ligante puente 1,4-chdc^{-2} y el ion Zn (II) ya que mantienen la arquitectura de sus cadenas poliméricas, en cambio, las sustituciones en el ligante auxiliar ejercen un papel preponderante en la estructura supramolecular derivada de las interacciones secundarias en cada polímero (Figura 40).

Los nuevos PCs luminiscentes sintetizados fueron estudiados para su aplicación en la detección de aniones inorgánicos por fluorescencia, mostrando una selectividad hacia el ion cianuro.

De los compuestos **(1-3)**, el polímero **(3)** exhibe una mayor intensidad fluorescente atribuida al factor de la sustitución de los átomos de hidrógeno por grupos alifáticos en el ligante auxiliar luminiscente, específicamente a que el proceso de relajación vibracional que experimenta un grupo tert-butilo **(3)** es menor al que reside por parte de los grupos metilo en los PCs **(1** y **2)**. Dada la mejor respuesta fluorescente, se eligió al polímero **(3)** como sensor representativo para los estudios de sensibilidad, selectividad, elucidación del mecanismo de sensado y caracterización adicional por diversas espectroscopias y técnicas analíticas.

A través de titulaciones en agua (pH = 7.0), se calculó el límite de detección de **(3)** hacia el ion cianuro LDD = 0.90 µM, magnitud menor a la permitida en agua potable por la OMS. En comparación con los otros sensores, el límite de detección se encuentra dentro del rango de otras redes metal-orgánicas (2 x 10^{-6}M a 1.9 x 10^{-8}M), no obstante, su preparación resulta mucho más conveniente por su fácil preparación en condiciones ambientales de presión y temperatura, además de ser más económico al partir del ion metálico Zn(II) como nodo de la red, en lugar de sus similares de Hf(IV) y Zr(IV).

También fue estudiado el efecto del pH en el sensor en los medios ácido (pH =5) y básico (pH =8), observando en ambos un menor apagamiento de la luminiscencia por menor competencia del ion cianuro ante las especies HCN en medio ácido, y $^{-}$OH en el básico.

Se comprobó la selectividad del compuesto **(3)** hacia el ion cianuro, a través de una titulación en presencia con ocho aniones distintos, demostrándose en los perfiles de las titulaciones fluorimétricas (Figura 43).

El mecanismo de sensado sucede mediante un ataque nucleofílico del ion cianuro al centro metálico, formando $Zn(CN)_2$,y apagando la fluorescencia. La demostración del mecanismo fue evidenciada por las técnicas de espectroscopia de infrarrojo, resonancia magnética nuclear, resonancia magnética nuclear ^{13}C CPMAS, microscopia de barrido electrónico SEM y espectroscopia de energía dispersiva EDS.

La medición del tiempo de vida de la fluorescencia establece que el mecanismo de apagado de la fluorescencia procede por un apagamiento dinámico.

Caracterización adicional del polímero **(3)** fue efectuada en los análisis de fluorescencia del estado sólido, difracción de rayos X de polvos y análisis termogravimétrico.

Dada las características que presenta la red metal-orgánica **(3)**, brindadas por la totalidad de sus estudios, se concluye el compuesto que puede servir como un sensor funcional en la detección luminiscente del anión CN^- en medio acuoso.

2.2 Sistema II: "MOF de Zn(II) y el ligante ácido terfenil-3,3",5,5" tetracarboxílico aplicado en la detección de aniones farmacéuticos de la familia de las estatinas."

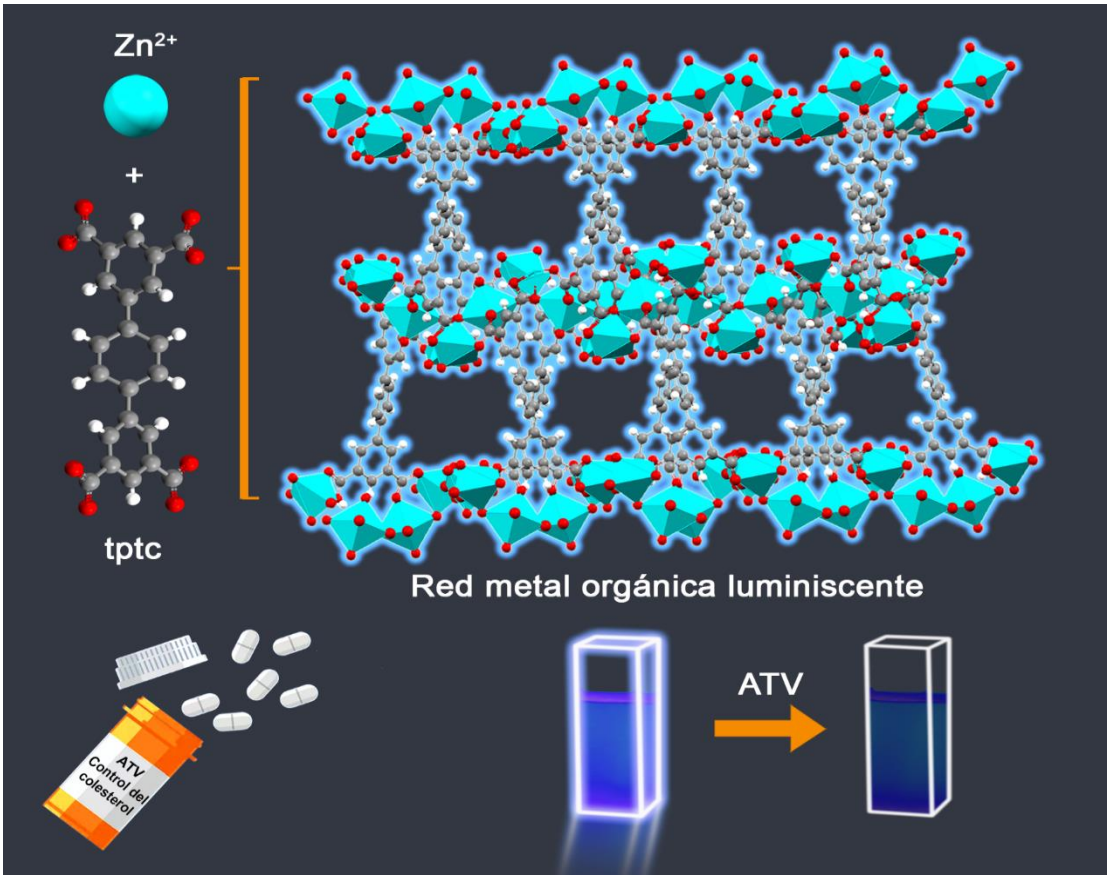

Figura 57. Resumen gráfico del sistema II

A través de una reacción solvotermal entre el ligante ácido terfenil-3,3",5,5" tetracarboxílico (tptc) y la sal $Zn(CF_3SO_3)_2$ se logró la síntesis de un nuevo MOF con USC y topología de red distintas a las descritas en la sección de antecedentes II: "Redes metal-orgánicas con el ligante tptc y el ion Zn(II)", La reacción es ilustrada en la Figura 58.

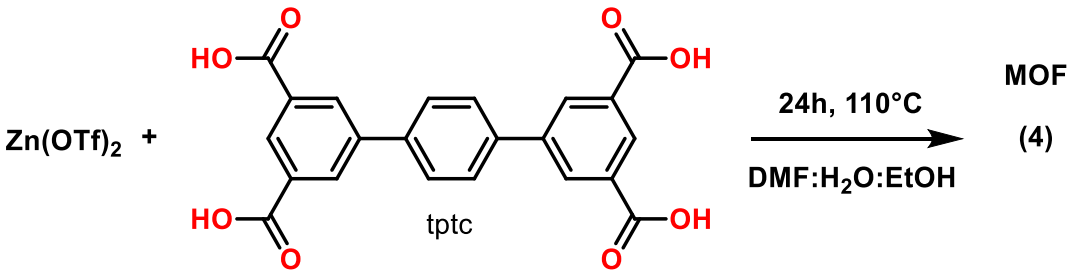

Figura 58. Reacción general para la obtención del MOF (4)

2.2.1 Análisis estructural

La obtención del producto como monocristal, permitió obtener su resolución estructural, haciendo posible la descripción de la red. En la Tabla 13 se agrupan los datos cristalográficos principales del MOF **(4)**.

Tabla 13. Datos cristalográficos para el compuesto (4)

Compuesto	**4**
Formula	C50.21 H43.23 O20.41 Zn3
Peso Molecular	1002.72
Temperatura K	100
Longitud de onda(Å)	1.54178
Sistema Cristalino	Monoclínico
Grupo Espacial	C2/c
***a* (Å)**	10.1439(6)
***b* (Å)**	28.6171(15)
***c* (Å)**	18.2650(10)
***α* (grados)**	90
β (grados)	90.938(3)
***γ* (grados)**	90
Volumen ($Å^3$)	5301.4(5)
Z	4
Densidad (calculada)	1.256 Mg/m^3
Coeficiente de absorción	2.090 mm^{-1}
F(000)	2016
Tamaño del cristal	0.172 x 0.098 x 0.059 mm^3
Rangos de los índices	-12<=h<=12 0<=k<=34 0<=l<=22
Reflexiones colectadas	4849
Final R índices [I>2sigma(I)]	R1 = 0.0749 wR2 = 0.02167
R índices (all data)	R1 = 0.0815 wR2 = 0.0230
Goodness-of-fit on F^2	1.120
Datos / Restricciones / Parámetros	4849/ 389 / 346

2.2.1.1 MOF $\{[Zn_3(Htptc)_2]\cdot(H_2O)_{1.3}\cdot(CH_3CH_2OH)_{3.1}\}_n$ (4)

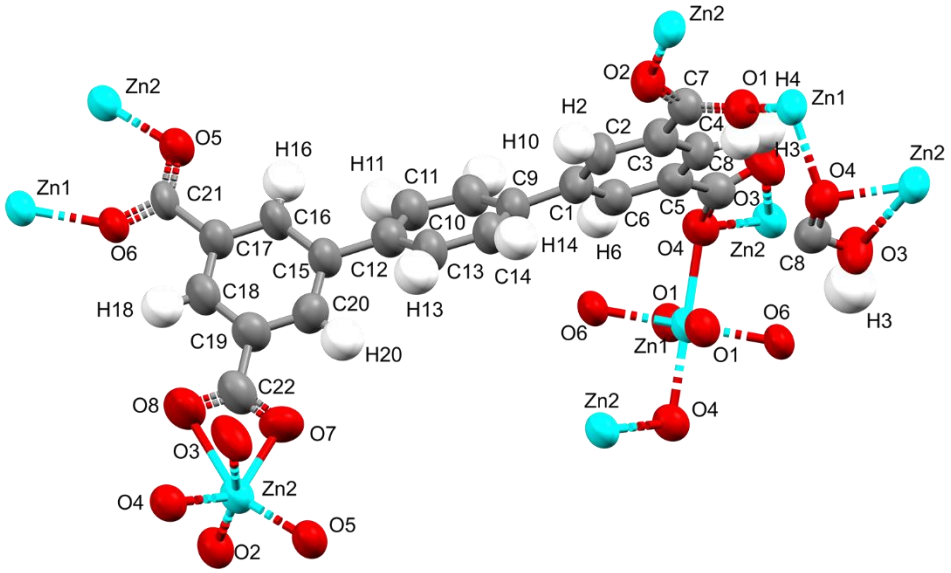

Figura 59. Representación elipsoidal al 50% del MOF $\{[Zn_3(Htptc)_2]\cdot(H_2O)_{1.3}\cdot(CH_3CH_2OH)_{3.1}$ (4) en los colores; Zn: azul cielo, C: gris, N: azul marino, H: blanco, O: rojo.

El MOF $\{[Zn_3(Htptc)_2]\cdot(H_2O)_{1.3}\cdot(CH_3CH_2OH)_{3.1}\}$ **(4)** cristaliza en el sistema cristalino monoclínico grupo espacial C2/c. La unidad asimétrica en la celda unitaria está conformada por dos iones Zn(II) cristalográficamente independientes, dos unidades del ligante tptc, además de moléculas de disolvente de cristalización como agua (1.3 moléculas) y etanol (3.1 moléculas) (Figura 59).

Ambas esferas de coordinación de los centros metálicos exhiben una geometría octaédrica distorsionada, y comparten un átomo de oxígeno O(4) en un oxo-enlace que los conecta directamente entre sí. Tanto Zn(1) como Zn(2), poseen esferas de coordinación con número de coordinación seis, saturadas por los átomos de oxígeno de los carboxilos del ligante tptc que presentan dos tipos de coordinación el enlace M-(C**OO**)-M y quelato bidentado. Las distancias y ángulos de enlace (Tablas 14 y 15) en ambos iones Zn(II) con los átomos de oxígeno son similares a los reportados en la literatura para MOFs de Zn y tptc.[117,119–121]

Tabla 14. Longitudes y ángulos de enlace selectos de la esfera de coordinación del ion Zn(II) en (4).

Enlace	Longitud (Å)	Enlace	Longitud (Å)
Zn(1)-O(1)	2.012(4)	Zn(2)-O(7)	2.000(5)
Zn(1)-O(1)#1	2.012(4)	Zn(2)-O(2)#6	2.008(4)
Zn(1)-O(6)#2	2.085(4)	Zn(2)-O(5)#7	2.013(4)
Zn(1)-O(6)#3	2.085(4)	Zn(2)-O(4)#8	2.038(4)
Zn(1)-O(4)#4	2.171(4)	Zn(2)-O(8)	2.425(6)
Zn(1)-O(4)#5	2.171(4)	Zn(2)-O(7)	2.000(5)

Tabla 15. Longitudes y ángulos de enlace selectos de la esfera de coordinación del ion Zn(II) en (4).

Enlaces	Ángulo (°)	Enlaces	Ángulo (°)
O(1)-Zn(1)-O(1)#1	180.0	O(7)-Zn(2)-O(2)#6	105.40(19)
O(1)-Zn(1)-O(6)#2	95.51(17)	O(7)-Zn(2)-O(5)#7	97.75(19)
O(1)#1-Zn(1)-O(6)#2	84.49(17)	O(2)#6-Zn(2)-O(5)#7	102.20(19)
O(1)-Zn(1)-O(6)#3	84.49(17)	O(7)-Zn(2)-O(4)#8	132.85(19)
O(1)#1-Zn(1)-O(6)#3	95.51(17)	O(2)#6-Zn(2)-O(4)#8	107.50(16)
O(6)#2-Zn(1)-O(6)#3	180.0(2)	O(5)#7-Zn(2)-O(4)#8	107.11(17)
O(1)-Zn(1)-O(4)#4	88.60(16)	O(7)-Zn(2)-O(8)	57.71(19)
O(1)#1-Zn(1)-O(4)#4	91.40(16)	O(2)#6-Zn(2)-O(8)	91.9(2)
O(6)#2-Zn(1)-O(4)#4	88.60(16)	O(5)#7-Zn(2)-O(8)	154.54(18)
O(6)#3-Zn(1)-O(4)#4	91.40(16)	O(4)#8-Zn(2)-O(8)	88.29(2)
O(1)-Zn(1)-O(4)#5	91.40(16)	O(6)#2-Zn(1)-O(4)#5	91.40(16)
O(1)#1-Zn(1)-O(4)#5	88.60(16)	O(6)#3-Zn(1)-O(4)#5	88.60(16)

2.2.1.1.1 Estructura polimérica de (4)

Interesantemente, debido a la existencia del oxo-enlace, los dos iones Zn(II) octaédricos forman una USC con ocho puntos de unión de los grupos carboxilo en un cluster tri-nuclear (Figuras 60 y 61). El ligante tptc conecta con cuatro USC resultando en un nuevo tipo de red tridimensional, descrita por la representación de clusters con el programa TOPOS PRO[143] como 3,3,8-c.

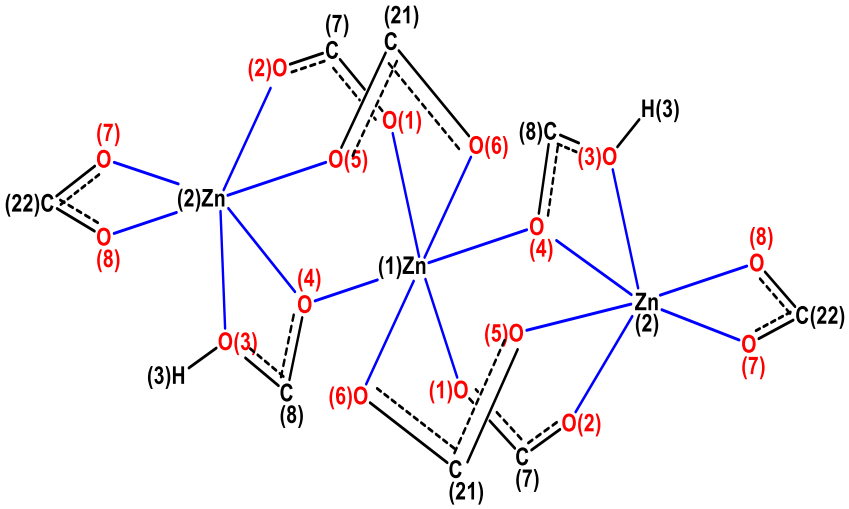

Figura 60. Representación simplificada de la conectividad del cluster del MOF(4)

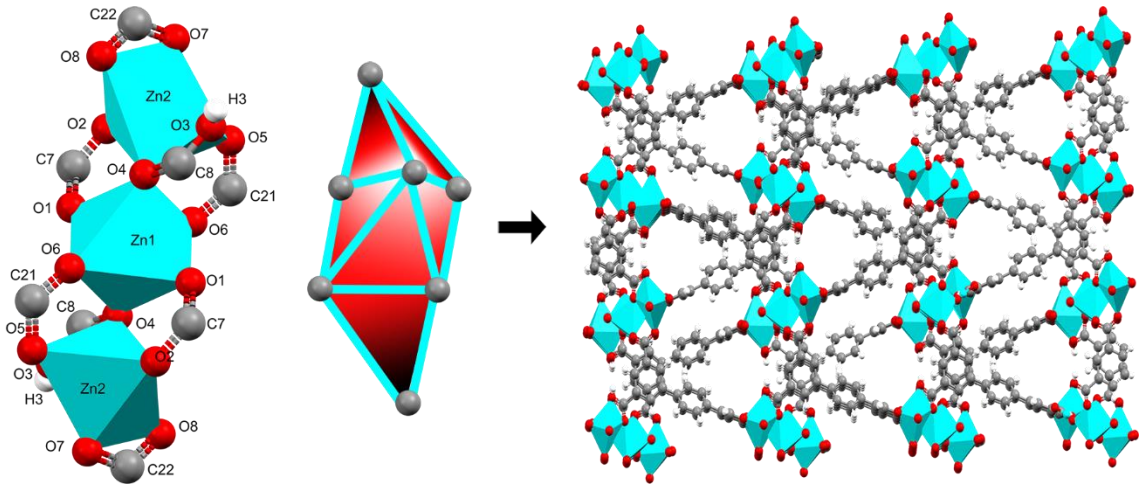

Figura 61. USC y construcción de red del MOF (4).

El arreglo reticular del MOF permite que se generan canales en las 3 dimensiones que son ocupados por las moléculas de disolventes de cristalización. Las formas de los canales dependen de su visualización en los ejes cristalográficos, en la Figura 61 adquieren una forma triangular en el eje cristalográfico ***b***, mientras que en el eje cristalográfico ***a*** poseen una forma oval. (Figura 62a). El espacio disponible en el MOF fue calculado con el programa Mercury en ausencia de las moléculas de disolvente (1886 Å) lo que corresponde al 33.5% del volumen total de la celda unitaria (5301 Å). La representación del volumen disponible en la estructura cristalina es ilustrada en la Figura 62b.

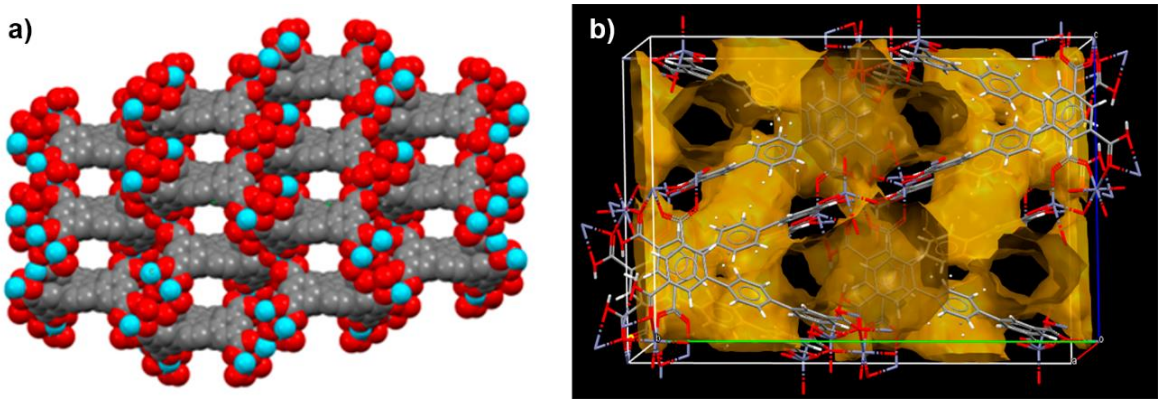

Figura 62. Representación "spacefill" de (4) en el eje cristalográfico *b*. b) Representación de volumen disponible en (4) en color mostaza

2.2.2 Estudios de las propiedades luminiscentes aplicadas al sensado de aniones y análisis espectroscópicos.

Tras la caracterización cristalográfica inicial, se continúa con la espectroscópica a través de estudios de fluorescencia en emulsiones en etanol por ser uno de los disolventes en que es sintetizado el MOF (véase Capítulo III: Desarrollo experimental). Con la finalidad de poder realizar el sensado fluorescente

de aniones, se plantea la incorporación de agua en el medio en una proporción de volumen 8:2 etanol:agua. Sin embargo, a diferencia de los PCs **(1-3)** que poseen moléculas de agua de coordinación y son cristalizados en agua-metanol, el uso de un medio parcialmente acuoso en las mediciones fluorescentes del compuesto **(4)** puede poner en cuestionamiento su estabilidad estructural. Para esclarecer ese plausible inconveniente, se decide realizar una cinética de estabilidad del MOF en el sistema 8:2 etanol:agua durante 10 horas con mediciones constantes cada 10 minutos. Tal y como se aprecia en la Figura 63, la intensidad fluorescente del MOF permanece constante pese a realizarse numerosas mediciones y permanecer en agitación constante durante todo el lapso del experimento. Otras pruebas adicionales de la estabilidad del MOF en el medio de medición, fueron la del análisis de difracción de rayos X de polvos del compuesto recién sintetizado y posterior a 24 de estar inmerso en la solución etanol:agua 8:2 (Figura 64), así como el correspondiente análisis de infrarrojo bajo ambas condiciones (Figura 65*) vide infra*.

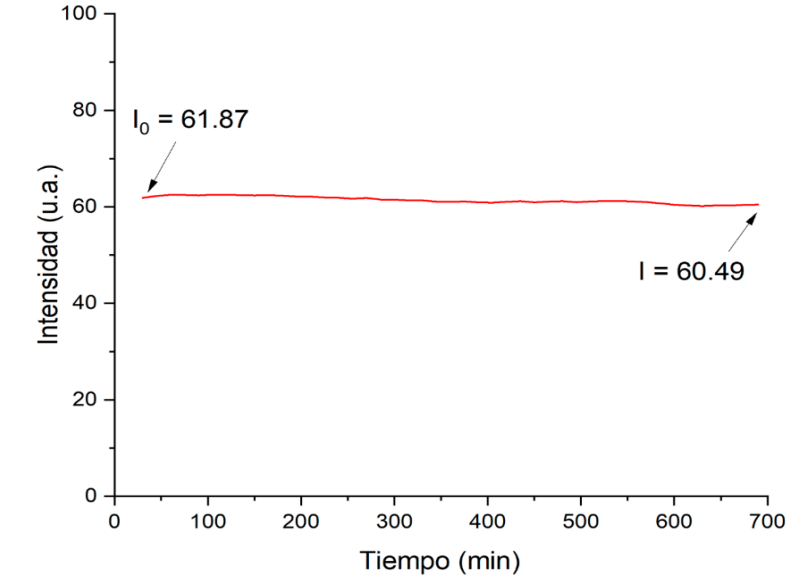

Figura 63. Mediciones de fluorescencia de (4) en el medio 8:2 etanol agua durante 10 horas

El análisis de difracción de rayos X de polvos de **(4)** muestra las mismas intensidades y desplazamiento de picos esperados con el simulado, denotando que el cristal elegido para su resolución es representativo de una muestra uniforme y pura. Además, después de permanecer 24 horas en el medio 8:2 etanol:agua, no presenta cambios con respecto al MOF recién sintetizado, disipando así las dudas de su estabilidad para sus mediciones fluorescentes. Información adicional del difractograma puede ser interpretada al observar picos a ángulos menores de 5°, ya que señales a ángulos pequeños ocurren cuando la muestra posee una celda unitaria muy grande, fenómeno recurrente en MOFs y que es acorde a los datos cristalográficos de **(4).** Las señales en forma de picos finos son consistentes con una muestra microcristalina. Por último, la cantidad de señales en el difractograma indican que la

muestra, de ser monocristal, cristaliza en un grupo espacial con baja de simetría, aunque mayor que la exhibida en el difractograma de la Figura 50. Lo cual es congruente ya que ambas redes **(3)** y **(4)** pertenecen al sistema monoclínico, pero difieren en su grupo espacial, Pn para **(3)** y C2/c para **(4),** teniendo el grupo C2/c una mayor cantidad de operaciones de simetría que relacionan las unidades asimétricas en la celda unitaria. Entre algunas de esas operaciones destacan el plano en el eje cristalográfico **c** y el desplazamiento a del eje cristalográfico **b**, implícitamente creando un plano de desliz axial o plano n.

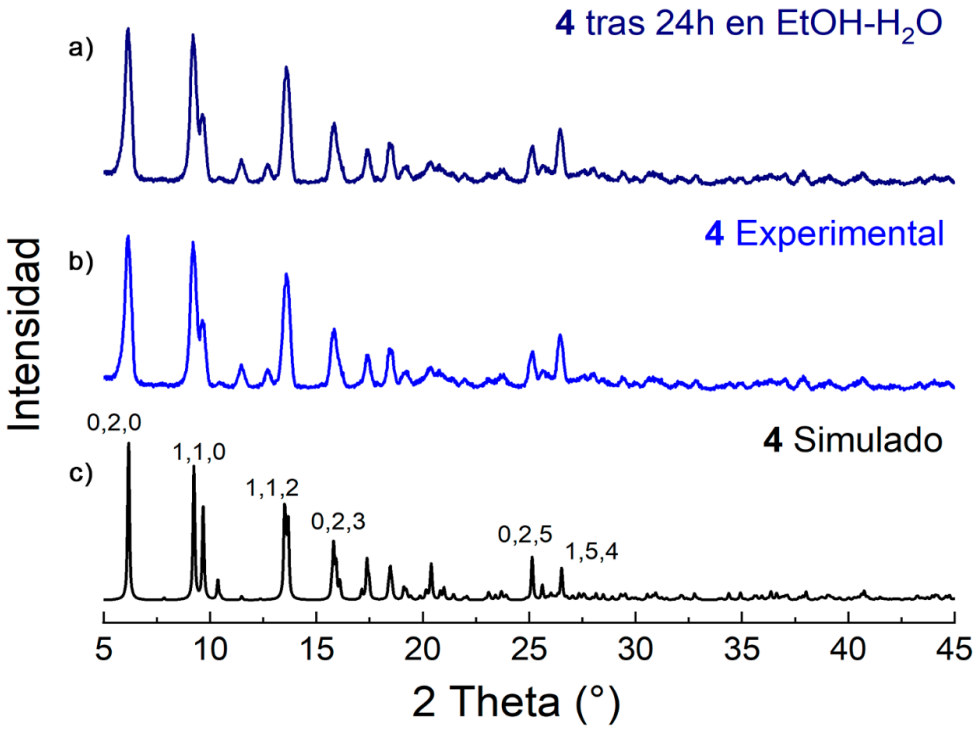

Figura 64. Difractograma del MOF (4) en: a) Tras permanecer en agitación constante en el sistema etanol-agua 8:2. b) Experimental. c) Simulado, con las respectivas asignaciones de los índices de Miller de los picos más intensos.

El espectro de infrarrojo de **(4)** (Figura 65) denota las mismas señales previo y posterior a permanecer en agitación constante en el medio etanol-agua, soportando los análisis previos como prueba de su estabilidad en el sistema elegido para el sensado de aniones. En lo concerniente a su interpretación (Figura 65a) se hace uso del mismo análisis aplicado en los PCs **(1-3)** para establecer el modo de unión de los carboxilos hacia el ión metálico. Como se ha mostrado en la Figura 61, la USC se conforma de quelatos bidentados. La asignación de las bandas de vibración asimétrica (1618 cm^{-1}) y simétrica (1572 cm^{-1}), coincide con el cálculo del valor de Δ para la unión de quelato bidentado, (1618 -1572 = 46 << 113). Asimismo, se identifican en la Figura 65a la banda del carboxilo del grupo amida de disolvente de síntesis DMF, y la vibración C-H de los átomos de hidrógeno del ligante aromático.

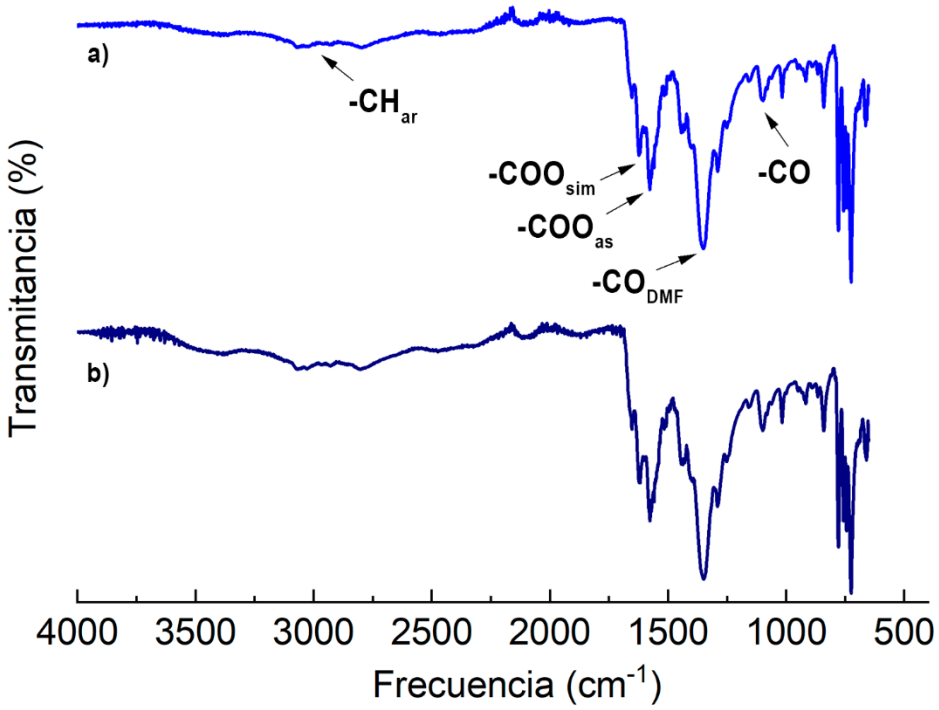

Figura 65. Espectros de infrarrojo de (4). a) Recién sintetizado. b) Tras 24h en el sistema etanol:agua (8:2).

El siguiente paso en la mediciones fluorimétricas fue el de colocar 1mg del MOF en el sistema etanol-agua y adicionar alícuotas de soluciones 10mM de aniones de interés: los farmaceúticos; atorvastatina (ATV), fluvovastatina (FV), pravastatina (PRV), rosuvastatina (RSV) y otros oxoaniones como ATP, AcO^-, $H_2PO_4^-$, $H_3PO_4^-$, SO_4^-, oxalato, malonato, succinato, glutarato, adipato, tartrato y citrato. La elección de esos aniones fue orientada en la importancia farmaceútica en el caso de las estatinas, mientras que para los oxoaniones se buscó determinar si existía algún cambio en la respuesta óptica de emisión por parte del MOF, ya que el nodo de la red tiene a los centros metálicos completamente rodeados por átomos de oxígeno, y era una cuestión importante estudiar cambios en la fluorescencia por posibles modificaciones en la esfera de coordinación o sustituciones en el ligante. En la Figura 66 se aprecia como existe un apagamiento de la fluorescencia en el MOF luminiscente con las estatinas fluvovastatina y atorvastatina, particularmente con la atorvastatina la emisión fue disminuida considerablemente.

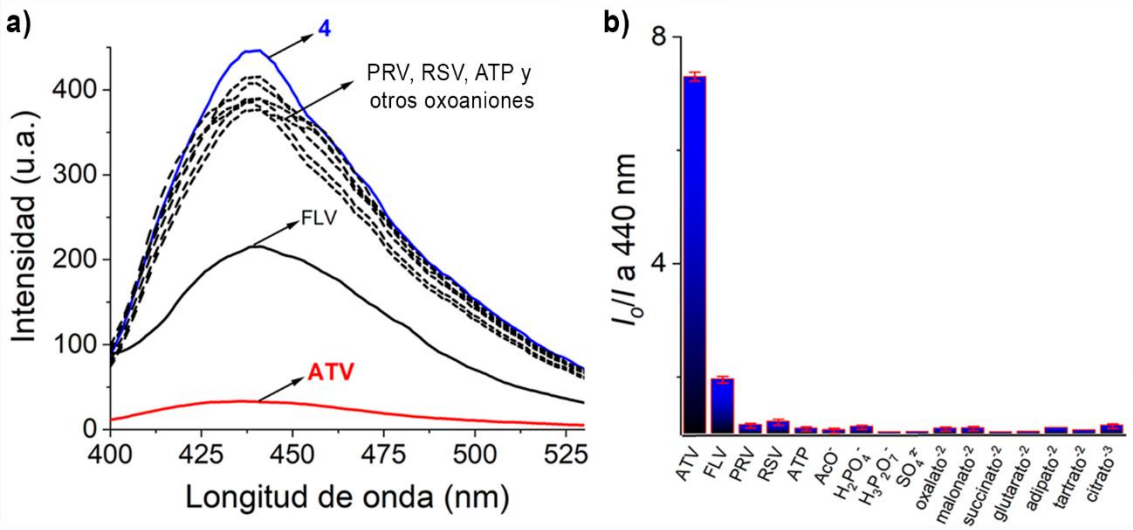

Figura 66. a) Espectro de fluorescencia de (4) y posterior a la adición de estatinas y oxoaniones. b) Emisión relativa de (4) tras la adición de los analitos sensados.

El siguiente paso, fue el de evaluar la respuesta del MOF luminiscente de forma cuantitativa ante la presencia de atorvastatina, la cual procedió a través de una titulación fluorimétrica (Figura 67).

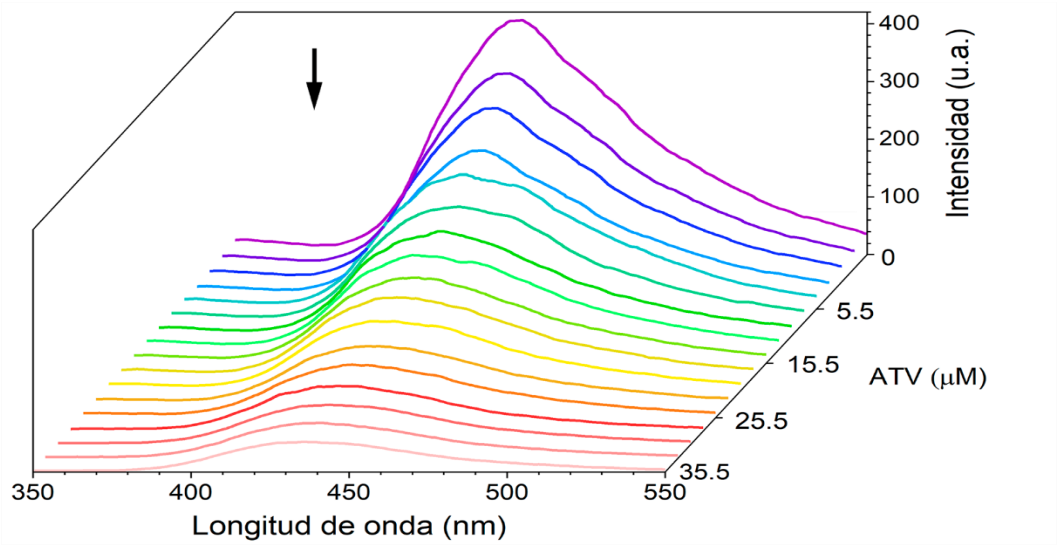

Figura 67. Curva de titulación fluorimétrica de (4) con ATV

Con la finalidad de determinar su sensibilidad hacia el analito, se procedió a realizar el perfil de la titulación calculándose por el método gráfico la ecuación de Stern-Volmer (Figura 68). El comportamiento de la curva exhibe una dependencia lineal de la intensidad fluorescente en función de la concentración de la atorvastatina, en el rango de 0-16 μM. A mayor concentración, la línea recta empieza a curvarse hacia arriba. La interpretación del perfil de titulación completo da indicios que

además de suceder un apagamiento dinámico, también se presenta el efecto de una interacción específica entre el MOF y la atorvastatina.

El efecto de apagamiento en el intervalo de 0-16 µM, es calculado por la ecuación lineal Stern-Volmer

$$\frac{I_0}{I} = (1 + K_{SV}[analito]) \qquad \text{Ecuación (2)}$$

Donde K_{SV} es la constante de apagamiento, I_0 es la intensidad fluorescente inicial, I la intensidad fluorescente final y ***[analito]*** es la concentración de la especie medida. Para describir el perfil completo de la titulación, se utiliza el modelo de Fabbrizzi[144] como una derivación de la ecuación Stern-Volmer que considera simultáneamente el apagamiento dinámico y estático en la formación de la interacción receptor-analito para formar un complejo cuya emisión es mínima o despreciable.

$$\frac{I_0}{I} = (1 + K_{SV}[analito])(1 + K_A[analito]) \qquad \text{Ecuación (3)}$$

Conjuntamente con las variables de la ecuación de Stern-Volmer, aparece en la ecuación (3) la constate de interacción aparente K_A relacionada al apagamiento estático. Considerando el valor de la constante K_{SV} del comportamiento total del perfil de titulación, se determina el límite de detección de atorvastatina por la red metal-orgánica **(4)** el cual es de 4.21µM y que es comparable con otros sensores reportados en la literatura (Tabla 16).

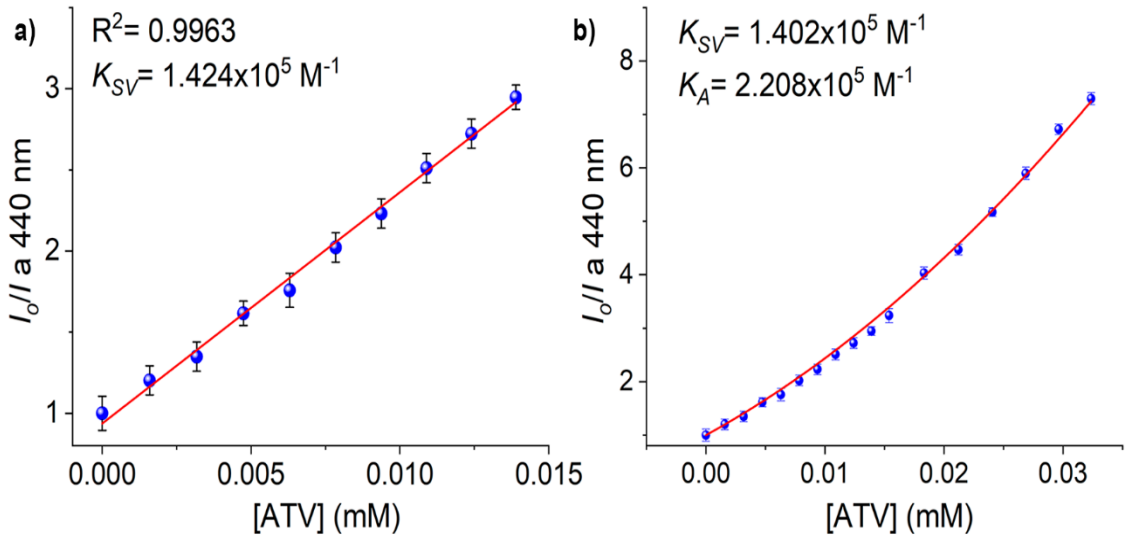

Figura 68. Perfil de titulación de ATV por el MOF (4) en el rango de 0 a 16mM. b) Perfil de titulación completo de ATV por el MOF (4).

Tabla 16. Sensores capaces de detectar atorvastatina.

Material	Técnica de detección	Límite de detección (M)	Referencia
AuNP-CNT/SPCE	Electroquímica	1.9×10^{-7}	145
Fe_3O_4@PPY / MWCNTs/ GE[b]	Electroquímica	2.3×10^{-8}	146
EPPGE[c]	Electroquímica	2.1×10^{-5}	147
PPY/CNTs/GCE[d]	Electroquímica	1.5×10^{-9}	148
ZnO/NS/ CPE[e]	Electroquímica	2.5×10^{-9}	149
VACNT-GO[f]	Electroquímica	9.4×10^{-9}	150
(4)	Fluorescencia	$4.21\ 10^{-6}$	151

[a]AuNP-CNT/SPCE = Nanopartículas de oro-nanotubos de carbono en un electrodo impreso.
[b]Fe_3O_4@PPY / MWCNTs/ GE= Electrodo de grafito modificado con polipirrol y nanopartículas de Fe_3O_4 nen un nanotube de carbono
[c]EPPGE = Electrodo de grafito pirolítico de borde plano
[d]PPY /CNTs / GCE = Polipirrol/nanotubo de carbono/ electrodo de carbono vítreo
[e]ZnO/NS/ CPE = Óxido de Zinc / nanopartículas y pasta de carbono en nano sílica
[f]VACNT-GO = Nanotubos alineados verticalmente/ óxido de grafeno.

Como se había mostrado en la Figura 66, un estudio previo de selectividad fue realizado por parte del MOF **(4)** en competencia de oxoaniones y estatinas, no obstante, debido a los resultados obtenidos hacia el anión farmacéutico atorvastatina, se decide efectuar un estudio adicional de selectividad involucrando a potenciales interferentes presentes en medios fisiológicos de sangre y orina: D-glucosa, creatinina, urea, L-prolina, NaCl, KCl, NH_4Cl, $MgCl_2$ y HCO_3^- efectuados en pH =7. De acuerdo con la Figura 68a-b, ninguno de los analitos biológicos afecta la intensidad de emisión de **(4)** como sucede con la atorvastatina, inclusive, aún en la coexistencia de atorvastatina con el resto de los analitos, se mantiene la misma respuesta óptica observada únicamente con la atorvastatina por lo que el sensor **(4)** posee una alta selectividad hacia el fármaco. Figura 68c. Adicionalmente, se tomó una fotografía con la soluciones de los potenciales bioanalitos competidores y atorvastatina con el MOF, bajo la lámpara de UV a 254 nm expuesta en la Figura 68d.

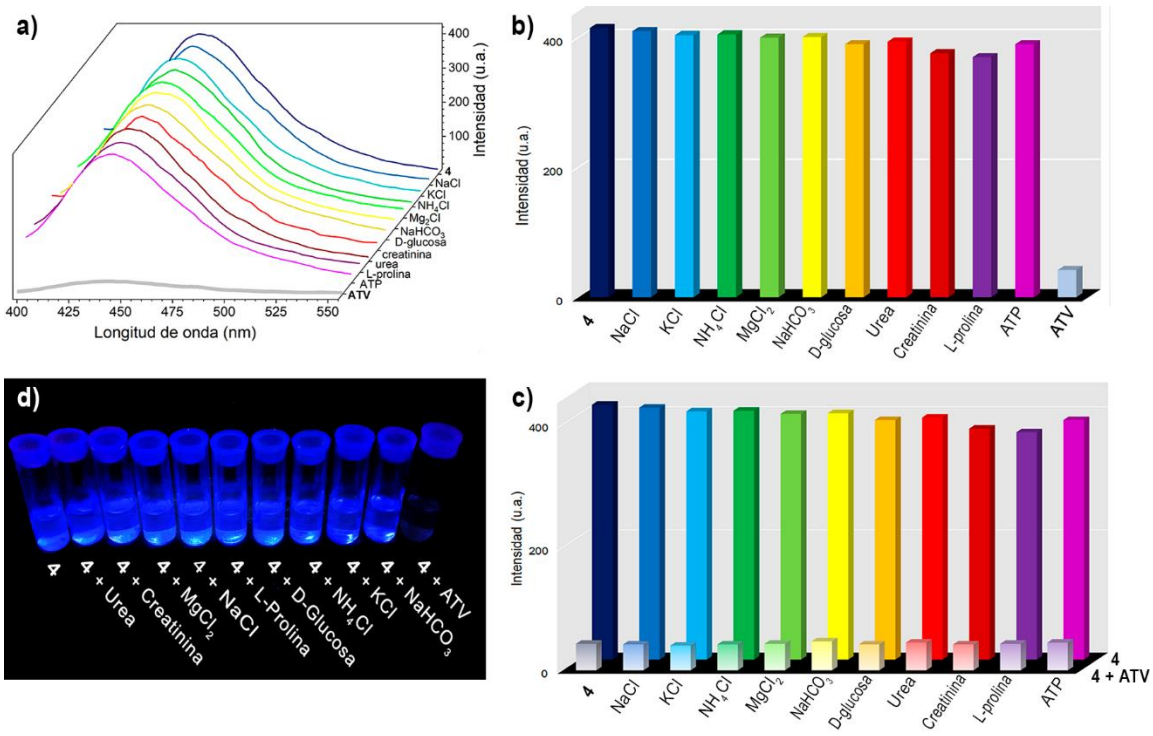

Figura 69. a) Espectro de fluorescencia de (4) con la adición de cada bioanalito. b) Histograma de la respuesta de los bioanalitos en la fluorescencia de (4). c) Histograma de la respuesta de los bioanalitos en la fluorescencia de (4) antes y después de añadir atorvastatina al sistema. d) Fotografía de las emulsiones de (4) con cada bionalito bajo la lámpara de uv a 254nm

Conocidas las características de sensibilidad y selectividad del MOF, se evalúa el mecanismo de reconocimiento hacia atorvastatina colocando 10 mg de los cristales del MOF **(4)** en 20 mL de una solución concentrada del fármaco (100 µM) dejándose en agitación constante por 24 horas. A continuación, se filtra la muestra y se realizan los análisis de infrarrojo y difracción de rayos X de polvos del sólido comparativos. Sin embargo, en el análisis de infrarrojo la banda atribuida a la coordinación metal-carboxilo se mantuvo sin desplazamiento alguno (Figura 70) y el patrón del difracción de rayos X de polvos es idéntico antes y después de la aplicación de atorvastatina (Figura 71). Por ende, se establece que no se ve comprometida la estabilidad estructural del MOF en presencia del anión farmacéutico, sino que, en su lugar, ocurre una interacción, resultado que también avala lo observado en el perfil de titulación de la fluorescencia (Figura 68).

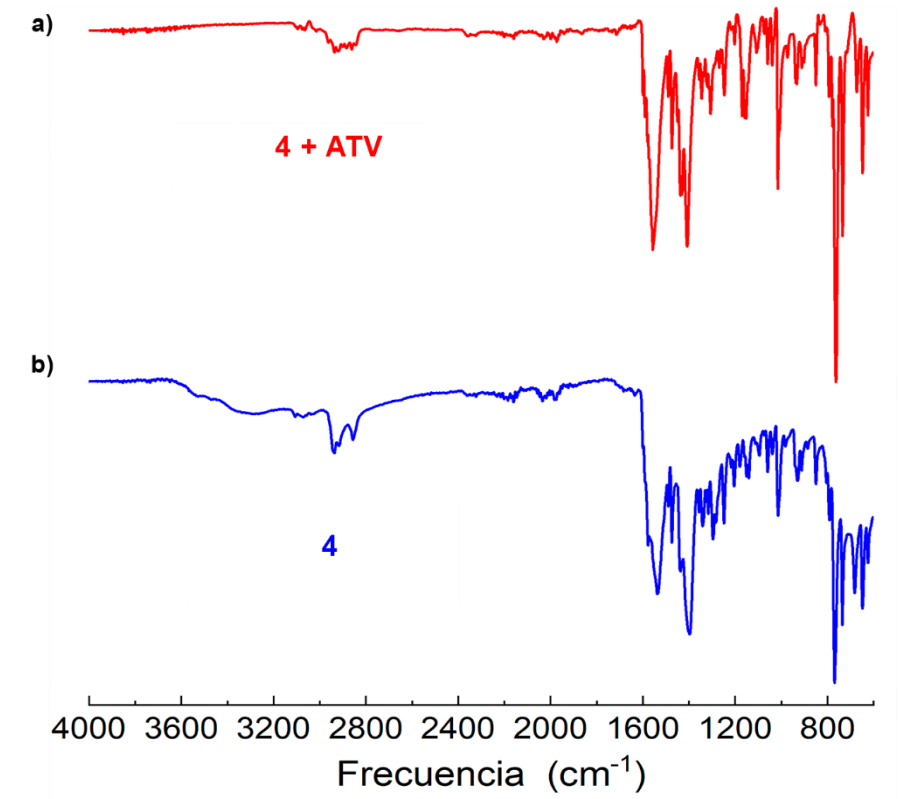

Figura 70. Espectro de infrarrojo de a) 4 tras la adición de atorvastatina y b) 4 recién sintetizado

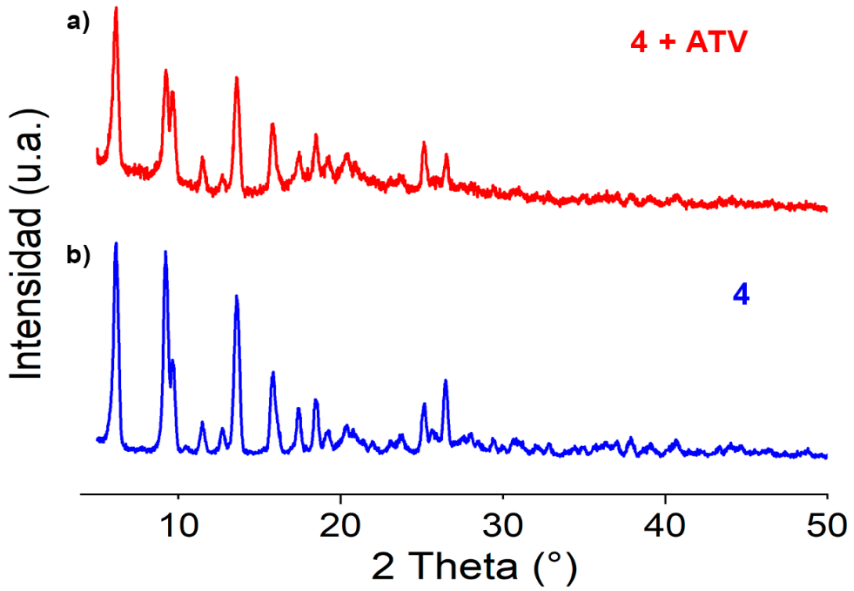

Figura 71. Difractograma de a) 4 tras la adición de atorvastatina y b) 4 recién sintetizado

Se recurrió entonces a otras técnicas de caracterización como la resonancia magnética nuclear de sólidos ^{13}C CPMAS, microscopia de barrido electrónico, espectroscopia de energía dispersiva, tiempos de vida de la fluorescencia, espectroscopía UV-visible, y de forma complementaria a estudios teóricos DFT.

En el análisis de la resonancia magnética nuclear de sólidos ^{13}C CPMAS (Figura 72), casi en su totalidad existió el solapamiento de las señales entre los carbonos aromáticos y del grupo carboxilo del ligante y de la propia atorvastatina, aunque las señales de los carbonos alifáticos de la atorvastatina en la región de 70 y 20 ppm si fueron observadas, en general las señales resultantes de la muestra tratada fueron ensanchadas considerablemente, probablemente debido a la disminución de la cristalinidad tras el tratamiento con atorvastatina. El ensanchamiento de las señales de una muestra amorfa con respecto a una cristalina es atribuido al incremento en el tiempo de la "relajación por la red", es decir, las moléculas se relajan en un intervalo de tiempo más corto al estar ordenadas como sucede en un cristal, a diferencia de lo que sucede en una muestra amorfa donde las moléculas poseen una diferencia de energía ligeramente menos homogénea y con ello ven ampliado el intervalo del tiempo de relajación.[152]

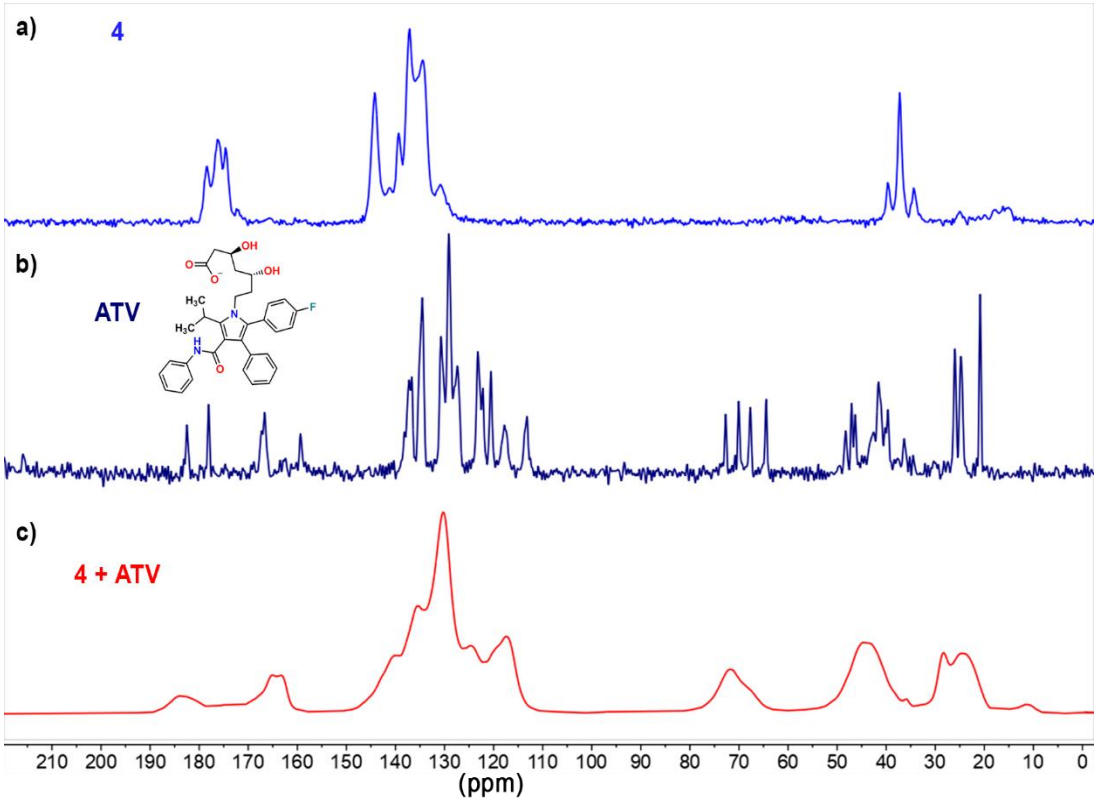

Figura 72. Espectro de ^{13}C por la técnica CPMAS del a) MOF 4, b) Atorvastatina y c) el MOF 4 con atorvastatina.

Por su parte, en el análisis de microscopia de barrido electrónico en conjunto con la espectroscopia de energía dispersiva, fue posible observar cambios superficiales en la morfología del cristal del compuesto **(4)** previa y posteriormente a su tratamiento con atorvastatina. En la Figura 73a se visualiza los cristales del MOF y su respectivo mapeo de los átomos de zinc y oxígeno presentes en la estructura

cristalina. La muestra tratada con el anión farmacéutico (Figura 73b) pierde un poco de su cristalinidad y, más importantemente, se logró mapear los átomos de nitrógeno y flúor que únicamente derivan de la presencia de atorvastatina la muestra.

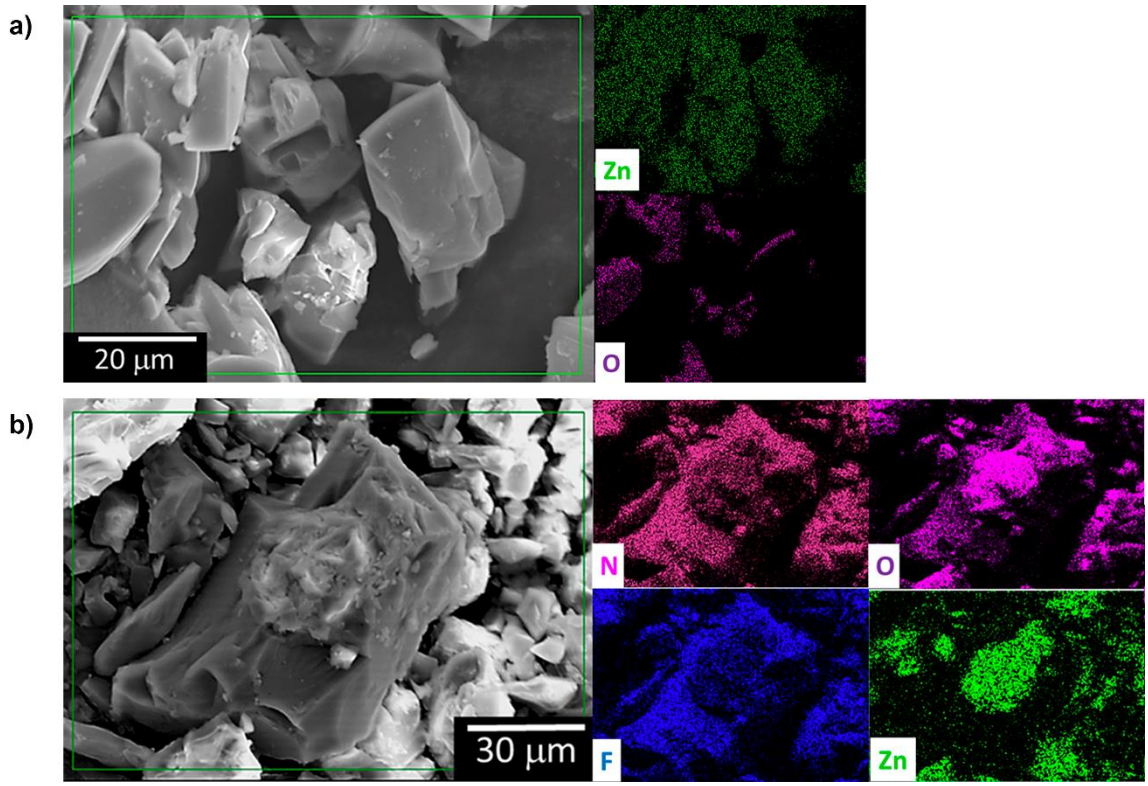

Figura 73. Micrografías tomadas por SEM con su respectivo mapeo por EDS de a) cristal del MOF 4) y b) muestra del MOF 4 tratado con atorvastatina

Teniendo indicios de un apagamiento tanto dinámico como estático por los perfiles de titulación (Figura 68) para la interacción MOF-atorvastatina, se procede a efectuar el estudio del tiempo de vida de la fluorescencia para elucidar el tipo de mecanismo responsable del apagamiento de la intensidad fluorescente. El tiempo de vida de la fluorescencia brinda, además de su definición,[viii] información importante sobre la interpretación de los mecanismos por los cuales sucede la disminución de la intensidad fluorescente, sea en un apagamiento dinámico relacionado con la pérdida de la energía a través de las colisiones moleculares entre el fluoróforo y el agente apagador, o el apagamiento estático, donde se presenta cuando el fluoróforo forma un complejo no fluorescente con el agente apagador limitando su emisión. Asimismo, en el apagamiento dinámico ocurre un cambio en los valores del tiempo de vida, y en del apagamiento estático se mantiene prácticamente la misma magnitud. En la Figura 74 se expone la gráfica de las mediciones, donde se presentan el conjunto de los tiempos de vida del MOF

[viii] Véase en el Capítulo I, sección 1.2.2.2.1 Fundamentos de luminiscencia

en solitario y del MOF con atorvastatina. Dos valores de tiempos de vida son resueltos debido a que el compuesto **(4)** tiene un decaimiento bi-exponencial probablemente atribuido a los estados singulete y triplete del ligante tptc.[153] Ambos pares de las magnitudes del tiempo de vida en las dos muestras tienen valores muy cercanos entre sí. El hecho de que permanezcan casi constantes para el receptor (MOF) y el complejo receptor-analito (MOF-ATV), es indicativo de un apagamiento estático derivado de una interacción.

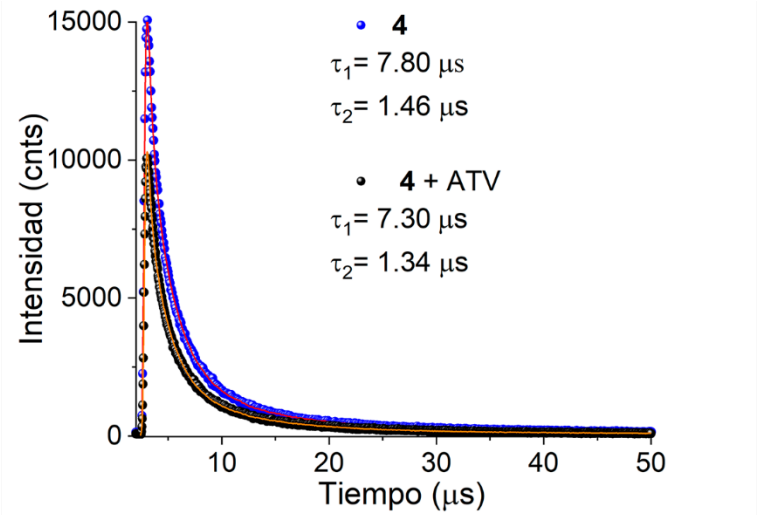

Figura 74. Tiempo de vida de la fluorescencia del MOF (4) y del MOF (4) tratado con atorvastatina

Una vez distinguido que existe una clara interacción entre la red metal-orgánica **(4)** y el anión farmacéutico, fue de interés cuantificar la cantidad de atorvastatina que es capaz de ser reconocida por el MOF. Bajo esa finalidad, se apoyó en la espectroscopía de UV-vis mediante el siguiente experimento: Se colocan 10 mg del compuesto **(4)** en 20 mL de una solución de atorvastatina 100 µM quedándose en agitación constante. Posteriormente se toman alícuotas de las aguas madres de la solución en diferentes horas, ya que el planteamiento del experimento se basa en que, al pasar el tiempo, una mayor cantidad de atorvastatina interactuará con el MOF, reduciendo así su concentración como analito libre en la solución. Para garantizar que se tomara únicamente atorvastatina disuelta en etanol, se detenía la agitación con 5 minutos de anticipación a la toma de las alícuotas dejándose asentar los cristales del MOF en el fondo del vaso de precipitados. Siete alícuotas fueron tomadas cada hora en la experimentación, a las cuales se les tomó un espectro de absorción UV-vis observándose la disminución de la concentración de atorvastatina libre en función al tiempo (Figura 75).

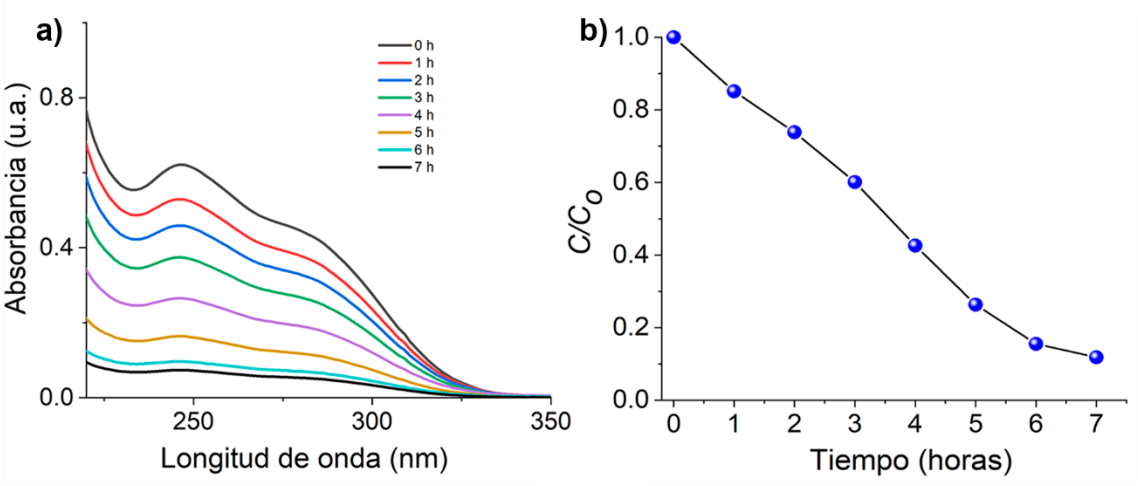

Figura 75. a) Espectro de UV-vis de la atorvastatina en presencia del MOF durante 7 horas. b) Relación de la concentración inicial de atorvastatina sobre la cuantificada a través del tiempo.

Con los datos del espectro de absorción, se elige la banda característica de la atorvastatina (247nm) para efectuar la cuantificación a través de la siguiente fórmula:

$$Q_{eq} = \frac{(C_o - C_{eq})V}{m} \qquad \text{Ecuación (4)}$$

Donde Q_{eq} es la cantidad de atorvastatina que interacciona con el MOF (mmol/g), C_0 es la concentración inicial de atorvastatina (mmol/L), C_{eq} es la concentración de atorvastatina en el equilibrio (mmol/L), V es el volumen de la solución (litros) y m corresponde a la cantidad en peso en gramos de los cristales del compuesto **(4)**. Los cálculos aplicados de la ecuación (4) permitieron determinar que interaccionan 0.193 mmol de atorvastatina por cada gramo de MOF. Desafortunadamente, el dato no puede ser comparable con el que brinda el ZIF-8/Fe_3O_4-OG, debido a que el material híbrido pasa por una serie experimentos de enriquecimiento en la adsorción de atorvastatina llegando al límite de lo que permite tanto la red metal-orgánica como el óxido de grafeno.[154] Sin embargo, el MOF **(4)** es pionero en la investigación de la interacción con atorvastatina y su cuantificación.

Desde el estudio del perfil de la titulación (Figura 68), se percibió una posible interacción entre el anión farmacéutico y el MOF, misma que fue comprobada por las técnicas de microscopia de barrido electrónico, espectroscopia de energía dispersiva, tiempo de vida de la fluorescencia, e inclusive fue cuantificada en cantidad por espectroscopía de UV-vis. No obstante, el siguiente paso radica en sugerir una propuesta de la interacción de la atorvastatina con el MOF. Haciendo uso de cálculos teóricos DFT con el programa Gaussian 16 suite con el nivel de teoría CAM-B3LYP, y, considerando los canales disponibles en la estructura cristalina, permitiendo que el analito se ubique libremente en ellos (y optimizándolos por DFT), se realizó una simulación de la interacción MOF-ATV (Figura 76).

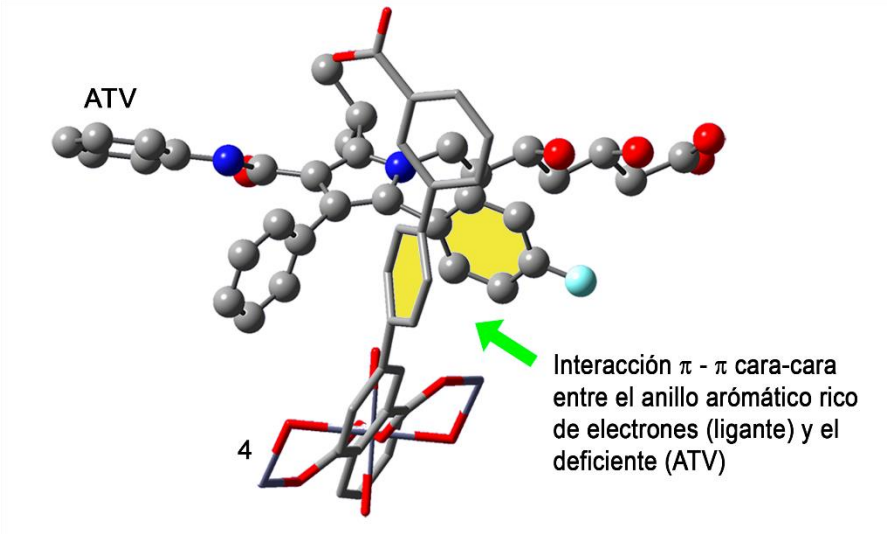

Figura 76. Propuesta de la interacción entre 4 (representación capped sticks) y la atorvastatina (representación ball sticks).

Adicionalmente se calculó la energía de interacción con el programa NBO3.1 (111.4 kcal/mol), que indirectamente ofrece una justificación del por qué existe una afinidad por atorvastatina sobre todos los analitos medidos en competencia, y que se encuentra ligado al diseño sintético de la red metal orgánica. El MOF está constituido por un ligante rico en electrones capaz de interaccionar con un analito deficiente de electrones en el cual existe una orientación favorable de tipo π-deficiente ··· π-rico entre los anillos aromáticos de la atorvastatina y el ligante tptc como lo demuestran la propuesta de los cálculos teóricos de la Figura 77. Asimismo, fue posible calcular la energía de los orbitales HOMO y LUMO del complejo MOF-ATV para brindar el mecanismo de apagamiento por el proceso PET reductivo (Figura 77).

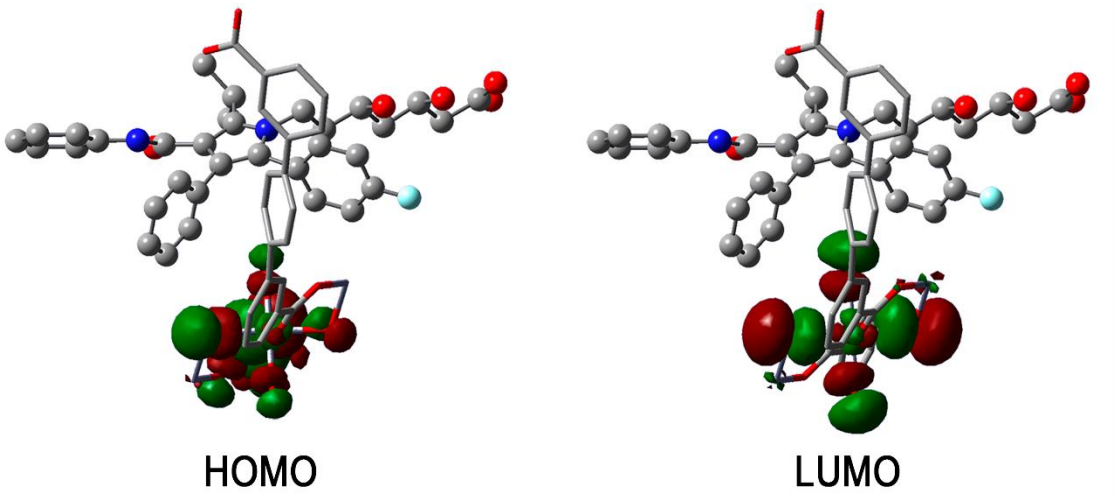

Figura 77. Representación en superficie de los orbitales HOMO y LUMO de la interacción MOF-atorvastatina.

Teniendo presente la gran cantidad de caracterización del MOF luminiscente y la explicación detallada de su interacción con atorvastatina por diferentes técnicas analíticas y teóricas. Se planteó llevar a cabo su aplicación en muestras reales consistentes en tabletas comerciales de atorvastatina, descrito en la siguiente sección.

3.4.3 Aplicación del MOF (4) en la detección fluorescente de atorvastatina en tabletas comerciales

Antes de abordar de lleno la aplicación de la determinación de atorvastatina en tabletas comerciales por el MOF, se consideró hacer pruebas de la reciclabilidad del sensor. Las prueba consiste en la determinación de su intensidad fluorescente por sí solo, y con la adición de atorvastatina bajo las mismas condiciones de las mediciones fluorescentes previas. Posteriormente, removiendo la atorvastatina tras pasar por una serie de lavados con etanol-DMF (8:2 v:v) (5 lavados con 40 mL de la solución) y un reposo en el mismo sistema por 24h, comprobando su estabilidad estructural mediante difracción de rayos X de polvos. El ciclo fue repetido 4 veces con una misma muestra. En la Figura 78 se ilustran las mediciones fluorescentes donde se aprecia una disminución en la intensidad fluorescente del MOF después de cada ciclo, manteniendo su integridad estructural de acuerdo a los difractogramas de rayos X de polvos (Figura 79). La decadencia aproximada de la emisión fluorescente fue del 94% con respecto al ciclo anterior, con la misma proporción para su respuesta de apagamiento ante la adición de atorvastatina. Por lo que el sensor exhibe una reciclabilidad modesta.

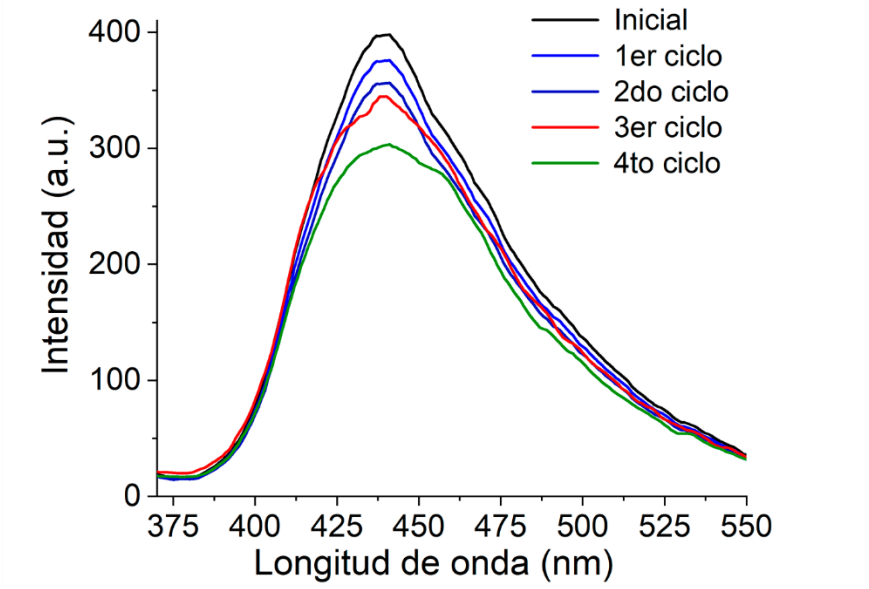

Figura 78. Espectro de fluorescencia de (4) tras cada ciclo

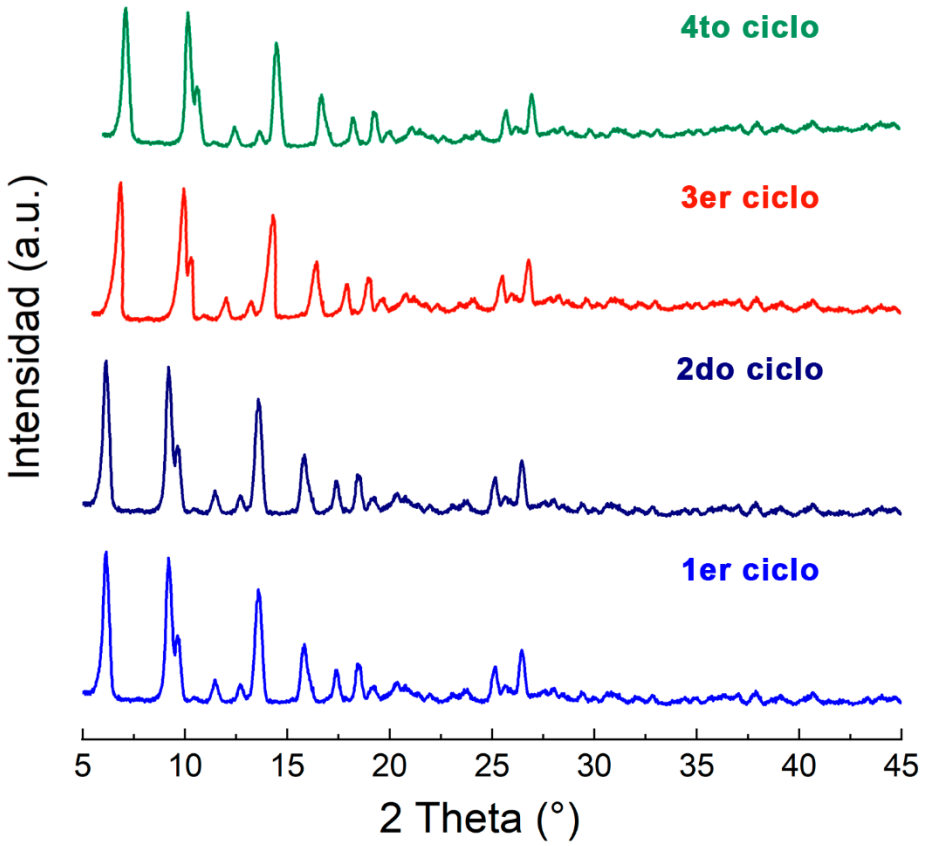

Figura 79. Difractograma de rayos X de polvos de (4) tras cada ciclo

En la detección de atorvastatina en tabletas farmacéuticas, se eligieron dos tipos de tabletas comerciales *Eturion* y *Sortis* ambas marcadas con 20 mg de atorvastatina por tableta. El procedimiento para su cuantificación consiste en la trituración de una tableta la cual es colocada en 50mL de etanol a 70°C y agitación vigorosa durante 30 minutos. A continuación, se filtra la solución dejando el excipiente en el filtrado y en la solución queda el analito de interés. La solución es llevada a sequedad con ayuda del rotavapor y al sólido blanco se le realiza un análisis de infrarrojo corroborando que se trata de atorvastatina (Figura 80). El sólido es nuevamente disuelto en 50 mL de etanol para tomar una alícuota de 50 µL y agregarla en la celda con un volumen de 1950 µL en el sistema etanol-agua 8:2 (v:v) en un pH =7 ajustado por MOPs, muestra a la cual se le determina su espectro de fluorescencia por triplicado (Figura 81).

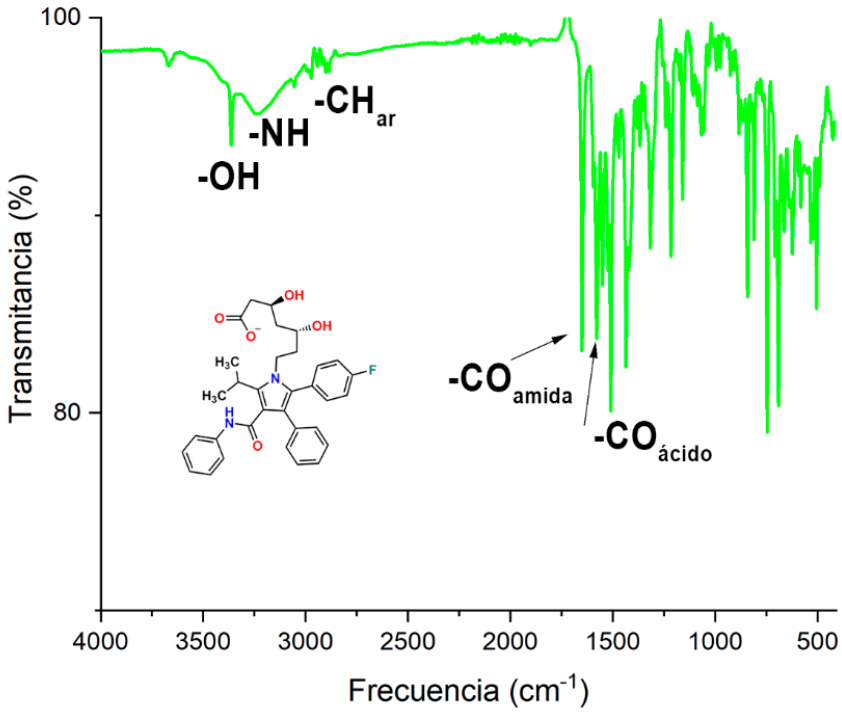

Figura 80. Espectro de infrarrojo de la atorvastatina comercial

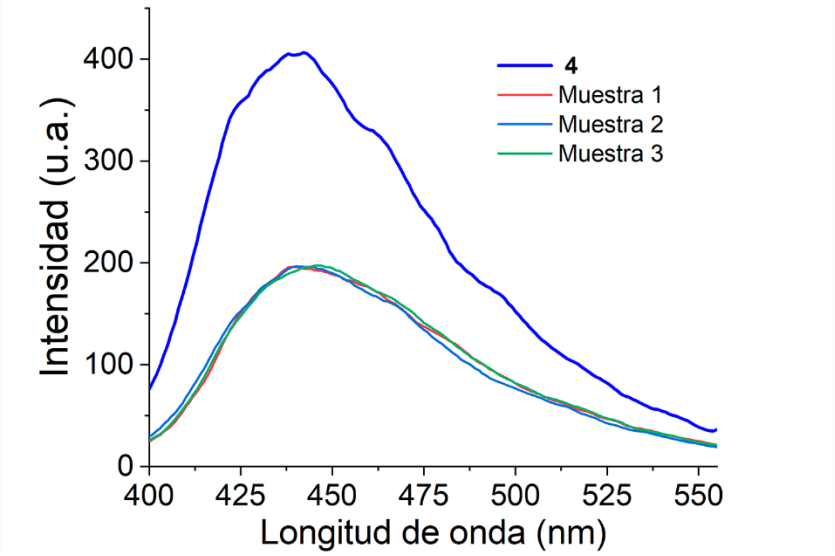

Figura 81. Espectro de fluorescencia de (4), y tras las correspondientes mediciones de atorvastatina en tabletas comerciales

Con ayuda de la titulación de atorvastatina y la ecuación Stern-Volmer ajustada al modelo de Fabbrizzi, fue posible calcular la cantidad de atorvastatina presente en la tableta. El mismo método del tratamiento de las tabletas fue aplicado para el fármaco Eturion y Sortis, así como sus cálculos respectivos, mismos que son expuestos en la Tabla 17. Además, un método de comprobación adicional del cálculo de atorvastatina en tabletas por el MOF luminiscente fue efectuado en cromatografía líquida de alta

eficiencia-espectroscopia ultravioleta (HPLC-UV). Ambos resultados son muy cercanos entre sí, permitiendo establecer que las mediciones de atorvastatina por el sensor metal-orgánico son correctas.

Tabla 17. Resultados de las mediciones de atorvastatina en tabletas comerciales

Tableta	mg de ATV por tableta	ATV cuantificada por (4)	% recuperado	ATV cuantificada por HPLC-UV
Eturion	20.00	18.86	94.03 ± 2.3	18.98
Sortis	20.00	19.34	96.70 ± 1.5	19.17

2.2.3 Conclusiones del sistema II

Se sintetizó un nuevo MOF cristalino y luminiscente con el centro metálico de Zn(II) y el ligante ácido terfenil-3,3”,5,5” tetracarboxílico.

Gracias a los datos de rayos X de monocristal, se efectuó el estudio estructural de la red metal-orgánica, resaltando la porosidad que posee el MOF en el espacio disponible en la celda unitaria superior al 33%, y la generación de una nueva topología.

El MOF **(4)** fue caracterizado por las técnicas de difracción de rayos X de polvos y monocristal, análisis de infrarrojo, análisis elemental, microscopia electrónica de barrido, espectroscopía de energía dispersiva, resonancia magnética de sólidos por ángulo mágico y espectroscopia fluorimétrica

Los estudios de fluorescencia permitieron identificar que el compuesto **(4)** tiene una respuesta de apagamiento de su intensidad de emisión en presencia del anión farmacéutico atorvastatina selectivo sobre otros aniones de la familia de las estatinas, oxoaniones y diversos bioanalitos presentes en sangre y orina.

A través de curvas de titulación se calculó el límite de detección de atorvastatina por el sensor luminiscente (LDD = 4.21 µM), magnitud comparable con otros sensores mencionados en la Tabla 16.

Con el uso del perfil de titulación, tiempos de vida de la fluorescencia, microscopia electrónica de barrido, espectroscopía de energía dispersiva se brindó evidencia inequívoca de que el mecanismo de apagado de la red luminiscente está relacionado con la interacción MOF-ATV.

Se propuso un modelo de la interacción MOF-ATV con ayuda de cálculos teóricos DFT, donde también fue posible calcular la energía de interacción, y de los orbitales HOMO y LUMO, apoyando éstos últimos datos, a establecer que el apagamiento fluorescente ocurre por el mecanismo PET reductivo.

El conjunto de las evidencias analíticas y teóricas conllevaron a la explicación de la selectividad del MOF por atorvastatina derivado de su diseño sintético. La explicación se fundamenta en que el MOF

constituido por un ligante rico en electrones interacciona con el anión farmacéutico electro-deficiente, por apilamiento π - π entre los anillos aromáticos de la atorvastatina y el ligante tptc.

El nuevo sensor fue aplicado exitosamente en la determinación fluorescente de atorvastatina en muestra reales, como fueron las tabletas farmacéuticas.

Los resultados de las mediciones en las muestras reales fueron contrastados por el método de cromatografía HPLC-UV, mostrando valores que solo difieren por décimas de gramo, estableciendo así que la nueva red metal-orgánica luminiscente es un compuesto funcional en la detección fluorescente de atorvastatina.

Capítulo III: Desarrollo experimental

3.1 Disolventes y reactivos:

Los reactivos y disolventes utilizados para el desarrollo sintético y la ulterior caracterización fueron adquiridos de fuentes comerciales (Sigma-Adrich, Tecsiquim), mismo que fueron empleados de forma directa a tal y como se recibieron. Los disolventes empleados son de grado reactivo.

3.2 Instrumentación.

Los espectros de infrarrojo se realizaron usando los equipos Perkin-Elmer Attenuated Total Reflactance FT-Spectrometer (ATR) y FT-IR NICOLET IS-50, Thermo Fisher Scientific; en todos los espectros obtenidos se muestra el número de onda (cm^{-1}) contra el porciento de transmitancia (T%).

El análisis elemental por combustión de los átomos de C, N, y S se realizaron en los equipos Vario Micro-Cube V2.0.11 y Thermo Scientific/Flash 2000.

Los estudios térmicos se realizaron en el equipo SDT Q600 V8.3 Build 101 Module DSC-TGA Standard bajo atmósfera de N_2 a una velocidad de calentamiento de 10°C por minuto, desde 20°C hasta 800°C.

Los espectros de RMN de ^{1}H y ^{13}C se realizaron utilizando TMS como referencia en el equipo Bruker Advanced 300 MHz. Los experimentos de CPMAS fueron realizados en el CPMAS ^{13}C NMR Bruker Advance II 300 en un rotor de 4mm de doble resonancia, a un tiempo de contacto de 2 milisegundos con un retraso de 5 segundos a 7kHz en temperatura ambiente.

Los experimentos por espectrofotometría de UV-Vis se hicieron con un espectrofotómetro Agilent Cary 100 UV-Vis, con resolución de 2nm con una precisión de longitud de onda <± 0.5nm y una precisión fotométrica <±0.005A a 1.2. Se emplearon celdas de cuarzo (paso óptico de 1cm, volumen de 3mL).

La espectroscopía de fluorescencia fue efectuada con un fluorímetro Agilent Cary Eclipse, con una exactitud de longitud de onda de ±0.5 nm y una relación señal ruido 550/1. Las celdas utilizadas son de cuarzo con un paso óptico de 1cm y volumen de 3mL. Las mediciones de las redes metal orgánicas fueron realizadas en emulsiones preparadas en un estándar que se mantiene en agitación constante por 20min a temperatura ambiente en los disolventes de grado reactivo, previo a cada medición. Asimismo, durante las mediciones se mantuvo la agitación de las emulsiones. Las mediciones de tiempo de vida media de la fluorescencia se realizaron usando un sistema de recuento de fotones individuales correlacionados en el tiempo (TCSPC) acoplado a un microscopio confocal construido a medida para adquirir la vida útil de la fluorescencia.

Para los experimentos de microscopia SEM se utilizó el equipo JSM-6510LV microscope from JEOL acoplado al equipo Bruker QUANTAX 200 energy-dispersive X-ray spectrometer en la obtención del

mapeo elemental por la técnica EDS. Los cristales fueron secados a temperatura ambiente y colocados en láminas de cita de carbono en una delgada película de oro usando un cabina Denton IV sputtering previo a la adquisición del experimento. La difracción de rayos X de polvos fue efectuada en el equipo Bruker D8 ADVANCE X-ray diffractometer (Cu-Kα, λ = 1.5418 Å) en el intervalo de 2 theta de 5-50°

3.3 Cristalografía de rayos X de monocristal.

Los cristales de los compuestos **(1-8)** fueron obtenidos directamente de la matriz de la solución. Los datos para los compuestos **(1-3)** y **(5-8)** fueron colectados en un difractómetro Bruker APEX II CCD a 100K y a 293K usando radiación de Mo-Kα (k = 0.71073 Å) de micro fuentes Incoatec ImuS y monocromador con óptica Helios (26). Los cristales adecuados para los análisis fueron separados y seleccionados en aceite de hidrocarburos de alto peso molecular (PARATONE) y posteriormente pegados con resina epóxica sobre una fibra de vidrio o sobre un loop de nylon y colocados en el goniómetro. Las estructuras fueron resueltas usando métodos directos (SHELXS-97) (27) y refinadas por mínimos cuadrados en F2 usando the shelXle GUI (28). Los átomos de hidrógeno de los enlaces C-H fueron colocados en posiciones idealizadas mientras que los átomos de hidrógeno de los enlaces O-H, N-H fueron localizados del mapa de densidad electrónica y sus posiciones fueron refinadas isotrópicamente U_{iso} con dependencia al átomo directamente unido usando adicionalmente restricciones de distancia. Los grupos desordenados fueron refinados usando restricciones de geometría y distancia (SAME, SADI) junto con restricciones de los valores U_{ij} (SIMU, RIGU) implementados in SHELXL Las ocupaciones fueron restringidas a valores unitarios.

3.4 Síntesis de los compuestos.

[Zn(4,4-dmbp)(e,a-cis-1,4-chdc)(H_2O)·2(H_2O)]n (1).

A una solución del ácido 1,4-ciclohexanodicarboxílico (0.0688 g; 0.4 mmol) en metanol (5mL), se adicionaron 2 equivalentes de NaOH (5mL; 0.16M) e inmediatamente después se mezcló con una solución de 4,4-dimetil-2,2´-bipiridina (0.0720g; 0.4mmol) en metanol (10mL). La solución resultante se mezcló con 10 ml de solución acuosa de $Zn(NO_3)_2·6H_2O$ (0.0941g; 0.4mmol). La mezcla de reacción se dejó en un vaso de precipitados, tapada con parafilm y transcurridos algunos días se obtienen cristales amarillos de buen tamaño, que son filtrados y lavados con agua destilada. El rendimiento con base en el metal precursor es 66%. Análisis elemental calculado para $C_{20}H_{28}N_2O_7Zn$: 50.69% C, 5.95% H, 5.91% N; encontrado: 50.56% C, 6.08% H 6.01% N. 3379(w,br), 2938(w,sh), 1543(s,sh), 1523(s,sh), 1473(m,sh), 1450(m,sh), 1408(s,sh), 840(s,sh), 757(s,sh), 692(s,br).

[Zn(5,5-dmbp)(*e,a-cis*-1,4-chdc)(H_2O)]*n* (2).

Se sigue la metodología descrita para **(1)** utilizando las siguientes cantidades: ácido 1,4-ciclohexanodicarboxílico (0.0688 g; 0.4 mmol), 5,5-dimetil-2,2´-bipiridina (0.0720g; 0.4mmol), $Zn(NO_3)_2 \cdot 6H_2O$ (0.0941g; 0.4mmol). Rendimiento: 80%. Análisis elemental calculado para $C_{20}H_{24}N_2O_5Zn$: 54.86% C, 5.52% H, 6.40% N; encontrado: 53.02% C, 5.61% H 6.20% N. IR (ATR, cm^{-1}): 3219(w,br), 2919(w,sh), 1574(m,sh), 1552(s,br), 1480(s,sh), 1396(s,sh), 836(s,sh), 780(s,sh), 730(s,sh), 585(s,sh).

[Zn_2(4,4-dtbp)$_2$(*e,a-cis*-1,4-chdc)$_2 \cdot$5(H_2O)]*n* (3).

Se calienta a 60°C una solución de 4,4-di-tert-butil-2,2´-bipiridina (0.0536g; 0.2mmol) en metanol (20ml) a la cual se adiciona una solución del ácido 1,4-ciclohexanodicarboxílico (0.0688 g; 0.4 mmol) mezcla de *cis* y *trans* al 99% en metanol (5ml) con 2 equivalentes de NaOH (5ml; 0.16M). Inmediatamente, a la solución resultante se añade 10ml de la solución acuosa de $Zn(NO_3)_2 \cdot 6H_2O$ (0.0941g; 0.4mmol). A la solución con todos los reactivos, se le añaden 20ml de agua y 20 ml de metanol, continuando con el calentamiento hasta llegar a 70°C, manteniéndose durante 20 minutos. La mezcla de reacción se dejó en un vaso de precipitados, tapada con parafilm y transcurridos algunos días se obtienen cristales traslúcidos de buen tamaño, que son filtrados y lavados con agua destilada. El rendimiento con base en el metal precursor es de 84%. Análisis elemental calculado para $C_{52}H_{86}N_4O_{17}Zn_2$: 53.38% C, 7.41% H, 4.79% N; encontrado; 53.25% C, 7.29% H 4.76% N. IR (ATR, cm^{-1}): 3303(w,br), 2964(w,sh), 1611(m,sh), 1553(s,br), 1547(s,br), 1445(w,sh), 1408(s,sh), 848(m,sh), 669(m,br), 604(s,sh).

[Zn_2(4,4-dtbp)$_2$(*e,a-cis*-1,4-chdc)$_2 \cdot$5(H_2O)]*n* (4).

Una mezcla de $Zn(CF_3SO_3)_2$ (172.0 mg, 0.5 mmol) y ácido tptc (98.1 mg, 0.2 mmol) en DMF(10mL) y H_2O (2 mL), se agitó y calentó a 90 ºC durante 5 min en un vial de vidrio de 15 mL. Enseguida seguida metió a la estufa a 100 ºC por 24 h. Posteriormente se dejó enfriar el sistema de reacción a razón de 0.5 ºCmin^{-1} hasta alcanzar temperatura ambiente. Se obtuvieron cristales incoloros que se separaron por filtración. Rendimiento: 70.0 % (110.0 mg). Análisis elemental calculado para $C_{50.21}H_{43.24}O_{20,41}Zn_3$: 51.57% C, 3.72% H, 4.79% N, 0.0%; encontrado; 51.38% C, 3.85% N, 0.0%. IR (ATR): ῡ 3069 (w, br), 2802 (w, br), 2117 (w, br), 1869 (w, br), 1653 (w, sh), 1618 (m, sh), 1577 (st, sh), 1559 (m, sh), 1516 (w, br), 1437 (m, sh), 1349 (st, sh), 1291 (m, sh), 1252 (m, sh), 1159 (w, sh), 1099 (w, br), 1017 (w, br), 917 (w, br), 866 (w, br), 841 (w, br), 779 (st, br), 757 (st, br), 745 (st, br), 725 (st, br), 660 (m, sh).

Capítulo IV: Anexos

4.1 Reconocimientos y constancias de eventos de divulgación científica

Sociedad Mexicana de Cristalografía

otorga el presente

RECONOCIMIENTO

a

Luis David Rosales Vázquez, Alejandro Dorazco González, Silvia Elena Castillo Blum y Víctor Sánchez Mendieta

Por la exposición del poster **Ftalamidas Tetracloradas Como Estrategia En La Obtención De Enlace De Halógeno En Cristales**
en modalidad virtual, en el marco de las actividades

X Congreso Nacional de Cristalografía - en línea
2 al 4 de diciembre, 2020

Dr. Màrius Ramírez Cardona
Presidente de la
Sociedad Mexicana de Cristalografía

EL INSTITUTO DE QUÍMICA
DE LA
UNIVERSIDAD NACIONAL AUTÓNOMA DE MÉXICO

otorga la presente

CONSTANCIA

a: Luis David Rosales Vázquez

Por su asistencia a la sesión de carteles se realizó el día 4 de diciembre de 2020, dentro del marco del ***"Simposio virtual del instituto de Química "***

Ciudad Universitaria, CDMX, a 22 de febrero de 2021

Dr. Fernando Cortés Guzmán
Secretario Académico

Simposio Virtual 2020 del Instituto de Química

CARTELES GANADORES

Departamento	Primer Lugar	Segundo Lugar
Química Inorgánica		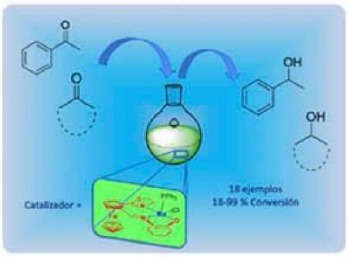

EDUCACIÓN
SECRETARÍA DE EDUCACIÓN PÚBLICA

TECNOLÓGICO NACIONAL DE MÉXICO

EL TECNOLÓGICO NACIONAL DE MÉXICO
A TRAVÉS DEL INSTITUTO TECNOLÓGICO DE ZITÁCUARO

OTORGA EL PRESENTE

RECONOCIMIENTO

A

LUIS DAVID ROSALES VÁZQUEZ

POR HABER IMPARTIDO LA CONFERENCIA DENOMINADA **"MOFS Y POLÍMEROS DE COORDINACIÓN EN LA DETECCIÓN LUMINISCENTE DE PESTICIDAS Y MEDICAMENTOS"** COMO PARTE DE LAS ACTIVIDADES DE LA SEMANA NACIONAL DE CIENCIA Y TECNOLOGÍA 2020, DIRIGIDA A LOS ESTUDIANTES DE LOS PROGRAMAS EDUCATIVOS DE INGENIERÍA EN INDUSTRIAS ALIMENTARIAS E INGENIERÍA EN INNOVACIÓN AGRÍCOLA SUSTENTABLE

H. ZITACUARO MICHOACÁN, A 29 DE OCTUBRE DE 2020.

M.C. DAVID RAFAEL TRIGUEROS CAZARES
DIRECTOR

SECRETARIA DE EDUCACIÓN PUBLICA
INSTITUTO TECNOLÓGICO DE ZITÁCUARO
DIRECCIÓN

Instituto Tecnológico de Zitácuaro

El enlace de halógeno

Luis David Rosales Vázquez; Alejandro Dorazco González

Instituto de Química, UNAM.
Av. Universidad 3000, Circuito Exterior S/N
Delegación Coyoacán, C.P. 04510
Ciudad Universitaria, D.F. México

ld_222@comunidad.unam.mx;
adg@unam.mx

El enlace de halógeno

El enlace de halógeno es una interacción que ocurre entre la región positiva del átomo de halógeno (sigma-hole), y una base de Lewis. Dicha interacción requiere que las distancias interatómicas entre la base de Lewis y el átomo de halógeno sean menores a la suma de sus respectivos de radio de Van der Waals. Adicionalmente, es necesario que exista un ángulo cercano a 180° entre el átomo aceptor (base de Lewis), el átomo donador (halógeno) y el grupo R unido directamente al átomo de halógeno. Dada mayor sea la cercanía entre los átomos participantes, así como mayor linealidad presenten, más fuerte será la interacción.[1,2]

Interesantemente, las estrategias utilizadas para formar la interacción están basadas en el incremento del carácter positivo de estos átomos altamente electronegativos. Congruentemente, los átomos de I y de Br protagonizan este tipo de interacciones debido a su menor electronegatividad, mientras que ejemplos con los átomos de Cl son bastante escasos y aún más raros para los átomos de F. No obstante, otras estrategias suelen incorporar al diseño de sus moléculas, grupos con alta demanda electronica (tambien denomindados como grupos electroatractores o desactivantes), o grupos cuya estructura conlleve la posibilidad de obtener una molécula cationiónica, siendo el caso de imidazoles, triazoles y piridinas. El átomo directamente enlazado al átomo de halógeno tambien juega un rol importante, ya que según sea su hibridación en el enlace, éste presentará una menor o mayor acidez que influirá en el carácter positivo resultante. [1,2]

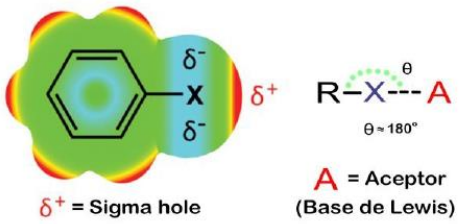

Figura 1. Fundamentos del enlace de halógeno

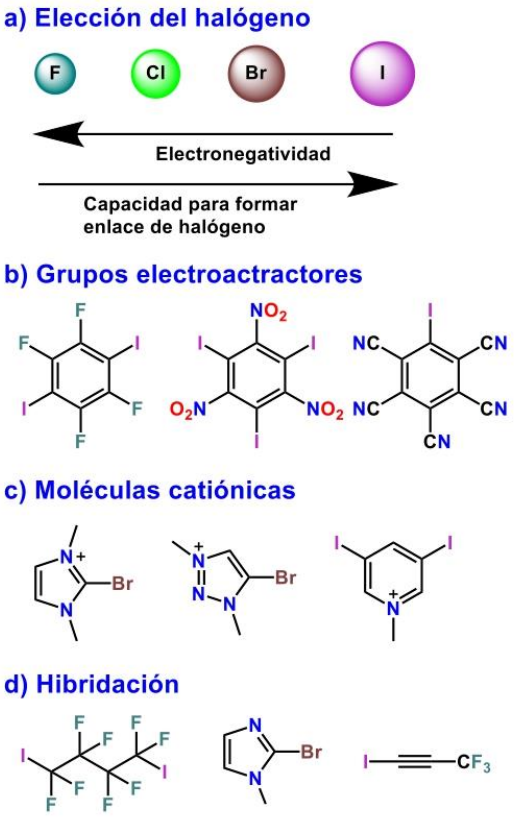

Figura 2. Estrategias utilizadas para su diseño

La correspondencia está directamente relacionada al porcentaje del orbital "s" en el enlace, entre mayor sea, la estabilidad de la interacción se verá incrementada ($sp > sp^2 > sp^3$). [1,2]

El correcto uso de las cuatro variantes conlleva a la construcción del enlace de halógeno teniendo como características derivadas de su diseño sintético, la capacidad de ser modulado, poseer una direccionalidad anticipada y un carácter hidrofóbico. Asimismo, su direccionalidad ha permitido la síntesis dirigida de redes mediante co-cristales orgánicos, polímeros, co-polímeros y polímeros de coordinación. Resaltando entre sus aplicaciones por direccionalidad su empleo y mejora de semiconductores orgánicos.[3]

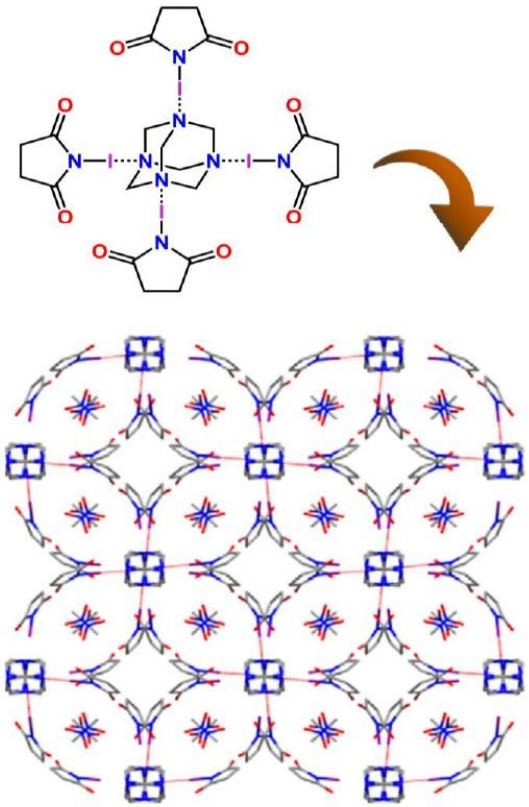

Figura 3. Arreglo supramolecular del co-cristal N-yodosuccinimida y hexametilentetramina.

Interesantemente, las estrategias utilizadas para formar la interacción están basadas en el incremento del carácter positivo de estos átomos altamente electronegativos

En el campo de los catalizadores, su aplicación ha ido progresivamente incrementando como un valioso ácido de Lewis altamente modificable, catalizando desde las reacciones orgánicas clásicas como Friedel-Crafts, Diels-Alder, la adición de Michael, Mannich, así como reacciones de tipo fotoquímicas, radicalarias, transposiciones tipo pinacólicas, reducción de quinolinas y de acoplamiento carbono-carbono. [4]

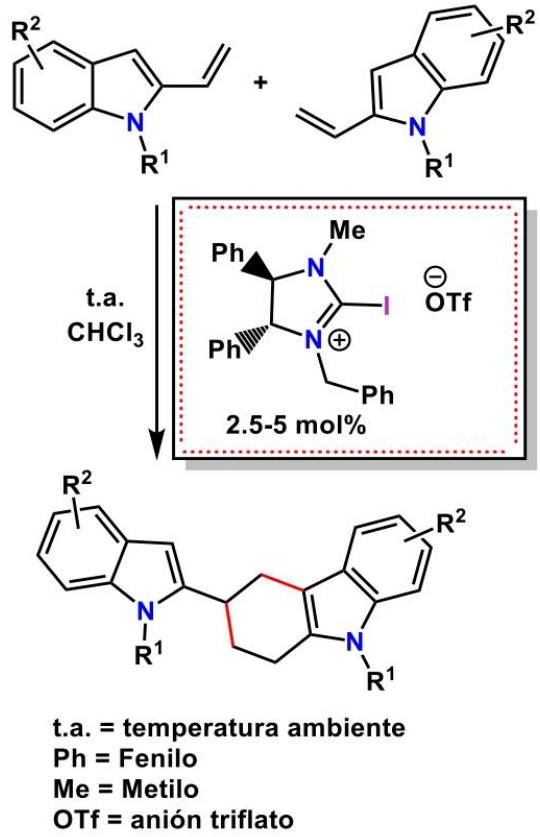

Figura 4. Reaccion de cicloadición [4+2] entre alquenilindoles catalizada por enlace de halógeno.

Su papel en los sistemas biológicos continuamente se sigue estudiando, principalmente localizándolo en varios sistemas complejo proteína- ligante, en busca de la comprensión de su especificidad y afinidad en la relación actividad-estructura por parte de la proteína. [5] Ejemplos selectos de estos sistemas se representan en la Figura 5 y Tabla 1. La estructura cristalográfica de las proteínas puede consultarse en la base de datos de proteínas: https://www.rcsb.org/.com

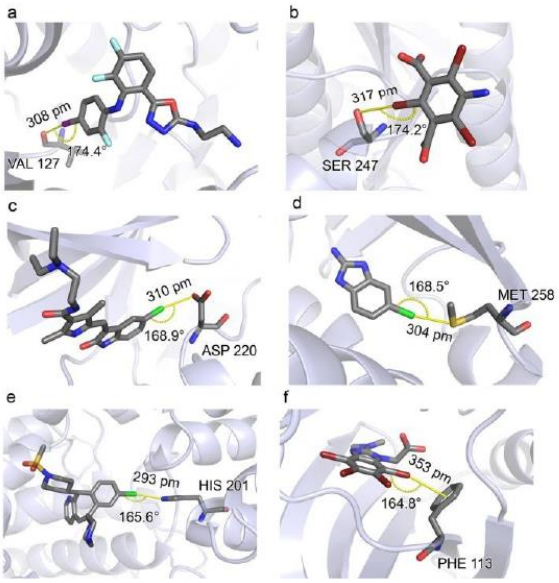

Figura 6. Ejemplos reelevantes de la interacción en sistemas biológicos.

Tabla 1. Sitios de interacción del enlace de halógeno en proteinas

Proteina	Interacción	Base de Lewis
3EQB	I - - - O	Valina 127
3GT3	Br - - - O	Serina 247
3HZT	Cl - - - O	Ácido aspártico 220
3KR1	Cl - - - S	Metionina 258
2BED	Cl - - - N	Histidina 258
2KXH	Br - - - π	Fenilalanina 113

Es en este contexto que varios equipos de investigación han volteado su atención a la importancia de la interacción, en la eficacia y mecanismo de acción de diversos fármacos. Tal es el caso de la molécula ***BI 201335*** misma que actúa como un inhibidor de la Proteasa NS3 a través de la interacción Br --- O del grupo carboxilato correspondiente al Aspartato 79 ubicado justo en el sitio activo de la enzima. Lemke *et. al*. determinaron que el enlace de halógeno fue una pieza clave para el incremento substancial de la especificidad y el aumento en la potencia antiviral del fármaco para el tratamiento contra la Hepatitis C. [6]

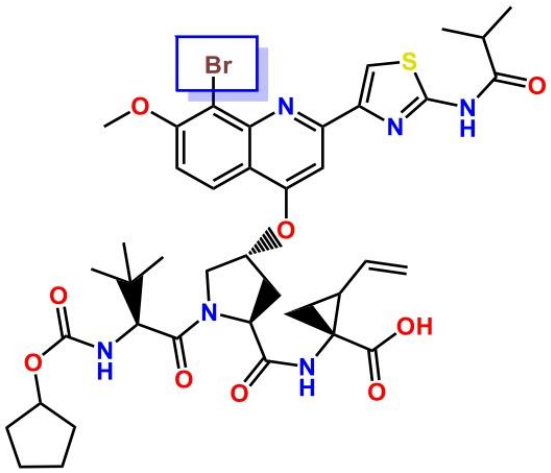

Figura 7. BI 201335

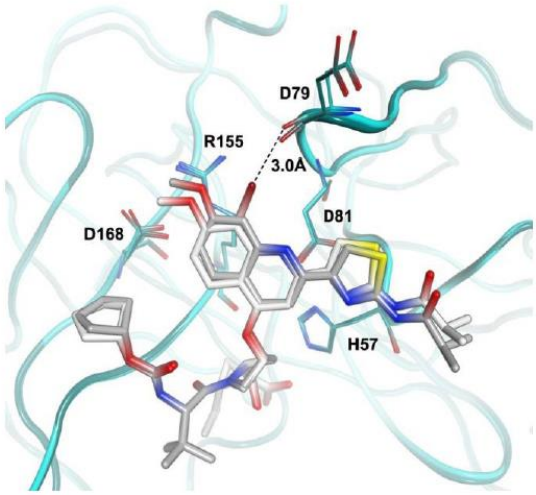

Figura 8. Inhibición del sitio activo del Proteasa NS3 por el fármaco BI 201335 a través del enlace de halógeno Br --- O.

El enlace de halógeno fue una pieza clave para el incremento substancial de la especificidad y el aumento en la potencia antiviral del fármaco para el tratamiento contra la Hepatitis C

El futuro y las oportunidades que presentan el enlace de halógeno lucen muy prometedoras en campos de la ciencia tan variados, y es que, a diferencia del puente de hidrógeno, el enlace de halógeno es una de las herramientas relativamente más nuevas de la química supramolecular, por lo que falta mucho por descubrir. Quedará en la tarea de sus investigadores el compromiso por realizarlo aprovechando al máximo sus cualidades, y comprendiendo, sobretodo, sus características aplicadas en su construcción con la mirada puesta en sus diversas aplicaciones.

Referencias

1. Cavallo, G. *et al.* The halogen bond. *Chem. Rev.* **116**, 2478–2601 (2016).
2. Gilday, L. C. *et al.* Halogen Bonding in Supramolecular Chemistry. *Chem. Rev.* **115**, 7118–7195 (2015).
3. Berger, G., Frangville, P. & Meyer, F. Halogen bonding for molecular recognition: new developments in materials and biological sciences. *Chem. Commun.* **56**, 4970–4981 (2020).
4. Sutar, R. L. & Huber, S. M. Catalysis of Organic Reactions through Halogen Bonding. *ACS Catal.* **9**, 9622–9639 (2019).
5. Wilcken, R., Zimmermann, M. O., Lange, A., Joerger, A. C. & Boeckler, F. M. Principles and applications of halogen bonding in medicinal chemistry and chemical biology. *J. Med. Chem.* **56**, 1363–1388 (2013).
6. Lemke, C. T. *et al.* Combined x-ray, NMR, and kinetic analyses reveal uncommon binding characteristics of the hepatitis C virus NS3-NS4A protease inhibitor BI 201335. *J. Biol. Chem.* **286**, 11434–11443 (2011).

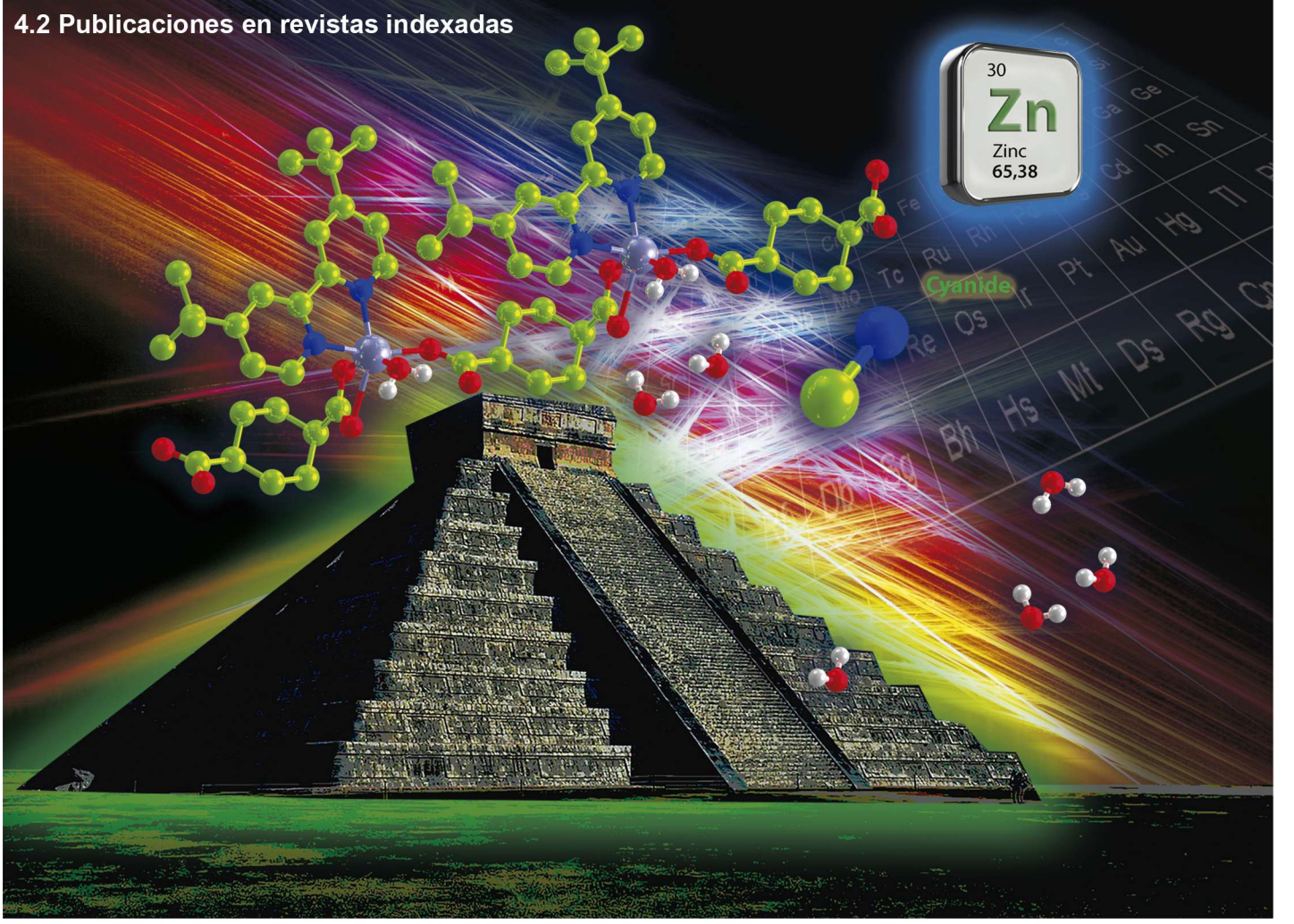

Showcasing research from Alejandro Dorazco's laboratory, Institute of Chemistry, University National Autonomous of Mexico, CDMX, México.

A sensitive photoluminescent chemosensor for cyanide in water based on a zinc coordination polymer bearing ditert-butyl-bipyridine

Using for the first time a Zn coordination polymer as an optical chemosensor for cyanide in pure water.

Image created by Hortensia Segura and Ari Kleinberg.

As featured in:

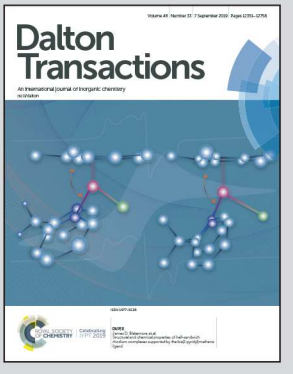

See Víctor Sánchez-Mendieta, Alejandro Dorazco-González *et al.*, *Dalton Trans.*, 2019, **48**, 12407.

ROYAL SOCIETY OF CHEMISTRY | Celebrating IYPT 2019

rsc.li/dalton

Registered charity number: 207890

Dalton Transactions

PAPER

View Article Online
View Journal | View Issue

Cite this: *Dalton Trans.*, 2019, **48**, 12407

A sensitive photoluminescent chemosensor for cyanide in water based on a zinc coordination polymer bearing ditert-butyl-bipyridine†

Luis D. Rosales-Vázquez,[a] Josue Valdes-García,[a] Iván J. Bazany-Rodríguez,[a] Juan M. Germán-Acacio,[b] Diego Martínez-Otero,[c] Alfredo R. Vilchis-Néstor,[c] Raúl Morales-Luckie,[c] Víctor Sánchez-Mendieta *[c] and Alejandro Dorazco-González *[a]

Sensitive and direct sensing of cyanide in buffered aqueous solutions at pH = 7.0 by three new blue photoluminescent zinc-1,4-cyclohexanedicarboxylato coordination polymers bearing di-alkyl-2,2′-bipyridines has been achieved. Specifically, a Zn-polymer with the general formula: $\{[Zn_2(H_2O)_2(e,a\text{-}cis\text{-}1,4\text{-}chdc)_2(4,4'\text{-}dtbb)_2]\cdot 7H_2O\}_n$, (1,4-chdc = 1,4-cyclohexanedicarboxylato and 4,4′-dtbb = 4,4′-ditert-butyl-2,2′-bipyridine) has been synthesized in high yield and studied as a luminescent chemosensor for halides, pseudohalides and a series of oxyanions in neutral water. CN^- ions can be quantitatively detected by this polymer based on complete quenching (λ_{em} = 434 nm) in the sub-micromolar concentration range with a pronounced selectivity over common anions such as acetate, bromide and iodide. The quenching response (K_{SV} = 9.7(±0.2) × 10^4 M^{-1}) by the addition of CN^- was also observed in the presence of typical interfering anions with a very low detection limit of 0.9 μmol L^{-1} in buffered water at pH = 7.0. On the basis of the crystal structure and solid state CPMAS ^{13}C-NMR correlation and ^{1}H NMR, IR-ATR, MS-ESI(+) and SEM-EDS experiments, the optical change is attributed to the efficient release of its corresponding ditert-butyl-bipyridine, with the simultaneous formation of a zinc cyanide complex. The CPMAS ^{13}C-NMR spectrum of the coordination polymer is consistent with the symmetry of the crystal structure. The use of flexible coordination polymers as fluorescent sensors for fast and selective detection of cyanide ions in pure aqueous solutions has been unexplored until now.

Received 3rd May 2019,
Accepted 27th June 2019

DOI: 10.1039/c9dt01861a

rsc.li/dalton

Introduction

The cyanide ion (CN^-) is a well-known toxic and lethal species because it inhibits cellular respiration in mammals by associating tightly to the trivalent iron atom in cytochrome c oxidase[1] causing the depression of the central nervous system and death.[2–4] The highest allowable level of CN^- in drinking water is 2.7 × 10^{-6} M according to the World Health Organization (WHO).[1] Nowadays, a large amount of metal salts of cyanide is widely used in several industrial processes (~1 400 000 tons per year)[5] such as gold mining and synthetic and plastic manufacturing.[6–8] Cyanide waste causes serious pollution in the environment, especially in natural water sources. Compared with the very toxic heavy-metal ions, CN^- can lead to the death of humans and aquatic life in minutes.[9] For this reason, the development of sensitive and selective CN^- sensors capable of operating in pure water has been a subject of intense research during the last few decades.[7]

The literature reports a large number of optical sensors for this anion based on artificial receptors containing convergent hydrogen bond donor groups as binding sites; however, the vast majority of these sensors operates in non-aqueous media or they require a considerable amount of organic co-solvents, which severely limits their applications.[10–25] The other common strategy is based on the nucleophilic addition of CN^- to some organic dyes containing functional groups such as

[a]*Instituto de Química, Universidad Nacional Autónoma de México, Circuito Exterior, Ciudad Universitaria, México, 04510 CDMX, México. E-mail: adg@unam.mx*
[b]*Red de Apoyo a la Investigación, Universidad Nacional Autónoma de México-CIC, Instituto Nacional de Ciencias Médicas y Nutrición SZ, C. P.14000 Ciudad de México, México*
[c]*Centro Conjunto de Investigación en Química Sustentable UAEM-UNAM, Carretera Toluca-Ixtlahuaca Km. 14.5, Tlachaloya, Toluca, Estado de México, México. E-mail: vsanchezm@uaemex.mx*

†Electronic supplementary information (ESI) available: CIF files and crystallographic data for **1–3**. IR-ATR, TGA and DSC analysis. PXRD pattern for **3**. ^{13}C *ss*-CPPI and CPMAS NMR for **3**, connectivity figures and a fluorescence titration experiment in the presence of interfering anions. CCDC 1579458–1579460. For ESI and crystallographic data in CIF or other electronic format see DOI: 10.1039/c9dt01861a

(>C═C<),[15,19,26,27] (>C═N–)[28,29] and (>C═O).[30,31] The demetallation of chromogenic heavy-metal complexes,[23] luminescent metal-based receptors[32,33] and gold nanoparticle probes have also been used.[22] Typically these dyes or optical sensors show a moderate affinity to CN^- with binding constants above 10^3 M^{-1} in neutral solutions. Consequently, they are suitable for sensing CN^- in the sub-millimolar concentration range, but not significantly below this range. Furthermore, these chemical sensors still suffer from various drawbacks such as highly laborious and costly synthesis, poor water solubility, poor signaling efficiency and the use of toxic heavy metals.

In principle, it should be possible to overcome these limitations by using a luminescent sensor with a high-affinity binding site to CN^-. However, the creation of a selective and potent receptor/sensor for CN^- is an ongoing challenge. The difficulty in making artificial receptors for CN^- ions is owing to their high hydration energy ($\Delta G° = -300$ kJ mol^{-1}).[34] Very few luminescent chemosensors capable of functioning in pure water have been reported so far, and these sensors are based on sulfonium boranes[35] and lanthanide complexes.[36,37] On the other hand, metal–organic frameworks (MOFs) have demonstrated attractive features in CN^- sensing compared to conventional organic luminophores, such as high affinity with a very low detection limit ($<10^{-7}$ M)[38] and outstanding photostability.[39,40] Reports on porous MOFs have shown that CN-bridged metal organic frameworks are hydrostable compounds which is an advantage for aqueous-phase sensing.[41,42] Taking this into account, this work is based on the idea that selective detection of CN^- can be achieved with a water-soluble and photoluminescent coordination polymer containing a non-toxic metal atom with available coordination sites and a high-affinity for this anion. In this context, Zn(II) coordination polymers that contain a highly water-soluble and flexible ditopic ligand such as 1,4-cyclohexanedicarboxylate and fluorescent N-donors such as bypiridines[43,44] are potential receptors/chemosensors for CN^- and related heavy-atom-containing anions. The results obtained for three blue photoluminescent Zn coordination polymers, including synthesis, X-ray crystal structures, and spectroscopic sensing of anions and microscopy studies, are summarized below.

Results and discussion

The color emission upon excitation of Zn-coordination polymers and related MOFs is a feature that has been recently employed in several applications including emitting devices,[39,40] sensing[45] and optical detection of gas.[46] However, anion sensing in pure water still remains largely unexplored, specifically for CN^- ions. Only two post-synthetically modified MOF-based chemical sensors for CN^- have been reported in the aqueous phase, both by Ghosh.[38,47] Herein, we report the use of a series of water-soluble dinuclear/mononuclear zinc-1,4-cyclohexanedicarboxylato coordination polymers **1–3** for luminescence detection of CN^- with a short response time and selectivity over common interfering anions. The 1D coordination polymers used in this study have the general formula: $\{[Zn(H_2O)(1,4\text{-chdc})(4,4'\text{-dmb})]\cdot 2H_2O\}_n$,**1**; $\{Zn(H_2O)(1,4\text{-chdc})(5,5'\text{-dmb})\}_n$, **2** and $\{[Zn_2(H_2O)_2(1,4\text{-chdc})_2(4,4'\text{-dtbb})_2]\cdot 7H_2O\}_n$, **3** (1,4-chdc = 1,4-cyclohexanedicarboxylato; 4,4′-dmb = 4,4′-dimethyl-2,2′-bipyridine; 5,5′-dmb = 5,5′-dimethyl-2,2′-bipyridine; 4,4′-dtbb = 4,4′-ditert-butyl-2,2′-bipyridine) and have been synthesized by self-assembly in the aqueous phase. The single crystals of **1–3** were obtained in water in order to explore their intrinsic hydrolytic stability in the solid state and promote the coordination of water molecules to Zn(II) that could work as specific recognition sites for CN^-. The crystal structure of **3** shows a high degree of hydration compared to those of **1** and **2**, and also uncommon structural features.

Structural description

$\{[Zn(H_2O)(e,a\text{-}cis\text{-}1,4\text{-chdc})(4,4'\text{-dmb})]\cdot 2H_2O\}_n$ 1. **1** crystallizes in a monoclinic system with the $P2_1/c$ space group and forms an infinite 1D coordination polymer. The repeating molecular unit contains one Zn center, one 1,4-chdc ligand, one 4,4′-dmb co-ligand and one aqua ligand. The coordination environment of Zn is shown in Fig. 1a; the metal center is six-coordinated and surrounded by four oxygen atoms from two different 1,4-chdc ligands and the *aqua*-ligand, and two nitro-

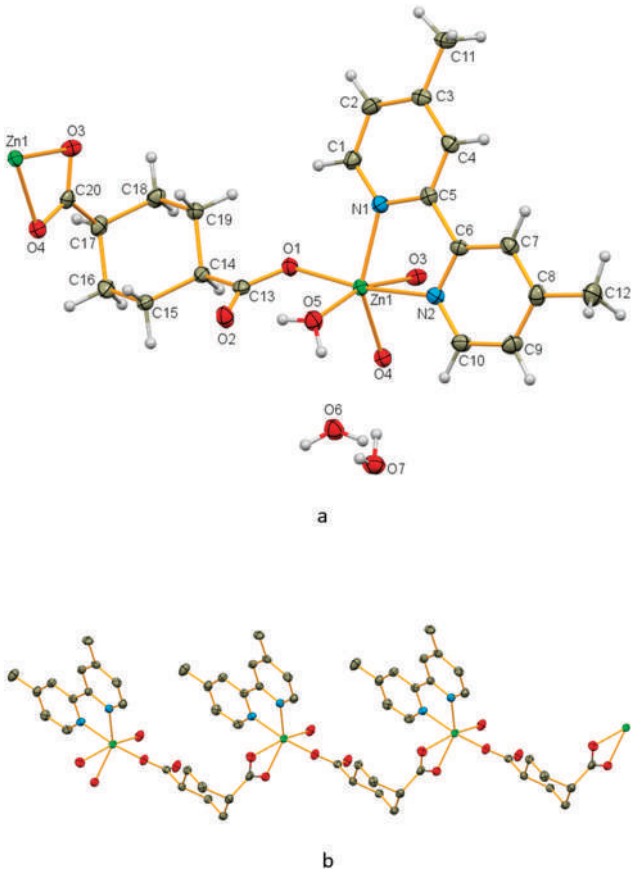

Fig. 1 (a) Molecular structure of $\{[Zn(H_2O)(e,a\text{-}cis\text{-}1,4\text{-chdc})(4,4'\text{-dmb})]\cdot 2H_2O\}_n$ **1** (ellipsoids shown at 60% probability) and (b) 1D V-shaped polymer chain of **1**; hydrogens are omitted for clarity.

gen atoms from one 4,4′-dmb ligand. The Zn ion has a distorted octahedral configuration. The Zn–O bond lengths range from 2.0409(12) to 2.2558(13) Å, while the Zn–N distances are 2.1092(15) and 2.1630(15) Å, and these values are similar to those found for related Zn(II) compounds.[48] In complex **1**, a 1D chain is formed due to the combined monodentate η^1 and chelate bidentate η^2 coordination modes of 1,4-chdc, along with the *equatorial*, *axial cis* configuration of its carboxylate groups bridging the metal centers (Fig. 1b). The way all Zn ions align to one side of the 1D chain, with the 1,4-chdc ligand completing a V-shape (Fig. 1b), is a new motif found in coordination polymers bearing the 1,4-chdc bridging ligand. Most of the motifs originated for this 1,4-chdc ligand while forming coordination polymers in both *trans* and *cis* conformations, have been reported.[49] Hence, this type of novel motif has been noticed only in a Co(II) coordination polymer built also on the *equatorial*, *axial cis* of the 1,4-chdc bridging ligand.[50] There is also one report of a similar motif in a Cu(II) coordination polymer built on 1,4-chdc and phenantroline,[51] nonetheless, the authors did not comment on the 1,4-chdc motif obtained. Hydrogen-bonding interactions assemble complex **1** into a 1D supramolecular array with two rows of Zn centers (Fig. S1†). These bindings originated from the presence of two molecules of water in the crystal, and their interactions with the aqua ligand and coordinated and non-coordinated oxygen atoms of the 1,4-chdc ligand. This is shown in Fig. S1,† where the main O–H···O interactions involve the O–H moiety (O5) of the aqua ligand with each oxygen atom (O2) of the non-coordinated side of one 1,4-chdc ligand, in an intramolecular hydrogen bond. Then, each aqua ligand (O5) generates a double hydrogen bridge; the one described above, and another with one water of crystallization (O6), which, in turn, bridges also with the other water of crystallization (O7) and with the non-coordinated side of the 1,4-chdc ligand (O2) (intermolecular hydrogen bonding). In addition, the coordinated side of the 1,4-chdc ligand (O4) makes also a hydrogen bridge with one water of crystallization (O7). These hydrogen-bonding fused rings cause the merger of two 1D polymeric chains, giving rise to a two-row Zn 1D supramolecular system (Fig. S1†).

$\{Zn(H_2O)(e,a\text{-}cis\text{-}1,4\text{-}chdc)(5,5'\text{-}dmb)\}_n$ 2. **2** crystallizes also in a monoclinic system with the $P2_1/c$ space group and forms an infinite 1D coordination polymer. The molecular unit contains one Zn center, one 1,4-chdc ligand, one 5,5′-dmb co-ligand and one aqua ligand. The coordination environment of the Zn is shown in Fig. 2a; the metal center is six-coordinated and surrounded by four oxygen atoms from two different 1,4-chdc ligands and the aqua ligand, and two nitrogen atoms from one 5,5′-dmb ligand. As in **1**, the Zn ion in **2** assumes a distorted octahedral configuration. The Zn–O bond lengths range from 1.9881(17) to 2.0502(19) Å, while the Zn–N distances are 2.1024(19) and 2.1722 Å; these values are similar to those found on comparable Zn(II) compounds.[52–54]

In complex **2**, a 1D chain is formed owing to the combined monodentate η^1 and chelate bidentate η^2 coordination modes of 1,4-chdc, alongside the *equatorial*, *axial cis* configuration of its carboxylate groups bridging the metal centers (Fig. 2b).

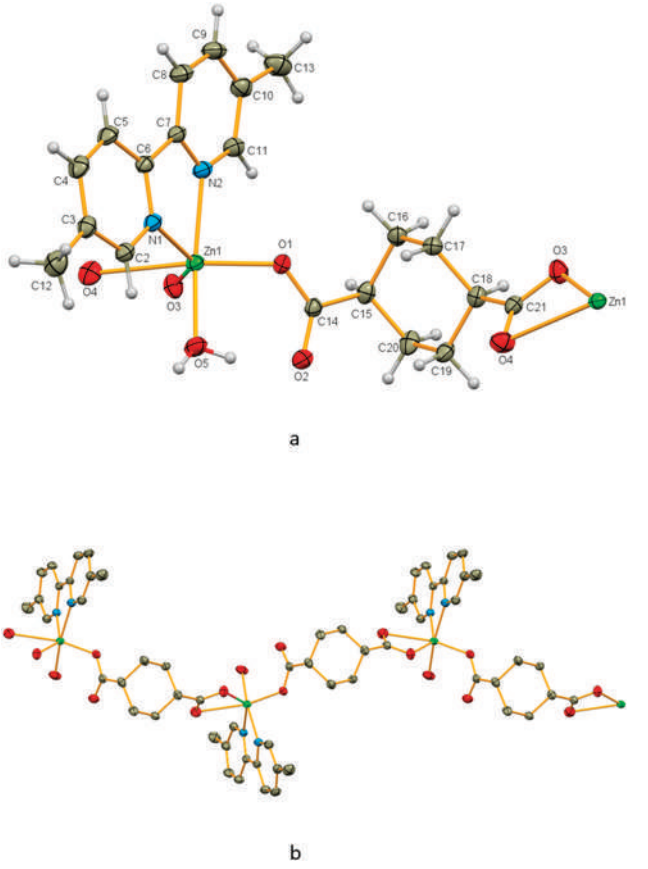

Fig. 2 (a) Molecular structure of $\{Zn(H_2O)(e,a\text{-}cis\text{-}1,4\text{-}chdc)(5,5'\text{-}dmb)\}_n$ **2** (ellipsoids shown at 60% probability) and (b) 1D zig-zag polymer chain of **2**; hydrogens are omitted for clarity.

Analogous to complex **1**, in the extended structure of **2**, the Zn metal centers align to one side of the 1D chain, with the 1,4-chdc ligand forming a kind of V-shape (Fig. 2b); it is a relatively new motif found in coordination polymers having 1,4-chdc as the bridging ligand. Hydrogen bond interactions gather complex **2** into a 2D supramolecular array (Fig. S2†). The main O–H···O interactions involve the O–H moiety (O5) of the aqua ligand with each oxygen atom (O2) of the non-coordinated side of one 1,4-chdc ligand, producing an intramolecular hydrogen bond. Also, each aqua ligand (O5) generates another hydrogen bond with an oxygen atom (O3) of the coordinated side of the 1,4-chdc ligand (O3), which is an intermolecular hydrogen bonding, thus giving rise to a 2D supramolecular system (Fig. S2†).

$\{[Zn_2(H_2O)_2(e,a\text{-}cis\text{-}1,4\text{-}chdc)_2(4,4'\text{-}dtbb)_2]\cdot 7H_2O\}_n$ 3. **3** crystallizes in a monoclinic system with the *Pn* space group and forms an infinite 1D coordination polymer. The remarkable building units in the crystal structure of **3** are the hydrogen-bonded dimer and high-degree hydration with seven lattice water molecules, as shown in Fig. 3a. Other similar dimer, trimer, tetramer, *etc*. complexes have been reported using malonato and bipyridine type ligands;[55–57] however, coordination polymers with this structural characteristic are uncommon. The asymmetric unit of **3** contains two Zn(II) ions, two *e*,*a*-*cis*-

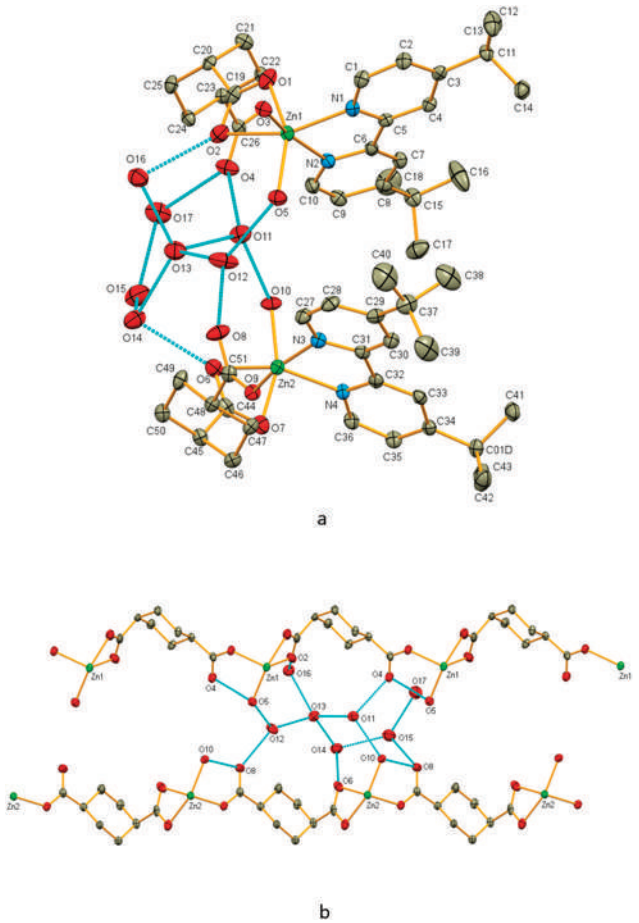

Fig. 3 (a) Supramolecular dinuclear repeating unit of $\{[Zn_2(H_2O)_2(e,a\text{-}cis\text{-}1,4\text{-}chdc)_2(4,4'\text{-}dtbb)_2]\cdot 7H_2O\}_n$ **3** (ellipsoids shown at 60% probability), hydrogens are omitted for clarity and (b) 1D V-shape dual-polymer chain of **3**; hydrogens and 4,4′-dtbb ligands are omitted for clarity.

1,4-chdc, two 4,4′-dtbb, two aqua ligands, and the corresponding lattice water molecules (Fig. 3a). The two crystallographically different Zn ions have a distorted octahedral configuration. The Zn–O bond lengths range from 2.0313 to 2.592(4) Å, while the Zn–N distances range from 2.1113 to 2.1733 Å. As mentioned, two $[Zn(H_2O)(e,a\text{-}cis\text{-}1,4\text{-}chdc)(4,4'\text{-}dtbb)]$ complex molecules are associated into a dinuclear $[Zn_2(H_2O)_2(e,a\text{-}cis\text{-}1,4\text{-}chdc)_2(4,4'\text{-}dtbb)_2]$ complex throughout O–H···O hydrogen bonding coming from the O4 and O8 from the non-coordinated oxygen atoms of the 1,4-chdc ligands, and O5 and O10 of the corresponding aqua ligands. In addition, O11 to O17, corresponding to lattice water molecules, also generate hydrogen bonds with some of the previously mentioned moieties, including those with O2 and O6 from the coordinated chelate side of the 1,4-chdc ligands (Fig. 3a). In **3**, a 1D polymer chain is formed due to the combined monodentate η^1 and chelate bidentate η^2 coordination modes of 1,4-chdc, along with the *equatorial*, *axial cis* configuration of its carboxylate groups bridging the metal centers (Fig. 3b), which also promotes the V-shape shown in **1** and **2**. In this array, Zn1 and Zn2 ions generate a parallel double-ion 1D chain (Fig. 3b). In comparison to those structures where the kinetic and thermodynamic forms are the same, this type of asymmetrical unit with more than one molecule ($Z' > 1$) is still considered a rarity in crystallography, since crystal structures with these characteristics are small in number.[58] Sometimes, the result of the structural prediction complexity in self-assembly reactions is the existence of compounds with high Z' or Z'' crystal structures, where $Z' = Z/M$, M is the multiplicity of the general position, Z is the number of residues in the unit cell, and Z'' denotes the number of crystallographic non-equivalent molecules.[59] It is believed that these high Z' structures signify high-energy minima in the crystallization path towards the final thermodynamic crystal. Even more, it has been identified that supramolecular synthons may play an important role in obtaining this type of crystal, as it could have been in the crystallization process of **3** with $Z'' = 2$. Thus, these kinds of dimers are found to be stabilized by weak intermolecular hydrogen bonds, due primarily to the lattice water molecules surrounding the complexes.[57,58]

Anion luminescence sensing

The crystalline sample and an aqueous solution of **3** (10 μM) exhibit a strong blue photoluminescence emission under ambient conditions with a band centred at 420 and 433 nm respectively upon excitation at 340 nm, as is shown in Fig. 4. In contrast, crystals and aqueous solutions of **1–2** (10 μM) show a modest emission centred at 410–420, which has a considerably lower intensity (~ 40%) than that observed for **3**.

The emission broad bands centred at 410–420 nm for **1–3** can be assigned to the effective coordination of the di-alkyl-bpy ligands (4,4′-dmb; 5,5′-dmb and 4,4′-dtbb) to the Zn(II) atom in comparison to the very weak fluorescence emission of the free di-alkyl-bpy ligands, this interaction is also supported by a considerable bathochromic shift ($\Delta\lambda_{em}$ = 35–45 nm).[60] Typically the emission located in the range of 380–420 nm for free aromatic N-donors is assigned to the intramolecular charge transfer (ICT) transition entailing filled p(HOMO) and empty p*(LUMO) orbitals.[61,62] and the enhancement of the luminescence emission of **1–3** can be attributed to the increase of the rigidity of the aromatic N-donor ligands in the polymeric final arrangement, which reduces the loss of energy through non-radiative processes.[60] Similar photochemical properties with blue emission bands in the range of 370–460 nm have been reported previously for several Zn(II) *aqua*-coordination polymers containing aromatic N-donors such as bipyridine derivatives and multicarboxylate anions; for recent examples see $[Zn_2(2,6\text{-}ndc)(NI\text{-}bpy\text{-}34)_2]\cdot H_2O$,[63] $[Zn_2(tpeb)_2(1,4\text{-}ndc)(1,4\text{-}Hndc)_2]\cdot 2.6H_2O$,[64] and $[Zn_2(bpt)(4,4'\text{-}bpy)(H_2O)_2]$[65] (2,6-ndc = naphthalene-2,6-dicarboxylate, NI-bpy-34 = *N*-(pyridin-3-yl)-4-(pyridin-4-yl)-1,8-naphthalimide, tpbe = 1,3,5-tri-4-pyridyl-1,2-ethenylbenzene, 1,4-ndc = 1,4-naphthalenedicarboxylate, bpt = biphenyl-3,30,5,50-tetracarboxylato and 4,4′-bpy = bipyridine). The emission maxima in these kinds of compounds are directly related to the involvement of the auxiliary bpy ligand[66,67] and their photoluminescence is assigned to

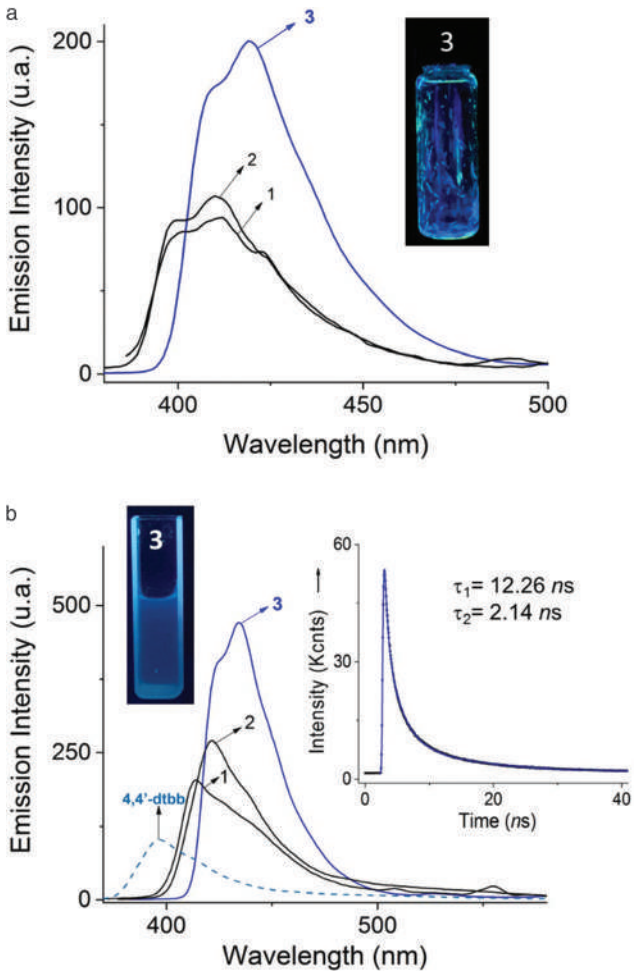

Fig. 4 (a) Solid-state photoluminescence spectra of **1–3**. The inset shows (a) the photograph of crystals of **3** under UV light of 365 nm and (b) photoluminescence spectra of the aqueous solutions of **1–3** at pH = 7.0 of **1–3** (10 μM) and 4,4′-dtbb in $CH_3OH–H_2O$ (1/1 v/v). The inset shows the fluorescence lifetime profile of **3**.

ligand-to-metal charge transfer (LMCT)[60,68] in combination with perturbed π–π* and π–n* transitions, namely, ligand-to-ligand charge transfer (LLCT)[61,69,70] between the aromatic ligands that are constrained by coordination to the Zn(II) atom.

The quantum yields of neutral aqueous solutions of **1–3** (Φ_1 = 0.08, Φ_2 = 0.09, Φ_3 = 0.14) were increased, compared to that of free bpy ligands ($\Phi_{4,4'\text{-dmb}}$ = 0.04; $\Phi_{5,5'\text{-dmb}}$ = 0.04 and $\Phi_{4,4'\text{-dtbb}}$ = 0.05), which is consistent with the LLCT.[43,64] In order to investigate the excited-state behavior, time-resolved fluorescence measurements were performed with **3**. An aqueous solution of **3** upon excitation with a 355 nm laser presents a double–exponential decay function with lifetimes: τ_1 = 12.26 and τ_2 = 2.14 ns. In a related study, the emission lifetimes of Zn(II)-4,4′-bipy MOFs having 1-D ladder and 2-D grid topologies were calculated in the ns range.[71] It is well known that the fluorescence lifetimes of several coordination polymers with d^{10} metals can be increased by the presence of supramolecular interactions (hydrogen bonds, C–H···π and π-stacking) between the luminescent units, which results in a greater contribution of LLCT.[71] Among the three synthesized compounds, **3** shows multiple interactions of type C–H···π, owing to the presence of *tert*-butyl groups which may explain its higher emission compared to **1** and **2**.

Compounds **1–3** can be dissolved in neutral aqueous solution in the sub-millimolar concentration range with chemical stability for several days, which was determined from the emission spectra corresponding to the fresh solutions and after 72 h. These spectra do not show obvious changes indicating a good stability in water; thus those aqueous solutions were used for further studies. Also, the purity of the as-synthesized bulk sample of **3** was investigated by PXRD at room temperature (Fig. S9†). The PXRD pattern of **3** is consistent with that simulated from its single-crystal structure, showing a good phase purity of the sample.

Next, the anion selectivity of **1–3** was analyzed. The sodium salts of inorganic anions (halides, AcO^-, NO_3^-, NO_2^-, $H_2PO_4^-$, $H_3P_2O_7^-$ HCO_3^-, $H_2AsO_4^-$, SO_4^{-2} and CN^-; $[X^-]_{final}$ = 100 μM) were added to buffered aqueous solutions of **1–3** (10 μM), and the emission intensities of **1** (at 413 nm), **2** (at 420) and **3** (at 434 nm) were recorded. In general, all oxoanions including $H_2PO_4^-$ and halides (F^-, Cl^- and Br^{-1}) gave a very low quenching response (Fig. 5a). In contrast, the addition of NaCN caused a decreased emission nearly total quenching for **1–3** (Fig. 5b) and the dynamic equilibrium was observed within 2.0 minutes. The addition of NaI resulted in a modest decrease in emission intensity, but they were still considerably lower than that observed for NaCN. The interference of heavy-halides is not unexpected, especially for iodide. Still, it is remarkable that the sensing with **1–3** is highly selective for CN^- over iodide because I^- ions have a lower solvation energy.[36] Compound **3** displayed the largest blue emission and the most significant quenching in the presence of CN^- ions (Fig. 5a and b), thus it was chosen as the representative sensor for investigating selectivity, sensitivity and the deactivation mechanism. In order to probe the sensitivity, a fluorescence titration experiment was carried out by addition of increasing amounts of NaCN (0–40 μM) to a buffered aqueous solution of **3** (10 μM) (Fig. 6a) under the same conditions as those used in the experiment shown in Fig. 5a.

At a low concentration of [NaCN] < 40 μM, the Stern–Volmer plot shows a good linear dependence (Fig. 6a, inset). The detection limit (LOD), defined as LOD = $3\sigma/s$, where σ is the standard deviation of the blank signals and s is the slope of the calibration curve (K_{SV} = 9.8(±0.1) × 10^4 M^{-1}, Fig. 6a), is 0.90 μmol L^{-1}, which is considerably lower than the maximum level of CN^- recommended by the WHO in drinking water (2.7 μmol L^{-1}).[1] In contrast, at a high concentration of NaCN ([NaCN] ≥ 100 μM, 10 equiv.) the photoluminescence spectrum resembled that recorded for the free ligand 4,4′-dtbb (Fig. 4b).

In order to know the possible effects of interfering anions, we have also conducted a fluorescence titration experiment in the presence of sodium salts of F^-, Cl^-, $H_2PO_4^-$, HCO_3^-, NO_3^-, $H_2AsO_3^-$ and SO_4^{-2} (1.0 mM each) under the same conditions as those used in the experiment shown in Fig. 6a. For concen-

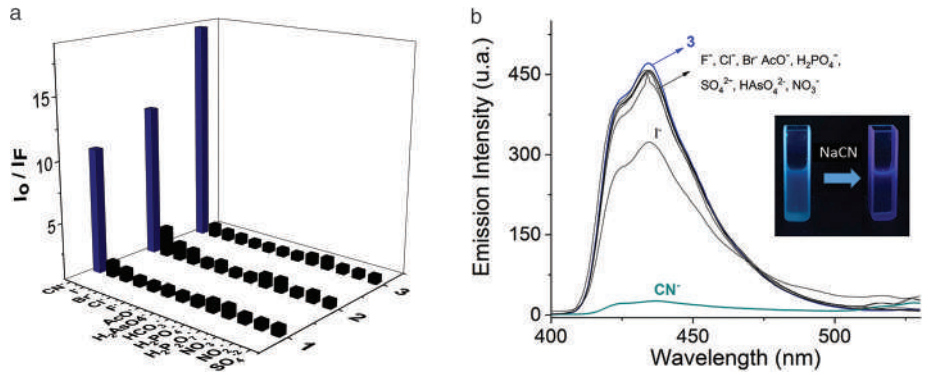

Fig. 5 (a) Change of emission intensity of buffered aqueous solutions of **1**–**3** (10 μM) at pH = 7.0, before and after the addition of 10 equiv. of different anions ($[X^-]_{final}$ = 100 μM) and (b) photoluminescence spectral changes of **3** upon addition of 10 equiv. of different anions. The inset shows a picture taken under irradiation with 365 nm UV light in the absence and presence of CN^-.

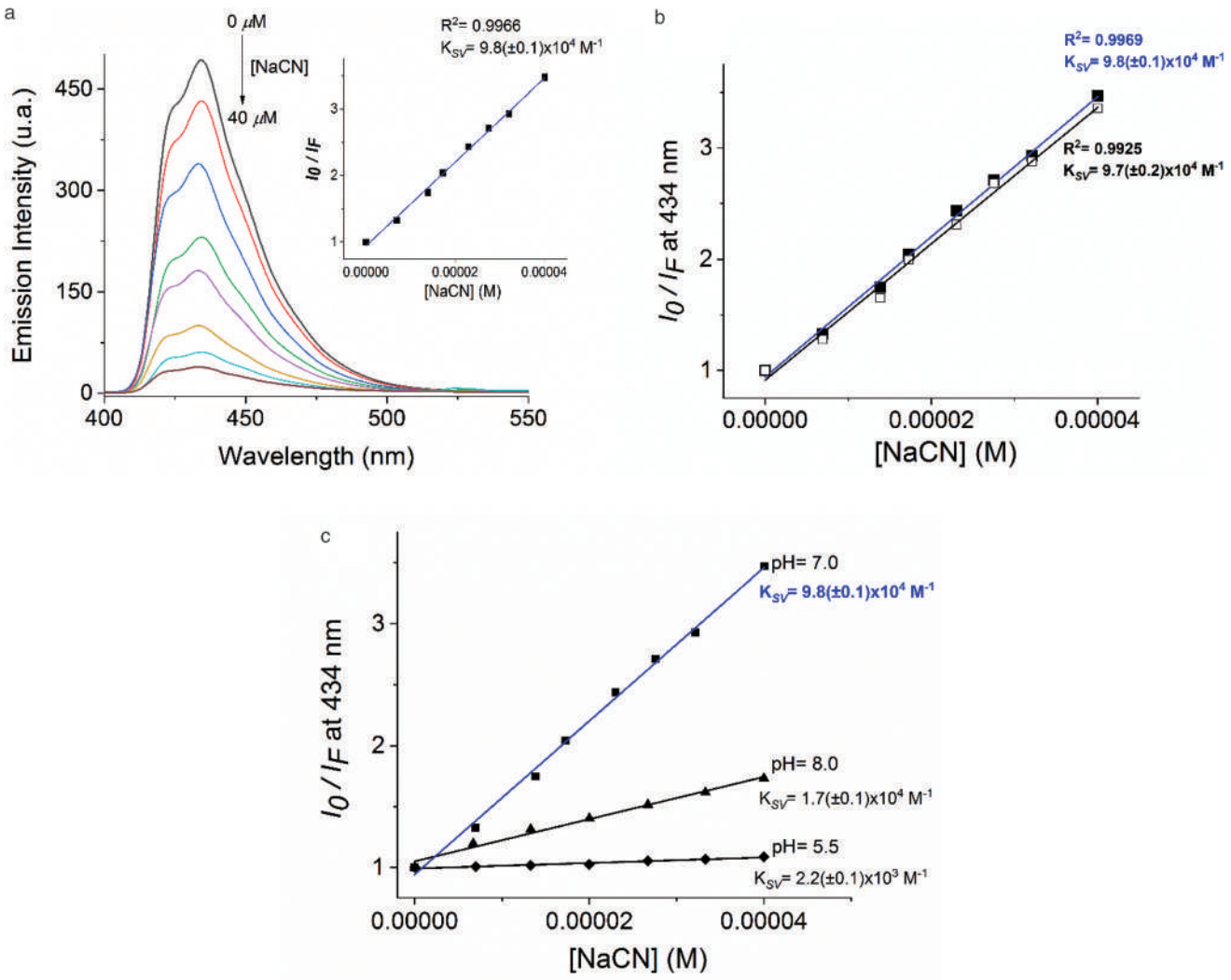

Fig. 6 (a) Photoluminiscence emission spectra of **3** (10 μM) upon addition of NaCN (0–40 μM) in buffered aqueous solution at pH = 7.0. The inset shows the Stern–Volmer plot at 434 nm. (b) Stern–Volmer plots of **3** upon addition of CN^- with (□) and without (■) potentially inorganic interfering anions (1.0 mM each) and (c) Stern–Volmer profiles at different pH values.

trations of $[CN^-]_{tot}$ < 40 μM, the two plots are practically superimposable as shown in Fig. 6b. Thus, polymer **3** seems to operate well in the presence of a millimolar concentration range of potentially interfering anions (K_{SV} = 9.7(±0.2) × 10^4 M^{-1}) including the I^- ions, because the presence of this ion provokes a quenching of about 29% of that observed for CN^-, which does not represent a problem in the analysis of the Stern–Volmer plot ($I_o/I_{F(CN^-)}$ = 18.64 and $I_o/I_{F(I^-)}$ = 1.43).

We also explored the effect of pH on the analytical response of **3** by the addition of NaCN. Fig. 6c shows Stern–Volmer profiles at pH values from 5.5 to 8.0. Clearly, a pH-dependent quenching effect is observed. pH = 7.0 is the most effective for CN^- sensing. On decreasing pH, the photoluminescence decreases and the quenching effect by CN^- becomes weaker.

This behavior is not unexpected due to the fact that CN^- is a weak acid ($CN^- + H_2O \rightleftharpoons HCN + OH^-$ pK_a = 9.36), thus there exists a high percentage of HCN. In contrast, an increase of the pH value decreases the degree of protonation of CN^- with a tighter affinity. However, at pH = 8.0, it is evident that the fluorescence intensity of **3** decreased by comparison with neutral pH possibly by the formation of hydroxides and the competition for Zn(II) atoms between CN^- and OH^- anions. In general, the quenching effect was maximized at pH = 7.0.

Some recent luminescent chemical sensors for the detection and quantification of CN^- in the aqueous phase are compiled in Table 1.

Crystal structure and solid-state CPMAS ^{13}C NMR correlations and SEM

The reactivity and quenching mechanism of CN^- ions to **3** were investigated by NMR, IR-ATR, MS-ESI(+) and SEM. Carbon 13 solid-state NMR and FT-IR spectra of the as-synthesized **3** and of a sample of **3** treated with NaCN, by stirring at r.t. in water, were obtained and compared. The ^{13}C CPMAS spectrum of **3** (Fig. 7) shows 20 signals expected for two crystallographically independent molecules in the asymmetric unit, which is consistent with its crystalline structure (Z = 2).

The four signals for $^{13}CH_2$ of 1,4-chdc are located from 25 to 32 ppm (green rectangle). Despite the presence of two crystallographically independent molecules in **3**, only four signals were observed due to the equivalence in the superimposed 1,4-chdc molecules, Fig. S10.† The unequivocal assignment of the methylene $^{13}CH_2$ atoms was based on ^{13}C cross-polarization polarization-inversion (CPPI) experiments (Fig. S11†). From the ^{13}C CPPI spectrum of **3** (Fig. S11†) it is possible to distinguish between methine atoms (^{13}CH, suppressed signals) and methylene atoms ($^{13}CH_2$, inversed phase signals).[73]

The methine (^{13}CH-CO_2) atoms (C20, C23, C45 and C48) of 1,4-chdc were observed at 38.3 and 47.1 ppm (purple rectangle). The signal corresponding to the $^{13}CH_3$ (*tert*-butyl groups) was located at 30 ppm (blue rectangle) and the $^{13}C_{quaternary}$ atoms (C11, C15, C37 and C01D) were assigned at 34.8 ppm (orange rectangle). On the other hand, the 10 signals from 110 to 170 ppm (black rectangle) are consistent with the $^{13}C_{arom}$ atoms of the 4,4′-dtbb, in accordance with the superimposition analysis (Fig S10†). The peaks observed at 183.7 and 184.7 ppm (red box) were assigned to the $^{13}CO_2^-$ groups.

The sample of **3** treated with 3.0 equiv. of NaCN in buffered water produces an abrupt loss of crystallinity with two observable solid phases. These phases were purified by methanolic extraction, for this extract the solvent was removed under reduced pressure to give a white powder. This powder corresponds to the free fluorescent ligand, 4,4′-dtbb, according to ^{13}C CPMAS (Fig. S12†). The spectrum is consistent with 7 signals and the related CPPI spectrum shows only $^{13}C_{quaternary}$ atoms.

Furthermore, the mass spectrum of the aqueous solution of **3** in the presence of NaCN by positive electrospray ionization shows a peak at 269.19 m/z corresponding to free ditert-butylbipyridine, $[4,4'\text{-dtbb} + H]^+$, which supports the discoordination from the Zn atom and it is consistent with the strong extinction of the fluorescence emission.

On the other hand, the residual solid phase is insoluble in alcohols/water and its FTIR spectrum shows characteristic

Table 1 Recent chemical sensors and materials for detection and quantification of CN^- in the aqueous phase

Chemosensor/materials	Method	LOD (M)	Comments	Ref.
Benzoindolium-triarylborane conjugates	Fluorescence turn-on	7.1×10^{-9}	– High selectivity and sensitivity – CH_3CN/water mixture (1 : 9, v/v) – Response time 5 seconds	35
Naphthoquinone-indole ensembles	Fluorescence turn-on	2.1×10^{-9}	– High selectivity and sensitivity – DMF/water mixture (1 : 1, v/v) – pH-dependent	72
Biometal-organic framework	Fluorescence turn-on	1.9×10^{-8}	– High selectivity and sensitivity – Response time 5–10 min – Efficiency of detoxification	47
Post-synthetically modified MOF (ZIF-90)	Fluorescence turn-off	2.0×10^{-6}	– Low detection limit – DMSO/water mixture (1 : 1, v/v) – Synthetic cost	40
Gold-nanocluster	Fluorescence turn-off	2.0×10^{-7}	– High selectivity and sensitivity – Response time 1–20 min – pH-dependent	8
Zn-coordination polymer	Fluorescence turn-off	0.9×10^{-7}	– High sensitivity – Rapid analytical response – Buffered water at pH = 7.0	This work

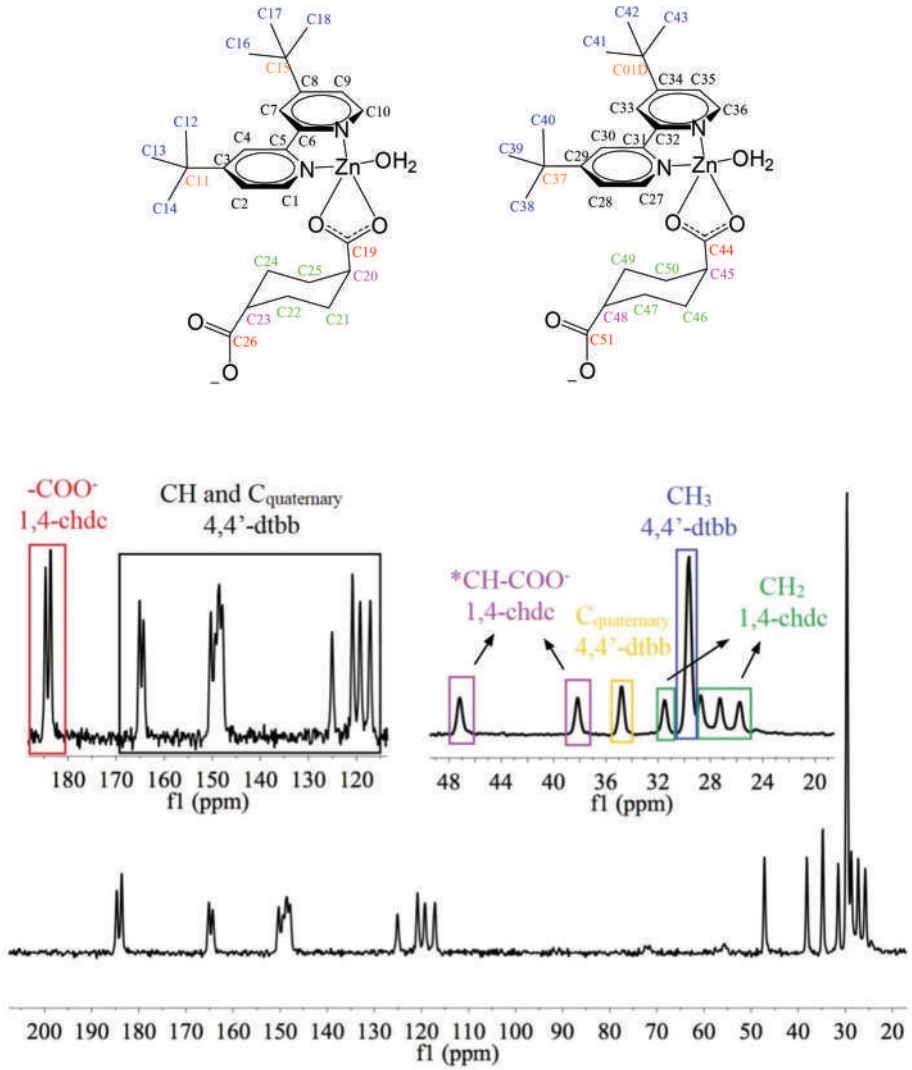

Fig. 7 ^{13}C CPMAS NMR (spinning rate at 7 kHz) spectrum for **3** and the schematic drawing for the two crystallographically independent molecules (above). The numbering used in the SCRXD of the two molecules is preserved.

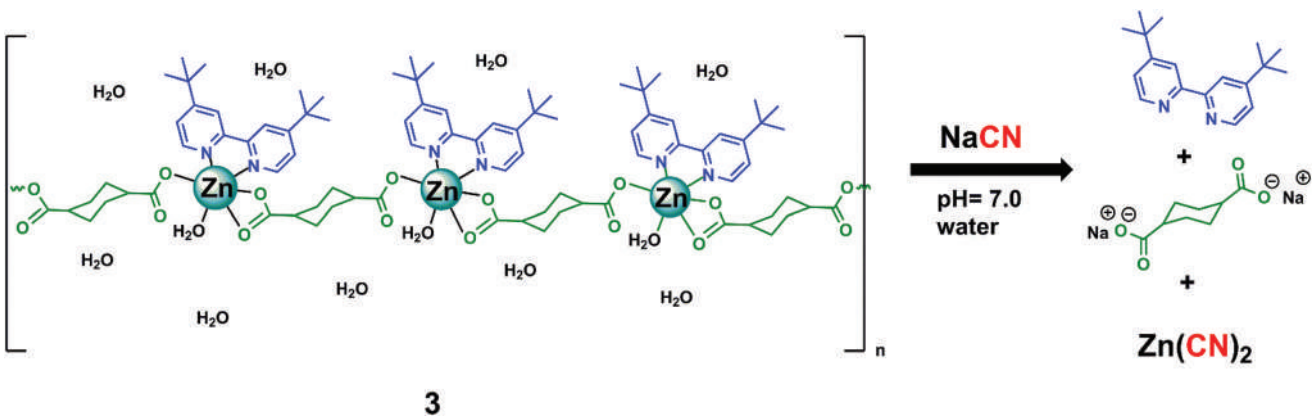

3

Scheme 1

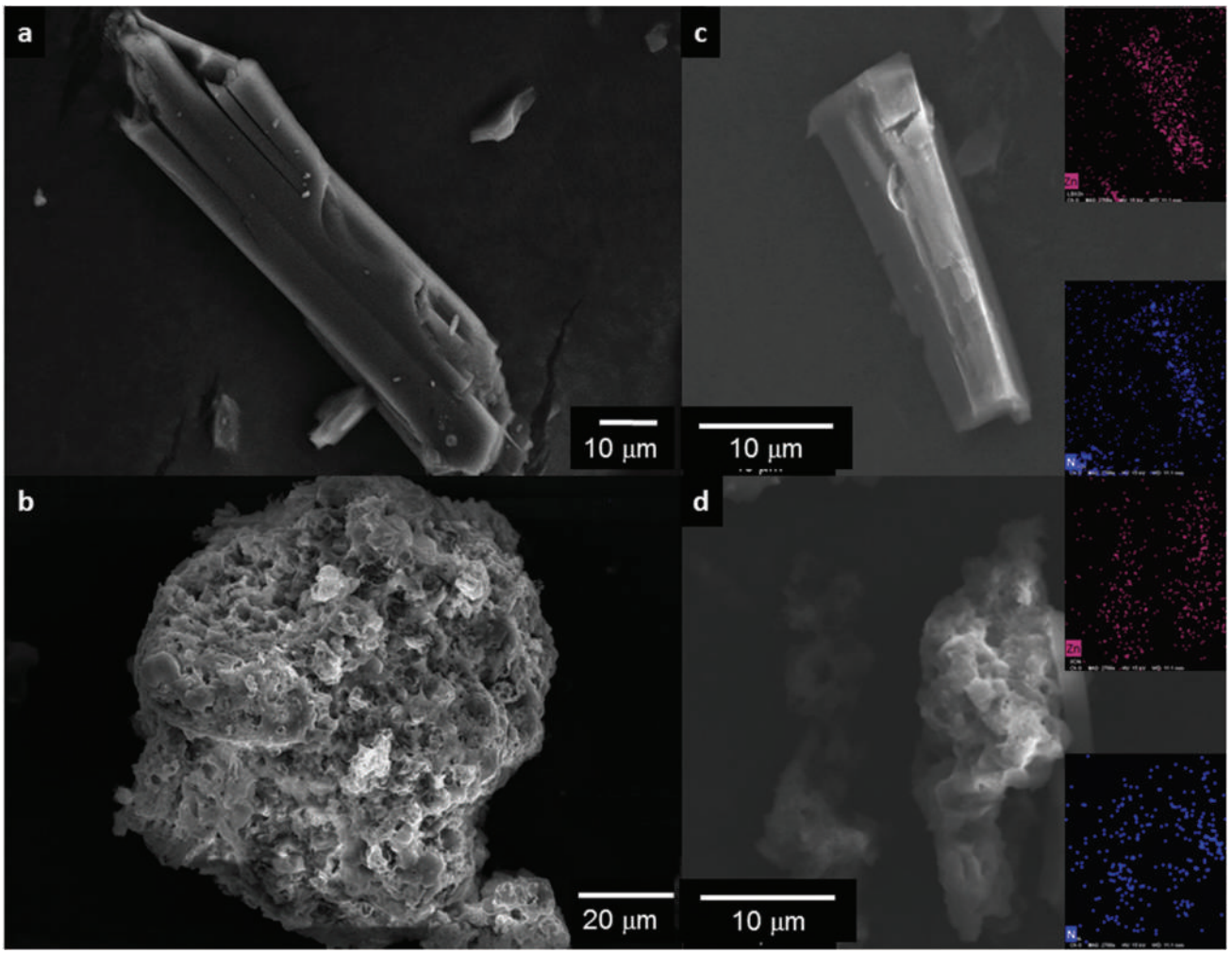

Fig. 8 SEM micrograph of **3** showing the change in morphology before (a) and after (b) the addition of CN^- ions. EDS mapping of elements Zn and N in compound **3** before (c) and after (d) the contact with the NaCN solution.

bands (cm^{-1}) for $Zn(CN)_2$ at 2217 (C≡N stretching vibration) and 455 (lattice/external vibrations of Zn/CN).[74] According to the vibrational spectral bands, the produced $Zn(CN)_2$, by the reaction between **3** and NaCN, corresponds to a cubic structure in which the ZnC4 tetrahedra are linked to the neighbouring ZnN4 tetrahedra with CN bonds.[74] Taking this into account, the quenching mechanism can be directly assigned to the discoordination of the fluorescent ligand (4,4′-dtbb) by the addition of NaCN to **3**. The initial phase, aqueous, was also analyzed by ^1H NMR in D_2O (Fig. S13†) and it corresponds to the ligand 1,4-chdc as sodium salt.

Accordingly, it is reasonable to conclude that the zinc(II) cyanide complex could be formed in the coordination polymer-based system upon addition of sodium cyanide in pure water, thus resulting in fluorescence quenching of **3** at 434 nm. The very weak residual fluorescence, as mentioned above, is characteristic of the aromatic free ligand 4,4′-ditert-butyl-2,2′-bipyridine. The underlying concept of our sensing system is illustrated in Scheme 1.

Finally, the morphology of the as-synthesized crystals of **3** and the corresponding treated sample with NaCN was studied by SEM. Representative micrographs of these crystals are presented in Fig. 8, where a change in the crystal shape is observed before (**8a**) and after **(8b)** the treatment with CN^- ions. EDS mapping of **3** is shown in the insets, where it can be observed that while the nitrogen content increases slightly (around 5.4 ± 1.3%), the Zn species are homogenously distributed around all of the crystals before **(8c)** and after **(8d)** the treatment with CN ions.

Conclusions

In summary, we have successfully synthesized three novel luminescent water-stable zinc-1,4-chdc coordination polymers: $\{[Zn(H_2O)(e,a\text{-}cis\text{-}1,4\text{-}chdc)(4,4'\text{-}dmb)]\cdot 2H_2O\}_n$ **1**, $\{Zn(H_2O)(e,a\text{-}cis\text{-}1,4\text{-}chdc)(5,5'\text{-}dmb)\}_n$ **2** and $\{[Zn_2(H_2O)_2(e,a\text{-}cis\text{-}1,4\text{-}chdc)_2(4,4'\text{-}dtbb)_2]\cdot 7H_2O\}_n$ **3**, by simple self-assembly. The

polymer **3** displays excellent photoluminescence chemosensing ability towards cyanide ions in the nanomolar concentration range in neutral water with selectivity over other common anions such as oxyanions and halides including iodide which is a common interferent. Under this condition, the addition of NaCN exhibits a fast response with total quenching of **3** (K_{SV} = 9.8(±0.1) × 10^4 M^{-1}) and a well-defined correlation between the emission intensities and the concentration of NaCN. The detection limit in the presence of potentially interfering anions is 0.90 ± 0.2 μmol L^{-1}, which is considerably lower than the standard level of CN^- recommended by the WHO in drinking water. The quenching mechanism can be attributed to the discoordination of the fluorescent ligand of the Zn atom by the addition of NaCN with the formation of the $Zn(CN)_2$ salt, which can be easily removed by filtration (detoxification). The present study provides the first example of a flexible and water-stable Zn-coordination polymer based sensor for cyanide ions. Overall, these results further highlight the utility of low-cost and simple d^{10} coordination polymers for toxic and pollutant anion sensing in pure water.

Experimental section

General conditions

All the materials of reagent grade were purchased from commercial sources and used without further purification. De-ionized water was used for synthetic procedures. Elemental analyses for C, H, and N were carried out by standard methods using a Vario Micro-Cube analyzer. IR spectra of the complexes were determined with a FT-IR Shimadzu spectrophotometer, IR Prestige-21, from 4000–400 cm^{-1}. Thermogravimetric analyses were performed with an SDT Q600 TA Instruments analyzer, under a N_2 atmosphere, at a heating rate of 10 °C min^{-1}, from 20 to 800 °C.

Synthesis

1. Initially, sodium 1,4-cyclohexanedicarboxylate was prepared by adding an aqueous solution of NaOH (5 ml; 0.16 M) to a methanol solution (5 ml) of 1,4-cyclohexanedicarboxylic acid (0.0688 g; 0.4 mmol). A solution of 4,4′-dimethyl-2,2′-bipyridine (0.0720 g; 0.4 mmol) in methanol (5 ml) was added to a solution of sodium 1,4-cyclohexanedicarboxylate while stirring. Then, a de-ionized water solution (10 ml) of $Zn(NO_3)_2{\cdot}6H_2O$ (0.0941 g; 0.4 mmol) was added. A translucent solution was obtained. After three days, white crystals were achieved; these were filtered out and washed with de-ionized water. Yield: 84% based on the metal precursor.

Elemental analysis (%), $C_{20}H_{28}N_2O_7Zn$, cal.: 50.69% C, 5.95% H, 5.91% N; found: 50.56% C, 6.08% H 6.01% N. IR cm^{-1} (ATR): 3379 (w, br), 2938 (w, sh), 1543 (s, sh), 1523 (s, sh), 1473 (m, sh), 1450 (m, sh), 1408 (s, sh), 840 (s, sh), 757 (s, sh), 692 (s, br).

2. The same conditions as in the synthesis of **1** were used, except that a solution of 5,5′-dimethyl-2,2′-bipyridine (0.0720 g; 0.4 mmol) in methanol (10 ml) was added to the solution of sodium 1,4-cyclohexanedicarboxylate while stirring. A translucent solution was obtained. After four days, white crystals were obtained; these were filtered out and washed with de-ionized water. Yield: 80% based on the metal precursor.

Elemental analysis (%), $C_{20}H_{24}N_2O_5Zn$, cal: C, 54.86; H, 5.52; N, 6.40; found: C, 54.62, H, 5.61; N, 6.20. IR (ATR, cm^{-1}): 3219(w, br), 2919(w, sh), 1574(m, sh), 1552(s, br), 1480(s, sh), 1396(s, sh), 836(s, sh), 780(s, sh), 730(s, sh), 585(s, sh).

3. Similar conditions as in the synthesis of **1** were used, except that a solution of 4,4′-di-*tert*-butyl-2,2′-bipyridine (0.0536 g; 0.2 mmol) in methanol (10 ml) was added to the solution of sodium 1,4-cyclohexanedicarboxylate. A translucent solution was obtained. After five days, white crystals were achieved; these were filtered out and washed with de-ionized water. Yield: 84% based on the metal precursor.

Elemental analysis (%), $C_{52}H_{86}N_4O_{17}Zn_2$: C, 53.38; H, 7.41; N, 4.79; found: C, 53.25; H, 7.29; N, 4.76. IR (ATR, cm^{-1}): 3303 (w,br), 2964(w,sh), 1611(m,sh), 1553(s,br), 1547(s,br), 1445(w, sh), 1408(s,sh), 848(m,sh), 669(m,br), 604(s,sh).

Crystallographic investigations

The relevant details of the crystals, data collection, and structural refinement can be found in Tables S1–3 (ESI†). Crystallographic data for **1–3** were collected on a Bruker APEX II CCD diffractometer, for **1** and **3** at 100 K and for **2** at 296 K, using Mo-Kα radiation (k = 0.71073 Å) for **1** and **2** and Cu-Kα radiation (k = 1.54178 Å) for **3**, from an Incoatec IμS source and Helios optic monochromator.[75] For **1** and **3**, suitable crystals were coated with hydrocarbon oil (Parabar), picked up with a nylon loop, and mounted in the cold nitrogen stream of the diffractometer. For **2**, suitable crystals were coated with hydrocarbon oil (Parabar), and the specimen was collected with a glass fiber and fixed with glue. The structures were solved using intrinsic phasing (SHELXT)[76] and refined by full-matrix least-squares on F^2 using the shelXle GUI.[77] The hydrogen atoms of the C–H bonds were placed in idealized positions whereas the hydrogen atoms from water molecules were localized from the difference electron density map, and their position was refined with U_{iso} linked to the parent atom with distance restraints. In compound **1**, the hydrogens from water molecules that are not coordinated to zinc present positional disorder in two positions, the occupation was set at 50% and their positions were localized from the difference electron density map and refined using the DFIX instruction. In compound **3**, one *tert*-butyl fragment presents positional disorder in two positions with a 68/32 ratio, and the disorder was modeled using SIMU, RIGU and SAME instructions.

Crystallographic data for **1–3** have been deposited at the Cambridge Crystallographic Data Center (CCDC) with the numbers 1579458–1579460,† respectively. The selected bond distances, bond angles and hydrogen bonds are specified in Tables S4–S9.†

Photoluminescence measurements. Luminescence spectra for solid-state and aqueous neutral solutions of polymers **1–3** were recorded on an Agilent Cary Eclipse spectrophotometer equipped with a crystal-holder or a cell thermostated holder

with a quartz cuvette. In all cases, crystalline samples of **1–3** were used for emission measurements upon excitation at 340 nm. Titration experiments were performed by adding aliquots of stock solutions of anions (10 mM) as sodium salts to the aqueous solutions of polymers **1–3** (10 μM, pH = 7.0, 10 mM MOPS). After the addition of anions, the solution was equilibrated for 1 min at room temperature before recording the emission spectrum (excited at 360 nm) using a quartz cuvette. The stock aqueous solutions of polymers **1–3** were prepared with double distilled water by stirring for 20 min at 25 °C using the corresponding crystal samples of polymers with a concentration of ~ 0.85 mM (0.25 mg mL^{-1}). Luminescence quantum yields were determined using an aqueous solution of quinine sulfate containing H_2SO_4 (0.5 M) as a standard (Φ = 0.546; excited at 360 nm). For the determination of the quantum yield, the excitation wavelength was chosen so that $A < 0.05$.[43]

Fluorescence lifetime measurements. A custom-built fluorescence lifetime imaging microscope system was used to acquire the fluorescence lifetimes. A 355 nm picosecond laser pulsed at 10 MHz (LDH-PFA-355, PicoQuant) was focused directly with a 0.40 NA reflective objective (LMM-40X-UVV-160, ThorLabs) on an aqueous solution of **3** into a 1.0 cm quartz cell. The epifluorescence passed through a 425 nm long-pass dichroic mirror (Chroma T425lpxr-UF2), a 405 nm notch filter (Chroma ZET405nf), and a 425 nm long pass emission filter (Chroma ET425lp) and was focused to a single photon avalanche photodiode (PD-050-CTE, MPD). The laser controller (PDL-800-D, PicoQuant) and the detector were connected to a TCSPC card (PicoHarp 300, PicoQuant). The intensity of irradiation was set to obtain less than 1% of detection events. Back-scattered light from a mirror was used to obtain the IRF under the same conditions of irradiation. All data were obtained and treated in SymphoTime 64 software (PicoQuant). The lifetime data were fitted with bi-exponential decay functions.

CPMAS and CPPI NMR

All the CPMAS and CPPI experiments were recorded with a Bruker Avance II 300 spectrometer (operating at: ^{1}H 300 MHz and ^{13}C 75 MHz). ssNMR measurements were carried out on a 4 mm rotor double resonance. All CPMAS and CPPI experiments were recorded with a contact time of 2 ms and a delay of 5 s at 7 kHz spinning rate at ambient temperature. In the CPPI experiments for **3** and 4,4′-dtbb 30 μs of a polarization inversion period was used.

SEM-EDS

The morphology of polymer **3** before and after the contact with NaCN solution was examined by SEM on a JSM-6510LV microscope from JEOL using a secondary electron detector. The specimen was dried under room conditions and fixed on aluminum stubs with carbon adequate tape, and then coated with gold under vacuum using a Denton IV sputtering chamber. Elemental chemical distribution analysis was performed with an energy-dispersive X-ray spectroscope QUANTAX 200 from Bruker attached to SEM.

Conflicts of interest

There are no conflicts to declare.

Acknowledgements

The authors are indebted to M. Sc. María de la Nieves Zavala Segovia and L.I.A. María Citlalit Martínez Soto, M. Sc. Alejandra Núñez Pineda and M. Sc. Lizbeth Triana Cruz (CCIQS UAEM-UNAM) for technical assistance. We thank B. Sc. María del Rocio Patiño Maya for IR-ATR analysis. Funding for this work was provided by Universidad Autónoma del Estado de México (UAEM). We thank CONACyT (PDCPN247495, CB239648 and ID-179 "Fronteras de la Ciencia") and UNAM (PAPIIT-IN203717) for financial support. L. D. R.-V., J. V.-G. and I. J. B.-R. are grateful to CONACyT for Ph.D. scholarships 713164, 626685, 577221 respectively.

References

1 *Guidelines for Drinking-Water Quality*, 3rd edn, vol. 1. WHO Libr. Cat., 2004.
2 H. Services, *Toxicological Profile for Cyanide*, ATSDR's Toxicol Profiles US. Dep. Heal. Hum. Serv., Atlanta, GA, 2006.
3 K. W. Kulig, *Cyanide Toxicity*, US Dep. Heal. Hum. Serv., Atlanta, GA, 1991, vol. 15.
4 M. Panda and N. C. Robinson, Kinetics and Mechanism for the Binding of HCN to Cytochrome c Oxidase, *Biochemistry*, 1995, **34**(31), 10009–10018.
5 H. Sun, Y. Y. Zhang, S. H. Si, D. R. Zhu and Y. S. Fung, Piezoelectric quartz crystal (PQC) with photochemically deposited nano-sized Ag particles for determining cyanide at trace levels in water, *Sens. Actuators, B*, 2005, **108**, 925–932.
6 C. A. Johnson, D. J. Grimes, R. W. Leinz and R. O. Rye, Cyanide speciation at four gold leach operations undergoing remediation, *Environ. Sci. Technol.*, 2008, **42**(4), 1038–1044.
7 J. Ma and P. K. Dasgupta, Recent developments in cyanide detection: A review, *Anal. Chim. Acta*, 2010, **673**(2), 117–125.
8 Y. Liu, K. Ai, X. Cheng, L. Huo and L. Lu, Gold-nanocluster-based fluorescent sensors for highly sensitive and selective detection of cyanide in water, *Adv. Funct. Mater.*, 2010, **20**(6), 951–956.
9 M. Jaishankar, T. Tseten, N. Anbalagan, B. B. Mathew and K. N. Beeregowda, Toxicity, mechanism and health effects of some heavy metals, *Interdiscip. Toxicol.*, 2014, **7**(2), 60–72.
10 S. S. Sun and A. J. Lees, Anion recognition through hydrogen bonding: A simple, yet highly sensitive, luminescent

metal-complex receptor, *Chem. Commun.*, 2000, (17), 1687–1688.

11 P. Anzenbacher, D. S. Tyson, K. Jursíková and F. N. Castellano, Luminescence lifetime-based sensor for cyanide and related anions, *J. Am. Chem. Soc.*, 2002, **124**(22), 6232–6233.

12 R. Rajamanikandan and M. Ilanchelian, Protein-Localized Bright-Red Fluorescent Gold Nanoclusters as Cyanide-Selective Colorimetric and Fluorometric Nanoprobes, *ACS Omega*, 2018, **3**(10), 14111–14118.

13 L. Somenath, K. Dhara, P. Roy, S. P. S. Babu and C. Pabitra, Highly Sensitive Ratiometric Chemosensor and Biomarker for Cyanide Ions in the Aqueous Medium, *ACS Omega*, 2018, **3**, 10145–10153.

14 P. Singh, H. Kaur and H. Singh, Rationally Designed Circularly Arranged Sextuple Molecule with Dimethoxyphenolic Tentacles for Ample Hunting of Cyanide, *ACS Omega*, 2018, **3**(7), 8003–8008.

15 A. M. Al-Soliemy, Novel asymmetrical phenothiazine for fluorescent detection of cyanide anions, *J. Mol. Struct.*, 2019, **1179**, 525–531.

16 J. Kang, F. Huo, Y. Zhang, J. Chao, T. E. Glass and C. Yin, A novel near-infrared ratiometric fluorescent probe for cyanide and its bioimaging applications, *Spectrochim. Acta, Part A*, 2019, **209**, 95–99.

17 Q. Li, Z. Wang, W. Song, M. Huiling, J. Dong, Y. Y. Quan, X. Ye and Z. S. Huang, A novel D–π-A triphenylamine-based turn-on colorimetric and ratiometric fluorescence probe for cyanide detection, *Dyes Pigm.*, 2019, **161**(September 2018), 389–395.

18 S. Maji, B. Chowdhury, S. Pal and P. Ghosh, An indolium ion functionalized naphtha imide chemodosimeter for detection of cyanide in aqueous medium, *Inorg. Chim. Acta*, 2018, **483**(July), 321–328.

19 Y. Sun, Y. Shan, N. Sun, Z. Li, X. Wu, R. Guan, D. Cao, S. Zhao and X. Zhao, Cyanide and biothiols recognition properties of a coumarin chalcone compound as red fluorescent probe, *Spectrochim. Acta, Part A*, 2018, **205**, 514–519.

20 J. B. Arockiam and J. S. Park, Fluorescence turn-on chemodosimetric sensing of cyanide by cyanovinylterpyridine modified phthalonitrile and subphthalocyanine, *Spectrochim. Acta, Part A*, 2019, **207**, 112–117.

21 M. Cherbuin, F. Zelder and W. Karlen, Quantifying cyanide in water and foodstuff using corrin-based CyanoKit technologies and a smartphone, *Analyst*, 2018, **144**, 130–136.

22 R. Rajamanikandan and M. Ilanchelian, β-Cyclodextrin protected gold nanoparticle based cotton swabs as an effective candidate for specific sensing of trace levels of cyanide, *Anal. Methods*, 2019, **97**, 97–104.

23 G. Emandi, K. J. Flanagan and M. O. Senge, Fluorescent imidazole-based chemosensors for the reversible detection of cyanide and mercury ions, *Photochem. Photobiol. Sci.*, 2018, **17**(10), 1450–1461.

24 P. S. Kumar, P. R. Lakshmi and K. P. Elango, An easy to make chemoreceptor for the selective ratiometric fluorescent detection of cyanide in aqueous solution and in food materials, *New J. Chem.*, 2019, **43**, 675–680.

25 H. J. Mo, Y. Shen and B. H. Ye, Selective recognition of cyanide anion via formation of multipoint NH and phenyl CH hydrogen bonding with acyclic ruthenium bipyridine imidazole receptors in water, *Inorg. Chem.*, 2012, **51**(13), 7174–7184.

26 C. H. Lee, S. H. Kim, S. J. Hong, J. Yoo, S. K. Kim and J. L. Sessler, Strapped Calix[4]pyrroles Bearing a 1,3-Indanedione at a beta-Pyrrolic Position: Chemodosimeters for the Cyanide Anion, *Org. Lett.*, 2009, **11**(16), 3626–3629.

27 E. Thanayupong, K. Suttisintong, M. Sukwattanasinitt and N. Niamnont, Turn-on fluorescent sensor for the detection of cyanide based on a novel dicyanovinyl phenylacetylene, *New J. Chem.*, 2017, **41**(10), 4058–4064.

28 T. F. Robbins, H. Qian, X. Su, R. P. Hughes and I. Aprahamian, Cyanide detection using a triazolopyridinium salt, *Org. Lett.*, 2013, **15**(10), 2386–2389.

29 B. Garg and Y. C. Ling, A highly selective phenothiazine-based fluorescence "turn-on" indicator based on cyanide-promoted novel protection/deprotection mechanism, *Chem. Commun.*, 2015, **51**(42), 8809–8812.

30 D. Cho and J. L. Sessler, The Benzil Rearrangement Reaction: Trapping of a Hitherto Minor Product and Its Application to the Development of a Selective Cyanide Anion Indicator Jonathan, *J. Am. Chem. Soc.*, 2008, **10**(7), 73–75.

31 K. S. Lee, H. J. Kim, G. H. Kim, I. Shin and J. I. Hong, Fluorescent chemodosimeter for selective detection of cyanide in water, *Org. Lett.*, 2008, **10**(1), 49–51.

32 M. K. Salomón-Flores, I. J. Bazany-Rodríguez, D. Martínez-Otero, M. A. Garcia-Eleno, J. J. Guerra-Garcia, D. Morales-Morales and A. Dorazco-Gonzalez, Bifunctional colorimetric chemosensing of fluoride and cyanide ions by nickel-POCOP pincer receptors, *Dalton Trans.*, 2017, **46**, 4950–4959.

33 C. Arivazhagan, R. Borthakur, R. Jagan and S. Ghosh, Benzoindolium-triarylborane conjugates: A ratiometric fluorescent chemodosimeter for the detection of cyanide ions in aqueous medium, *Dalton Trans.*, 2016, **45**(12), 5014–5020.

34 S. J. Butler and D. Parker, Anion binding in water at lanthanide centres: From structure and selectivity to signalling and sensing, *Chem. Soc. Rev.*, 2013, **42**(4), 1652–1666.

35 Y. Kim, H. Zhao and F. P. Gabbai, Sulfonium boranes for the selective capture of cyanide ions in water, *Angew. Chem., Int. Ed.*, 2009, **48**(27), 4957–4960.

36 J. D. Routledge, X. Zhang, M. Connolly, M. Tropiano, O. A. Blackburn, A. M. Kenwright, P. D. Beer, S. Aldridge and S. Faulkner, Lanthanide Complexes that Respond to Changes in Cyanide Concentration in Water, *Angew. Chem., Int. Ed.*, 2017, **56**(27), 7783–7786.

37 S. Y. Huang and V. C. Pierre, A turn-on luminescent europium probe for cyanide detection in water, *Chem. Commun.*, 2018, **54**(66), 9210–9213.

38 A. Karmakar, N. Kumar, P. Samanta, A. V. Desai and S. K. Ghosh, A Post-Synthetically Modified MOF for Selective and Sensitive Aqueous-Phase Detection of Highly Toxic Cyanide Ions, *Chem. – Eur. J.*, 2016, **22**(3), 864–868.

39 L. Mei, W. Q. Shi and Z. F. Chai, Ordered entanglement in actinide-organic coordination polymers, *B. Chem. Soc. Jpn.*, 2018, **91**(4), 554–562.

40 S. Yuan, L. Feng, K. Wang, J. Pang, M. Bosch, C. Lollar, Y. Sun, J. Qin, X. Yang, P. Zhang, Q. Wang, L. Zou, Y. Zhang, L. Zhang, Y. Fang, J. Li and H. C. Zhou, Stable Metal–Organic Frameworks: Design, Synthesis, and Applications, *Adv. Mater.*, 2018, **30**(37), 1–35.

41 S. Kitagawa and R. Matsuda, Chemistry of coordination space of porous coordination polymers, *Coord. Chem. Rev.*, 2007, **251**, 2490–2509.

42 M. Li, D. Li, M. O'Keeffe and O. M. Yaghi, Topological analysis of metal-organic frameworks with polytopic linkers and/or multiple building units and the minimal transitivity principle, *Chem. Rev.*, 2014, **114**(2), 1343–1370.

43 J. C. Rendón-Balboa, L. Villanueva-Sánchez, L. D. Rosales-Vázquez, J. Valdes-Garcia, A. R. Vilchis-Nestor, D. Martínez-Otero, S. Martínez-Vargas and A. Dorazco-González, Structure of a luminescent 3D coordination polymer constructed with a trinuclear core of cadmium-trimesate and isoquinoline, *Inorg. Chim. Acta*, 2018, **483**, 235–240.

44 J. Li and J. Li, A luminescent porous metal–organic framework with Lewis basic pyridyl sites as a fluorescent chemosensor for TNP detection, *Inorg. Chem. Commun.*, 2018, **89**, 51–54.

45 X. Zhang, W. Wang, Z. Hu, G. Wang and K. Uvdal, Coordination polymers for energy transfer: Preparations, properties, sensing applications, and perspectives, *Coord. Chem. Rev.*, 2015, **284**(October 2014), 206–235.

46 P. Kumar, A. Deep and K. H. Kim, Metal organic frameworks for sensing applications, *TrAC, Trends Anal. Chem.*, 2015, **73**, 39–53.

47 A. Karmakar, B. Joarder, A. Mallick, P. Samanta, A. V. Desai, S. Basu and S. K. Ghosh, Aqueous phase sensing of cyanide ions using a hydrolytically stable metal-organic framework, *Chem. Commun.*, 2017, **53**(7), 1253–1256.

48 E. Y. Semitut, T. S. Sukhikh, E. Y. Filatov, G. A. Anosova, A. A. Ryadun, K. A. Kovalenko and A. S. Potapov, Synthesis, crystal structure, and luminescent properties of novel zinc metal-organic frameworks based on 1,3-Bis(1,2,4-triazol-1-yl)propane, *Cryst. Growth Des.*, 2017, **17**(10), 5559–5567.

49 T. F. Liu, J. Lü and R. Cao, Coordination polymers based on flexible ditopic carboxylate or nitrogen-donor ligands, *CrystEngComm*, 2010, **12**(3), 660–670.

50 L. D. Rosales-Vázquez, V. Sánchez-Mendieta, I. García-Orozco, S. Hernández-López, D. Martínez-Otero, R. A. Morales-Luckie, R. Escudero and F. Morales, 1,4-Cyclohexanedicarboxylato-bridged cobalt coordination polymers: Synthesis, crystal structures and magnetic properties, *Inorg. Chim. Acta*, 2018, **471**, 674–679.

51 A. Q. Ma, M. X. Yu and L. G. Zhu, Crystal structure of (μ_2-4-cyclohexanedicarboxylato)(1,10-phenanthroline)-copper(II) monohydrate, $Cu(C_{12}H_8N_2)(C_8H_{10}O_4) \cdot H_2O$, *Z. Kristallogr. NCS*, 2004, **219**, 63–64.

52 M. Arici, Luminescent 2D+2D → 2D interpenetrated Zn(II)-coordination polymer based on reduced schiff base tricarboxylic acid and bis(imidazole) ligand for detection of picric acid and Fe^{3+} ions, *Cryst. Growth Des.*, 2017, **17**(10), 5499–5505.

53 W. Yang, C. Wang, Q. Ma, C. Liu, H. Wang and J. Jiang, Synthesis, crystal structures, and luminescence properties of seven tripodal imidazole-based Zn/Cd(II) coordination polymers induced by tricarboxylates, *CrystEngComm*, 2014, **16**(21), 4554–4561.

54 H. Wang, X. Y. Yang, Y. Q. Ma, W. B. Cui, Y. H. Li, W. G. Tian, S. Yao, Y. Gao, S. Dang and W. Zhu, Imidazole-based zinc(II) complexes: Highly selective fluorescent probes for acetone detection, *Inorg. Chim. Acta*, 2014, **416**, 63–68.

55 Y. Q. Zheng, X. S. Zhai, L. Jin, H. L. Zhu, J. L. Lin and W. Xu, Insight into self-assembly of malonate-based copper (II) phenanthroline complexes: Syntheses, crystal structures and properties, *Polyhedron*, 2014, **68**, 324–333.

56 C. Ruiz-Pérez, M. Hernández-Molina, P. Lorenzo-Luis, F. Lloret, J. Cano and M. Julve, Magnetic coupling through the carbon skeleton of malonate in two polymorphs of $\{[Cu(bpy)(H_2O)][Cu(bpy)(mal)(H_2O)]\}(ClO_4)_2$ (H_2mal = malonic acid; bpy = 2,2′-bipyridine), *Inorg. Chem.*, 2000, **39**(17), 3845–3852.

57 S. R. Choudhury, H. M. Lee, T. H. Hsiao, E. Colacio, A. D. Jana and S. Mukhopadhyay, Co-operation of π···π, Cu(II)···π, carbonyl···π and hydrogen-bonding forces leading to the formation of water cluster mimics observed in the reassessed crystal structure of $[Cu(mal)(phen)(H_2O)]_2 \cdot 3H_2O$ (H_2mal = malonic acid, phen = 1,10-phenanthroline), *J. Mol. Struct.*, 2010, **967**(1–3), 131–139.

58 D. Das, R. Banerjee, R. Mondal, J. A. K. Howard, R. Boese and G. R. Desiraju, Synthon evolution and unit cell evolution during crystallisation. A study of symmetry-independent molecules ($Z' > 1$) in crystals of some hydroxyl compounds, *Chem. Commun.*, 2006, (5), 555–557.

59 B. P. Van Eijck and J. Kroon, Structure predictions allowing more than one molecule in the asymmetric unit, *Acta Crystallogr., Sect. B: Struct. Sci.*, 2000, **56**(3), 535–542.

60 J. Heine and K. Müller-Buschbaum, Engineering metal-based luminescence in coordination polymers and metal–organic frameworks, *Chem. Soc. Rev.*, 2013, **42**(24), 9232.

61 X. Wang, C. Qin, E. Wang, Y. Li, N. Hao, C. Hu and L. Xu, Syntheses, structures, and photoluminescence of a novel class of d^{10} metal complexes constructed from pyridine-3,4-dicarboxylic acid with different coordination architectures, *Inorg. Chem.*, 2004, **43**(6), 1850–1856.

62 L. Ma, N. Yu, S. Chen and H. Deng, Construction of diverse Cd(II)/Zn(II) coordination polymers based on 5-(quinolyl)

tetrazolate generated via in situ hydrothermal synthesis, *CrystEngComm*, 2013, **15**(7), 1352.

63 M. J. Tsai, C. Y. Li and J. Y. Wu, Luminescent Zn(II) coordination polymers as efficient fluorescent sensors for highly sensitive detection of explosive nitroaromatics, *CrystEngComm*, 2018, **20**(42), 6762–6774.

64 T. Y. Gu, M. Dai, D. J. Young, Z. G. Ren and J. P. Lang, Luminescent Zn(II) Coordination Polymers for Highly Selective Sensing of Cr(III) and Cr(VI) in Water, *Inorg. Chem.*, 2017, **56**(8), 4668–4678.

65 L. T. Wu, Z. J. Wang, X. Wu, C. Y. Zhou, F. Su and C. Han, Synthesis, structure and selective luminescence sensing for iron(III) ions of a three-dimensional zinc(II) (4,6)-connected coordination network, *Acta Crystallogr., Sect C, Cryst. Struct. Commun.*, 2019, **75**(2), 141–149.

66 L. Y. Zhang, G. F. Liu, S. L. Zheng, B. H. Ye, X. M. Zhang and X. M. Chen, Helical Ribbons of Cadmium(II) and Zinc (II) Dicarboxylates with Bipyridyl-Like Chelates– Syntheses, Crystal Structures and Photoluminescence, *Eur. J. Inorg. Chem.*, 2003, **2003**(16), 2965–2971.

67 L. Zhang, Z. Kang, X. Xin and D. Sun, Metal–organic frameworks based luminescent materials for nitroaromatics sensing, *CrystEngComm*, 2016, **18**(2), 193–206.

68 K. Müller-Buschbaum, F. Beuerle and C. Feldmann, MOF based luminescence tuning and chemical/physical sensing, *Microporous Mesoporous Mater.*, 2014, **216**, 171–199.

69 Y. Rachuri, B. Parmar, K. K. Bisht and E. Suresh, Solvothermal self-assembly of Cd^{2+} coordination polymers with supramolecular networks involving N-donor ligands and aromatic dicarboxylates: synthesis, crystal structure and photoluminescence studies, *Dalton Trans.*, 2017, **46**, 3623–3630.

70 L. D. Rosales-Vázquez, V. Sánchez-Mendieta, A. Dorazco-González, D. Martínez-Otero, I. García-Orozco, R. A. Morales-Luckie, J. Jaramillo-García and A. Téllez-López, Cadmium–1,4-cyclohexanedicarboxylato coordination polymers bearing different di-alkyl-2,2′-bipyridines: syntheses, crystal structures and photoluminescence studies, *Dalton Trans.*, 2017, **46**(37), 12516–12526.

71 M. D. Allendorf, C. A. Bauer, R. K. Bhakta and R. J. T. Houk, Luminescent metal-organic frameworks, *Chem. Soc. Rev.*, 2009, **38**(5), 1330–1352.

72 P. Jayasudha, R. Manivannan, S. Ciattini, L. Chelazzi and K. P. Elango, Selective sensing of cyanide in aqueous solution by quinone-indole ensembles – quantitative effect of substituents on the HBD property of the receptor moiety, *Sens. Actuators, B*, 2017, **242**, 736–745.

73 X. L. Wu, S. T. Burns and K. W. Zilm, Spectral Editing in CPMAS NMR. Generating Subspectra Based on Proton Multiplicities, *J. Magn. Reson., Ser. A*, 1994, **111**(1), 29–36.

74 T. R. Ravindran, A. K. Arora and T. N. Sairam, A spectroscopic resolution of the structure of Zn(CN)2, *J. Raman Spectrosc.*, 2007, **38**, 283–287.

75 *APEX 2 Software suite*, Bruker AXS Inc., Madison, Wisconsin, USA.

76 SHELXTG. M. Sheldrick, *Acta Crystallogr., Sect. A: Found. Adv.*, 2015, **A71**, 3.

77 ShelXleC. B. Hübschle, G. M. Sheldrick and B. Dittrich, *J. Appl. Crystallogr.*, 2011, **44**, 1281.

Journal of Materials Chemistry C

ROYAL SOCIETY OF CHEMISTRY

PAPER

View Article Online
View Journal | View Issue

Cite this: J. Mater. Chem. C, 2022, 10, 5944

A water-stable luminescent Zn-MOF based on a conjugated π-electron ligand as an efficient sensor for atorvastatin and its application in pharmaceutical samples†

Luis D. Rosales-Vázquez, [a] Josue Valdes-García, [a] Juan M. Germán-Acacio, [b] José C. Páez-Franco, [b] Diego Martínez-Otero, [c] Alfredo R. Vilchis-Nestor, [c] Joaquín Barroso-Flores, [c] Víctor Sánchez-Mendieta *[c] and Alejandro Dorazco-González *[a]

Received 19th January 2022,
Accepted 14th March 2022

DOI: 10.1039/d2tc00291d

rsc.li/materials-c

Atorvastatin is amongst the most worldwide-prescribed drugs for cholesterol-lowering treatment. In this work, a novel water-stable 3D porous metal–organic framework $\{[Zn_3(Htptc)_2]\cdot(H_2O)_{1.3}\cdot(CH_3CH_2OH)_{3.1}\}_n$, **1** ($H_4$tptc= terphenyl-3,3″,5,5″-tetracarboxylic acid) was synthesized, structurally determined by single-crystal X-ray diffraction, and studied in-depth as a luminescent sensor for a series of statins and common biological ions (oxyanions, dicarboxylates, citrate, and adenosine 5′-triphosphate) in 20% aqueous ethanol. The luminescence of **1** can be effectively quenched by atorvastatin (K_{SV} = 1.40 × 10^5 M^{-1}) with a pronounced selectivity over other typical statins such as fluvastatin, pravastatin, and rosuvastatin. The efficient quenching response exhibits excellent selectivity even in the presence of coexisting species in blood plasma and urine with a detection limit of 4.2 μmol L^{-1}. On the basis of multiple spectroscopic tools (fluorescence, UV-Vis, powder X-ray diffraction, lifetimes), the crystal structure of **1**, SEM observations, EDS analysis, and DFT calculations, the sensing mechanism is proposed *via* a static-complexation PET process driven through π-stacking interactions between π-electron-rich terphenyl ligand and two aromatic rings from the atorvastatin. Neutral aqueous-phase dispersions of **1** allow for the detection of atorvastatin in real pharmaceutical samples. The utilization of MOFs-based materials as luminescent sensors for selective and sensitive detection of atorvastatin has not been explored till now.

1. Introduction

Luminescent metal–organic frameworks (LMOFs) are light-emitting crystalline solids based on supramolecular complexes with a fascinating structural diversity, typically, these materials are constructed by the combination of fluorescent multidentate linkers and diamagnetic or lanthanide metal centers.[1–8] Of particular interest are porous d^{10} transition-metal LMOFs containing conjugated π-electron multicarboxylate ligands owing to their functionality as host matrix materials,[9–11] light-emitting devices,[12–14] materials for gas adsorption/separation,[15–17] catalysis,[18–20] and as receptors of small molecules.[21,22] Generally, d^{10} metal LMOFs with accessible pore volumes undergo a guest binding-induced fast photoluminescence change.[1,12,23–28]

Reports in the context of reticular chemistry have shown that Zn-MOFs constructed with terphenyl-tetracarboxylic acid (H_4tptc) generate crystalline networks based on a $[Zn_2(COO)_4]$ complex as paddlewheel secondary building unit (SBUs). These materials are blue/green luminescent and possess well-defined nanoporous[12,16,17] or 1D channels[14,29–33] where the solvent accessible volume is >20% of the total volume.[32]

Up to now, luminescent Zn-MOFs constructed with derivatives of π-electron-rich terphenyl-carboxylate ligand have proven to be useful in the quantitative detection of inorganic ions,[31] explosive nitroaromatic compounds,[14,30,32–35] and pesticides.[4,36,37] However, optical detection of drugs with global relevance such as statins practically remains unexplored.

[a] Instituto de Química, Universidad Nacional Autónoma de México. Circuito Exterior, Ciudad Universitaria, Ciudad de México, 04510, Mexico. E-mail: adg@unam.mx; Tel: +52-55-56224514

[b] Red de Apoyo a la Investigación, Coordinación de la Investigación Científica-UNAM, Instituto Nacional de Ciencias Médicas y Nutrición SZ, Ciudad de México, CP 14000, Mexico

[c] Centro Conjunto de Investigación en Química Sustentable UAEM-UNAM, Carretera Toluca-Ixtlahuaca Km. 14.5, San Cayetano, Toluca, Estado de México, 50200, Mexico. E-mail: vsanchezm@uaemex.mx

† Electronic supplementary information (ESI) available: Crystallographic data, IR and ^{13}C CPMAS NMR spectra, TGA plots, powder XRD data, SEM images and luminescent measurements. CCDC 2116896. For ESI and crystallographic data in CIF or other electronic format see DOI: 10.1039/d2tc00291d

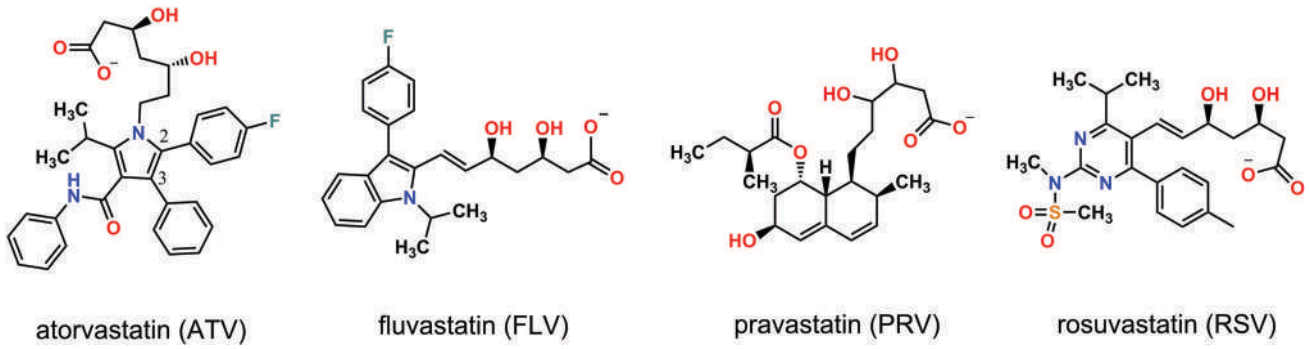

Fig. 1 Statins used as analytes in this study. Sodium salts for FLV/PRV and calcium salts for ATV/RSV.

Statins are among the most used drugs worldwide for decreasing blood cholesterol and cardiovascular medication.[38,39] Heart diseases are the leading cause of death worldwide and commonly, are the result of coronary atherosclerosis. A central factor of atherosclerosis is the accumulation of cholesterol in arterial walls, making lipid modification critical to heart diseases prevention.[40]

The most used cholesterol-lowering statins in medical purposes include sodium or calcium salts of atorvastatin, fluvastatin, pravastatin, and rosuvastatin (Fig. 1).[38] Among these drugs, atorvastatin is one of the oldest and worldwide-prescribed because it has shown the highest lipoprotein cholesterol lowering efficacy in humans at a maximum daily dose $\approx$ 80 mg.[41]

Common analytic methods for the quantitative detection of atorvastatin include electrochemical sensors,[42–45] Raman spectroscopy,[46–48] electrophoresis,[38] spectrophotometry[49] and chromatographic-mass spectrometry.[38,41,50–55] However, many of these methods require considerable setup, analysis time and/or high-cost instruments. While the need for direct, and timely selective sensors for atorvastatin, capable of operating in real samples is evident, so far, a very limited number of systems have been described which are based on carbon nanotubes functionalized with polypyrrole films,[44] Fe_3O_4-nanoparticles,[42] Au-nanoparticles,[56] graphene,[57] and zinc oxide[58] or by oxidative coupling reactions with Ce(IV)-complexes.[59]

Frequently, these electrochemical nanosensors show limits of detection between 10^{-4} and, 10^{-9} M, and their sensing mechanisms are based on the electro-oxidation reaction of the pyrrole ring[57,60] or oxidative reaction of aromatic fragments.[59] Consequently, they are not particularly selective and interferences from other statins containing these rings such as fluvastatin or pravastatin can be a problem.

Reports in the field of sorbent materials have shown that the porous Zn(II)-zeolite imidazolate framework-8 (ZIF-8) is able to capture atorvastatin directly from urine.[61] However, the creation of a potent and selective luminescent sensor/receptor for atorvastatin is an ongoing challenge.

Taking the highly π-electron-rich density, porosity, and strong luminescent of d^{10}-MOFs with terphenyl derivatives, into account we surmised that a sensitive atorvastatin sensor can be achieved by a water-stable Zn-LMOF derivative of terphenyl-tetracarboxylate where the selectivity can be driven through π–π stacking between π-electron-rich surface of the ligand and the fluorinated aromatic π-electron-deficient ring from atorvastatin.[62]

With the objective of constructing the first example of a metal–organic framework-based sensor for atorvastatin, we have prepared a new luminescent Zn-MOF, **1** with selective performance for atorvastatin sensing in aqueous media and pharmaceutical samples. The results obtained for this system including synthesis, crystal structure, multiple spectroscopic sensing studies, SEM-EDS characterization, and theoretical DFT calculations are summarized below.

2. Results and discussion

2.1 Structural description and characterization

By solvothermal method, the LMOF $\{[Zn_3(Htptc)_2]\cdot(H_2O)_{1.3}\cdot(CH_3CH_2OH)_{3.1}\}_n$, **1** was synthesized through the reaction of $Zn(OTf)_2$ with H_4tptc ligand in DMF–ethanol–water (v/v, 8/2/2) (Fig. 2A). Single-crystal X-ray diffraction reveals that crystallized in a monoclinic *C*2/*c* space group (Table S1, ESI†). There are two crystallographically independent Zn(II) ions, each one is coordinated by six oxygen atoms forming a distorted octahedral geometry (Fig. 2B). The carboxylate oxygen atoms of two Htptc ligands link the three Zn(II) ions, generating thus trinuclear SBUs (Fig. 2C, for schematic SBU see Fig. S1, ESI†). The Zn–O bond lengths range from 1.996(5) to 2.428(6) Å (Table S2, ESI†).

Zn(II)-Based MOFs with $tptc^{4-}$ ligand have recently been described having paddlewheel dinuclear SBUs and different topologies; $\{[Zn_2(tptc)(aminopyridine)_x(H_2O)]\cdot H_2O\}_n$ with a **NbO** net,[32] $\{[Zn_2(tptc)(DMF)_3]\cdot(H_2O)_4\cdot(DMF)_{5.5}\}_n$ and $\{[Zn_2(tptc)(DMA)(H_2O)]\cdot(H_2O)\cdot(DMA)_{3.5}\}_n$ (DMA = dimetilacetamide) with **dia** an **lon** nets, respectively.[35] Due to the combining chelate bidentate, bridging monodentate and oxo-bridging coordination modes of the carboxylate oxygen atoms of $Htptc^{3-}$ in **1**, each SBU is bridged by eight Htptc ligands (Fig. 2C) and each ligand is linked to four trinuclear clusters, which results in a three-dimensional framework (Fig. 2C). The network topology of **1** was studied by software package TOPOS-PRO, which consists of a new underlying 4,6,7-*c* net and a new 3,3,8-*c* net in standard and cluster representations of valence-bonded MOFs, respectively (Fig. 2D and Fig. S2, ESI†).[63]

In this assembly, there are connected oval-shape pores along *a*-axis as shown in Fig. 3 and Fig. S3 (ESI†). SQUEEZE/PLATON

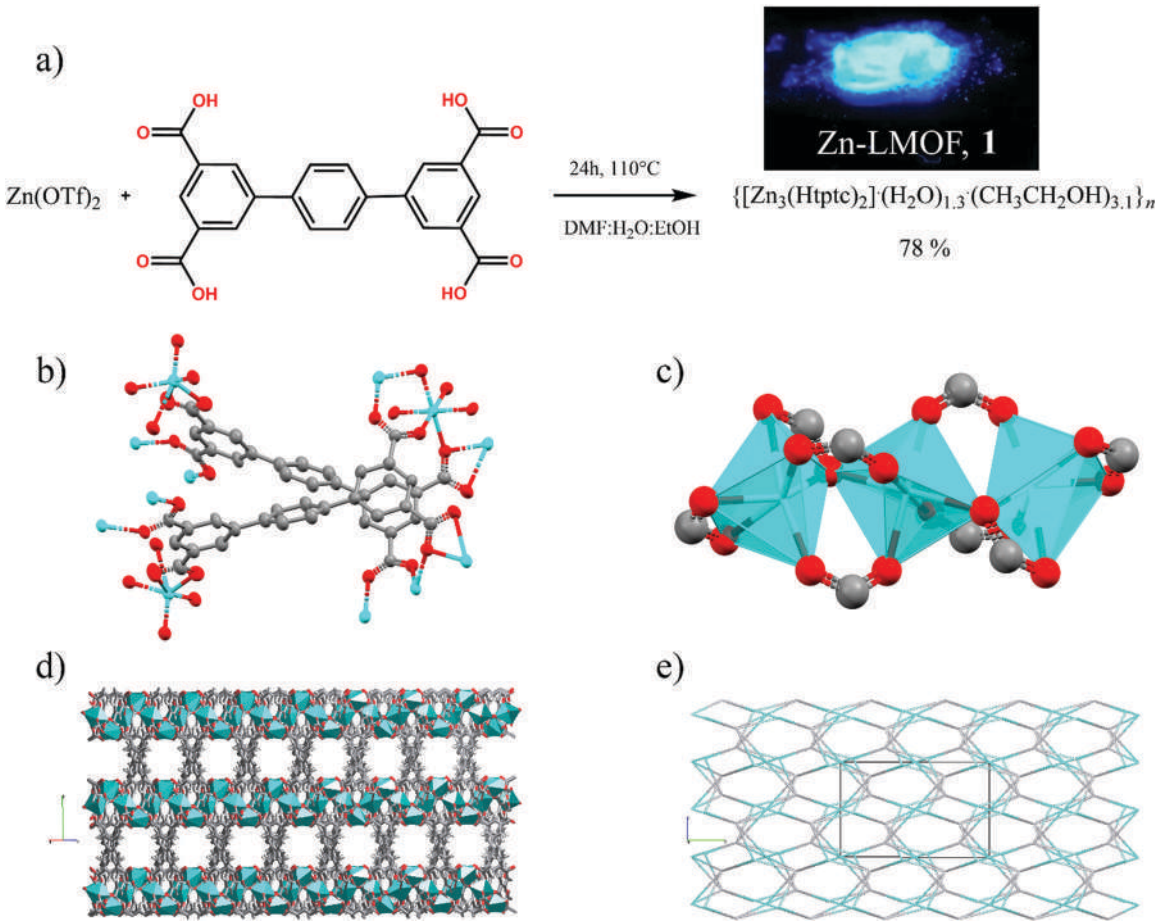

Fig. 2 (a) Synthesis path for **1**. Inset: **1** under irradiation at 365 nm UV illumination. (b) Molecular structure of **1** (hydrogen atoms and lattice molecules are omitted for clarity; ellipsoids shown at 50% probability). (c) Trinuclear SBU of **1**. (d) 3-D framework of **1** (solvent molecules are omitted for clarity). (e) Simplified topology network of **1**.

calculations[64] yield a solvent accessible volume of 33.5% of the total volume; this is, 1886 Å^3 out of 5301.0 Å^3 per unit cell volume. Further studies of voids in **1** were performed using the Mercury software,[65] which provided a representation of the free

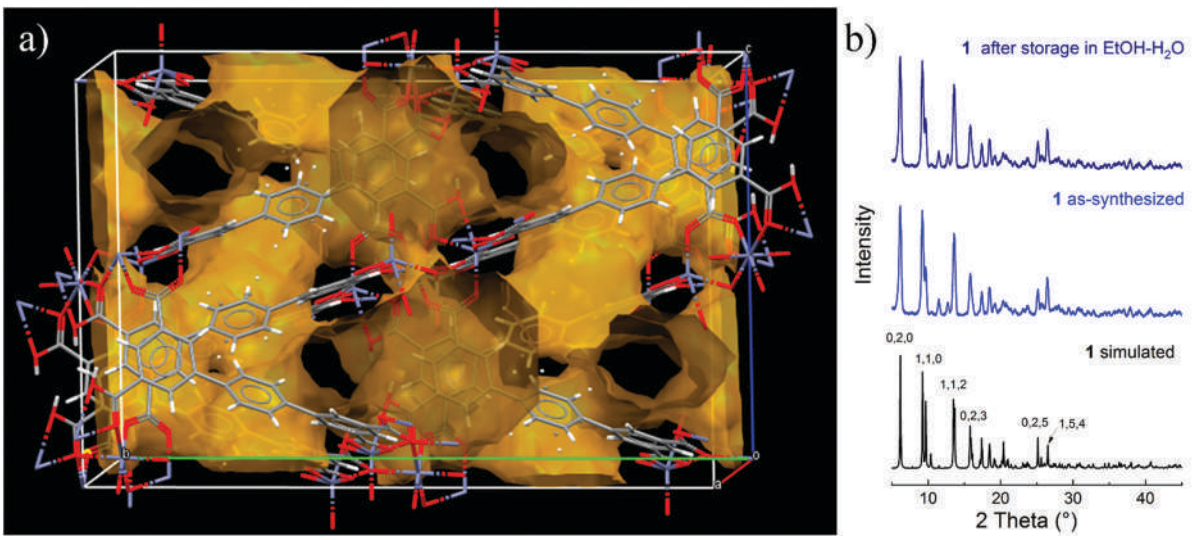

Fig. 3 (a) Depiction of void surfaces for a packing section of **1**. Atom codes: Zn (blue), C (grey), O (red) and H (white). (b) Simulated (bottom) and experimental powder X-ray diffraction patterns of **1** before (middle) and after (top) storage in aqueous media for 24 hours.

volume available in the crystalline structure of **1** (Fig. 3 and Fig. S4, ESI†). The free volume is extended through the array; although the irregular channels seem small, they lead to larger voids that have the peculiarity of having carboxylic oxygen atoms exposed along the walls of these cavities.

Comparison of the experimental powder X-ray diffraction (PXRD) patterns with those calculated from the crystal structure of the as-synthesized **1** match well regarding to positions and the relative intensities of the peaks (Fig. 3B), confirming high phase purity, thus, this sample was used for further experiments.

Elemental analysis (C, N, H) was consistent with the composition of a single crystal of **1**. Next, the chemical stability of **1** in an aqueous medium was carried out by PXRD and IR-ATR. The main diffraction peaks of **1** in the range from 5 to 27° after immersion in an aqueous solution containing 50% ethanol at room temperature for 24 h are in good agreement with the starting compound Zn-LMOF **1** as is depicted in Fig. 3B. The water stability of **1** was also confirmed by FTIR-ATR spectroscopy (Fig. S5, ESI†).

The thermal analyses of **1** were measured in the temperature range from 25 to 450 °C (Fig. S6, ESI†), with a heating rate of 10 °C per min under a N_2 atmosphere. The TGA profile shows a weight loss of a calculated 13.28% during the 120–297 °C interval which can be ascribed to the loss of 3.1 molecules of ethanol and one water molecule. The percentage is congruent with the estimated theoretical expected weight loss from the solvent molecules (13.73%).

The solid-state ^{13}C cross-polarization/magic angle–spinning NMR spectrum of **1** (Fig. S7, ESI†) is consistent with the asymmetric unit of the crystal structure and supports the purity of **1**. The spectrum shows four expected signals for the four crystallographically independent atoms of $-CO_2$ in the range of 170–178 ppm. Similar solid-state ^{13}C-atoms chemical shifts have been observed with Zn-coordination polymers and Zn-MOFs based on benzene-dicarboxylates.[66] The six signals located in the range 138–150 ppm can be ascribed to the $^{13}C_{quaternary}$ atoms[67] and, the intense and broad signals between 128 and 137 ppm can be assigned to aromatic ^{13}CH atoms.[6]

In general, all peaks of the aromatic ^{13}CH atoms are broad and are not fully resolved, which makes their assignment difficult. From the crystal structure of **1**, the central phenyl ring presents a rotational disorder that causes the signals to widen (Fig. S8, ESI†).[67]

Solvent-free form of **1** was successfully obtained by heating at 90 °C under vacuum for 2 h. Comparison of the PXRD patterns of **1** and its solvent-free form is in agreement with regard to both positions and the relative intensities of the peaks indicating good framework stability (Fig. S9, ESI†). This fact is not unexpected due to the structural rigidity of **1** and the weak interaction with solvent molecules observed in its crystal structure.

The TGA curve (Fig. S10, ESI†) shows no obvious weight loss between 25 and 310 °C which confirms the absence of the lattice solvents in **1**.

2.2 Luminescence study and sensing of statins

The luminescence spectra of **1** and free ligand (H_4tptc) in the solid-state were examined at room temperature (Fig. S11, ESI†). Upon excitation at 330 nm, **1** displays an enhanced blue emission peak at 430 nm in comparison to free ligand with an emission peak at 465 nm. This blue emission enhancement ($\approx$34 nm) can be assigned mainly to ligand-centered electronic transitions (IL) perturbed by the coordination of the π-conjugated ligand to the Zn(II) ions.[35] The fluorescence intensity enhancement of **1** can be assigned to the increase of the rigidity of the ligand in the final crystal arrangement, which reduces the loss of energy through non-radiative relaxation processes.[68,69]

On the other hand, aqueous dispersions of **1**, containing 80 vol% ethanol, are blue-emitting mixtures with a maximum at 440 nm (λ_{ex} = 330 nm). The quantum yield (Φ_{PL}) of the aqueous dispersion of **1** is 32.51%, this value is higher compared to the free ligand in ethanol–water ($\Phi_{PL(H4tptc)}$ = 14.25%).[70]

The emission spectra of the ethanol–water dispersions of **1** (20 μM) at pH = 7.0 before and after 24 h show no obvious changes in luminescent intensities compared to the original spectrum, indicating high stability. Thus, those conditions were used for further studies.

Taking the π-electron-rich fragment, porosity, water-stability, and luminescent performance of **1**, into account, we studied its utility as an optical sensor towards statins containing fluorinated π-electron-deficient rings such as ATV and FLV, additionally, other statins lacking those fluorinated aromatic rings were investigated for comparison purposes. To quantitatively sense the calcium salt of ATV, a fluorescent titration experiment was carried in ethanol–water (v/v, 8/2) at neutral pH. As shown in Fig. 4A, an efficient quenching response (87%) of the aqueous dispersion of **1** occurs upon the incremental addition of ATV in a micromolar concentration range. The quenching effect can be quantitatively analyzed by the linear Stern–Volmer (S–V) eqn (1).

$$\frac{I_0}{I} = (1 + K_{SV}[\text{analyte}]) \quad (1)$$

where K_{SV} (M^{-1}) is the quenching constant, I_0 and I are the luminescent intensities before and after the addition of the analyte and [analyte] is the molar concentration of the target species. Fig. 4B shows the S–V plot at 440 nm (λ_{ex} = 330 nm) with increasing ATV concentration up to 35 μM. Notably, there was a linear dependence of the luminescence intensity on the ATV concentration in the range of 0–16 μM (inset, Fig. 4B). This linear data can be well fitted to I_0/I = 0.987 + 142.466[ATV], with a correlation coefficient (R^2 = 0.9963).

In addition, the complete profile at higher concentration shows a clear upward curvature, which is typically observed when static quenching contributes to the effect involving a specific binding between the receptor and the analyte.[71] The profile at high concentrations can be well fitted to the theoretical eqn (2) proposed by Fabbrizzi *et al.*,[72] (Fig. 4B), which considers a simultaneous dynamic and static quenching process when the ground state complexation quenches the emission completely and the receptor–analyte complex practically does not emit.

$$\frac{I_0}{I} = (1 + K_{SV}[\text{analyte}])(1 + K_A[\text{analyte}]) \quad (2)$$

In this expression, K_{SV} and K_A correspond to quenching (dynamic process) and apparent binding (static process)

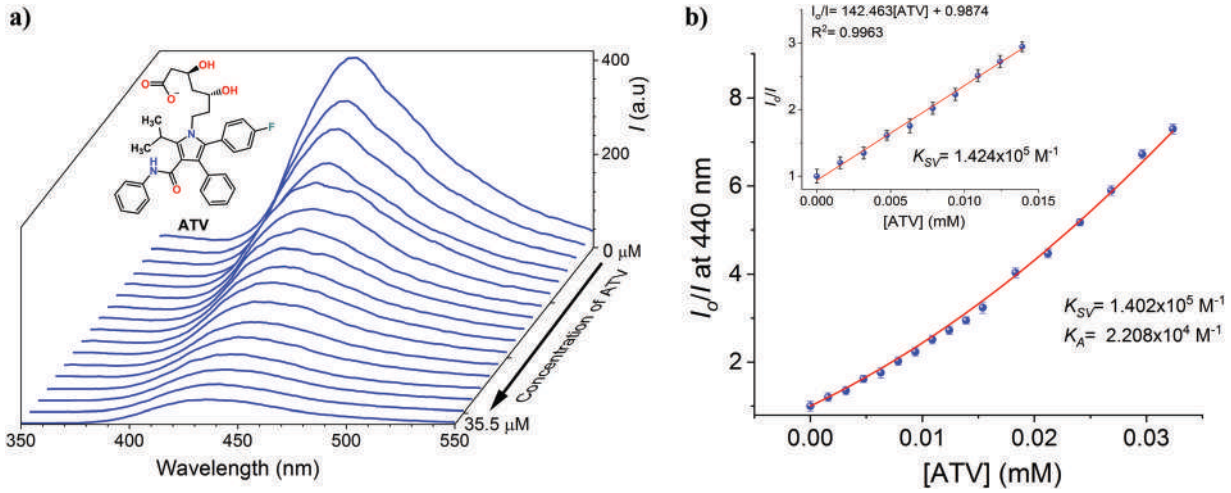

Fig. 4 (a) Emission spectra (λ_{ex} = 330 nm) of **1** dispersed in ethanol–water (v/v, 8/2) at pH = 7.0 upon additions of increasing amounts of ATV calcium. (b) S–V plot at 440 nm, the solid line was obtained by fitting to eqn (2). Inset: Solid line was obtained by fitting to linear S–V eqn (1).

constants, respectively. K_{SV} value of **1** by the addition of ATV is $1.402(\pm0.11) \times 10^5$ M^{-1}. The value of K_{SV} is consistent both in the linear fit at low concentrations ($\leq$16 μM) and, at high concentrations. The apparent binding constant was estimated with a value of $K_A = 2.208(\pm0.13) \times 10^4$ M^{-1}, this finding is interesting because suggests a binding-induced quenching partial process between **1** and ATV.

The detection limit (LOD) of **1** towards ATV was calculated by the equation $3\sigma/S$,[47] where σ is the standard deviation of luminescent intensity of blank for ten times and S is the slope (K_{SV}) of the calibration curve obtained from concentration-dependent luminescence intensity profile at 440 nm (inset: Fig. 4B). LOD was estimated to be 4.21 μM.

As is shown in Table S3 (ESI†), the LOD of **1** is comparable to other recent electrochemical and chromogenic sensors reported in the literature.[42,44,56–60,73,74] Next, the anion selectivity of **1** was analyzed. Salts of an extensive series of anions including FLV, PRV, RSV, inorganic oxyanions, organic (di)carboxylates, citrate and ATP ($[X]_{final}$ = 200 μM) were added to a buffered ethanol–water dispersion of **1**, and the emission intensity at 440 nm was recorded. All oxyanions, carboxylates, PRV, and RSV gave a very low response, Fig. 5A. The addition of FLV resulted in a modest quenching in emission intensity, but it was still significantly lower than that observed for ATV. The quenching fluorescence parameters with FLV were also determined by a titration experiment under the same conditions as in Fig. S12 (ESI†).

The S–V profile of FLV showed also slight upward curvature at high concentrations, the fitting using eqn (2) afforded a quenching constant of 2 orders of magnitude lower than for

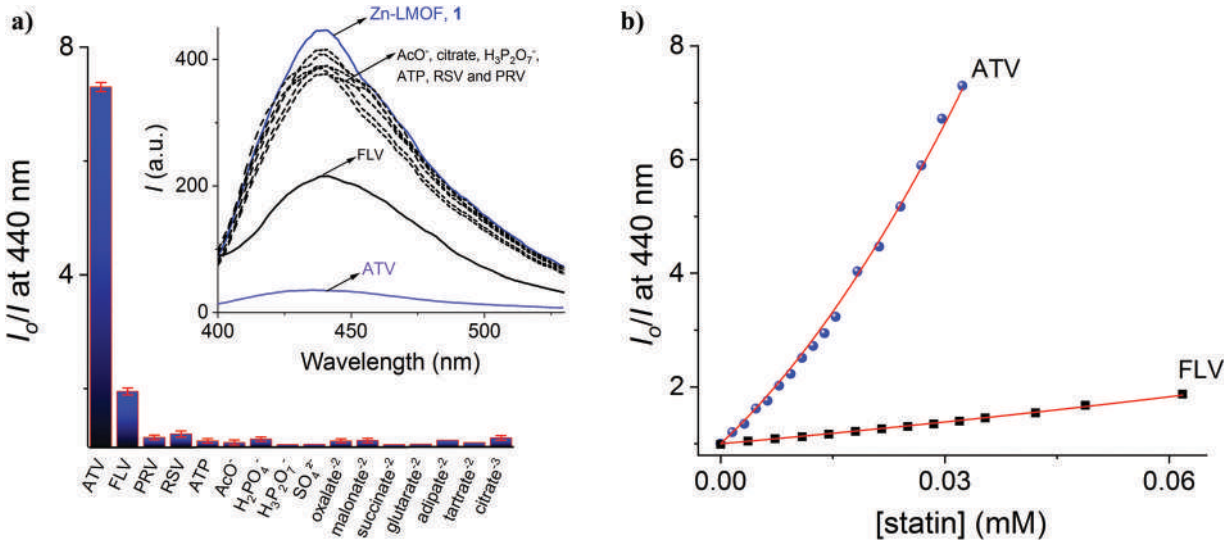

Fig. 5 (a) Relative emission intensities at 440 nm of ethanol–water (v/v, 8/2) dispersion of **1** upon additions of different anions ($[X]_{final}$ = 100 μM). Inset: The corresponding luminescence spectra (λ_{ex} = 330 nm) at 25 °C. In all measurements, the ionic strength was adjusted to 50 mM of NaCl. (b) Profiles of emission titration experiments at 440 nm of **1** by ATV (0–35 μM) and FLV (0–62 μM). The solid lines were obtained by fitting the data to the eqn (2).

ATV (K_{SV}(FLV) = 6.68(±0.08) × 10^3 M^{-1}). The S–V profiles for both statins are shown in Fig. 5B.

2.3 Selective and sensing performance for ATV

For practical applications, luminescent statin-sensors are required to have not only a good optical response but also selectivity in the presence of coexistent potential interferences in physiological samples.[75] Therefore, a selectivity experiment of **1** toward common interfering species in blood plasma and urine, such as D-glucose, creatinine, urea, L-proline, ATP, NaCl, KCl, NH_4Cl, $MgCl_2$, and HCO_3^-, was carried out at neutral pH.

Addition of these species to an aqueous dispersion of **1** induced a negligible change of its emission as shown in Fig. 6A and B. Fig. 6D shows that the quenching response at 440 nm generated by ATV ($I_0/I \approx 7.5$) is not affected by the background ingredients of the common blood plasma and urine demonstrating thus selectivity performance.

As a result, only ATV induces a strong quenching with color change from blue to colorless under UV light (Fig. 6C). This indicates that **1** can act as a visual sensor for recognizing ATV in aqueous media. Undoubtedly **1** can potentially act as a selective luminescent sensor for ATV in presence of interfering species components of urine and blood plasma even in pharmaceutical samples; however, the presence of other components with a blue emission, specifically, in real blood plasma as proteins or tryptophan derivatives could elicit an interference. The reusability of **1** by removal of ATV was investigated. After the detection experiments, **1** was immersed in 10 ml of ethanol–DMF (v/v, 9 : 1) for **1** h at 40 °C. Then, the structural stability and emission properties were monitored by PXRD and fluorescence spectroscopy. In general, the intensity of blue-luminescence of **1** could only be recovered to 94% after the first run and decreased steadily during 4 cycles to 76% (Fig. S13, ESI†) but could still be fully quenched by the addition of ATV ([X] = 100 μM) in each cycle. PXRD pattern of **1** after 4 cycles was practically the same to that of the starting material, indicating that structure was preserved (Fig. S14, ESI†).

2.4 Determination of ATV in pharmaceutical samples

To probe the utility of **1**, we have determined the ATV concentration in pharmaceutical samples. ATV calcium salt extraction and purification from commercial tablets were carried out as described below.[56]

A table of the corresponding pharmaceutical product containing ATV calcium (Eturion 20 or Sortin 20, both from Pfizer) was triturated, and dissolved in warm ethanol. After ultrasonication for 20 min., the resulting mixture was filtered, and effluent was collected. Then, the solvent was evaporated until dryness, obtaining solid white powder corresponding to ATV, which was characterized by FTIR-ATR spectroscopy and used to prepare a stock solution in 50 mL of ethanol. For the luminescent detection, a portion of this stock solution (50 μL) was added to 1950 μL of an ethanol–water (v/v, 8/2) dispersion of **1** (20 μM) containing 50 mM of NaCl and 10 mM MOPS (pH = 7.0), and the emission intensity at 440 nm was recorded (Fig. S15, ESI†). The ATV concentration was then calculated using the fitting equation derived from the S–V plot experiment (Inset Fig. 4B). A comparison between reported and determined ATV concentrations is given in Table 1. The percentage recoveries were obtained ranging from 94.03 to 96.70%, and the relative standard deviations (RSD) were less than 2.3%

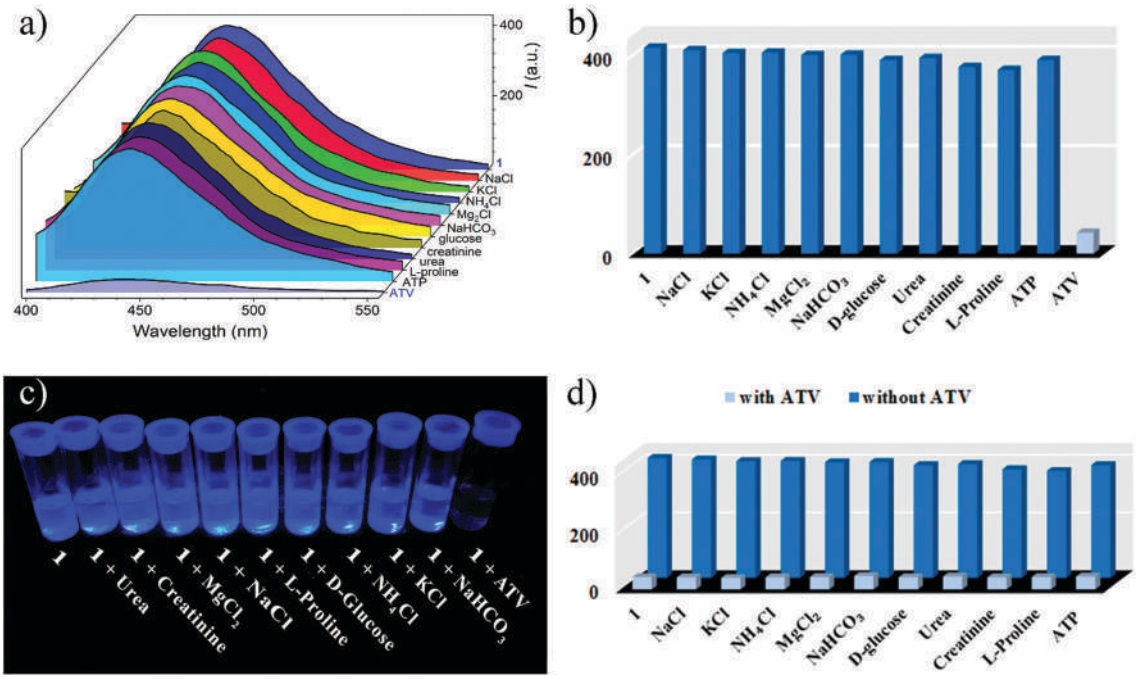

Fig. 6 (a) Luminescence spectra. (b) Intensities at 440 nm of ethanol–water dispersions of **1** at pH = 7.0 with several blood plasma and urine components. (c) The corresponding photographs under UV light at 254 nm. (d) Luminescence responses of **1** towards ATV in the presence of a background of several blood plasma and urine species, 1.0 mM (bottom).

which indicated the proposed sensor could be used to analyze ATV in real pharmaceutical samples. The luminescent method with **1** was validated by an HPLC-UV quantification (Fig. S16, ESI†).

2.5 Recognition mechanism investigation

The recognition mechanism of ATV by **1** was investigated by spectroscopic tools, electron microscopy and DFT calculations. The first evidence of the interaction process was obtained by UV-Vis spectrophotometry measurements. Crystals of **1** (10 mg) were immersed in 20 mL of an ethanolic solution of ATV (100 μM). Then, an aliquot (350 μL) of this solution was added to a cell containing 2500 μL of ethanol and the absorbance was recorded. The amount of this statin in the supernatant was measured using the characteristic absorbance at 247 nm ($\log \varepsilon$ = 4.674) over a period of 7 h. The results are plotted in Fig. 7A and B, these clearly show a continuous decrease of the amount of ATV in the supernatant, and this fact strongly suggests capture or strong interaction process between MOF and the statin. The quantity of recognized/captured ATV at the equilibrium was computed using the following eqn (3).[76]

$$Q_{eq} = \frac{(C_o - C_{eq})V}{m} \quad (3)$$

where Q_{eq} is the amount of ATV captured by **1**, (expressed in mmol g^{-1}), C_0 is the initial concentration of ATV (in mmol L^{-1}), C_{eq} (mmol L^{-1}) is the concentration of ATV at the equilibrium, V (L) is the volume of ATV solution and m is the mass of crystals that we soaked (given in grams). By calculations the value of Q_{eq} for recognized/captured ATV was 0.193 mmol g^{-1}.

Next, FTIR-ATR spectrum and PXRD pattern of **1** soaked in a water-ethanol concentrated solution of ATV for 24 h were recorded. IR spectrum and the PXRD pattern of **1** treated with ATV were very similar to that of the starting material, indicating that the Zn-LMOF structure was preserved (Fig. S17 and S18, ESI†). Therefore, the luminescence quenching is not due to the structural decomposition of **1**.

To study the fluorescence quenching process, the fluorescence lifetimes of **1** before and after the addition of concentrate solution of ATV were measured. An ethanol–water dispersion of **1** upon excitation with a 354 nm laser displayed a biexponential decay with values of τ_1 = 7.80 and τ_2 = 1.46 μs (Fig. 7B). Similar photophysical properties and values of luminescence lifetime have been previously reported for a structurally related MOF, $[Zn_2(tptc)(apy)_2(H_2O)_x]\cdot H_2O$ (apy = aminopyridine) where the microsecond time-scale luminescence is mainly attributed to singlet and triplet states from the organic linker tptc.[32]

The lifetime of **1** after the addition of a concentrated solution of ATV has a negligible change, in comparison with original aqueous suspension, confirming that a static quenching is dominant in the quenching mechanism.[77]

SEM images of **1** are shown in Fig. S19A (ESI†), a crystalline material with well-defined facets, edges and ends can be observed, higher magnification micrographs revels flower-like morphology formed from crystals assembly of individual MOF's.

In contrast, **1** after the contact with ATV is evident that the morphology is altered, from triangular prisms to rough material, formed with scales and agglomerates of different sizes, as can be observed in Fig. S19B of the ESI.†

Fig. 7C and D show the EDS elemental chemical mapping of **1** before and after contact with ATV, respectively. Zn signals with a homogeneous distribution are observed in the as-synthesized **1**, as it expected for this compound (Fig. 7C). The presence of F and N signals in the EDS maps of Fig. 7D can be associated with the absorption of the ATV, which is evenly distributed along all the MOF structure. From this analysis is evident that the Zn-LMOF-based sensor interacts homogeneously with the ATV inducing a change in the morphology of the original material. To gain further insight into the interaction mode and selectivity of **1** towards ATV, density functional theory calculations were carried out using the Gaussian 16 suite programs[78] at the CAM-B3LYP/cc-pVDZ level of theory with a simulated solvent (acetonitrile) under the SMD continuum model.

The interaction energy, Eint, was calculated with the NBO Deletion (NBODel) formalism using the NBO3.1 program[79] as provided within the aforementioned suite.

A representative section of the MOF that includes the asymmetric unit of the crystal (Fig. S20, ESI†) was selected to calculate their interaction with the analyte. The hydrogen atoms of the **1** section were optimized at the DFT level of theory mentioned above and the analyte was docked onto it manually and later was fully optimized at the same DFT level to allow for the analyte to freely move around the MOF section.

4-Fluorophenyl and phenyl rings substituted at positions 2 and 3 of the pyrrole moiety respectively (see Fig. 1 for the numbering of the structure) interact strongly with the central phenyl ring of terphenyl ligand from **1** section.

A large interaction energy of 111.04 kcal mol^{-1} between atorvastatin and the selected portion of the MOF as shown in Fig. 8A, was obtained with the NBODel method.

However, given the fact that both HOMO and LUMO reside on the Zn carboxylate moiety of the MOF section, this large value stems mainly from electrostatic interactions π-type stacking between the aromatic rings (Fig. 8B and C).

Table 1 Results of the luminescent sensing method of ATV calcium in pharmaceutical samples using **1** and HPLC-UV method

Sample	ATV labeled (mg per table)	ATV found by luminescence using **1**[a] (mg per tablet)	Recovery (%) ± RSD (%)	ATV found by HPLC-UV method
Eturion 20	20.00	18.86	94.03 ± 2.3	18.98
Sortis 20	20.00	19.34	96.70 ± 1.5	19.17

[a] Average of three measurements.

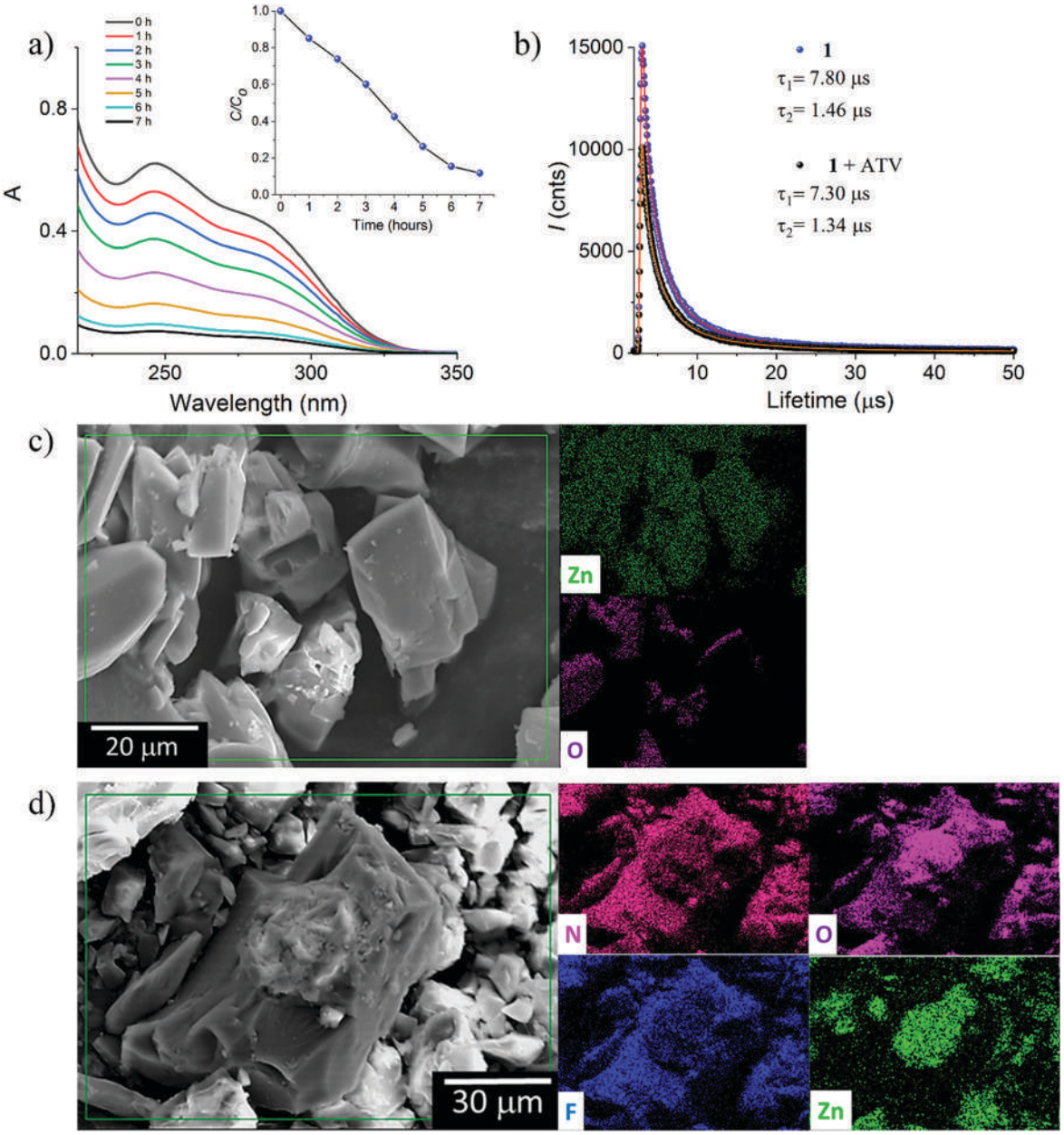

Fig. 7 (a) Temporal evolution of UV-Vis spectra of ATV in the presence of crystals of **1** in ethanol. Inset: Concentration changes of ATV in ethanol with increasing time. (b) Fluorescence decay profiles of **1** in neutral ethanol–water dispersion before and after the addition of ATV (λ_{ex} = 354 nm). (c) SEM images of the as-synthesized **1**. (d) **1** treated with ATV showing EDS mapping elements O and Zn before and O, Zn, F and N signals after the contact with ATV solution.

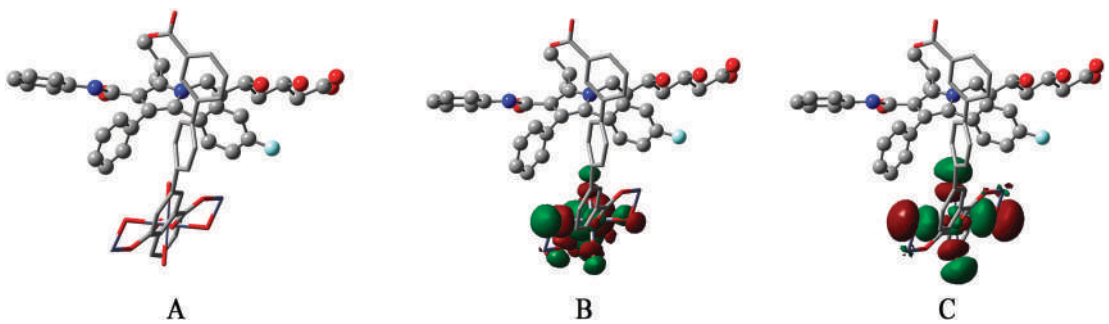

Fig. 8 (a) Interacting fragments for all calculations (ATV ball&stick style; **1** section tube style), isosurfaces for frontier orbitals: (b) HOMO and (c) LUMO.

It is known that aromatic rings with electron deficiency have a strong luminous quenching ability when are bound to LMOFs through a photoinduced electron transfer (PET) process.[80,81]

Thus, a static-complexation PET mechanism possibly in both the excited and the ground state could explain the efficient quenching process of **1** by ATV. Finally, the HOMO–LUMO gap for the interacting fragments was estimated with a value of 3.2 eV.

3. Conclusions

In conclusion, we have reported for the first time the selective and sensitive aqueous-phase detection of atorvastatin using MOF-based system. The porous nature, hydrolytic stability, and luminescent properties of Zn-MOF, **1** based on the π-electron-rich terphenyl-3,3″,5,5″-tetracarboxylic acid ligand have been utilized for designing a chemosensor that selectively detects atorvastatin at the micromolar concentration range in aqueous media at pH = 7.0.

Under these conditions, the addition of atorvastatin calcium exhibits a rapid and high luminescence quenching effect (K_{SV} = 1.402 × 10^5 M^{-1}) without the interference by other common anions such as dicarboxylates, oxyanions, and ATP, even in the presence of coexisting species in plasma and urine. The detection limit was estimated to be 4.21 μM.

Based on the crystal structure of **1**, spectroscopic titrations, lifetime measurements, SEM-EDS analysis, and DFT calculations the quenching process can be explained by a π-stacking PET-static quenching possibly in both the excited and the ground state.

Moreover, the Zn-MOF **1** can be used as an efficient luminescent sensor for the practical detection of atorvastatin in commercial pharmaceutical tablets.

Overall, these results highlight further the utility of luminescent metal–organic frameworks for sensing globally used drugs with potential application in real samples.

4. Experimental section

General considerations

Chemicals, solvents, and instrumentations are listed in the ESI.† Synthesis of $\{[Zn_3(tptc)_2]\cdot(H_2O)_{1.3}\cdot(CH_3CH_2OH)_{3.1}\}_n$, **1**. A mixture of [1,1′:4′,1″]terphenyl-3,3″,5,5″-tetracarboxylic acid (50 mg, 0.123 mmol) and $Zn(OTf)_2$ (89.46 mg, 0.246 mmol) in DMF : H_2O : EtOH (10 : 2 : 2 mL) was put into a 25 mL Teflon-lined stainless steel reactor. The reaction mixture was heated at 110 °C for 24 h, and slowly cooled to room temperature. The crystalline product of **1** was separated out by filtration, washed thoroughly with DMF/Ethanol and dried in vacuum at room temperature. Colorless crystals were obtained in 78% yield based on $Zn(OTf)_2$.

Anal. calcd for $\{[Zn_3(Htptc)_2]\cdot(H_2O)_{1.3}\cdot(CH_3CH_2OH)_{3.1}\}_n$, **1** $C_{50.21}H_{43.24}O_{20.41}Zn_3$ C, 51.57; H, 3.72; N, 0.0. Found: C: 51.38; H, 3.85, N, 0.0.

Crystallographic investigations. The crystallographic data and refinement details for **1** are summarized in Table S1 (ESI†). Selected bond lengths and angles for **1** are listed in Table S2 (ESI†). Data were collected on a Bruker APEX II CCD diffractometer at 100 K; using Mo-K_α radiation (k = 0.71073 Å) from an Incoatec ImuS source and a Helios optic monochromator.[82] Suitable crystals were coated with hydrocarbon oil, picked up with a nylon loop, and mounted in the cold nitrogen stream of the diffractometer.

The structures were solved using intrinsic phasing (SHELXT) and refined by full-matrix least-squares on $F2$ using the ShelXle GUI.[83,84] The hydrogen atoms of the C–H bonds were placed in idealized positions.

The compound **1** crystalized as non-merohedral twin with 2 domains and BASF parameter 0.14517, the hklf4 format file was used to do the solventless refinement and use the ZQUEEZE/PLATON tool while the file with hlkf5 format was used to refine the proportion of solvent inside the crystal obtaining 3.10 of ethanol, 1.30 of water per unit of $C_{44}H_{22}O_{16}Zn_3$ as well as to obtain the proportion of the two domains of the twin.

CCDC 2116896 contains the supplementary crystallographic data for this paper.†.

Luminescence measurements. Luminescence spectra for solid-state and aqueous dispersions of **1** were recorded on an Agilent Cary Eclipse spectrophotometer equipped with a crystal-holder and a cell thermostated holder with a quartz cuvette, respectively. The as-synthesized **1** was dispersed (1 mg mL^{-1}) into a mixture ethanol/double distilled water (v/v 8/2), and this mixture was stirring for 20 min at 25 °C. Fluorimetric titration experiments were carried out by adding aliquots of stock solutions of statins (10 mM) to the buffered ethanol/water (v/v, 8/2) dispersions of **1** (20 μM, pH = 7.0, 10 mM MOPS). After the addition of statins, the dispersion was equilibrated for 3 min before recording the emission spectrum (λ_{ex} = 330 nm) using a quartz cuvette. Luminescence quantum yields were determined using an aqueous solution of quinine sulfate containing H_2SO_4 (0.5 M) as a standard (Φ = 0.546; excited at 360 nm). For the determination of the quantum yield, the excitation wavelength was chosen so that $A < 0.05$.[70]

Fluorescence lifetime measurements. A custom-built Fluorescence Lifetime Imaging Microscope system was used to acquire the fluorescence lifetimes. A 354 nm picosecond laser pulsed at 10 MHz (LDH-P-FA-355, PicoQuant) was focused with a 0.40 NA reflective objective (LMM-40X-UVV-160, ThorLabs) into a 1.0 cm quartz cell containing the dispersion of **1** or directly on the crystalline sample in case of measurements in solid-state. The epifluorescence passed through a 425 nm long-pass dichroic mirror (Chroma T425lpxr-UF2), a 405 nm notch filter (Chroma ZET405nf), a 425 nm long pass emission filter (Chroma ET425lp) and was focused to single photon avalanche photodiode (PD-050-CTE, MPD). The laser controller (PDL-800-D, PicoQuant) and the detector were connected to a TCSPC card (PicoHarp 300, PicoQuant). The intensity of irradiation was set to obtain less than 1% of detection events.

Back-scattered light from a mirror was used to obtain the IRF under the same conditions of irradiation. All data were obtained and treated in SymphoTime 64 software (PicoQuant). The lifetime data were fitted by bi-exponential decay functions.

SEM-EDS. Morphological changes of **1** before and after the contact with ethanolic solution of atorvastatin calcium were evaluated by Scanning Electron Microscopy (SEM) on a JSM-6510LV microscope from JEOL using the secondary electron detector. For sample preparation, the specimen was dried under room conditions and fixed on aluminum stubs with conductive double-stick tape and then coated with gold under vacuum using a Denton IV sputtering chamber. Elemental chemical distribution analysis was performed with an energy-dispersive X-ray spectroscope QUANTAX 200 from Bruker attached to SEM.

Conflicts of interest

There are no conflicts to declare.

Acknowledgements

We thank Chem. María A. Peña González, Chem. María de la Paz Orta Pérez, MSc Elizabeth Huerta Salazar, MSc Lucia del Carmen Márquez Alonso, PhD Adriana Romo Perez, PhD Beatriz Quiroz-García, and MSc Elizabeth Huerta Salazar for technical assistance. We thank PAPIIT-UNAM-216220 for financial support. L. D. R.-V and J. V.-G. are grateful to CONACyT for scholarships 713164 and 848787, respectively. J. M. G.-A. thanks to the financial support granted by PAPIIT-DGAPA IT200920 from the National Autonomous University of Mexico.

Notes and references

1 J. Dong, D. Zhao, Y. Lu and W. Y. Sun, *J. Mater. Chem. A*, 2019, **7**, 22744–22767.
2 M. O'Keeffe and O. M. Yaghi, *Chem. Rev.*, 2012, **112**, 675–702.
3 M. D. Allendorf, C. A. Bauer, R. K. Bhakta and R. J. T. Houk, *Chem. Soc. Rev.*, 2009, **38**, 1330–1352.
4 P. Raja Lakshmi, P. Nanjan, S. Kannan and S. Shanmugaraju, *Coord. Chem. Rev.*, 2021, **435**, 213793.
5 L. E. Kreno, K. Leong, O. K. Farha, M. Allendorf, R. P. Van Duyne and J. T. Hupp, *Chem. Rev.*, 2012, **112**, 1105–1125.
6 J. Heine and K. Müller-Buschbaum, *Chem. Soc. Rev.*, 2013, **42**, 9232–9242.
7 Y. Liu, X. Y. Xie, C. Cheng, Z. S. Shao and H. S. Wang, *J. Mater. Chem. C*, 2019, **7**, 10743–10763.
8 M. Huangfu, M. Wang, C. Lin, J. Wang and P. Wu, *Dalton Trans.*, 2021, **50**, 3429–3449.
9 H. Deng, S. Grunder, K. E. Cordova, C. Valente, H. Furukawa, M. Hmadeh, F. Gándara, A. C. Whalley, Z. Liu, S. Asahina, H. Kazumori, M. O'Keeffe, O. Terasaki, J. F. Stoddart and O. M. Yaghi, *Science*, 2012, **336**, 1018–1023.
10 X. Zhang, W. Wang, Z. Hu, G. Wang and K. Uvdal, *Coord. Chem. Rev.*, 2015, **284**, 206–235.
11 Y. Cui, Y. Yue, G. Qian and B. Chen, *Chem. Rev.*, 2012, **112**, 1126–1162.
12 H. Wu, M. Li, C. Sun, X. Wang and Z. Su, *Dalton Trans.*, 2020, **49**, 5087–5091.
13 N. Zhang, D. Zhang, J. Zhao and Z. Xia, *Dalton Trans.*, 2019, **48**, 6794–6799.
14 X. Y. Wan, F. L. Jiang, L. Chen, J. Pan, K. Zhou, K. Z. Su, J. D. Pang, G. X. Lyu and M. C. Hong, *CrystEngComm*, 2015, **17**, 3829–3837.
15 J. Li, S. Chen, L. Jiang, D. Wu and Y. Li, *Inorg. Chem.*, 2019, **58**, 5410–5413.
16 L. Li, H. Xue, Y. Wang, P. Zhao, D. Zhu, M. Jiang and X. Zhao, *ACS Appl. Mater. Interfaces*, 2015, **7**, 25402–25412.
17 D. Asnaghi, R. Corso, P. Larpent, I. Bassanetti, A. Jouaiti, N. Kyritsakas, A. Comotti, P. Sozzani and M. W. Hosseini, *Chem. Commun.*, 2017, **53**, 5740–5743.
18 X. Zhang, Z. Zhang, J. Boissonnault and S. M. Cohen, *Chem. Commun.*, 2016, **52**, 8585–8588.
19 D. De, T. K. Pal, S. Neogi, S. Senthilkumar, D. Das, S. Sen Gupta and P. K. Bharadwaj, *Chem. – Eur. J.*, 2016, **22**, 3387–3396.
20 X. C. Lu, H. L. Wang, X. Wang, Q. Z. Li and L. Liao, *J. Clust. Sci.*, 2019, **30**, 1673–1681.
21 R. Haldar, R. Matsuda, S. Kitagawa, S. J. George and T. K. Maji, *Angew. Chem., Int. Ed.*, 2014, **53**, 11772–11777.
22 Y. Shu, Q. Ye, T. Dai, Q. Xu and X. Hu, *ACS Sens.*, 2021, **6**, 641–658.
23 W. P. Lustig, S. Mukherjee, N. D. Rudd, A. V. Desai, J. Li and S. K. Ghosh, *Chem. Soc. Rev.*, 2017, **46**, 3242–3285.
24 K. Müller-Buschbaum, F. Beuerle and C. Feldmann, *Microporous Mesoporous Mater.*, 2014, **216**, 171–199.
25 M.-L. Hu, S. A. A. Razavi, M. Piroozzadeh and A. Morsali, *Inorg. Chem. Front.*, 2020, **7**, 1598–1632.
26 M. Pamei and A. Puzari, *Nano-Struct. Nano-Objects*, 2019, **19**, 100364.
27 P. Kumar, K. H. Kim, V. Bansal, A. K. Paul and A. Deep, *Microchem. J.*, 2016, **128**, 102–107.
28 B. Yan, *J. Mater. Chem. C*, 2019, **7**, 8155–8175.
29 Z. Xiao, Y. Wang, S. Zhang, W. Fan, X. Xin, X. Pan, L. Zhang and D. Sun, *Cryst. Growth Des.*, 2017, **17**, 4084–4089.
30 J. C. Jin, J. Wu, Y. X. He, B. H. Li, J. Q. Liu, R. Prasad, A. Kumar and S. R. Batten, *CrystEngComm*, 2017, **19**, 6464–6472.
31 E. Zhang, P. Ju, Z. Zhang, H. Yang, L. Tang, X. Hou, J. You and J. J. Wang, *Spectrochim. Acta, Part A*, 2019, **222**, 117207.
32 R. X. Yao, X. Cui, X. X. Jia, F. Q. Zhang and X. M. Zhang, *Inorg. Chem.*, 2016, **55**, 9270–9275.
33 X. Y. Wan, F. L. Jiang, C. P. Liu, K. Zhou, L. Chen, Y. L. Gai, Y. Yang and M. C. Hong, *J. Mater. Chem. A*, 2015, **3**, 22369–22376.
34 J. Liu, J. Wu, Z. Luo, B. Li, A. Singh and K. Abhinav, *J. Coord. Chem.*, 2017, **70**, 3946–3958.
35 J. Yang, L. Zhang, X. Wang, R. Wang, F. Dai and D. Sun, *RSC Adv.*, 2015, **5**, 62982–62988.
36 X. Xu, Y. Guo, X. Wang, W. Li, P. Qi, Z. Wang, X. Wang, S. Gunasekaran and Q. Wang, *Sens. Actuators, B*, 2018, **260**, 339–345.
37 L. D. Rosales-Vázquez, A. Dorazco-González and V. Sánchez-Mendieta, *Dalton Trans.*, 2021, **50**, 4470–4485.

38 H. Sirén and J. Pharmacol, *Clin. Toxicol.*, 2017, **5**, 1092.
39 M. Patel and C. Kothari, *TrAC, Trend Anal. Chem.*, 2017, **86**, 206–221.
40 R. M. Calderon, L. X. Cubeddu, R. B. Goldberg and E. R. Schiff, *Mayo Clin. Proc.*, 2010, **85**, 349–356.
41 L. Cai, Z. Zheng, X. Wang, L. Tang, L. Mai, G. He, H. Lei and S. Zhong, *Anal. Methods*, 2017, **9**, 1038–1045.
42 A. Tavousi, E. Ahmadi, L. Mohammadi-Behzad, V. Riahifar and F. Maghemi, *Microchem. J.*, 2020, **158**, 105159.
43 T. A. Silva, H. Zanin, F. C. Vicentini, E. J. Corat and O. Fatibello-Filho, *Sens. Actuators, B*, 2015, **218**, 51–59.
44 Z. Kamalzadeh and S. Shahrokhian, *Bioelectrochemistry*, 2014, **98**, 1–10.
45 S. Altinöz and B. Uyar, *Anal. Methods*, 2013, **5**, 5709–5716.
46 S. Mazurek and R. Szostak, *J. Pharm. Biomed.*, 2009, **49**, 168–172.
47 J. J. M. Nasr, N. H. Al-Shaalan and S. M. Shalan, *Spectrochim. Acta, Part A*, 2020, **237**, 118332.
48 D. Skorda and C. G. Kontoyannis, *Talanta*, 2008, **74**, 1066–1070.
49 H. W. Darwish, S. A. Hassan, M. Y. Salem and B. A. El-Zeany, *Spectrochim. Acta, Part A*, 2013, **104**, 70–76.
50 L. Nováková, D. Šatínský and P. Solich, *TrAC, Trend Anal. Chem.*, 2008, **27**, 352–367.
51 S. N. Ortega, A. J. Santos-Neto and F. M. Lancas, *Anal. Methods*, 2017, **9**, 3039–3048.
52 V. Sree Janardhanan, R. Manavalan and K. Valliappan, *Arab. J. Chem.*, 2016, **9**, S1378–S1387.
53 A. L. Assassi, C. E. Roy, P. Perovitch, J. Auzerie, T. Hamon and K. Gaudin, *J. Chromatogr. A*, 2015, **1380**, 104–111.
54 N. Sultana, M. S. Arayne, N. Shafi, F. A. Siddiqui and A. Hussain, *Anal. Methods*, 2010, **2**, 1571–1576.
55 X. S. Miao and C. D. Metcalfe, *J. Chromatogr. A*, 2003, **998**, 133–141.
56 R. O. Gunache (Rosca), A. V. Bounegru and C. Apetrei, *Inventions*, 2021, **6**, 57.
57 T. A. Silva, H. Zanin, F. C. Vicentini, E. J. Corat and O. Fatibello-Filho, *Analyst*, 2014, **139**, 2832–2841.
58 S. D. Bukkitgar, N. P. Shetti and R. M. Kulkarni, *Sens. Actuators, B*, 2018, **255**, 1462–1470.
59 S. Ashour, M. Bahbouh and M. Khateeb, *Spectrochim. Acta, Part A*, 2011, **78**, 913–917.
60 J. C. Abbar and S. T. Nandibewoor, *Colloids Surf., B*, 2013, **106**, 158–164.
61 J. Peng, H. Tian, Q. Du, X. Hui and H. He, *Microchim. Acta*, 2018, **185**, 1–9.
62 J. M. Serrano-Becerra, S. Hernández-Ortega, D. Morales-Morales and J. Valdés-Martínez, *CrystEngComm*, 2009, **11**, 226–228.
63 V. A. Blatov, A. P. Shevchenko and D. M. Proserpio, *Cryst. Growth Des.*, 2014, **14**, 3576–3586.
64 A. L. Spek, *Acta Crystallogr., Sect. D: Struct. Biol.*, 2009, **65**, 148–155.
65 C. F. Macrae, I. J. Bruno, J. A. Chisholm, P. R. Edgington, P. McCabe, E. Pidcock, L. Rodriguez-Monge, R. Taylor, J. Van De Streek and P. A. Wood, *J. Appl. Crystallogr.*, 2008, **41**, 466–470.
66 H. A. Habib, A. Hoffmann and C. Janiak, *Dalton Trans.*, 2009, 1742–1751.
67 H. C. Hoffmann, M. Debowski, P. Müller, S. Paasch, I. Senkovska, S. Kaskel and E. Brunner, *Materials*, 2012, **5**, 2537–2572.
68 X. Wang, C. Qin, E. Wang, Y. Li, N. Hao, C. Hu and L. Xu, *Inorg. Chem.*, 2004, **43**, 1850–1856.
69 L. D. Rosales-Vázquez, J. Valdes-García, I. J. Bazany-Rodríguez, J. M. Germán-Acacio, D. Martínez-Otero, A. R. Vilchis-Néstor, R. Morales-Luckie, V. Sánchez-Mendieta and A. Dorazco-González, *Dalton Trans.*, 2019, **48**, 12407–12420.
70 J. Carlos Rendón-Balboa, L. Villanueva-Sánchez, L. David Rosales-Vázquez, J. Valdes-García, A. R. Vilchis-Nestor, D. Martínez-Otero, S. Martínez-Vargas and A. Dorazco-González, *Inorg. Chim. Acta*, 2018, **483**, 235–240.
71 M. K. Salomón-Flores, C. L. Hernández-Juárez, I. J. Bazany-Rodríguez, J. Barroso-Flores, D. Martínez-Otero, R. López-Arteaga, J. Valdés-Martínez and A. Dorazco-González, *Sens. Actuators, B*, 2019, **281**, 462–470.
72 V. Amendola, L. Fabbrizzi and E. Monzani, *Chem. – Eur. J.*, 2004, **10**, 76–82.
73 O. Fazlolahzadeh, A. Rouhollahi and M. Hadi, *Anal. Bioanal. Electrochem.*, 2016, **8**, 566–577.
74 B. Dogan-Topal, B. Uslu and A. S. Ozkan, *Comb. Chem. High Throughput Screen.*, 2007, **10**, 571–582.
75 I. J. Bazany-Rodríguez, M. K. Salomón-Flores, J. M. Bautista-Renedo, N. González-Rivas and A. Dorazco-González, *Inorg. Chem.*, 2020, **59**, 7739–7751.
76 L. L. Lv, J. Yang, H. M. Zhang, Y. Y. Liu and J. F. Ma, *Inorg. Chem.*, 2015, **54**, 1744–1755.
77 J. R. Lakowicz, *Principles of fluorescence spectroscopy*, 2nd edn, Plenum Press, New York, 1999.
78 M. J. Frisch, G. W. Trucks, H. B. Schlegel, G. E. Scuseria, M. A. Robb, J. R. Cheeseman, G. Scalmani, V. Barone, G. A. Petersson, H. Nakatsuji, X. Li, M. Caricato, A. V. Marenich, J. Bloino, B. G. Janesko, R. Gomperts, B. Mennucci, H. P. Hratchian, J. V. Ortiz, A. F. Izmaylov, J. L. Sonnenberg, D. Williams-Young, F. Ding, F. Lipparini, F. Egidi, J. Goings, B. Peng, A. Petrone, T. Henderson, D. Ranasinghe, V. G. Zakrzewski, J. Gao, N. Rega, G. Zheng, W. Liang, M. Hada, M. Ehara, K. Toyota, R. Fukuda, J. Hasegawa, M. Ishida, T. Nakajima, Y. Honda, O. Kitao, H. Nakai, T. Vreven, K. Throssell, J. A. Montgomery Jr., J. E. Peralta, F. Ogliaro, M. J. Bearpark, J. J. Heyd, E. N. Brothers, K. N. Kudin, V. N. Staroverov, T. A. Keith, R. Kobayashi, J. Normand, K. Raghavachari, A. P. Rendell, J. C. Burant, S. S. Iyengar, J. Tomasi, M. Cossi, J. M. Millam, M. Klene, C. Adamo, R. Cammi, J. W. Ochterski, R. L. Martin, K. Morokuma, O. Farkas, J. B. Foresman and D. J. Fox, *Gaussian 16, Revision C.01*, Gaussian, Inc., Wallingford CT, 2016.
79 E. D. Glendening, A. E. Reed, J. E. Carpenter and F. Weinhold, *NBO Version 3.1*.
80 W. Liu, C. Chen, Z. Wu, Y. Pan, C. H. Ye, Z. Mu, X. Luo, W. Chen and W. Liu, *ACS Sustainable Chem. Eng.*, 2020, **8**, 13497–13506.

81 A. P. de Silva, H. Q. N. Gunaratne, T. Gunnlaugsson, A. J. M. Huxley, C. P. McCoy, J. T. Rademacher and T. E. Rice, *Chem. Rev.*, 1997, **97**, 1515–1566.
82 *APEX 2 Softw. Suite*, Bruker AXS Inc., Madison, Wisconsin, USA, 2004.
83 C. B. Hübschle, G. M. Sheldrick and B. Dittrich, *J. Appl. Crystallogr.*, 2011, **44**, 1281–1284.
84 G. M. Sheldrick, *SHELXL-97, Progr. Cryst. Struct. Refinement*, Univ. Göttingen, Germany, 1997.

Dalton Transactions

ROYAL SOCIETY OF CHEMISTRY

FRONTIER

View Article Online
View Journal | View Issue

Cite this: *Dalton Trans.*, 2021, **50**, 4470

Efficient chemosensors for toxic pollutants based on photoluminescent Zn(II) and Cd(II) metal–organic networks

Luis D. Rosales-Vázquez, [a] Alejandro Dorazco-González *[a] and Victor Sánchez-Mendieta *[b]

Optical sensors with high sensitivity and selectivity, as important analytical tools for chemical and environmental research, can be realized by straightforward synthesis of luminescent one-, two- and three-dimensional Zn(II) and Cd(II) crystalline coordination arrays (CPs and MOFs). In these materials with emission centers typically based on charge transfer and intraligand emissions, the quantitative detection of specific analytes, as pesticides or anions, is probed by monitoring real-time changes in their photoluminescence and color emission properties. Pesticides/herbicides have extensive uses in agriculture and household applications. Also, a large amount of metal salts of cyanide is widely used in several industrial processes such as mining and plastic manufacturing. Acute or chronic exposure to these compounds can produce high levels of toxicity in humans, animals and plants. Due to environmental concerns associated with the accumulation of these noxious species in food products and water supplies, there is an urgent and growing need to develop direct, fast, accurate and low-cost sensing methodologies. In this critical frontier, we discuss the effective strategies, chemical stability, luminescence properties, sensitivity and selectivity of recently developed hybrid Zn(II)/Cd(II)–organic materials with analytical applications in the direct sensing of pesticides, herbicides and cyanide ions in the aqueous phase and organic solvents.

Received 29th December 2020,
Accepted 1st March 2021

DOI: 10.1039/d0dt04403b

rsc.li/dalton

Introduction

Coordination polymers (CPs) have attracted the attention of the scientific community for several decades.[1–3] Originally from the structural–property relationship point of view, and more recently, from the perspective of developing novel applications, CPs have risen in the past twenty-five years as one of the top functional materials to be studied, MOFs being the superstars.[4–7] The relatively easy chemical structural tuning of CPs, based on archetypal coordination chemistry, allowed the appearance, development and enhancement of their properties such as magnetism,[8] catalysis,[9] adsorption[10] and separation,[11] and luminescence;[12] it is the main reason for the increasing relevance of these interesting compounds. CPs having d-block metal ions are amongst the most prolific hybrid materials, including those containing Zn(II) and Cd(II) as metal centres, which are usually assembled using di-, tri-and tetra-carboxylate compounds or/and nitrogen compounds as bridging ligands.[13–15] These CPs are commonly exposed in a fascinating structural diversity due to their inherent metal-linker joining in the current and on-going, well-documented, secondary building units (SBUs).[16,17] Regardless of the substantial number of Zn and Cd based coordination frameworks structurally characterized, thorough studies in relation to their fluorescence properties, and their use as chemosensors for diverse analytes, remain an open challenge.[18,19] Hence, growing interest in their applications towards the recognition and detection of environmental hazardous species has been reflected in freshly day-to-day emerging literature and, consequently, in cutting-edge and excellent reviews.[4,19–21] Special attention in this line has been focused on toxic compounds, such as energetic materials (explosives), cations and anions.[4,19,20] Even though the detection of those compounds is important and, therefore, further studies should continue, in the last years there has been a bullish awareness for the sensing of pesticides and herbicides, which, at some level, had been an overshadowed issue in detection studies of hazardous pollutants by luminescent CPs and MOFs. Taking into consideration the crucial role that farming activities play in our lives, at least one-third of the global agricultural production is highly dependent on pesticides and herbicides.[22] Some of the biggest problems of these anthropogenic pollutants are their high tox-

[a]*Instituto de Química, Universidad Nacional Autónoma de México. Circuito Exterior, Ciudad Universitaria, Ciudad de Mexico, 04510, Mexico. E-mail: adg@unam.mx*
[b]*Centro Conjunto de Investigación en Química Sustentable UAEM-UNAM, Carretera Toluca-Ixtlahuaca Km. 14.5, San Cayetano, Toluca, Estado de Mexico, 50200, Mexico. E-mail: vsanchezm@uaemex.mx*

icity, along with their poor selectivity to differentiate between target and non-target populations. This indiscriminate usage has been exposed in studies where only 1% (sometimes even lower[23]) of the sprayed pesticides actually reaches the targeted species. The remaining 99% of the applied pesticides tends to bio-accumulate in the food chain and drift in the environment *via* rivers, lakes or other bodies of water causing irreparable damage to the flora and fauna, and also to humans in the form of numerous health-related issues.[22–26] Although some political measures have been addressed in order to reduce the negative impact of pesticides and herbicides (programs like ECOPHYTO by the French government),[23] there is still a long road ahead to lessen this trouble. In addition, to the best of our knowledge, the extremely lethal cyanide ion represents another example of an overlooked toxic pollutant not often mentioned in the up-to-date literature of luminescent CPs.[20,27,28] Despite its inherent danger, curiously, the cyanide ion is repeatedly ignored in the research of anionic contaminants detected using coordination frameworks.[4,15,19,27–29] Bearing this in mind, we decided to integrate this interesting yet dangerous anion to the discussion in order to raise awareness for further related investigations.

This Frontier article highlights selected examples and current advances in the effectiveness of luminescent Zn and Cd CPs and MOFs as highly sensitive, selective, and relatively low-cost fluorescent sensors for the real-time detection of pesticides, herbicides and the cyanide ion, believing that these versatile hybrid materials would eventually contribute to the monitoring and control of the excessive use of hazardous pollutants, minimizing their effects on the environment.

General design outline of luminescent Zn(II)/Cd(II) coordination polymers for pesticide/herbicide sensing

From a synthetic point of view, the straightforward combination of d^{10} metal centers (Zn(II) or Cd(II)) and appropriate organic polytopic linkers, such as aromatic multicarboxylates or N-donor ligands, can be used to obtain CPs with appealing structural diversity,[30] exhibiting a large number of photoluminescence processes.[12,19,31–33]

The effective interaction between diamagnetic d^{10} transition-metal centers and this type of ligand enhances the fluorescence emission due to the increase of the rigidity of the aromatic ligand inside the final crystal arrangement, which reduces the loss of energy through non-radiative processes.[31,34]

The rational design of efficient Zn(II)/Cd(II) CPs for luminescence sensing of pesticides and anions must include materials with the following features: (1) chemical stability, specifically under the desired sensing conditions (aqueous media, physiological environments, real samples with multiple interferents), (2) a stable luminescence source, and (3) specific sites of recognition for the target analyte capable of generating a selective optical response (Scheme 1).

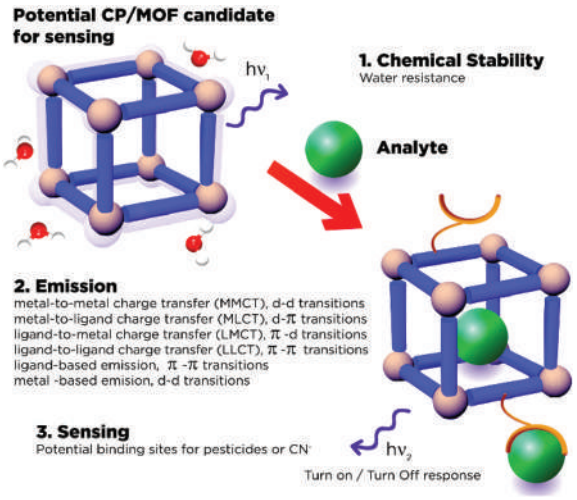

Scheme 1 Schematic overview of the design of a potential transition-metal CP/MOF for real world sensing applications considering the importance of chemical stability in water and specific binding sites.

Chemical stability of Zn(II)/Cd(II) CPs and MOFs in water

Luminescent Zn(II)/Cd(II) CPs and MOFs have been widely used as chemosensors for direct optical detection of anions (halides, pseudohalides and carboxylates),[35–37] transition-metal ions (Cu(II), Zn(II), Hg(II) Cr(III), Cr(VI), Fe(III)),[29,34,38–42] amino acids (*e.g.*, histidine and aspartic acid),[28,43] nitroaromatic explosives,[44–47] volatile organic compounds (VOCs),[48–50] organoamines,[51] and pollutant gases,[27] as pH-sensors,[35] and in lesser use for antibiotics[52–55] and biomarkers of carcinoid tumors.[56]

Although the literature shows very recent examples (made post 2014) of sensors based on Zn(II)/Cd(II) CPs for pesticides (Schemes 2–4) such as parathion,[23,57,58] paraoxon,[57] fenitrothion,[57] glyphosate,[25] azinphos-methyl,[59,60] chlorpyrifos,[61] 2,6-dichloro-4-nitroaniline, (DCN);[24,29,37,62,63] trifluralin, (TFL);[24] nitenpyran,[64] simazine,[65,66] 2,4,6-trichloroanisole, (TCA);[65] diquat, (DQ);[67] and paraquat (PQ),[68] some analytical aspects such as selectivity, efficient optical response, functionality in complex or real samples, and chemical stability in aqueous media persist as central drawbacks in these reported systems.

On the other hand, cyanide sensing by luminescent Zn(II)/Cd(II) CPs in pure water still remains largely unexplored, despite the fact that the examples reported in the literature (only three studies) show efficient analytical responses with very low detection limits ($<10^{-6}$ M), selectivity over common interfering anions and structural advantages compared to conventional organic luminophores.[69–71] In general, the development of d^{10} metal CP/MOF-based sensors has been largely restricted to non-aqueous media which seriously limits their applications.[24,57,62,65,66,72,73]

The chemical stability of CPs and MOFs in the presence of water is a critical property and prerequisite when considering

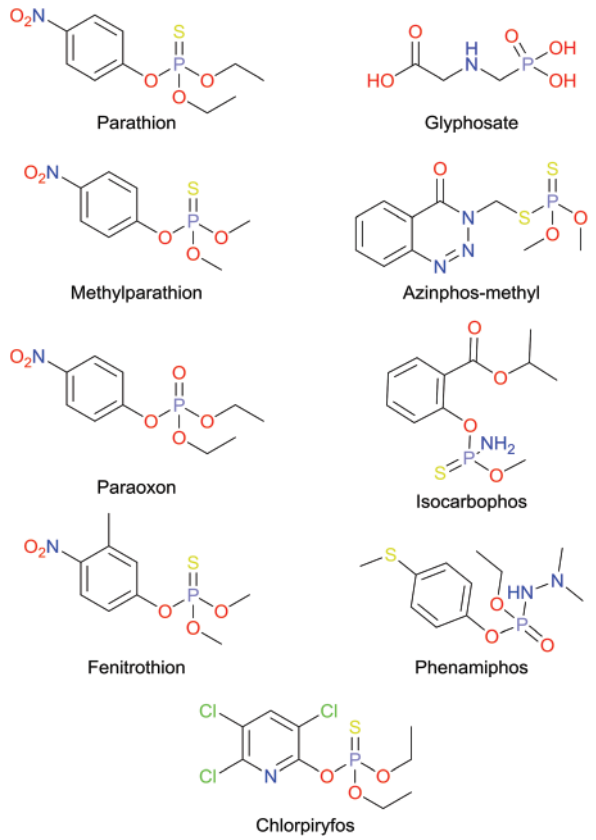

Scheme 2 Chemical structures of the main organophosphate pesticides.

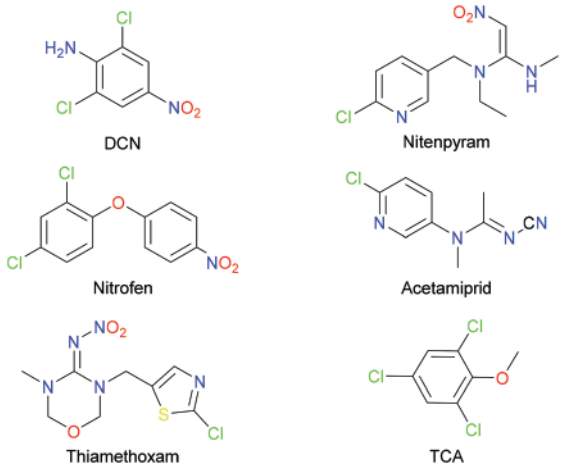

Scheme 3 Chemical structures of the main organochlorine pesticides.

these materials for luminescence sensing applications in real-world samples.

A hydrostable CP/MOF is a material that can be handled in aqueous solutions and is expected to maintain its chemical structure. Experimentally, this stability can be inferred through exposure of the sample (CP) to aqueous conditions and subsequent comparison of the sample's structural properties before and after water exposure *via* methods such as fluorescence spectroscopy, IR-spectroscopy and powder X-ray diffraction.[74] For luminescent CPs/MOFs, the simplest and most common method to study the chemical stability in aqueous media is to record the emission spectra of aqueous suspensions or solutions as a function of time and to compare them with the initial spectrum of the starting material.[71] This method works well as a first-pass evaluation of hydrolytic stability, but a sample with small changes in its emission intensity, even without displacements of its emission maxima, can undergo changes in its chemical structure, for example, a dynamic solvent exchange by water molecules.[75]

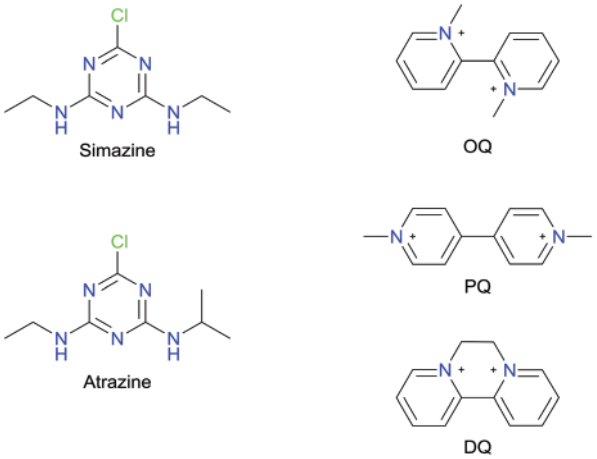

Scheme 4 Chemical structures of the main herbicides.

In thermodynamic terms, hydrostable CPs include a combination of inert metal nodes (mononuclear or cluster) and ligands which makes energetically unfavourable the irreversible hydrolysis reaction (1).

$$\Delta G_{\mathrm{hyd}} = \Delta G_{\mathrm{prod}}(\mathrm{CP} + n\mathrm{H_2O}) + \Delta G_{\mathrm{react}}\ (\mathrm{CP} + n\mathrm{H_2O}) \qquad (1)$$

where ΔG_{prod} is the free energy of the aqua coordination polymer formed between the CP and the water molecules after the hydrolysis reaction takes place and $\Delta G_{\mathrm{react}}$ is the free energy of the CP and the water molecules before the hydrolysis occurs.

In these materials, the strength of metal–ligand coordination bonds can be a strong indicator of their hydrolytic stability. As a weak point in these synthetic structures, usually, the metal–ligand bond strength is less compared to that of natural hydrostable materials such as zeolites. In principle, the hydrolytic stability of these CPS and MOFs requires sufficient metal–ligand binding free energy to overcome the high hydration energies of Zn(II)/Cd(II) ions (ΔG = −2043 and −1843 kJ mol^{-1} for Zn(II) and Cd(II), respectively).[76]

Because Zn(II)/Cd(II) CPs are governed by Lewis acid–base coordination chemistry, the pK_a of the coordinating atom on the ligand can be used as a first approximation of the metal–ligand bond strength. This correlation was previously

studied by Long and used as a strategy for the preparation of a series of highly hydrostable Co(II), Zn(II), Ni(II), and Cu(II) based MOFs containing the pyrazolate ligand.[77]

As the hydrolysis reaction of Zn(II)/Cd(II)-based CPs can only proceed if the water molecule comes sufficiently close to the metal to allow the interaction between the electron orbitals on the electrophilic metal and nucleophilic water molecule, the introduction of hydrophobic fragments in the ligands is a common approach to improve the hydrostability and decrease the degree of hydration of the metallic nodes without compromising the chemical structure of Zn(II)/Cd(II)-CP based sensors.[50,74]

Luminescence of Zn(II)/Cd(II) CPs and MOFs

The luminescence of Zn(II)/Cd(II)-CPs containing aromatic multicarboxylates or N-donor ligands stems from several processes such as ligand-centered emission (LC), metal-centered emission (MC), ligand-to-metal charge transfer (LMCT), metal-to-ligand charge transfer (MLCT) and ligand-to-ligand charge transfer (LLCT) and even analyte-induced luminescence as depicted in Scheme 1. Among these kinds of emissions, the most commonly reported ones for CPs and MOFs containing Zn(II)/Cd(II) are LC, LLCT and LMCT, the latter is observed especially when CPs and MOFs have Zn(II)/Cd(II) clusters as nodes.[19,78]

In this context, organic carboxylate ligands included in the most common CPs and MOFs contain π-conjugated backbones which have little spin–orbit coupling, so the emission is determined basically by the excited states of the ligand with the electronic transition π–π* or n–π* and the symmetry of the singlet ground state.[79] Thus, the emission is typically from the lowest excited singlet state to the singlet ground state (fluorescence). LMCT-based emission has been reported in a wide range of Zn(II) and Cd(II) CPs/MOFs, which involve electronic transitions from an organic linker localized orbital to a metal-centred orbital; this mechanism occurs primarily in structures containing benzene-multicarboxylates as linkers and N-donors as auxiliary ligands.[79] Usually, these materials display intense blue and green emissions in the range of 380 nm–500 nm.[79–81] For recent examples see: $[Cd_{1.5}(dpb)(2,2'\text{-bpy})]$,[32] [Zn(dbpy)(DMF)],[44] $[Cd(tptc)_{0.5}(2,2'\text{-bipy})]$,[82] $[Cd_3(dtba)_3(bbp)_3]$[83] and $[Cd_3(tma)_2(iQ)_3(DMF)]$[84] (Hdpb = 3-(2′,3′-dicarboxylphenoxy)-benzoic acid; H_2dbpy = 2,2′-bipyridine-4,4′-dicarboxylate, H_4tptc=(1,1′:4′,1″-terphenyl)-2′,3,3″,5′-tetracarboxylic acid, H_2dtba = 2,2′-dithiobisbenzoic acid, bpp = 1,3-bis(4-pyridyl)-propane, H_3tma = trimesic acid and iQ = isoquinoline), where the trinuclear Cd-MOFs display room temperature blue luminescence at ∼435 nm with a lifetime in the nanosecond range attributed to a combination of intraligand emission and LMCT. Generally, these types of metal–organic networks containing Zn(II)/Cd(II) ions with benzene-multicarboxylate and aromatic N-donors exhibit enhanced blue emission peaks at 400–500 nm in comparison to free ligands, which can be attributed primarily to a combination of metal perturbed intra-ligand emissions (LC and LLCT) and LMCT.[5,24,29,37,47,57,58,79,86]

The possible electronic states involved in the luminescence phenomenon of Zn(II)/Cd(II)-based MOFs are listed in Scheme 1. To understand the nature and general aspects of this luminescence concept, the readers should refer to specific reviews on the subject.[12,78,81]

Frequent photophysical approaches, based on luminescence signal changes, for the detection of heavy-atom anions, cyanide ions and pesticides in Zn/Cd metal–organic networks, include (1) photoinduced electron transfer (PET),[5,24,37,62,67,68,86,103] (2) Förster resonance energy transfer (FRET)[5,19,27,36,52,63,79] and (3) charge transfer.[79]

For toxic pollutant and cyanide sensing, the PET mechanism is the most popular, and has been used to develop many "turn-off" fluorescent chemosensors.[5,24,37,62,67,68,86,103] PET-based electron donor–acceptor metal–organic networks can be understood in the light of frontier molecular orbital theory. In the presence of the analyte, the HOMO of the donor (anion or analyte) lies higher in energy than the acceptor (luminescent chemosensor), which results in an electron transfer to the acceptor's HOMO immediately after excitation and before emission, thereby quenching luminescence.[5]

Selectivity towards pesticides/herbicides

The use of commercial pesticides with life-threatening health effects (*e.g.*, neurotoxicity, genotoxicity and cancer)[85] and serious adverse environmental impacts[22] forces the development of efficient real-time quantification sensing systems, with high sensitivity and selectivity. While the need for efficient and highly selective optical chemosensors for pesticides is evident, to date, very few sensory systems capable of operating in 100% water and real samples have been described, which is highly desirable for practical application.

For CPs/MOFs with one type of emission source, the change in the monochromatic luminescence signal in the presence of a pesticide is good and enough for the quantitative analysis; however, the selectivity is still not comparable to those of HPLC techniques and mass spectrometry (GC-MS); furthermore, most reports lack studies on complex or real samples (Table 1).

In contrast, remarkable progress in the development of systems with very high sensitivity and low detection limits, in the nanomolar range ($<10^{-7}$ M), for several pesticides has been achieved using high-dimensional porous d^{10}-based MOFs such as $[Zn_4(TCPP)_2(TCPB)_2]$,[23] $[Cd_3(PDA)(tz)_3Cl(H_2O)_4]$,[59] $[Cd_2(tib)(btb)(H_2O)_2]$,[64] and ZnPO-MOF[86] and Zn(II)-coordination polymers such as Zn-NDC-MI[63] (see Table 1 for abbreviations).

Owing to the toxicity of these pollutants, the World Health Organization (WHO) is under a strong vigilance of their permissible limits in drinkable water (glyphosate: 4.14×10^{-6} M; chlorpyrifos: 8.57×10^{-8} M; trifluralin 5.96×10^{-8} M; simazine 1.98×10^{-8} M; atrazine 1.39×10^{-8} M and DQ 1.08×10^{-7} M), keeping also close monitoring of several other pesticides and herbicides in accord to their impact on human health.[94] Additionally, the Food and Agriculture Organization (FAO) from the United Nations has also established rigorous maximum residue limits (MRL) for each pesticide and herbicide varying according to the type of fruit, vegetable or seed.[95]

Table 1 Comparison of the structural characteristics and analytical parameters of selected chemosensors for toxic pollutants

Sensor	Compound	Structural dimensionality	Synthesis method	Fluorescence response	Target analyte	System	λ_{em}	Sensitivity (LOD) M	Ref./ year
1	MOF-5	3D	Room temperature	Turn-off	Parathion, methyl-parathion, paraoxon, fenilthion	EtOH	493	10^{-5}	57
2	NMOF1 ([Cd(atc)(H_2O)$_2$]n, antíparathion complex	3D	Room temperature	Turn-off	Parathion	H_2O	424	3.43×10^{-6}	58
3	[Zn_4(TCPP)$_2$(TCPB)$_2$]n	[a]	Solvothermal	Turn-off	Parathion	H_2O (real irrigation sample)	380	6.69×10^{-9}	23
4	[Zn(pbdc)(bimb)·(H_2O)]n	3D	Solvothermal	Turn-off	Methylparathion	DMF	355	2.5×10^{-6}	72
5	ZnPO-MOF	3D Micropore structure	Solvothermal	Turn-off	Methylparathion	EtOH–H_2O (real irrigation sample)	≈410[a]	4.56×10^{-10}	86
6	[Cd_8(D-cam)$_8$(bimb)$_4$]n	2D	Solvothermal	Turn-off	Methylparathion	DMF	370	3.6×10^{-6}	73
7	MOF-Calix	2D Nanosheets	Solvothermal	Turn-on	Glyphosate	MeOH–isopropanol–H_2O	329	2.25×10^{-6}	25
8	[$Cd_{2.5}$(PDA)(tz)$_3$]n	3D	Solvothermal	Turn-off	Azinphos-methyl	H_2O (extract from apples)	290	5×10^{-5}	60
9	[Cd_3(PDA) (tz)$_3$Cl(H_2O)$_4$]·3H_2O	3D	Room temperature	Turn-off	Azinphos-methyl	H_2O (extract from apples and tomatos)	290	2.5×10^{-8}	59
10	{[Zn_3(Hdpa)(OH) (H_2O)$_2$]·6H_2O}n	3D	Solvothermal	Turn-off	Chlorpyrifos	H_2O	350	[a]	61
11	[Cd_2((1*R*,2*R*/1*S*,2*S*)-Hcpba)$_2$(phen)$_2$]n	1D	Solvothermal	Turn-off	DCN	DMF	≈420[a]	1.12×10^{-6}	62
12	(H_3O)[Zn_2L(H_2O)]·3NMP·6H_2O	3D	Solvothermal	Turn-off	DCN, TFL	NMP	440	1.41×10^{-5}	24
13	[Zn_3(DDB)(DPE)]·H_2O	3D	Solvothermal	Turn-off	DCN	H_2O (extract from carrots, nectarines and grapes)	≈450[a]	2.7×10^{-7}	37
14	[Zn_2(L^2)$_2$(TPA)]·2H_2O	2D	Solvothermal	Turn-off	DCN	MeOH	432	1.9×10^{-3}	29
15	{[Zn(L^3)(1,4-bdc)$_2$·2(1,4-H_2bdc)]}n	3D	Solvothermal	Turn-off	DCN	H_2O	≈375[a]	1.29×10^{-3}	96
16	Zn-NDC-MI	2D	Solvothermal	Turn-off	DCN	H_2O	369	6×10^{-8}	63
17	[Cd_2(HDDB)(bimpy)(NMP) (H_2O)]·3H_2O	2D	Solvothermal	Turn-off	DCN	H_2O	462	3.6×10^{-7}	97
18	{[Cd(tptc)$_{0.5}$(bpz)(H_2O)]·0.5H_2O}n	2D	Solvothermal	Turn-off	DCN	H_2O	392	5.4×10^{-7}	98
19	[Cd (tptc)$_{0.5}$(bpy)]n	2D	Solvothermal	Turn-off	DCN	H_2O	392	3.08×10^{-6}	98
20	NUC-6	3D	Solvothermal	Turn-off	DCN	H_2O	392	5.6×10^{-7}	99
21	[Zn_2(bpdc)$_2$(BPyTPE)]	3D	Solvothermal	Turn-off	DCN	DCM	498	6.27×10^{-7}	100
22	[Cd_3(CBCD)$_2$(DMAc)$_4$ (H_2O)$_2$]·10DMAc	3D	Solvothermal	Turn-off	DCN	DMAc	≈430[a]	7×10^{-7}	101
23	Rho B@ [Cd_2(tib)(btb)(H_2O)$_2$]·NO_3·2DMF	3D	Solvothermal	Turn-off	Nitenpyram	H_2O, DMF	590, 606	4.8×10^{-10}	64
24	Rho 6G@ [Cd_2(tib)(btb) (H_2O)$_2$]·NO_3·2DMF	3D	Solvothermal	Turn-off	Nitenpyram	H_2O, DMF	590	3×10^{-9}	64
25	{[Cd(μ_2-BA)$_2$(ClO_4)$_2$]·n(DCM)}n	2D	Room temperature	Turn-off	Simazine, TCA	MeCN	450	4.78×10^{-7}	65
26	Cd·AHP·2,6-NDS·DMF·2H_2O	2D	Solvothermal	Turn-off	Simazine	DMF	≈440[a]	2.25×10^{-4}	66
27	[$Zn_{1.5}$(DBC)·(H_2O)·(DMF)·Me_2NH_2]n	3D	Solvothermal	Turn-off	DQ	H_2O	420	1.52×10^{-5}	67
28	[Zn_2(cptpy)(btc)(H_2O)]n	3D	Solvothermal	Turn-off	PQ	H_2O	400	9.73×10^{-6}	68
29	{[Zn_2(H_2O)$_2$(*e*,*a*-cis-1,4-chdc)$_2$(4,4′-dtbb)$_2$]·7H_2O}n	1D	Room temperature	Turn-off	CN^-	H_2O	434	9×10^{-8}	71
30	M-ZIF-90	3D	Solvothermal	Turn-off	CN^-	H_2O–DMSO	450	2×10^{-6}	69
31	Bio-MOF-1 ⊃ DAAC	3D	Solvothermal	Turn-on	CN^-	H_2O	510	1.9×10^{-8}	70

Abbreviations: [a] = Not specified, atc = aminoterephthalic acid, TCPP = tetrakis (4-carboxyphenyl)porphyrin, TCPB = 1,2,4,5-tetrakis (4-carboxyphenyl)benzene, pbdc = 5-(4-pyridyl)-isophthalic acid, bimb = 4,4′-bis(1-imidazolyl)biphenyl), ZnPO-MOF = [Zn_2(Zn-(5,15-dipyridyl-10,20-bis(pentafluorophenyl))porphyrin)(1,2,4,5-tetrakis(4-carboxyphenyl)benzene)]n, D-cam = D-camphor acid, Calix-MOF = {[Cd_2(5-NO_2-BDC)$_2$$L^4$(MeOH)]$_2$·MeOH}$n$ L^4 = 25,26,27,28-tetra-[(4-pyridylmethyl)oxy]calix[4]arene, PDA = 1,4-phenylenediacetate, tz = 1,2,4-triazolate, (1*R*,2*R*/1*S*,2*S*)-H_3cpba = (1*R*,2*R*/1*S*,2*S*)-2,2′-((5-carboxy-1,3-phenylene)bis(oxy))dipropionic acid, phen = 1,10-phenanthroline, L = 2,5-(6-(4-carboxyphenylamino)-1,3,5-triazine-2,4-diyldiimino, BPyTPE = (*E*)-1,2-diphenyl- 1,2-bis(4-(pyridin-4-yl)phenyl)ethane, DDB = 3,5-di(2′,4′-dicarboxylphenyl)benzoic acid, DPE = 1,2-di(4-pyridyl)ethylene, L^2 = 4-(tetrazol- 5-yl)phenyl-4,2′:6′,4″-terpyridine, TPA = terephthalic acid, L^3 = bis(4-(4*H*-1,2,4-triazol-4-yl)phenyl)methane, bdc = 1,4-benzenedicarboxylic acid, NDC = 2,6-naphthalenedi-carboxylate, MI = 2-methylimidazole, CBCD = 4,4′-(9-(4′-carboxy-[1,1′-biphenyl]-4-yl)-9*H*-carbazole-3,6-diyl)dibenzoic acid, DMAc = *N*,*N*-dimethylacetamide, Rho = Rhodamine, btb = 1,3,5-benzenetribenzoic acid, tib = 1,3,5-tri(1-imidazolyl)benzene, H_6dpa = 3,4-di(3,5-dicarboxyphenyl)phthalic acid, NMP = *N*-methylpyrrolidone, tptc = *p*-terphenyl-2,2″,5″,5‴-tetracarboxylate acid, bpz = 2-(1*H*-pyrazol-3-yl)pyridine, bpy = 2,2′-bipyridine, bpdc = biphenyl-4,4′-dicarboxylic acid, BPyTPE = (*E*)-1,2-diphenyl-1,2-bis(4-(pyridin-4-yl)phenyl)ethene), BA = bis-9,10-(pyridine-4-yl)-anthracene, DMF = *N*,*N*-dimethylformamide, AHP = 1,1′-(anthracene-9,10-diylbisIJmethylene))bisIJpyridin-1-ium-4-olate), 1,5-NDS = 1,5- naphthalenedisulfonic acid, SIA = 5-sulfoisophthalic acid, DBC = 2,7,10,15-tetrakis[2,6-dimethyl-4-(α-carboxy)methoxyphenyl]-dibenzo[*g*,*p*]chrysene, cptpy = 4-(4-carboxyphenyl)-2,2′:4′,4″-terpyridine, btc = 1,3,5-benzenetricarboxylic acid, 1,4-chdc = 1,4-cyclohexanedicarboxylato, 4,4′-dtbb = 4,4′-di-*tert*-butyl-2,2′-bipyridine, DAAC = 3,6-diaminoacridinium cation DCN = 2,6-dichloro-4-nitroaniline, ZIF = zeolitic imidazolate framework DQ = diquat, PQ = paraquat, TCA = 2,4,6-trichloroanisole, and TFL = trifluralin.

In this context, luminescent Zn(II) and Cd(II) crystalline metal–organic networks have gained extensive attention as optical sensors for pesticides because of their straightforward synthesis, fast response, high selectivity and sensitivity, and recyclability. A notable example is the 2D nano-sheets of MOF-Calix[25] (Table 1) which showed excellent sensing performance of glyphosate, which is the most frequently used herbicide worldwide, with a low limit of detection of 2.25×10^{-6} M with a luminescence "turn-on" response. This limit of detection is below the maximum permissible limit of the WHO in drinking water (4.1×10^{-6} M).[25,94]

Although great advances have been made in the development of chemosensors based on metal–organic materials for the detection of pesticides, most reports lack studies on complex or real samples. Some notable examples are the compounds $[Zn_4(TCPP)_2(TCPB)_2]n$[23] and ZnPO-MOF,[86] which were used in the determination of parathion and methyl-parathion directly in irrigation water with detection limits in the nanomolar concentration range (Table 1) with excellent recovery rates. These detection values are much lower than the maximum residual limits in the European Pesticides databases (*e.g.*, 1.7×10^{-6} M for parathion)[23]

On the other hand, the literature shows a very few examples of these types of chemosensors for pesticides in fruits and vegetables. Water-stable trinuclear MOFs $[Cd_3(PDA)(tz)_3Cl(H_2O)_4]\cdot 3H_2O$[59] and $[Zn_3(DDB)(DPE)]\cdot H_2O$[37] (Table 1) are able to detect azinphos-methyl and 2,6-dichloro-4-nitroaniline (DCN), respectively, in apples, fruit extracts and tomatoes with the detection limit in the nanomolar concentration range. These detection limits meet the maximum residue limits established by the Food and Agriculture Organization (FAO) of the United Nations (*e.g.*, MRL = 3.15×10^{-6} M for azinphos-methyl in tomatoes).[37,59]

CP/MOF-based sensors have immense possibilities for the functionalization of specific binding sites, the activation of pendant groups, pore size modulation, suitable signal transduction and post-synthetic modification.[22] Despite the significant advances that have been made in luminescence sensing systems for pesticides, the selectivity is a current unsolved challenge.[22]

Regarding biological receptors, the substrate molecules selectively bind to a specific site typically with multiple converged and complementary host–guest interactions.[87] To date, the pore size modulation of MOFs and the electron-donating property modulation of the ligands have been an important strategy to provide close interactions between the metal–organic frameworks and analytes (pesticides), thus generating selective systems. Some notable examples are Zn(II)-MOFs $[Zn_4(TCPP)_2(TCPB)_2]n$ and ZnPO-MOF where the selectivity towards parathion and methyl parathion over several organophosphate derivatives is attributed to the strong electron transfer from the electron-donating ligands to the highly electron-withdrawing nitroaromatic group in the pesticides.[23,86] These materials were used in the determination of methyl parathion in irrigation water with satisfactory results.

Previously mentioned MOF-Calix is a selective sensor designed with the concept of host–guest chemistry, where the MOF binds to glyphosate by multiple hydrogen bonding and π···π stacking interactions.[25] The selectivity of the three-dimensional MOF $[Cd_3(PDA)(tz)_3Cl(H_2O)_4]\cdot 3H_2O$ is attributed by the authors to the integration of various convergent interactions such as hydrogen bonding and π···π stacking between the MOF and the pesticides, whilst the selectivity of $[Cd_{2.5}(PDA)(tz)_3]n$ is the result of the combination of π···π interactions between the aromatic part of azinphos-methyl and the aromatic panel of the MOF together with a strong coordination bond (Cd···S=P) between the terminal S atom of azinphos-methyl and the Cd(II) atom.

Selectivity towards cyanide

Nowadays, a large amount of metal salts of cyanide is widely used in several industrial processes (~1 400 000 tons per year)[88] such as gold mining, and plastic manufacturing.[89] Cyanide waste causes serious pollution in the environment, especially in natural water sources. Compared with very toxic heavy-metal ions, CN^- can lead to the death of humans and aquatic species in minutes.[90] For this reason, the development of sensitive and selective CN^- sensors capable of operating in the aqueous phase has been a subject of intense research during the last few decades.[91]

The literature shows very few examples of cyanide sensing by metal–organic materials.[69–71] Ghost and coworkers reported the first two examples of post-synthetically modified MOF-based chemical sensors for CN^- in the aqueous phase.[69,70] Post-synthetic modification was employed to incorporate a specific recognition site for CN^- (reactive free aldehyde groups aligned within the pores) with selectivity over halides, oxoanions and pseudohalides.

Recently, Sánchez-Mendieta and co-workers reported a series of hydrolytically stable zinc-1,4-cyclohexanedicarboxylato coordination polymers, with blue emission, capable of selectively quantifying cyanide ions with a detection limit of 9×10^{-8} M.[71] The selectivity was attributed by the authors to the coordination of the cyanide anion with the metallic centre, which resulted in the formation of the salt $Zn(CN)_2$ with the simultaneous release of the ligands. The nucleophilicity of the cyanide anion together with the high hydration energies of other anions such as halides and oxoanions makes these polymers efficient to function as cyanide-selective fluorescent chemodosimeters over a wide pH range.

Interestingly, Zn(II)-metal–organic materials designed for cyanide sensing have detection limits ($\sim 10^{-8}$ M) considerably lower than the maximum level of CN^- recommended by the WHO in drinking water (2.7×10^{-6} M).[69–71]

CPs and MOFs as fluorescent sensors of pesticides

In one of the earliest instances, the well-known MOF-5 has been applied by Kumar's group in the luminescence detection

of organophosphate pesticides (OPPs) such as parathion, methylparathion, paroxon (an initial degradation product of parathion) and fenitrothion (Scheme 2).[57]

Usually, most of the OPPs are potent nerve agents that can irreversibly inhibit the activity of the acetylcholinesterase enzyme (AChE), which is responsible for the proper functioning of the nervous system by hydrolysing the neurotransmitter acetylcholine (ACh). Since ACh is an important neurotransmitter, the over-accumulation of ACh eventually leads to respiratory paralysis and death.[23,59] Although no selectivity over any of the OPPs mentioned was shown for MOF-5, Kumar's group continued their investigations into the recognition of OPPs with NMOF1, a cadmium and 2-aminoterephthalic acid based 3D MOF, with the particular characteristic of a non-coordinative –COOH group, which was post-synthetically converted into an amide by the reaction with EDC (1-ethyl-3-(3-dimethyl aminopropyl) carbodiimide), enhancing in the MOF the capacity of bioconjugation with a selective antibody against parathion (NMOF1/anti-parathion) (Fig. 1). The sensitivity of the system was increased up to 5-fold in comparison to that of MOF-5 and the analysis was proceeded in an aqueous medium with a quenching response.[58]

Likewise, the fluorescence recognition of methylparathion has been achieved using ZnPO-MOF, a 3D microporous MOF constituted of a metalloporphyrin (Zn-(5,15-dipyridyl-10,20-bis(pentafluorophenyl))porphyrin) and a tetracaboxylate linker (1,2,4,5-tetrakis(4-carboxyphenyl)benzene) assembled together through the typical Zn-paddlewheel SBU.[86] The MOF experienced a significant change in its fluorescence signals with a selective turn-off response for methyl-parathion, which was attributed to the PET mechanism.[86] Importantly, methyl-parathion detection can be carried out in competition with several OPPs and other nitroaromatic compounds, and it has confirmed its efficacy in real irrigation samples from a lake.[86]

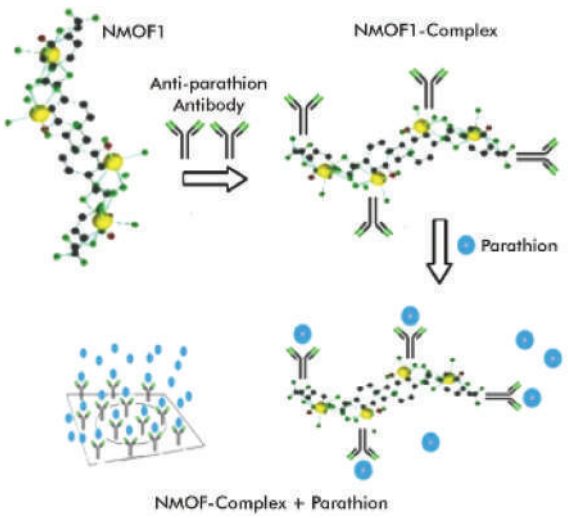

Fig. 1 Mechanism for parathion detection using NMOF1. Modified with permission from ref. 58 copyright (2020) Elsevier.

Furthermore, in an on-going process, glyphosate, the active ingredient in most Roundup® brand pesticides and other weed-control products of the same producing company, has been in the spotlight for recent carcinogenic allegations. With the growing importance of the rapid detection of glyphosate, Yu's group has designed a specific glyphosate fluorescent sensor.[25] Their synthetic strategy relies on the incorporation of a predesigned tetra-pyridyl-functionalized calix[4]arene ligand (25,26,27,28-tetra-[(4-pyridylmethyl)oxy]calix[4]arene) which reacted with 5-nitro-1,3-benzenedicarboxylic acid (5-NO_2-BDC) and $Cd(NO_3)2{\cdot}4H_2O$, producing a 2D functionalized cup-shaped feature structure attributable to the calix[4]arene ligands, where those layers are connected into a 3D architecture, denoted as MOF-Calix (Fig. 2).[25] MOF-Calix crystallizes in the triclinic space group $P\bar{1}$ and shows two crystallographic independent Cd atoms. The Cd1 atom adopts an octahedral coordination geometry and is six-coordinated by four O atoms of the carboxylate groups from 5-NO_2-BDC and two N atoms from the calix[4]arene ligand. The Cd2 atom also takes an octahedral coordination geometry, coordinated by four O atoms of the carboxylate groups from 5-NO_2-BDC, one O atom from MeOH and one N atom from one calix[4]arene ligand, leaving in the 2D layer an uncoordinated N atom of the pyridine group from tetra-pyridyl-functionalized calix[4]arene. Since the 3D bulk material is integrated by the 2D layer array, the authors transformed MOF-Calix through a simple and easy exfoliation process where the 2D layers are separated into ultrathin single (2.20 nm) or double-layer (3.73 nm) 2D MOF-Calix nanosheets. Apparently, taking advantage of the host–guest interaction pro-

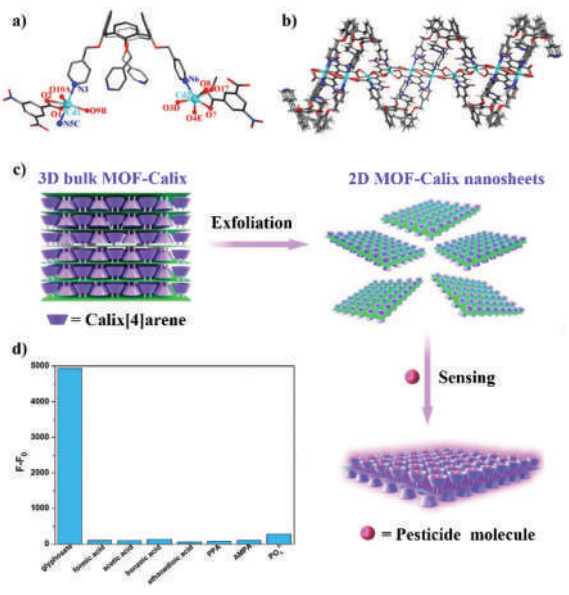

Fig. 2 (a) View of the coordination environment of the Cd centers in MOF-Calix. (b) View of the 2D structure in MOF-Calix extending along the *bc* plane. (c) Schematic illustration of the fabrication of 2D MOF-Calix nanosheets and sensitive detection of pesticides through host–guest chemistry. (d) The fluorescence response of the MOF-Calix nanosheets towards various organic acids and PO_4^{3-} (45 μM for each). Adapted with permission from ref. 25 copyright (2020) Elsevier.

vided by calix[4]arene, the cavities were able to self-adjust to better incorporate glyphosate molecules by varying their size and shape as the pyridine group from calix[4]arene could freely rotate *via* the methylene groups. As the glyphosate molecules were immobilized in the host of calix[4]arene by the host–guest interaction, the rigidity of the backbone was amplified, facilitating the electron transfer through a radiative decay process after the photoexcitation process, increasing the fluorescence intensity.[25] The selectivity of MOF-Calix was explored by competition of plenty inorganic ions as well of additional carboxylic and phosphonic acid compounds (formic acid, acetic acid, benzoic acid, ethanedioic acid, phenylphosphonic acid (PPA), (amino-methyl)phosphonic acid (AMPA) and PO_4^{3-}). Under the same experimental conditions, no noticeable interference nor fluorescence variation was observed for these analytes. To find out whether the guest size played a decisive role in the selective sensing or not, the fluorescence intensity of MOF-Calix nanosheets was determined in the presence of organic molecules with a similar size to glyphosate: glutaric acid and iminodiacetic acid. After adding a solution of 45 μM glutaric acid and iminodiacetic acid independently, the fluorescence intensity increased by 6.3% and 10.9% respectively, while for glyphosate 240% fluorescence enhancement was observed emphasizing its selectivity for glyphosate with a detection limit of 2.25×10^{-6} M.[25]

Moreover, azinphos-methyl, a widely employed OPP to control many insect pests on a variety of fruits, vegetables, nuts, grapes, apples, crop fields and shade trees, and a key ingredient in the preparation of several commercially available pesticides, was analyzed in real samples from the extract of apples[59,60] and tomatoes[59] by Singha's group. Two different compounds derived from the same metal ion (Cd(II)) and ligand (1,4-phenylenediacetic acid (PDA) and 1,2,4-triazol (tz)) were studied.[59,60] $[Cd_{2.5}(PDA)(tz)_3]n$ was the product from the solvothermal reaction,[60] whilst $[Cd_3(PDA)(tz)_3Cl(H_2O)_4]\cdot 3H_2O$ was obtained from the reaction at room temperature with minor solvent changes.[59] The first one is a 3D MOF with an asymmetric unit integrated by one PDA, three tz and two and a half crystallographically independent Cd(II) ions. The coordination environment of Cd1 plays an important role in the recognition as this central ion has an unsaturated coordination vacancy in a distorted trigonal bipyramidal geometry. The authors suggest that the π···π interactions along with this vacancy are both responsible for the detection of azinphos-methyl (Fig. 3).[60] On the other hand, although $[Cd_3(PDA)(tz)_3Cl(H_2O)_4]\cdot 3H_2O$ is also a 3D MOF, its asymmetric unit consists of one PDA, three tz, one chloride ion, four coordinated water molecules, three lattice water molecules and three crystallographically independent Cd(II) ions, where all the Cd(II) ions have a distorted octahedral geometry. As a consequence, the interaction with the OPPs is limited by the π···π interactions solely.[59] Both of the coordination frameworks exhibited a turn-off response for the azinphos-methyl pesticide. The evaluation of the interference and competition with other OPPs were carried out with the simultaneous existence of parathion, chlorpyrifos, diazinon, endosulfan, malathion and

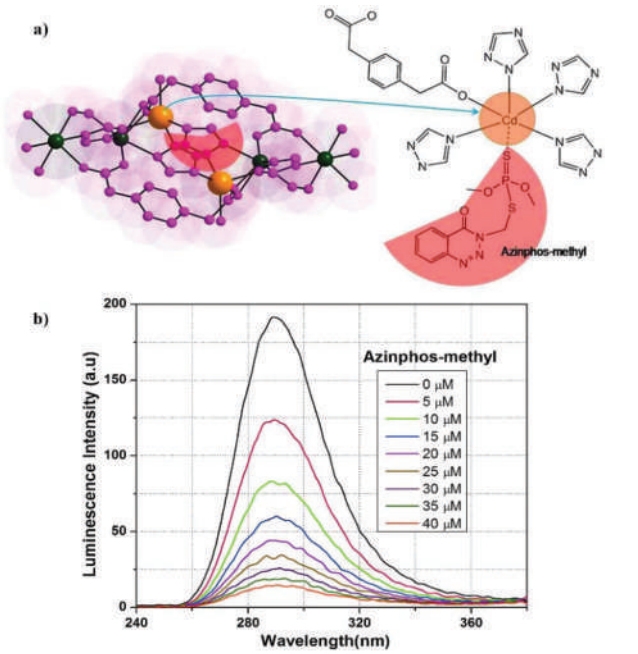

Fig. 3 (a) Schematic of five coordinated Cd(II) ions (Cd1-Orange) and the proposed coordination interaction of azinphos-methyl through the S atom inside the cage. (b) Emission spectra of 1 dispersed in water upon incremental addition of the acetonitrile solution of azinphos-methyl (λ_{ex} = 225 nm). Adapted with permission from ref. 60 copyright (2020) Wiley Online Library.

dichlorvos in water, resulting in an exclusive quenching for azinphos-methyl by $[Cd_{2.5}(PDA)(tz)_3]n$; meanwhile, the solvothermal product showed 90%, 52%, and 49% luminescence quenching for azinphos-methyl, chlorpyrifos, and parathion respectively.[60] Probably, this phenomenon was caused by the absence of unsaturated coordination sites in the network, even though no further explication was given. Additionally, the LOD of the room temperature product is lower than that of the solvothermal product (25×10^{-9} M and 5×10^{-5} M).[59,60] As both systems show the same emission band (derived from the PDA ligand) and both detect azinphos-methyl, the quenching mechanism has been attributed to the absorption of the excitation light from the MOF to the azinphos-methyl molecule in a resonance energy transfer process which is in congruence with the UV-spectra of the sensors and target molecule.[59]

Besides OPPs, organochlorine pesticides (OCPs) constitute another significant division of hazardous pollutants in anthropogenic activities (Scheme 3). 2,6-Dichloro-4-nitroaniline (DCN) is found to be one of the most important and widely used pesticides for protecting crops from various diseases such as fruit trees, cotton rotten bells and wheat powdery mildew.[24,37,63] Nevertheless, its high toxicity, slow degradation rate and insoluble properties cause severe damage to living organisms, and it can enter the human body through the skin and lungs. Also, its absorption through the gut wall affects the central nervous system leading to convulsions, hyper-reflexia, ataxia and tremor, and it is even suspected to be a

carcinogen.[24,37,63] Hence, Zhang's group has developed an interesting enantiomeric chiral pair of CPs based on the chiral ligand (1*R*,2*R*/1*S*,2*S*)-2,2′-((5-carboxy-1,3-phenylene)bis(oxy)) dipropionic acid ((1*R*,2*R*/1*S*,2*S*)-Hcpba), phenantroline (phen) and cadmium (Fig. 4).[62] Obviously, since the enantiomeric pair is isomorphic, only $[Cd_2((1S,2S)\text{-Hcpba})_2(phen)_2]n$ was described.[62] The crystalline compound belongs to the $P2_1$ space group, and the asymmetric unit contains two Cd(II) ions, two (1*S*,2*S*)-Hcpba and two phen as ligands. The metallic ion is located at the center of a twisted octahedron defined by four O atoms from three different (1*S*,2*S*)-Hcpba, and two chelating N atoms from the phen molecule.[62] As has been observed, the use of 2,2′-bipyridine type ligands[80] is usually limited in coordination polymers with low dimensionality (1D). Yet, attention-grabbing properties like circular dichroism (with a negative Cotton effect at 275 nm) and the luminescence recognition of pesticides, antibiotics and chiral nitroaromatic analytes were studied. The most remarkable achievement for the pesticide detection was the selective quenching response for DCN (LOD = 3.79×10^{-7} M) with negligible interference from glufosinate, glyphosate, 2,4-dichlorophenol and atrazine in DMF.[62] The turn-off behavior was explained by the combination of PET and FRET mechanisms supported by electrochemical data and UV-vis spectra. Nonetheless, the enantiomeric recognition by the pair of chiral CPs in chiral nitroaromatic molecules was unsuccessful, as both the CPs could not discriminate between the nitroaromatic enantiomers.[12,62]

Similarly, the 3D MOF $(H_3O)[Zn_2L(H_2O)]\cdot 3NMP\cdot 6H_2O$ (L = 2,5-(6-(4-carboxyphenylamino)-1,3,5-triazine-2,4-diyldiimino) diterephthalic acid) is also capable of detecting DCN.[24] This particular MOF crystallized in the space group $P2_12_12_1$ with a 4-connected 3D framework. The negative charge of the framework was balanced with H_3O^+. Two crystallographically independent zinc ions are part of the asymmetric unit and both metallic ions adopted a distorted tetrahedral geometry with four atoms of oxygen provided by three carboxylate ligands constructing a relatable Zn paddlewheel SBU in the network (Fig. 5).[24] Curiously, $(H_3O)[Zn_2L(H_2O)]\cdot 3NMP\cdot 6H_2O$ shows a distinctive luminescence performance against some pesticides. Strong quenching is shown in the presence of DCN and trifluralin (TFL); however, its selectivity was achieved through a unique bathochromic shift of 43 nm after the addition of TFL that can even be appreciated under naked-eyed conditions. Still, a higher sensitivity for DCN was achieved with a lower detection limit (4.76×10^{-9} M). The quenching mechanism considers the electron-withdrawing nature of the $-NO_2$ and

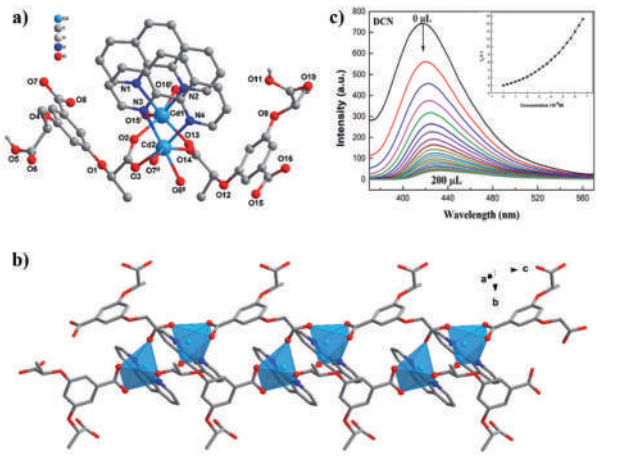

Fig. 4 (a) Stick–ball representation of the structural unit of $[Cd_2((1S,2S)\text{-Hcpba})_2(phen)_2]n$. (b) 1D-chain structural representation along the *c* axis. (c) Luminescence spectra and the SV plots with DCN (10 mM, 10 mL addition each time). Adapted with permission from ref. 62 copyright (2020) The Royal Society of Chemistry.

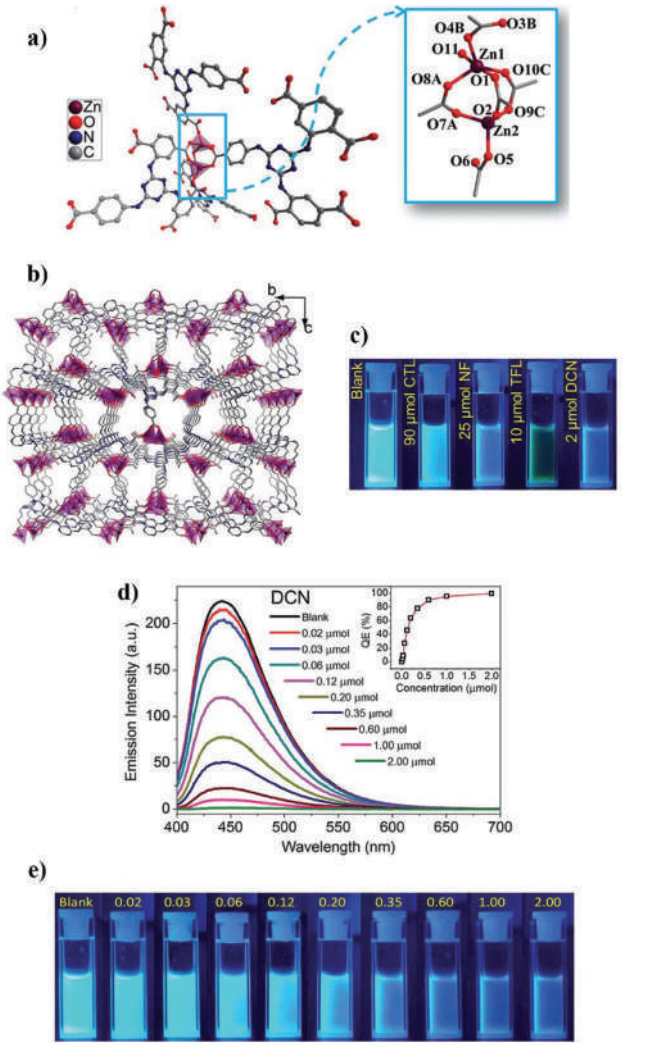

Fig. 5 (a) The coordination environment of the binuclear Zn(II) centers of $(H_3O)[Zn_2L(H_2O)]\cdot 3NMP\cdot 6H_2O$. (b) The 3D framework observed along the *a* axis. (c) Fluorescence variation of $(H_3O)[Zn_2L(H_2O)]\cdot 3NMP\cdot 6H_2O$ with trace addition of pesticides under 365 nm UV light. (d) Concentration-dependent fluorescence responses of $(H_3O)[Zn_2L(H_2O)]\cdot 3NMP\cdot 6H_2O$ at different concentrations of DCN (λ_{ex} = 365 nm) inset: luminescence quenching efficiency (QE) *versus* addition concentration of DCN. (e) Fluorescence variations with step-by-step addition of DCN (mmol) under 365 nm UV light. Adapted with permission from ref. 24 copyright (2020) The Royal Society of Chemistry.

–CF_3 groups in the energy level calculations by density functional theory, converging in the synergistic effect of the PET and FRET processes.[24]

Correspondingly, DCN has been detected in real samples as well. The 3D MOF $[Zn_3(DDB)(DPE)]\cdot H_2O$ (DDB = 3,5-di(2′,4′-dicarboxylphenyl)benzoic acid and DPE = 1,2-di(4-pyridyl) ethylene) has accomplished the fluorescence recognition of DCN in extracts from carrots, nectarines and grapes.[37] The analysis of the crystal structure reveals that the framework crystallizes in the $P2_1/c$ space group. Its asymmetric unit contains three Zn(II) ions, one μ_3-OH^- ion, one DPE and one DDB ligand. Three Zn(II) ions are connected by one μ_3-OH^- ion and four carboxylate groups to form a trinuclear $[Zn_3(OH)(COO)_4]$ cluster. Then, two trinuclear clusters are linked by two carboxylate groups to form a six-nuclear $[Zn_6(OH)_2(COO)_{10}]$ cluster constructing a 4,12-connected net (Fig. 6).[37] Thus, the DCN fluorescence sensing was explored among other eight OCPs.[37] Non-significant changes except for the notorious quenching from DCN were revealed. The quenching efficiency in the DCN detection scales up to 93.5% with a limit of detection equal to 2.7×10^{-7} M in water. These favorable results allowed the determination of DCN by the MOF in the above-mentioned fruits and vegetables. It is worth noting that the turn-off mechanism was studied with the assistance of computational chemistry concluding in a PET process caused by the electron-withdrawing –NO_2 group.[37]

In an interesting methodology for the luminescence recognition of Nitenpyram, Yang *et al.*[64] have incorporated fluorescent guest molecules in the $[Cd_2(tib)(btb)(H_2O)_2]\cdot NO_3\cdot 2.5DMF$[92] MOF with the intention to create a dual-emitting platform system. Rhodamine B (Rho B) and Rhodamine 6G (Rho 6G) were the guest molecules selected.[64] X-Ray crystallographic analysis revealed that the MOF crystallized in the space group $P2_12_12_1$. The asymmetric unit consists of two Cd(II) ions, one tib ligand, one btb ligand, two coordination water molecules, one NO_3^- and two and a half DMF molecules. Each Cd(II) ion has a diverse coordination environment. Cd1 is seven-coordinated by five O atoms from three btb ligands, one O atom from one coordination H_2O molecule and one N atom from one tib ligand, whereas Cd2 has a distorted octahedral geometry integrated by three O atoms from three different btb ligands, one O atom from one coordinated H_2O molecule and two N atoms. A binuclear {Cd2} unit is formed through the carboxylate groups of btb ligands, and subsequently, these binuclear units are connected by the tib ligand constructing a 3D network with empty one dimensional channels, having an effective pore volume of 53% (3417 Å^3) per unit cell (6514 Å^3) calculated by the PLATON program.[92] The loaded MOF with the guest molecules shows two main emissions at 370 nm and approximately 600 nm, respectively. The emission at 370 nm originated from the MLCT, while the emission at approximately 600 nm comes directly from the dye molecules of rhodamine B or 6G.[64] Both the dual-emitting systems have been applied in the sensing of nitenpyram, thiamethoxam, cypermethrin, carbaryl and rotenone. Changes in the fluorescence intensity were observed with the following quenching efficiency: nitenpyram > thiamethoxam > cypermethrin ≈ carbaryl > rotenone. This tendency is equally valid for both systems independent of the type of rhodamine guest in the MOF. For Rho B@MOF the detection limit was estimated to be 4.8×10^{-10} M, while 3×10^{-9} M was the corresponding value for Rho 6G@MOF. Remarkably, each system has distinctive dual emission behavior (Fig. 7). The extinguishing of the fluorescence properties was explained by computing the HOMO and LUMO energies of the five pollutants by applying density functional theory agreeing in a PET process.[64]

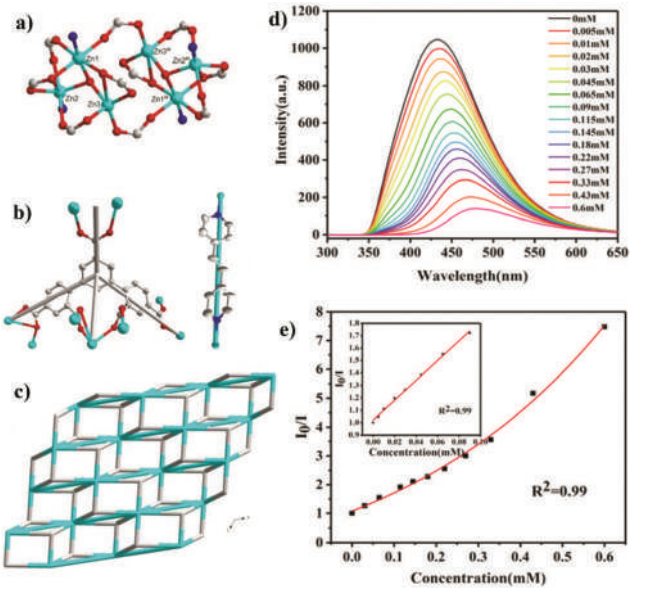

Fig. 6 (a) SBU in $[Zn_3(DDB)(DPE)]\cdot H_2O$ MOF (b) Linkage mode of the DPE and DDB ligands. (c) Simplified representation of the network in $[Zn_3(DDB)(DPE)]\cdot H_2O$ along the *b* axis. (d) Fluorescence spectra of the MOF at different concentrations of DCN in aqueous solution including 100 μL carrot extract. (e) Stern–Volmer plot for the detection of DCN in aqueous solution including 100 μL carrot extract. Inset: linear fitting part. Adapted with permission from ref. 37 copyright (2020) The Royal Society of Chemistry.

CPs and MOFs as fluorescent sensors of herbicides and the cyanide ion

Simazine is a frequently used general-purpose herbicide considered as a toxic contaminant with potential endocrinal disrupting activity (Scheme 4).[65] Vasylevskyi's group has employed the 2D coordination polymer $\{[Cd(\mu_2\text{-}BA)_2(ClO_4)_2]\cdot n(DCM)\}n$ (BA = bis-9,10-(pyridine-4-yl)-anthracene) as a fluorescent sensor for the detection of simazine.[65] $\{[Cd(\mu_2\text{-}BA)_2(ClO_4)_2]\cdot n(DCM)\}n$ is one of the series of Zn and Cd CPs connected through the BA ligand. Structural differences in those coordination polymers (beside the metallic ions and crystallization solvent molecules) arise according to the counter-ion responsible for the charge balance. However, among all the anions that lead to the synthesis of the CPs, the use of ClO_4^- as a counter-ion directed the construction to the

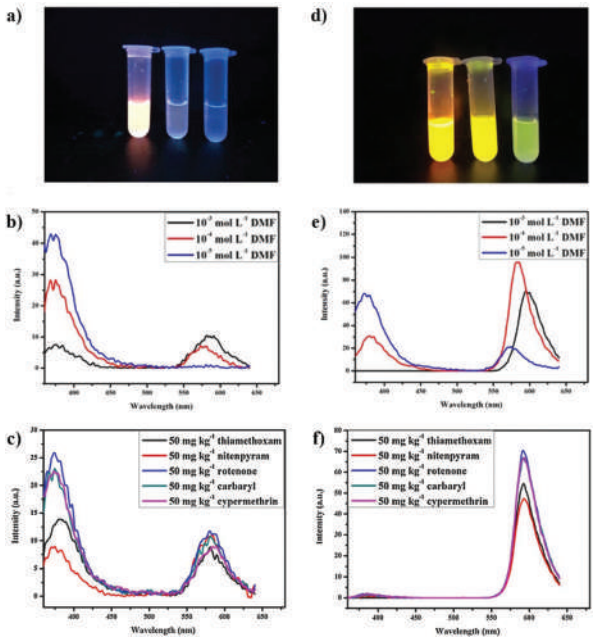

Fig. 7 (a) Photograph of the changes in solution colors under UV light (365 nm) according to the concentration in the "(b) plot" for Rho B@MOF in DMF. (b) Emission spectra of Rho B@MOF in DMF. (c) Fluorescence intensity of Rho B@MOF with different pesticides at 50 mg kg^{-1}. (d) Photograph of the changes in solution colors under UV light (365 nm) according to the concentration in the ("e) plot" for Rho 6G@MOF in DMF. (e) Emission spectra of Rho 6G@MOF in DMF. (c) Fluorescence intensity of Rho 6G@MOF with different pesticides at 50 mg kg^{-1}. Adapted with permission from ref. 102 copyright (2020) Elsevier.

most porous framework with potential host–guest interaction (cages of 11.2 × 11.2 Å). The cadmium CP crystallizes in the monoclinic space group *C*2/*c*. The central ion has a distorted coordination geometry occupied by four N-atoms from the BA ligand in the equatorial positions. Axial positions are fulfilled by the ClO_4^- ions. The BA ligand acts a bridge assembling the two-dimensional net. The interaction of simazine with $\{[Cd(\mu_2\text{-}BA)_2(ClO_4)_2]\cdot n(DCM)\}n$ in MeCN provides a turn-off response in the luminescence properties (LOD = 4.783×10^{-7} M).[65] Thus, an exclusive selectivity could not be achieved since the CP also exhibited strong quenching for 2,4,6-trichloroanisole (TCA) (and for other nitrocompounds) under the same conditions.[65] Nevertheless, TCA is a secondary product from the microbial action on trichlorophenol used as a fungicide; although it has not been considered particularly toxic for humans, it is responsible for the appearance of corked wine fault in wines. The detection limit for TCA was as well calculated to be up to 6.13×10^{-8} M.[65]

Beyond organochlorine herbicides, "quats" have gained tremendous attention as nonselective and quick-acting weed killers.[67] The term quat comes from dicationic molecules containing a diquaternary bipyridyl motif, *e.g.* 1,1′-Dimethyl-4,4′-bipyridinium ((PQ) or paraquat), 6,7-dihydrodipyrido[1,2-*a*2′,1′-*c*]pyrazinediium ((DQ) or diquat), 1,1′-di-methyl-2,2′-bipyridinium (OQ), (Scheme 4) and 1,1′-bis(3,5-di-*tert*-butyl-benzyl)-4,4′-bipyridinium (TBPQ).[67] Its mechanism of action involves the quat species as an electron acceptor available from the plant photosynthetic system I (PSI), leading to the generation of radicals, which in turn react with molecular oxygen disrupting the photosynthetic process. In the case of humans, it is known that the direct exposure to PQ results in dangerous health consequences, which may include pulmonary fibrosis, pulmonary edema, erythema, dermatitis, mouth ulceration, kidney failure and brain damage.[67] In general, quats are considerably toxic and do not have a specific antidote.[68] Conveniently, Mukhopadhyay's group has designed a selective fluorescent "Zn-DBC" MOF capable of distinguishing between the dicationic bipyridinium salts, accordingly to its size and redox properties (Fig. 8).[67] The $[Zn_{1.5}(DBC)\cdot(H_2O)\cdot(DMF)\cdot Me_2NH_2]n$ crystals belong to the *Pbcn* space group. The asymmetric unit was found to contain 1.5 Zn(II) ions, one DBC linker, H_2O and DMF as crystallization molecules and one dimethylammonium (DMA) cation as a counter-ion for the charge balance in the anionic framework. This special feature allowed the 3D MOF to undergo a post-synthetic cation exchange with the dicationic quats. For this purpose, PQ, DQ, OQ, and TBPQ were investigated.[67] It is important to mention that the exchange process as well the luminescence studies occurred in water solution. A gradual decrease in the fluorescence intensity was observed for all the bipyridyl dications; however, DQ stood out from the rest. The authors justify the selectivity for diquat through the calculation of the reduction potential for all the series against the saturated calomel electrode (SCE) reference. The tendency goes as: OQ(−0.60 V) < PQ

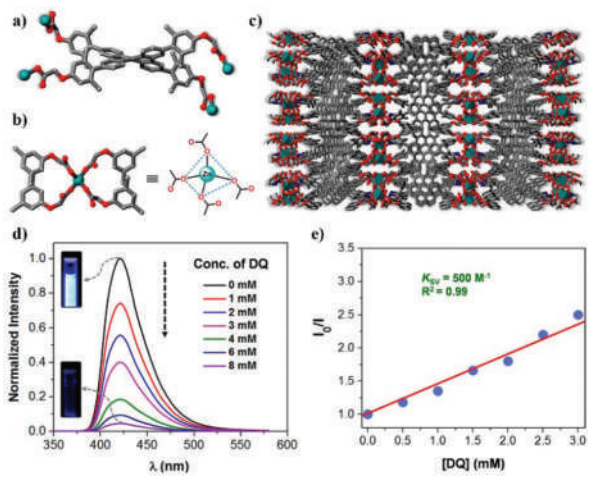

Fig. 8 (a) The coordination modes of the carboxylate groups of DBC and (b) the tetrahedral coordination environment of Zn(II) in Zn-DBC. (c) Crystal packing diagram of Zn-DBC down the *c* axis; note that Zn, O, and N atoms are represented in cyan, red, and blue, respectively. (d) Quenching of the fluorescence intensity of Zn-DBC with increasing concentration of DQ(PF6)2 in water (λ_{ex} = 350 nm) at rt. Note the changes in the fluorescence images (insets) of the aqueous dispersion of the MOF before and after quenching titration. (e) Corresponding Stern–Volmer quenching plot with increasing concentration of DQ. Adapted with permission from ref. 67 copyright (2020) American Chemical Society.

(−0.45 V) < TBPQ(−0.37 V) < DQ(−0.35 V). Unsurprisingly, DQ showed the lowest fluorescence intensity (according to the PET mechanism), as PQ and OQ followed the expected behaviour. TBPQ, on the other hand, showed almost no turn-off effect in the luminescent material. Here is where the size comes to place. Due to the highly hindered *tert*-butyl groups of TBPQ, its transportation to the accessible voids in the crystal was more difficult minimizing its interaction with the MOF, highlighting its size-selective character. The LOD for diquat was estimated to be 1.52×10^{-5} M.[67] An honorific mention corresponds to the NKU-101 [93] MOF, where, in an almost identical manner, this anionic framework suffered from the post-synthetic cation exchange of diethylammonium with PQ. Nonetheless, the PQ determination was only carried out by the UV-Vis technique.[93]

Quats fluorescence recognition is not limited exclusively to anionic frameworks, neutral frameworks such as $[Zn_2(cptpy)(btc)(H_2O)]n$ (cptpy = 4-(4-carboxyphenyl)-2,2′:4′,4″-terpyridine; btc = 1,3,5-benzenetricarboxylic acid) has proved its competence as well.[68] The Zn-MOF crystallized in the $P2_1/c$ space group. Two crystallographically independent Zn(II) ions, one coordinated water molecule, one cptpy ligand and one btc ligand integrated the asymmetric unit. The two Zn(II) ions showed different coordination geometries. Zn1 shows a tetrahedral environment, whilst the geometry of Zn2 is defined as a pentacoordinate square pyramid. One-dimensional chains are generated by adjacent Zn1 and Zn2 atoms alternately connected through btc ligands. At the same time, the neighboring Zn1 and Zn2 atoms were bridged by cptpy ligands to form 2D layers. As a result, the 1D chains and 2D layers were inter-connected with each other to produce a 3D framework with 1D channels in all three directions.[68] The luminescence intensity of $[Zn_2(cptpy)(btc)(H_2O)]n$ weakened almost completely after the addition of PQ in water solution. Unfortunately, no further herbicide or pesticide was analyzed to appreciate the complete discriminatory potential against these pollutants. The quenching mechanism could have occurred by a PET process since the UV-Vis absorption spectra of PQ show a large overlap with the excitation spectrum of the MOF. Moreover, the authors suggested that hydrogen bonds and interactions could also be responsible for quenching.[68]

Alongside pesticides and herbicides, it is one of our deepest interest to enrich the luminescence detection of environmental hazardous compounds by complementing the ion sensing reported previously in the relevant literature[20,27,28] with the scarcely mentioned cyanide ion. Compared to the very toxic heavy-metal ions, CN^- can lead to the death of humans and aquatic life in minutes. The lethal effect of cyanide in physiological systems lies in the inhibition of respiration in the mitochondrial respiratory chain, occasioned by the cyanide binding to the Fe^{3+} ion of cytochrome oxidase, affecting the normal functioning of the lungs and brain.[69,70] Nowadays, the luminescence recognition of the CN^- ion by applying coordination framework materials is still very rare.[35] Nevertheless, recent achievements have come to light in three distinctive compounds based on Zn(II) ions. The first one is a one-dimensional CP with the formula $\{[Zn_2(H_2O)_2(e,a\text{-}cis\text{-}1,4\text{-}chdc)_2(4,4'\text{-}dtbb)_2]\cdot 7H_2O\}n$, 1,4-chdc = 1,4-cyclohexanedicarboxylato, 4,4′-dtbb = 4,4′-di-*tert*-butyl-2,2′-bipyridine, which crystallizes in the *Pn* space group with two Zn(II) ions, two *e*,*a*-*cis* 1,4-chdc, two 4,4′-dtbb, two aqua ligands, and seven lattice water molecules in its asymmetric unit. The two crystallographically different Zn(II) ions have a distorted octahedral configuration with a similar coordination environment surrounded by four oxygen atoms from two different 1,4-chdc ligands and the aqua ligand, and two nitrogen atoms from one 4,4′-dtbb. Each 1D polymer chain is formed as a result of the combined monodentate η^1 and chelate bidentate η^2 coordination modes of 1,4-chdc, along with the *e*,*a*-*cis* conformation of its carboxylate groups connecting the metal centers in a characteristically V-shaped fashion (Fig. 9). Simultaneously, both 1D chains are attached together by several hydrogen bonds from the lattice water molecules. The presence of competing anions (F^-, Cl^-, Br^-, I^-, AcO^-, NO_3^-, NO_2^-, $H_2PO_4^-$, $H_3P_2O_7^-$, HCO_3^-, $H_2AsO_4^-$ and SO_4^{2-}) displays almost an exclusive prominent turn-off response for the cyanide ion in pure water at different pH values (LOD = 9×10^{-8} M in pH = 7.0). The explanation behind this quenching behavior was attributed to the displacement of the ligands in the CP for the cyanide ion to form $Zn(CN)_2$, which was demonstrated by IR and SEM techniques with the solid residue, while in the aqueous phase the presence of the ligands was verified by ^1H NMR and MS-ESI(+) methods.[71]

Alternatively, Ghosh *et al.* have focused on the post-synthetically modifications of ZIF-90 and bio-MOF-1 for the cyanide

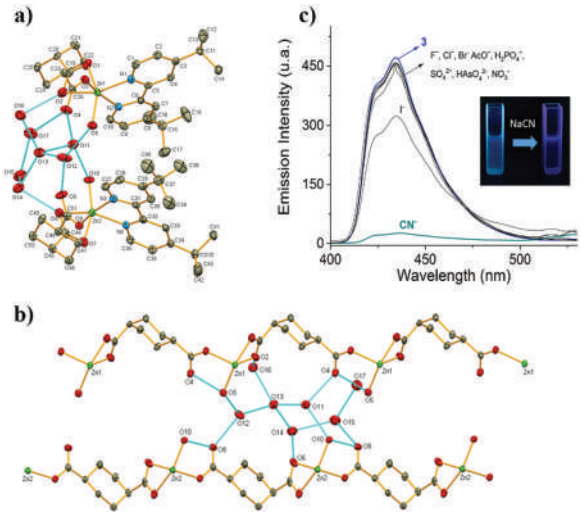

Fig. 9 (a) Supramolecular dinuclear repeating unit of $\{[Zn_2(H_2O)_2(e,a\text{-}cis\text{-}1,4\text{-}chdc)_2(4,4'\text{-}dtbb)_2]\cdot 7H_2O\}n$ (ellipsoids shown at 60% probability); hydrogens are omitted for clarity. (b) 1D V-shaped dual-polymer chain of $\{[Zn_2(H_2O)_2(e,a\text{-}cis\text{-}1,4\text{-}chdc)_2(4,4'\text{-}dtbb)_2]\cdot 7H_2O\}n$; hydrogens and 4,4′-dtbb ligands are omitted for clarity. (c) Photoluminescence spectral changes of the CP upon addition of 10 equiv. of different anions. The inset shows a picture taken under irradiation with 365 nm UV light in the absence and presence of CN^-. Adapted with permission from ref. 71 copyright (2020) The Royal Society of Chemistry.

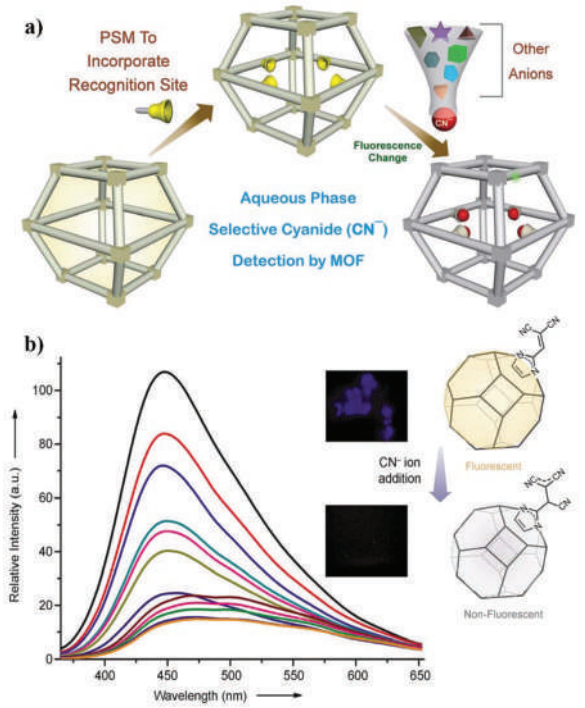

Fig. 10 (a) Schematic overview of the post-synthetic modification in the MOF leading to the selective sensing of the cyanide ion. (b) Fluorescence response of M-ZIF-90 upon incremental addition of CN^- ions showing a turn-off response. The inset shows confocal images before and after the addition of CN^-. Adapted with permission from ref. 69 copyright (2016) Wiley Online Library.

sensing.[35,69,70] In the particular case of ZIF-90 (Fig. 10),[69] as the structure possesses an aldehyde group aligned within the pores of the extended 3D sodalite framework, the ZIF undergoes a Knoevenagel reaction with malononitrile, transforming the aldehyde group into a dicyanovinyl group with the retention of crystallinity (M-ZIF-90).[69] Herein, the dicyanovinyl group undergoes a nucleophilic addition of cyanide, resulting in a significant quenching effect, justified by the loss of conjugation in the dicyanovinyl group and also supported by the electronic potential maps of the LUMO and HOMO energy states of the ligand. Furthermore, no interference from other anions was observed as F^-, Cl^-, Br^-, N_3^-, SCN^-, NO_3^- and NO_2^- were analysed in DMSO–H_2O (1 : 1) medium.[69] A different strategy was followed for the corresponding bio-MOF-1. Due to its inherent 3D anionic porous architecture, successive cation exchange between dimethylammonium, 3,6-diaminoacridinium (DAAC) and tetrabutylammonium (TBA) was successfully attempted. In the first stage, the original counter-ion in bio-MOF-1 (DMA) was switched by the cationic dye DAAC. Once loaded in the MOF, DAAC is susceptible to attack by the nucleophilic cyanide ion of the TBACN salt, *via* Michael type addition, rendering a neutral dye and once again exchanging the counter-ion DAAC for TBA. The release of the neutral cyanide containing dye promotes the turn-on response in the fluorescence with great selectivity, and even *in vitro* studies could be performed with human breast cancer cell lines (MCF-7), monitoring the trace of cyanide inside the cytoplasm with a limit of detection equal to 1.9×10^{-8} M.[35]

Significantly, other luminescent coordination frameworks have turned their focus on the recognition of pesticides, herbicides and the cyanide ion and those valuable contributions are listed in Table 1.

Conclusions

At times where the vulnerability of humans due to dangerous biomolecules or chemical substances is evident, it is of the upmost necessity to continue developing functional compounds and materials with synergy among their chemical, structural and optical properties to become sensitive instant probes aimed at the detection of these unwanted compounds. Hence, Zn(II) and Cd(II) CPs and MOFs are at the forefront as luminescent sensors due, mainly, to their straightforward synthesis, and also due to their crystalline and modifiable structures, which by simply tuning the ligands' chemical nature, can favour optical and textural (*i.e.*, porosity) properties effective in chemosensing through host–guest interactions.

Moreover, many luminescent Zn and Cd coordination arrays have been demonstrated to be stable enough for convenient, affordable, sensitive, and sometimes selective and reusable, immediate sensing of divergent analytes both in water and organic solvent media. Although new substitute less-toxic chemicals can be developed and stricter environmental regulations can be implemented, without doubt, poisonous chemicals such as pesticides, herbicides and cyanide, will be around us for some time, demanding, at least, facile, rapid and low-cost detection of those substances. Therefore, the advancement in the design of novel luminescent Zn and Cd coordination arrays that can be stable predominantly in the aqueous environment is gaining relevance since water sources around the world are frequently, and increasingly, polluted with these types of hazardous and toxic compounds.

Finally, it is also significant to be aware of those opening areas of research that this topic offers, among them perhaps the more appealing are the following: thorough studies of the mechanisms behind the photoluminescence sensing phenomena, using in cooperation empirical and theoretical approaches; the creation of new Zn and Cd coordination networks with the capability of high sensitivity and, most importantly, selectivity towards a certain substance or analyte.

In a nutshell, the development of sensitive, selective and reusable Zn and Cd luminescent chemosensors can provide new directions toward real-time detection and quantification of industrially and environmentally relevant molecules with real-life applications.

Conflicts of interest

There are no conflicts to declare.

Acknowledgements

VSM thanks Universidad Autónoma del Estado de México for funding (Project: 6171/2020CIB). The authors thank UNAM (DGAPA-PAPIIT-216220). LDRV thanks CONACyT for the PhD scholarship (713164).

Notes and references

1 S. Kitagawa and R. Matsuda, *Coord. Chem. Rev.*, 2007, **251**, 2490–2509.
2 W. L. Leong and J. J. Vittal, *Chem. Rev.*, 2011, **111**, 688–764.
3 X. Zhang, W. Wang, Z. Hu, G. Wang and K. Uvdal, *Coord. Chem. Rev.*, 2015, **284**, 206–235.
4 M. Mon, R. Bruno, J. Ferrando-Soria, D. Armentano and E. Pardo, *J. Mater. Chem. A*, 2018, **6**, 4912–4947.
5 W. P. Lustig, S. Mukherjee, N. D. Rudd, A. V. Desai, J. Li and S. K. Ghosh, *Chem. Soc. Rev.*, 2017, **46**, 3242–3285.
6 H. L. Nguyen, C. Gropp and O. M. Yaghi, *J. Am. Chem. Soc.*, 2020, **142**, 2771–2776.
7 X. Cai, Z. Xie, D. Li, M. Kassymova, S. Q. Zang and H. L. Jiang, *Coord. Chem. Rev.*, 2020, **417**, 213366.
8 S. R. Batten and K. S. Murray, *Coord. Chem. Rev.*, 2003, **246**, 103–130.
9 E. Loukopoulos and G. E. Kostakis, *J. Coord. Chem.*, 2018, **71**, 371–410.
10 K. A. Cychosz, A. G. Wong-Foy and A. J. Matzger, *J. Am. Chem. Soc.*, 2008, **130**, 6938–6939.
11 J. Duan, W. Jin and S. Kitagawa, *Coord. Chem. Rev.*, 2017, **332**, 48–74.
12 J. Heine and K. Müller-Buschbaum, *Chem. Soc. Rev.*, 2013, **42**, 9232–9242.
13 A. Erxleben, *Coord. Chem. Rev.*, 2003, **246**, 203–228.
14 A. M. Cheplakova, K. A. Kovalenko, D. G. Samsonenko, A. S. Vinogradov, V. M. Karpov, V. E. Platonov and V. P. Fedin, *CrystEngComm*, 2019, **21**, 2524–2533.
15 Y. S. Shi, Q. Q. Xiao, L. Fu and G. H. Cui, *CrystEngComm*, 2020, **22**, 4875–4886.
16 D. J. Tranchemontagne, J. L. Tranchemontagne, M. O′ keeffe and O. M. Yaghi, *Chem. Soc. Rev.*, 2009, **38**, 1257–1283.
17 A. Schoedel, M. Li, D. Li, M. O'Keeffe and O. M. Yaghi, *Chem. Rev.*, 2016, **116**, 12466–12535.
18 M. Ui, Y. Tanaka, Y. Araki, T. Wada, T. Takei, K. Tsumoto, S. Endo and K. Kinbara, *Chem. Commun.*, 2012, **48**, 4764–4766.
19 B. Parmar, K. K. Bisht, Y. Rachuri and E. Suresh, *Inorg. Chem. Front.*, 2020, **7**, 1082–1107.
20 T. Rasheed and F. Nabeel, *Coord. Chem. Rev.*, 2019, **401**, 213065.
21 H. Y. Li, S. N. Zhao, S. Q. Zang and J. Li, *Chem. Soc. Rev.*, 2020, **49**, 6364–6401.
22 K. Vikrant, D. C. W. Tsang, N. Raza, B. S. Giri, D. Kukkar and K. H. Kim, *ACS Appl. Mater. Interfaces*, 2018, **10**, 8797–8817.
23 L. Wang, K. He, H. Quan, X. Wang, Q. Wang and X. Xu, *Microchem. J.*, 2020, **153**, 104441.
24 L. Di, Z. Xia, J. Li, Z. Geng, C. Li, Y. Xing and Z. Yang, *RSC Adv.*, 2019, **9**, 38469–38476.
25 C. X. Yu, F. L. Hu, J. G. Song, J. L. Zhang, S. S. Liu, B. X. Wang, H. Meng, L. L. Liu and L. F. Ma, *Sens. Actuators, B*, 2020, **310**, 127819.
26 Y. Zhao, X. Xu, L. Qiu, X. Kang, L. Wen and B. Zhang, *ACS Appl. Mater. Interfaces*, 2017, **9**, 15164–15175.
27 S. Wu, H. Min, W. Shi and P. Cheng, *Adv. Mater.*, 2020, **32**, 1805871.
28 G. Liu, Y. Li, J. Chi, N. Xu, X. Wang, H. Lin, B. Chen and J. Li, *Dalton Trans.*, 2020, **49**, 737–749.
29 X. Y. Guo, Z. P. Dong, F. Zhao, Z. L. Liu and Y. Q. Wang, *New J. Chem.*, 2019, **43**, 2353–2361.
30 M. Li, D. Li, M. O'Keeffe and O. M. Yaghi, *Chem. Rev.*, 2014, **114**, 1343–1370.
31 X. Wang, C. Qin, E. Wang, Y. Li, N. Hao, C. Hu and L. Xu, *Inorg. Chem.*, 2004, **43**, 1850–1856.
32 K. Xing, R. Fan, S. Gao, X. Wang, X. Du, P. Wang, R. Fang and Y. Yang, *Dalton Trans.*, 2016, **45**, 4863–4878.
33 Y. Rachuri, K. K. Bisht, B. Parmar and E. Suresh, *J. Solid State Chem.*, 2015, **223**, 23–31.
34 M. Pamei and A. Puzari, *Nano-Struct. Nano-Objects*, 2019, **19**, 100364.
35 A. Karmakar, P. Samanta, S. Dutta and S. K. Ghosh, *Chem. – Asian J.*, 2019, **14**, 4506–4519.
36 L. Yang, Y. Song and L. Wang, *J. Mater. Chem. B*, 2020, **8**, 3292–3315.
37 X. Q. Wang, D. D. Feng, J. Tang, Y. Di Zhao, J. Li, J. Yang, C. K. Kim and F. Su, *Dalton Trans.*, 2019, **48**, 16776–16785.
38 Y. Li, D. Ma, C. Chen, M. Chen, Z. Li, Y. Wu, S. Zhu and G. Peng, *J. Solid State Chem.*, 2019, **269**, 257–263.
39 P. Kumar, A. Deep and K.-H. Kim, *TrAC, Trends Anal. Chem.*, 2015, **73**, 39–53.
40 T. Y. Gu, M. Dai, D. J. Young, Z. G. Ren and J. P. Lang, *Inorg. Chem.*, 2017, **56**, 4668–4678.
41 L.-T. Wu, Z.-J. Wang, X. Wu, C.-Y. Zhou, F. Su and C. Han, *Acta Crystallogr., Sect. C: Cryst. Struct. Commun.*, 2019, **75**, 141–149.
42 R. Goswami, S. C. Mandal, B. Pathak and S. Neogi, *ACS Appl. Mater. Interfaces*, 2019, **11**, 9042–9053.
43 P. Chandrasekhar, A. Mukhopadhyay, G. Savitha and J. N. Moorthy, *Chem. Sci.*, 2016, **7**, 3085–3091.
44 L. Zhang, Z. Kang, X. Xin and D. Sun, *CrystEngComm*, 2016, **18**, 193–206.
45 X. Zhang, X. Zhuang, N. Zhang, C. Ge, X. Luo, J. Li, J. Wu, Q. Yang and R. Liu, *CrystEngComm*, 2019, **21**, 1948–1955.
46 J. H. Qin, Y. D. Huang, M. Y. Shi, H. R. Wang, M. Le Han, X. G. Yang, F. F. Li and L. F. Ma, *RSC Adv.*, 2020, **10**, 1439–1446.
47 R. Dalapati and S. Biswas, *Sens. Actuators, B*, 2017, **239**, 759–767.
48 S. L. Jackson, A. Rananaware, C. Rix, S. V. Bhosale and K. Latham, *Cryst. Growth Des.*, 2016, **16**, 3067–3071.

49 J. Zhang, X. Zhang, J. Chen, C. Deng, N. Xu, W. Shi and P. Cheng, *Inorg. Chem. Commun.*, 2016, **69**, 1–3.
50 H. Zhang, J. Ma, D. Chen, J. Zhou, S. Zhang, W. Shi and P. Cheng, *J. Mater. Chem. A*, 2014, **2**, 20450–20453.
51 L. G. Qiu, Z. Q. Li, Y. Wu, W. Wang, T. Xu and X. Jiang, *Chem. Commun.*, 2008, 3642–3644.
52 C. Li, W. Yang, X. Zhang, Y. Han, W. Tang, T. Yue and Z. Li, *J. Mater. Chem. C*, 2020, **8**, 2054–2064.
53 X. Q. Yao, G. B. Xiao, H. Xie, D. D. Qin, H. C. Ma, J. C. Liu and P. J. Yan, *CrystEngComm*, 2019, **21**, 2559–2570.
54 Z. Liao, T. Xia, E. Yu and Y. Cui, *Crystals*, 2018, **8**, 338.
55 Y. M. Ying, C. L. Tao, M. Yu, Y. Xiong, C. R. Guo, X. G. Liu and Z. Zhao, *J. Mater. Chem. C*, 2019, **7**, 8383–8388.
56 Y. Liu, X. Y. Xie, C. Cheng, Z. S. Shao and H. S. Wang, *J. Mater. Chem. C*, 2019, **7**, 10743–10763.
57 P. Kumar, A. K. Paul and A. Deep, *Microporous Mesoporous Mater.*, 2014, **195**, 60–66.
58 P. Kumar, K. H. Kim, V. Bansal, A. K. Paul and A. Deep, *Microchem. J.*, 2016, **128**, 102–107.
59 D. K. Singha, P. Majee, S. Mandal, S. K. Mondal and P. Mahata, *Inorg. Chem.*, 2018, **57**, 12155–12165.
60 D. K. Singha, P. Majee, S. K. Mondal and P. Mahata, *ChemistrySelect*, 2017, **2**, 5760–5768.
61 J. C. Jin, Y. J. Zhu, J. Li, Y. L. Zhang and C. G. Xie, *Inorg. Chem. Commun.*, 2020, **119**, 108062.
62 L. Q. Zhang, X. W. Wang, L. Gu, Y. H. Yu and J. S. Gao, *RSC Adv.*, 2020, **10**, 9476–9485.
63 T. Kumar, M. Venkateswarulu, B. Das, A. Halder and R. R. Koner, *Dalton Trans.*, 2019, **48**, 12382–12385.
64 L. Yang, Y. L. Liu, C. G. Liu, F. Ye and Y. Fu, *J. Hazard. Mater.*, 2020, **381**, 120966.
65 S. I. Vasylevskyi, D. M. Bassani and K. M. Fromm, *Inorg. Chem.*, 2019, **58**, 5646–5653.
66 A. Mohanty, U. P. Singh, R. J. Butcher, N. Das and P. Roy, *CrystEngComm*, 2020, **22**, 4468–4477.
67 A. Mukhopadhyay, S. Jindal, G. Savitha and J. N. Moorthy, *Inorg. Chem.*, 2020, **59**, 6202–6213.
68 H. Chen, P. Fan, X. Tu, H. Min, X. Yu, X. Li, J. L. Zeng, S. Zhang and P. Cheng, *Chem. – Asian J.*, 2019, **14**, 3611–3619.
69 A. Karmakar, N. Kumar, P. Samanta, A. V. Desai and S. K. Ghosh, *Chem. – Eur. J.*, 2016, **22**, 864–868.
70 A. Karmakar, B. Joarder, A. Mallick, P. Samanta, A. V. Desai, S. Basu and S. K. Ghosh, *Chem. Commun.*, 2017, **53**, 1253–1256.
71 L. D. Rosales-Vázquez, J. Valdes-García, I. J. Bazany-Rodríguez, J. M. Germán-Acacio, D. Martínez-Otero, A. R. Vilchis-Néstor, R. Morales-Luckie, V. Sánchez-Mendieta and A. Dorazco-González, *Dalton Trans.*, 2019, **48**, 12407–12420.
72 X. Zheng, L. Zhou, Y. Huang, C. Wang, J. Duan, L. Wen, Z. Tian and D. Li, *J. Mater. Chem. A*, 2014, **2**, 12413–12422.
73 L. Wen, X. Xu, K. Lv, Y. Huang, X. Zheng, L. Zhou, R. Sun and D. Li, *ACS Appl. Mater. Interfaces*, 2015, **7**, 4449–4455.
74 N. C. Burtch, H. Jasuja and K. S. Walton, *Chem. Rev.*, 2014, **114**, 10575–10612.
75 J.-H. Wang, M. Li and D. Li, *Chem. Sci.*, 2013, **4**, 1793.
76 K. P. Kepp, *J. Phys. Chem. A*, 2019, **123**, 6536–6546.
77 V. Colombo, S. Galli, H. J. Choi, G. D. Han, A. Maspero, G. Palmisano, N. Masciocchi and J. R. Long, *Chem. Sci.*, 2011, **2**, 1311–1319.
78 M. D. Allendorf, C. A. Bauer, R. K. Bhakta and R. J. T. Houk, *Chem. Soc. Rev.*, 2009, **38**, 1330–1352.
79 J. Dong, D. Zhao, Y. Lu and W. Y. Sun, *J. Mater. Chem. A*, 2019, **7**, 22744–22767.
80 L. D. Rosales-Vázquez, V. Sánchez-Mendieta, A. Dorazco-González, D. Martínez-Otero, I. García-Orozco, R. A. Morales-Luckie, J. Jaramillo-Garcia and A. Téllez-López, *Dalton Trans.*, 2017, **46**, 12516–12526.
81 K. Müller-Buschbaum, F. Beuerle and C. Feldmann, *Microporous Mesoporous Mater.*, 2014, **216**, 171–199.
82 Y. Wu, G.-P. Yang, X. Zhou, J. Li, Y. Ning and Y.-Y. Wang, *Dalton Trans.*, 2015, **44**, 10385–10391.
83 R. Feng, F. L. Jiang, L. Chen, C. F. Yan, M. Y. Wu and M. C. Hong, *Chem. Commun.*, 2009, 5296–5298.
84 J. C. Rendón-Balboa, L. Villanueva-Sánchez, L. D. Rosales-Vázquez, J. Valdes-García, A. R. Vilchis-Nestor, D. Martínez-Otero, S. Martínez-Vargas and A. Dorazco-González, *Inorg. Chim. Acta*, 2018, **483**, 235–240.
85 G. K. Sidhu, S. Singh, V. Kumar, D. S. Dhanjal, S. Datta and J. Singh, *Crit. Rev. Environ. Sci. Technol.*, 2019, **49**, 1135–1187.
86 X. Xu, Y. Guo, X. Wang, W. Li, P. Qi, Z. Wang, X. Wang, S. Gunasekaran and Q. Wang, *Sens. Actuators, B*, 2018, **260**, 339–345.
87 I. J. Bazany-Rodríguez, D. Martínez-Otero, J. Barroso-Flores, A. K. Yatsimirsky and A. Dorazco-González, *Sens. Actuators, B*, 2015, **221**, 1348–1355.
88 H. Sun, Y. Y. Zhang, S. H. Si, D. R. Zhu and Y. S. Fung, *Sens. Actuators, B*, 2005, **108**, 925–932.
89 Y. Liu, K. Ai, X. Cheng, L. Huo and L. Lu, *Adv. Funct. Mater.*, 2010, **20**, 951–956.
90 M. Jaishankar, T. Tseten, N. Anbalagan, B. B. Mathew and K. N. Beeregowda, *Interdiscip. Toxicol.*, 2014, **7**, 60–72.
91 J. Ma and P. K. Dasgupta, *Anal. Chim. Acta*, 2010, **673**, 117–125.
92 L. Yang, L. Cao, X. Li, C. Qin, L. Zhao, K. Z. Shao and Z. M. Su, *Dalton Trans.*, 2017, **46**, 7567–7576.
93 Y. Y. Jia, Y. H. Zhang, J. Xu, R. Feng, M. S. Zhang and X. H. Bu, *Chem. Commun.*, 2015, **51**, 17439–17442.
94 World Health Organization, *Guidelines for drinking-water quality: fourth edition incorporating the first addendum*, Switzerland, 4th edn, 2017.
95 Codex Alimentarius, Pesticides | CODEXALIMENTARIUS FAO-WHO, http://www.fao.org/fao-who-codexalimentarius/thematic-areas/pesticides/en/#c452840, (accessed 19 February 2021).
96 C. S. Wang, Q. Huang, X. Wang, Y. T. Zhang, D. S. Ma, Y. H. Yu and J. S. Gao, *RSC Adv.*, 2019, **9**, 42272–42283.
97 D. Feng, J. Tang, J. Yang, X. Ma, C. Fan and X. Wang, *J. Mol. Struct.*, 2020, **1221**, 128841.

98 L. Fan, F. Wang, D. Zhao, X. Sun, H. Chen, H. Wang and X. Zhang, *Spectrochim. Acta, Part A*, 2020, **239**, 118467.
99 L. Fan, F. Wang, D. Zhao, Y. Peng, Y. Deng, Y. Luo and X. Zhang, *Appl. Organomet. Chem.*, 2020, **34**, 1–10.
100 C. L. Tao, B. Chen, X. G. Liu, L. J. Zhou, X. L. Zhu, J. Cao, Z. G. Gu, Z. Zhao, L. Shen and B. Z. Tang, *Chem. Commun.*, 2017, **53**, 9975–9978.
101 N. Xu, Q. Zhang and G. Zhang, *Dalton Trans.*, 2019, **48**, 2683–2691.
102 L. Yang, Y. L. Liu, C. G. Liu, F. Ye and Y. Fu, *J. Hazard. Mater.*, 2020, **381**, 120966.
103 J. Valdes-García, L. D. Rosales-Vazquez, I. J. Bazany-Rodríguez and A. Dorazco-González, *Chem. – Asian J.*, 2020, **15**, 2925–2938.

SUSTAINABLE MATERIALS FOR SENSING AND REMEDIATION OF NOXIOUS POLLUTANTS

EDITED BY
INDERJEET TYAGI
JOANNA GOSCIANSKA
MOHAMMAD HADI DEHGHANI
RAMA RAO KARRI

ELSEVIER

Chapter 12

Luminescent metal-organic frameworks for sensing of toxic organic pollutants in water and real samples

Luis D. Rosales-Vázquez[a], Alejandro Dorazco-González[a,*], and Víctor Sánchez-Mendieta[b]

[a]*Institute of Chemistry, National Autonomous University of Mexico, Mexico City, Mexico,* [b]*CCIQS—Joint Center for Research in Sustainable Chemistry UAEM-UNAM, Toluca, Estado de México, Mexico*

[*]*Corresponding author: A. D.-G.*

1 Introduction

In the coming years, food production and supply are considered two of the most important and challenging issues, mainly, due to the ever-increasing problem of maintaining the production rate as the world population increases.[1] Since decades ago, the growing of crops, fruits, and vegetables, principally, have been challenging to achieve without the application of chemicals, for instance, pesticides and herbicides. Despite emerging techniques to produce more efficiently and trying to avoid the treatment with those hazardous chemicals, to this day, most of the world's production of vegetable-origin food stocks makes use of them.[2] Consequently, it will surely take several years more before an effective and massive food production process could eliminate the usage of pesticides and herbicides. Due to the well-known health implications that these noxious chemicals provoke in humans and animals, it is relevant to have analytical tools that detect toxic organic pollutants in our food and the water used for irrigation in their production.[3] Moreover, it has been acknowledged that only around 1% of the applied pesticides reach the aimed application.[4] The remaining 99% of the used pesticides and herbicides tend to bioaccumulate and reach water sources, triggering irreversible damage and extending to humans as serious health-related problems, usually via the food chain.[4–8]

Currently, few analytical techniques can detect pesticides and herbicides, with good sensitivity and detection limit, in diverse media. However, methods like gas chromatography, surface-enhanced Raman spectroscopy, mass spectrometry, among others, are challenging to perform in situ since they usually require special sample preparation and expensive equipment.[9–11] Here is where luminescence analytical tools come as very efficient and simpler detection techniques of organic compounds, particularly those, that can be harmful to humans and the environment by their chemical nature. In recent years, photoluminescence has been demonstrated to be an efficient, highly sensitive, and selective method for the sensing of widespread types of substances ranging from metal ions, inorganic and organic anions, solvents, and explosives, to more complex organic molecules.[12]

Luminescent-sensing techniques require probe compounds that could possess luminescence properties. Among the divergent chemical structures found in luminescent compounds, metal-organic frameworks (MOFs) have lately delivered outstanding results as fast, highly selective, sensitive, and sometimes, recyclable luminescent probes of a great variety of analytes.[13] Nowadays, crystalline CPs and MOFs are used as fine luminescent chemosensors due to two main advantages. Firstly, their relatively facile structural changes can be performed based on coordination chemistry principles, which can tune their luminescent properties. Secondly, the fact that there are increasingly examples of these coordination arrays that are becoming more stable in water, is a desirable condition for practical applications as luminescent sensors, particularly, on real samples. Many MOFs having luminescent properties are assembled using mixed ligands, among them, the aromatic carboxylates and N-donor π-conjugated ligands are the most used. Thus, the luminescence process in these systems can occur mainly from processes such as ligand-centered emission (LC), metal-centered emission (MC), ligand-to-metal charge transfer (LMCT), metal-to-ligand charge transfer (MLCT), and ligand-to-ligand charge transfer (LLCT) mechanisms. The most frequent emissions reported for Zn(II)- and Cd(II)-MOFs are related to LC, LMCT, and LLCT processes.[14,15]

Sustainable Materials for Sensing and Remediation of Noxious Pollutants. https://doi.org/10.1016/B978-0-323-99425-5.00005-0

Hence, this chapter emphasizes contemporary developments of the application and efficiency of luminescent Zn(II)- and Cd(II)-MOFs as low-cost fluorescent sensors to detect pesticides and herbicides in water and real samples, such as fruits and vegetables. Thus, aiming these functional hybrid materials could efficiently detect and ultimately help control these dangerous pollutants, diminishing their undesired consequences on the environment and human health.

2 General features for the design of LMOF in the detection of pesticides and herbicides

The general strategy for the development of Zn(II) and Cd(II)-LMOFs with application in optical detection of common pesticides and herbicides has to include light-emitting materials with the following features.

(1) Chemical stability in complex samples and real-world samples (e.g., irrigation water, lake water, fruits, vegetables, and physiological samples); (2) stable photoluminescence units; and (3) complementary interaction sites with pesticides capable of inducing a selective binding process and analytical response. These general characteristics are shown in Fig. 1.[16]

2.1 Water stability in Zn(II)-, Cd(II)-LMOFs

Zn(II)- and Cd(II)-LMOFs have been extensively used as chemosensors for selective quantification of inorganic anions (halides, oxyanion),[17,18] metal ions,[19–23] explosives based on nitroaromatic derivatives,[24–26] volatile organic compounds,[27,28] amino acids,[29–31] pollutant gases,[32] and antibiotics.[33–35] The literature features relative few examples of chemosensors based on Zn(II)- and Cd(II)-LMOFs for the detection of common pesticides (Fig. 2) such as parathion,[36] azinphos-methyl,[37,38] 2,6-dichloro-4nitroaniline,[39] parathion-methyl,[40,41] acephate,[42] and chlorpyrifos[43] in real-world samples (e.g., irrigation water, lake water, tap water, fruits, vegetables, and living cells).

Despite considerable progress, some analytical parameters, such as an efficient luminescent response and sensitivity in complex samples, remain a central challenge in these systems.

Water stability of LMOFs is a crucial property and requisite when considering these compounds for luminescent sensing applications in real-world samples.

In general, a water-stable MOF is a compound that can be handled in aqueous media without any change in its structure. The water stability can be probed experimentally by exposing the LMOFs in contact with water and subsequent comparison of the structural and spectroscopic properties before and after water contact through spectroscopic tools (e.g., fluorescence spectroscopy, Raman, IR spectroscopy, X-ray photoelectron spectroscopy, and powder X-ray diffraction).[44,45]

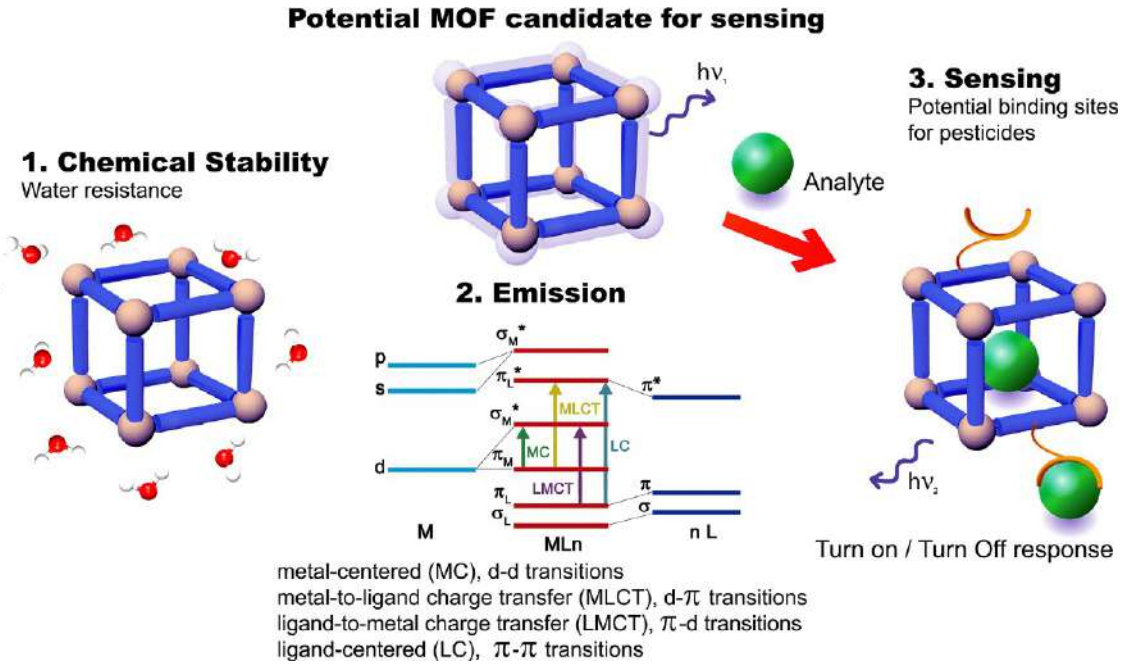

FIG. 1 The general strategy for the design of LMOFs with application in the luminescent detection of pesticides and herbicides, considering of relevance of (1) chemical stability in water, (2) emission processes, and (3) binding sites for the analyte.

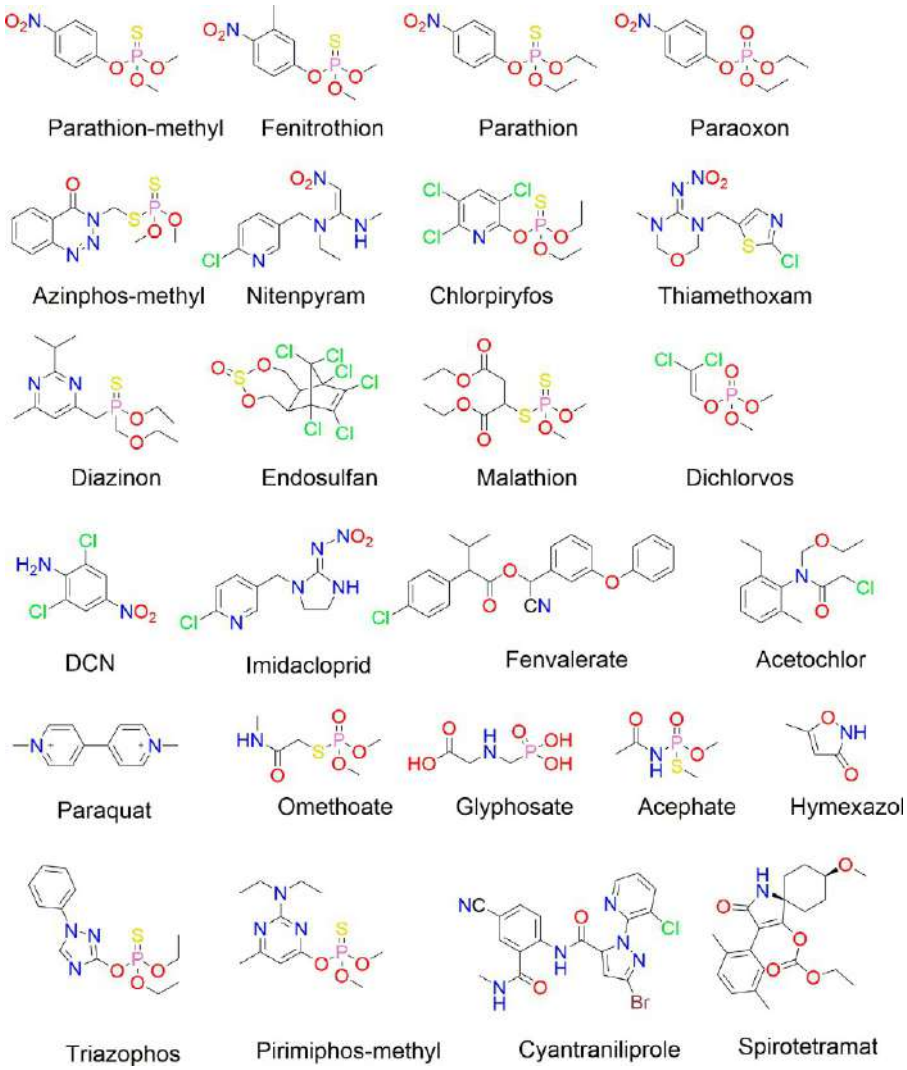

FIG. 2 Structure of common herbicides and pesticides.

In structural and thermodynamic terms, water-stable LMOFs comprehend a suitable combination of inert organic linkers and hydrostable metal clusters, which makes energetically unfavorable the following hydrolysis reaction.

$$\Delta G_{\text{hyd}} = \Delta G_{\text{prod}}(\text{LMOF} + n\text{H}_2\text{O}) + \Delta G_{\text{react}}(\text{LMOF} + n\text{H}_2\text{O})$$

where ΔG_{prod} is the Gibbs free energy of the LMOF, formed between the LMOF and the water after the hydrolysis process takes place, and ΔG_{react} is the Gibbs free energy of the LMOF and the water molecules before the hydrolysis occurs.

In these compounds, the strength of metal-ligand coordination bonds can be a strong indicator of their hydrolytic stability. The major drawback of synthetic LMOFs is that their metal-ligand bond strength is lower than natural zeolite frameworks based on aluminosilicate minerals.[45]

Hence, the water stability of the MOFs requires sufficient metal-ligand binding Gibbs free energy to overcome the very high hydration energies of divalent Zn and Cd ions ($-\Delta G^0 = 2040$ and -1840 kJmol^{-1} for Zn(II) and Cd(II), respectively).[46]

2.2 Emission

The origin of the emission of LMOFs based on d^{10} transition metals that include π-conjugated carboxylates ligands and N-donor ligands stems from photophysical mechanisms such as follows: (1) ligand-centered photoemission (LC),

(2) metal-centered photoemission (MC), (3) ligand-to-metal charge transfers (LMCTs), (4) metal-to-ligand charge transfers (MLCTs), and (5) ligand-to-ligand charged transfers (LLCTs). The electronic transitions involved in the photoluminescence mechanisms of Zn(II)- and Cd(II)-based LMOFs are depicted in Fig. 1. To understand the general concepts of these photoluminescence phenomena, the readers are referred to particular reviews on this issue.[13,15,16]

Among these emission processes, the most commonly reported for LMOFs containing divalent Zn and Cd ions are ligand-centered photoemission and charge transfers.[16,45] Metal-centered photoemission is exhibited particularly when MOFs have metal clusters with high nuclearity as nodes. Ligand-centered photoemission and ligand charge transfers in Zn(II)- and Cd(II)-LMOFs are determined basically by the symmetry of the single ground of the ligands and their vibrational excited states, which can induce electronic transitions of the kind n-π^* and π-π^*.[14] This emission originates from the lowest excited singlet state to the singlet ground state of the ligand and corresponds to a short lifetime's emission ($\sim 10^{-9}$ s).[15]

On the other hand, the emissions based on ligand-to-metal charge transfers are displayed in a large number of Zn(II)- and Cd(II)-LMOFs. It involves electronic transitions from a π-conjugated ligand localized orbital to a metal-centered orbital. This mechanism is primarily in structures bearing benzene-multicarboxylate and aromatic N-donors ligands.[14] Typically, this kind of emitting materials show visible strong emission from blue to green, in the range of 390–520 nm.[13–16,47]

A frequent emission mechanism for the sensing of pesticides and herbicides based on LMOFs includes: (1) Photoinduced electron transfer (PET), (2) Charge transfers (CT), and (3) Förster resonance energy transfer (FRET).[22]

2.3 Selectivity

The exposition of commercial pesticides is associated with impaired health (neurotoxic effect, particularly Parkinson's disease, and risk of cancer)[48] and severe adverse environmental effects such as water and soil contamination,[4] which force the creation of efficient chemosensors. While the need for practical chemosensors for pesticides and herbicides is evident, to date, very few luminescent MOFs have been reported capable of operating in real samples and cellular environments.

For LMOFs with a stable emission source, the change in luminescence induced by the interaction of a pesticide or herbicide is enough for the accurate quantitative analysis. However, the selectivity is still not comparable to the high-performance liquid chromatography techniques, electrochemical methodologies, and high-resolution mass spectrometry.[45] Table 1 lists some outstanding examples of Zn(II) and Cd(II) LMOFs for the luminescent detection of pesticides in real samples with their analytical and structural features.

Despite notable advances in the development of sensitive chemosensors for pesticides based on LMOFs, its application in real samples remains largely unexplored. The most outstanding examples consist of nanomaterials, 3D LMOFs, such as $[Zn_4(TCPP)_2(TCPB)_2]$ (**1**),[36] $[Cd_3(PDA)(tz)_3Cl(H_2O)_4]$ (**3**)[38], and $[Zn_3(DDB)(DPE)]$ (**4**)[39] (see Table 1 for abbreviations).

In general, LMOF-based chemosensors have large possibilities for chemical and structural modulation of interaction sites and the emission properties, in addition to pore-volume modulation, which makes these LMOFs very versatile systems for the efficient detection of pesticides.[2]

Thus, Cd(II)-LMOFs chemosensors (**2**) and (**3**) are noteworthy examples where the selectivity toward azinphos-methyl, over several organophosphate derivatives, is attributed to various convergent supramolecular interactions, such as hydrogen bond interactions, π stacking, and coordination bonds (Cd ⋯ S═P) between the metal center and the azinphos-methyl.

A selective chemosensor for parathion over several organophosphate derivatives (e.g., azinphos-methyl, chlorpyrifos, etc.) is the LMOF (**1**) $[Zn_4(TCPP)_2(TCPB)_2]$ where the preference toward parathion is attributed to strong electron transfer from the electron-donating ligands to the electron-withdrawing nitroaromatic moieties of parathion.[36,40] Meanwhile, other more elaborated systems, such as $Ru(bpy)_3^{2+}$-ZIF-90-MnO_2 (**5**), AuNCs@ZIF-8 (**6**), and CBZ-BOD@ZIF-8 (**7**), utilize the inhibition of specific enzymes to accomplish the selectivity toward organophosphate pesticides.[40,42,43]

3 Zn(II) and Cd(II) LMOFs as fluorescent chemosensor for pesticides in real samples

Organophosphate pesticides (OPPs) (Fig. 2) are chemicals that attack the nervous system and permanently stop the acetylcholinesterase-enzyme activity.[36] The MOF $[Cd_{2.5}(PDA)(tz)_3]$ (**2**) (PDA = 1,4-phenylenediacetate and tz = 1,2,4-triazolate)[38] (Table 1) was assembled through a solvothermal methodology. The 3D MOF structure consisted of a cage connected 3D structure having three different coordination geometries in the Cd(II) centers. This MOF exhibited emission at 290 nm, upon excitation at 225 nm, in an aqueous medium. Thus, this hybrid material was

TABLE 1 Structural features and analytical conditions of selected Zn(II)- and Cd(II)-LMOF-based sensors for pesticides in real sample.

	Formula	Structure	Synthesis method	Fluorimetric response	Pesticide/ herbicide	Real sample	λ_{em}	Limit of detection (M)	Refs.
1	$[Zn_4(TCP)_2(TCPB)_2]$	[a]	Solvothermal	Turn off	Parathion	– Irrigation water	380	6.69×10^{-9}	36
2	$[Cd_{2.5}(PDA)(tz)_3]$	3D	Solvothermal	Turn off	Azinphos-methyl	– Extract from apples	290	5×10^{-5}	38
3	$[Cd_3(PDA)(tz)_3Cl(H_2O)_4]$	3D	Slow evaporation	Turn off	Azinphos-methyl	– Extract from apples and tomatoes	290	2.5×10^{-8}	37
4	$[Zn_3(DDB)(DPE)]$	3D	Solvothermal	Turn off	DCN	– Extract from carrots, nectarines, and grapes	450	2.7×10^{-7}	39
5	Nanocomposite $Ru(bpy)_3^{2+}$-ZIF-90-MnO_2	3D	Solvothermal	Turn off	Parathion-methyl	– Tap and lake water – Extract from cabbages	600	1.40×10^{-10}	40
6	Nanocomposite AuNCs@ZIF-8	3D	Solvothermal	Turn on	Acephate	– Tap and lake water – Extract from lettuce	600	3.66×10^{-9}	42
7	CBZ-BOD@ZIF-8	3D	Solvothermal	Turn on	Chlorpyrifos	Living cells	624	1.6×10^{-7}	43

Ligands: *TCP*, tetrakis (4-carboxyphenyl)-porphyrin; *TCPB*, 1,2,4,5-tetrakis (4-carboxyphenyl) benzene; *PDA*, 1,4-phenylenediacetate; *tz*, 1,2,4-triazolate; *DDB*, 3,5-di(2′,4′-dicarboxylphenyl)benzoic acid; *DPE*, 1,2-di(4-pyridyl)ethylene; *DCN*, 2,6-dichloro-4-nitroaniline; *bpy*, 2,2′-bipyridine; *ZIF*, zeolitic imidazolate framework; *NC*, nanocluster; *CBZ-BOD*, (*E*)-4-(3-(2-(9-ethyl-9H-carbazol-2-yl)vinyl)-5,5-difluoro-1,7,9-trimethyl-5H-5,6-dipyrrolo[1,2-c:2′,1′-f][1,3,2]diazaborinin-10-yl)phenyl-benzoate.
[a]*Not specified.*

capable to detect azinphos-methyl pesticide in water through luminescence quenching; remarkably, this was performed with a limit of detection of 16 ppb in the presence of several other pesticides, such as parathion, chlorpyrifos, diazinon, endosulfan, malathion, and dichlorvos (see Fig. 2). As discussed in the corresponding article, $\pi\cdots\pi$ interactions, along with the coordination vacancy generated in Cd1 (distorted-trigonal bipyramidal coordination geometry), are both accountable for the azinphos-methyl sensing (Fig. 3).[38] Azinphos-methyl is a usual component in the formulation of commercial pesticides. It is widely used to treat insect pests in fruits (e.g., apples, grapes), vegetables, nuts, and crop fields. Another structurally similar compound 3D MOF $[Cd_3(PDA)(tz)_3Cl(H_2O)_4]\cdot 3H_2O$ (**3**)[37] (Table 1), also exhibited a luminescence quenching response for the azinphos-methyl; apparently, the interaction of this Cd(II)-MOF with the pesticide is restricted to the $\pi\cdots\pi$ interactions between the aromatic ligands (PDA and tz ligands) and the azinphos-methyl molecule (Fig. 3). In this case, the limit of detection of azinphos-methyl in water was 8 ppb. Moreover, this water-stable MOF has been capable of detecting azinphos-methyl in apples and tomato extracts. According to the Food and Agriculture Organization (FAO), the maximum residue limits of azinphos-methyl in tomatoes is 3.15×10^{-6} M[37]; therefore, the low detection limits obtained in these previously mentioned studies make these Cd(II)-LMOF sensors susceptible and selective to comply with those limits.

Since these two last Cd(II)-LMOFs systems have equivalent emission signal, which is provoked by the PDA ligand, and both are capable of azinphos-methyl detection, the luminescence quenching mechanism can be ascribed to a resonance energy transfer process promoted by the absorption of the excitation light from the MOF to the azinphos-methyl molecule.[37,38]

Organochlorine pesticides (OCPs) are another important branch of harmful organic compounds pollutants. Particularly, 2,6-dichloro-4-nitroaniline (DCN) is a very popular pesticide, which is employed in crops to combat infections such as cotton rotten bell and wheat powdery mildew. DCN possesses high toxicity, slow-degradation rate, and it is insoluble, which may cause severe damage to living organisms. It can get into human skin and lungs.[6,49] A water-stable trinuclear MOF $[Zn_3(DDB)(DPE)]\cdot H_2O$ (**4**) (H5DDB = 3,5-di(2′,4′-dicarboxylphenyl) benzoic acid and DPE = 1,2-di(4-pyridyl)ethylene)[39] (Table 1) has efficiently achieved the sensing of DCN in carrot, grape, and nectarine extracts, with nanomolar sensing limits.

The secondary building units in this MOF are made of three Zn(II) ions connected by one μ_3-OH^- and four carboxylates to form the trinuclear cluster: $[Zn_3(OH)(COO)_4]$. Moreover, two of these trinuclear units are connected by two carboxylate groups to generate an hexanuclear cluster $[Zn_6(OH)_2(COO)_{10}]$, yielding thus a 4,12-c net (Fig. 4).[39]

Fluorescence quenching coming from DCN was the only effect revealed when the experiments were performed in the presence of eight other OCPs. An increase to 93.5% in the quenching efficiency of the DCN sensing was achieved, reaching a limit of detection of 2.7×10^{-7} M in water. These outcomes prompted the sensing of DCN using this Zn(II)-MOF in carrot, grape, and nectarine extracts. The fluorescence quenching mechanism occurring was supported by theoretical studies, which resulted in a proposal of a PET mechanism triggered by the nitro moiety in the DCN molecule.

In an interesting and novel approach, the luminescent recognition of organic pesticides has taken a step further by not just focusing solely on the pesticide by itself. Instead, those strategies rely directly on the mechanism of how the corresponding enzyme is affected by the pesticide. Consequently, an all-around sensor based on ($Ru(bpy)_3$-ZIF-90-MnO_2) has been synthesized[40] (**5**), Table 1. This MOF design exploits all the advantages of its components in a synergic way. First, it is assembled in a robust, and facile to prepare, ZIF-90,[40] which is used as a platform, where the complex $[Ru(bpy)_3]^{2+}$ is encapsulated within the ZIF architecture. The $[Ru(bpy)_3]^{2+}$ molecules exhibit modest luminescent properties.

However, by being attached to the MOF, the fluorescent behavior is improved by limiting the aggregation-induced quenching of the fluorophore and increasing its photostability. The complementary fragment (MnO_2) is incorporated in the form of nanosheets to the composite, developing a dual role in the sensing probe, acting as a quencher and, at the same time, bringing a colorimetric response in the detection of OPPs. The nanocomposite ($Ru(bpy)_3$-ZIF-90-MnO_2) is a stable brownish probe in water solution, and its activity is centralized in the inhibition of the acetylcholinesterase (AChE) by OPPs. As depicted in Fig. 5, the process of determination of the OPPs occurs in the presence of composite (**5**) following the enzymatic reaction of the acetylthiocholine (ATCh) to thiocholine (TCh) by the AChE. The product, TCh, simultaneously reacts with the MnO_2 molecules of the composite, reducing the MnO_2 nanosheets to Mn(II) ions, "turning-on" the fluorescent feature of ($Ru(bpy)_3$-ZIF-90), and changing the brown color into a colorless solution. The introduction of an organophosphorus pesticide to the system parathion-methyl blocks the production of TCh by the AChE, leaving the ($Ru(bpy)_3$-ZIF-90-MnO_2) probe unaltered. Consequently, the detection of parathion-methyl could be traced by naked eye or through fluorescence with a limit of detection equals to 1.40×10^{-10} M. The selectivity for parathion-methyl was examined in the competition of several coexisting electrolytes and biological species in water such as Ca^{2+}, K^+, Mg^{2+}, Na^+,

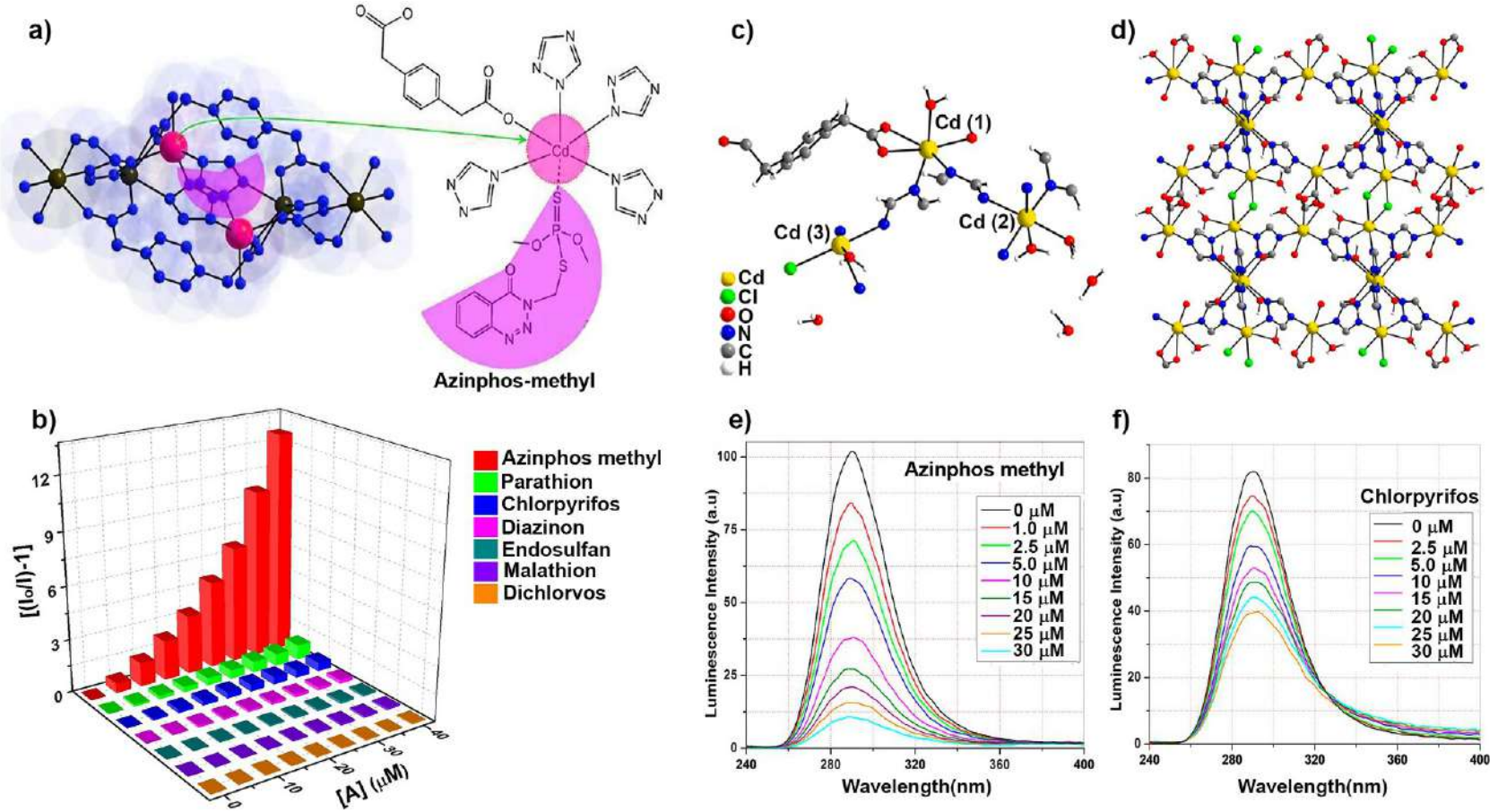

FIG. 3 (A) Scheme showing the penta-coordinated Cd(II) ions and the suggested interaction of azinphos-methyl, through the sulfur atom, within the coordination cage. (B) Changes in emission spectra of $[Cd_{2.5}(PDA)(tz)_3]$ (**2**) dispersed in water upon increasing amounts of azinphos-methyl. (C) Perspective view of the asymmetric unit and (D) two-dimensional arrangement in the crystal of $[Cd_3(PDA)(tz)_3Cl(H_2O)_4]\cdot 3H_2O$ (**3**). (E) Changes in the emission spectra of (**3**) in water as concentration of azinphos-methyl and (F) chlorpyrifos increase ($\lambda_{ex} = 225$ nm). *(Adapted with permission from (B) Singha DK, Majee P, Mondal SK, Mahata P. Highly selective aqueous phase detection of azinphos-methyl pesticide in ppb level using a cage-connected 3D MOF*. ChemistrySelect. *2017;2(20):5760–5768. doi:10.1002/slct.201700963, ©2020, Wiley Online Lib. (F) Singha DK, Majee P, Mandal S, Mondal SK, Mahata P. Detection of pesticides in aqueous medium and in fruit extracts using a three-dimensional metal-organic framework: experimental and computational study*. Inorg Chem. *2018;57(19):12155–12165. https://doi.org/10.1021/acs.inorgchem.8b01767, ©2018, ACS.)*

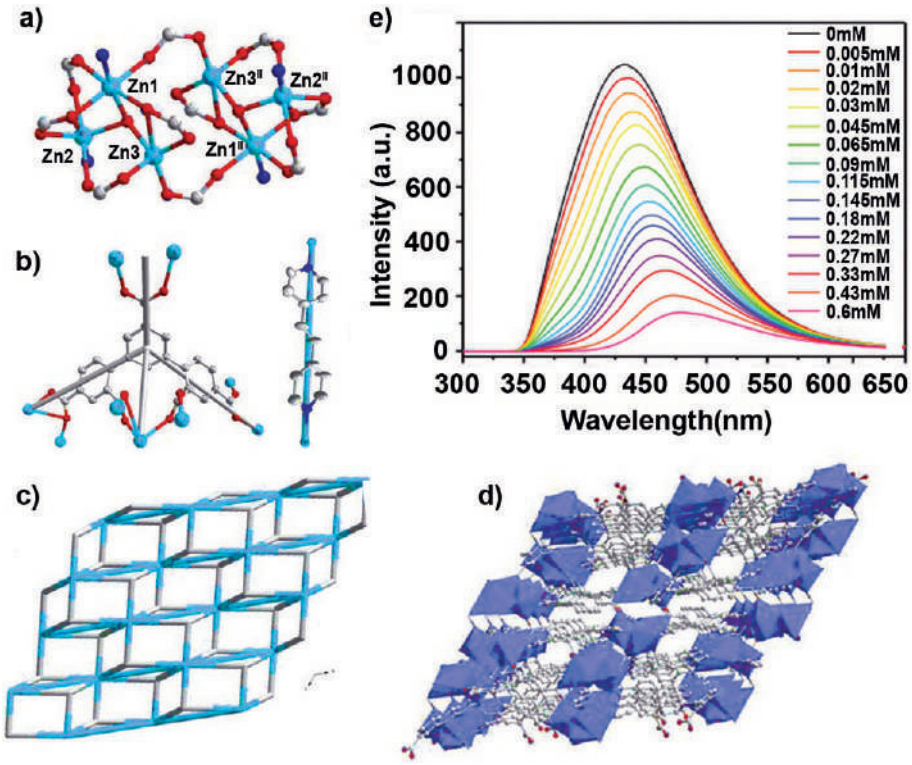

FIG. 4 (A) Secondary building unit of sensor (**4**), $[Zn_3(DDB)(DPE)]\cdot H_2$ (B) Coordination modes of DPE and DDB ligands. (C) Simplified topological scheme of the array along the *b* axis. (D) Projection view of the 3D open framework along the *b* axis. (E) Fluorescence spectra of the MOF at several concentrations of DCN in water, including carrot extract (100 µL). *(Adapted with permission from Wang XQ, Feng DD, Tang J, Zhao YD, Li J, Yang J, Kim CK, Su F. A water-stable zinc(II)-organic framework as a multiresponsive luminescent sensor for toxic heavy metal cations, oxyanions and organochlorine pesticides in aqueous solution.* Dalton Trans. *2019;48(44):16776–16785. https://doi.org/10.1039/c9dt03195b, ©2019, The Royal Society of Chemistry.)*

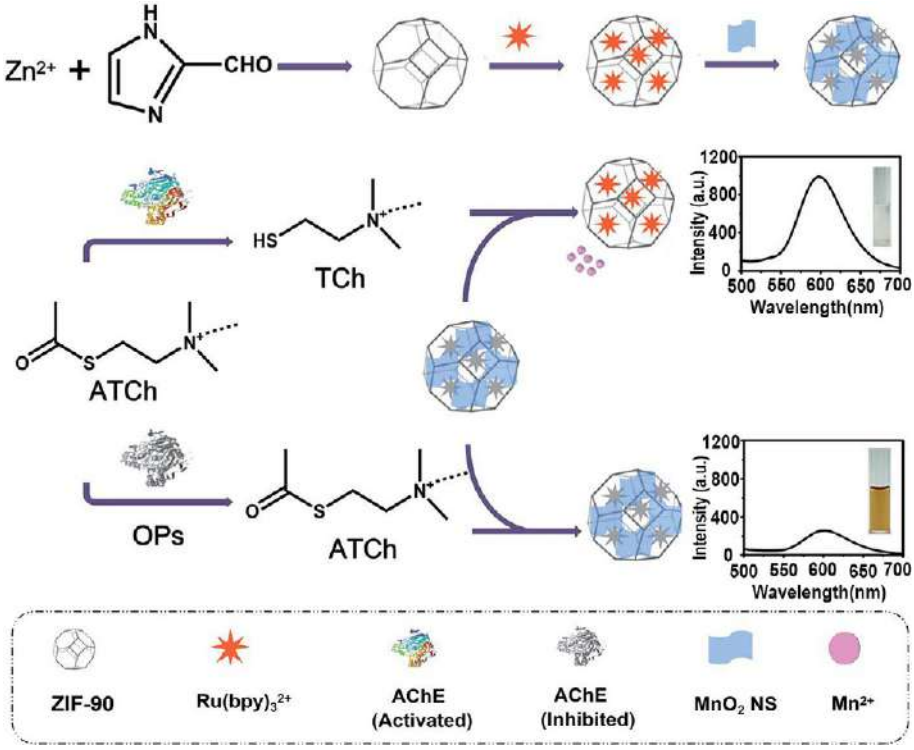

FIG. 5 Synthetic path of the $(Ru(bpy)_3$-ZIF-90-$MnO_2)$ nanocomposite (**5**) and its schematic detection mechanism of OPPs. *(Adapted with the permission from Li J, Weng Y, Shen C, Luo J, Yu D, Cao Z. Sensitive fluorescence and visual detection of organophosphorus pesticides with a Ru(bpy)32 +-ZIF-90-MnO2 sensing platform.* Anal Methods. *2021;13(26):2981–2988. https://doi.org/10.1039/d1ay00841b, ©2021, The Royal Chemical Society.)*

Zn^{2+}, Cl^{-}, NO_3^{-}, SO_4^{2-}, glycine, L-cysteine, bovine serum albumin (BSA), catalase, glucose oxidase, and L-glutamic acid, with negligible interference. More importantly, other pesticides were also tested: acetochlor, fenvalerate, imidacloprid, nitenpyram, and quaternary ammonium compounds as paraquat with the same good results. Nevertheless, the organophosphorus-based pesticides like chlorpyrifos, dichlorvos, malathion, omethoate, triazophos, and paraoxon also showed an inhibition effect in the AChE, interfering with the specific detection of parathion-methyl, as can be obtained an almost identical response for paraoxon in comparison with parathion-methyl. The sensing platform has been applied in real samples such as lake water, tap water and cabbage extract with successful results.

In a remarkable analogy, the election of ZIF-8 in the AuNCs@ZIF-8 sensor (**6**)[42] obeys the same intention of ZIF-90 for ($Ru(bpy)_3$-ZIF-90-MnO_2), to serve as matrix support for the guest species and enhance its luminescent properties. The emission of AuNCs (Au-nanoclusters) is linked to the restriction of intramolecular movement. Hence, their disposition inside the ZIF conveys increased fluorescence as the intramolecular movement was limited.[42]

The luminescent-sensing process addressed by the probe can be divided into three consecutive steps as illustrated in Fig. 6. (1) The enzymatic hydrolyzation of the acetylcholine by the AChE-producing choline. (2) Choline in the presence of O_2 is catalyzed by the choline oxidase generating H_2O_2. (3) The H_2O_2 molecules rip the structure of the ZIF-8, liberating the AuNCs and quenching the fluorescence. When an OPPs participate in the first step of the reaction cascade, inhibition in the AChE arises, causing a decrease in the production of H_2O_2. By this means, the presence of OPPs avoids the destruction of the AuNCs@ZIF-8 probe, allowing fluorescence emission.

Additionally, the authors have also considered including colorimetric techniques besides the fluorimetric determination through the addition of 3′,5,5′-tetramethylbenzidine (TMB).[42] Thus, once the release of the AuNCs from the MOFs has been ensured in the absence of OPPs, the TMB molecules become prone to be oxidized, transforming the colorless solution into a blue one (oxTMB). The oxidation proceeds as the Au atoms in AuNCs (which tend to exist in both of the oxidation states, Au(0) and Au(I)) decompose the O—O bond in H_2O_2, forming hydroxyl radicals (•OH) that are responsible for reacting with TMB, turning the solution blue.

The study contemplated numerous pesticides to be analyzed, including OPPs (acephate, fenitrothion, glyphosate, malathion, parathion, and pirimiphos-methyl) and non-OPPs (cyantraniliprole, hymexazol thiamethoxam, tebuconazole, and spirotetramat). As expected, the non-OPPs caused no signal in the detection process, but the OPPs did it with a similar intensity. A detection limit was given for acephate as a representative pesticide (3.66×10^{-9} M). Notably, further studies were accomplished by implementing the compounds AuNCs@ZIF-8 and TMB in the paper stripes tests.

Taking advantage of the colorimetric signals, the paper stripes were evaluated as a portable kit in a quantitative measurement of OPPs in lake water, tap water, and lettuce extract with the utilization of photography and a downloaded application of a smartphone concluding in a good and replicable detection performance by the sensor.[42] The use of colorimetric methods has been contemplated in other two enzymatic pesticide MOFs sensors (MIP-CoZn-ZIF[50] and AChE@ZIF-8[51]), although those probes exhibited no luminescent properties.

Remarkably, the use of ZIF-8 as a sensing platform has also been reached in the indirect detection of chlorpyrifos by CBZ-BOD@ZIF-8 due to its robustness, practicality, and biocompatibility.[43] Still, the enzyme target for the analysis was carboxylesterase (CES1) as an alternative for AChE. Likewise, CES1 gets inhibited in the presence of OPPs. The background strategy in the synthetic design of CBZ-BOD was to construct a selective and dual fluorogenic and colorimetric molecule capable of achieving a specific binding to CES1, which can be encapsulated inside the LMOF.[43] The recognition process starts with the incubation of CES1 and the red emission probe (CBZ-BOD@ZIF-8) in the interior of the micropores of the ZIF architecture. Then, fluorescence intensity changes as the hydrolysis of the carboxylic group in CBZ-BOD evolves into a non-emitting molecule (BOD-OH) triggered by CES1. The pesticide determination proceeds as chlorpyrifos blocks the CES1, impeding the catalytic reaction over CBZ-BOD@ZIF-8, leaving the characteristic fluorescence and red colored probe unaltered (Fig. 7).[43] Significantly, all those steps in the study had taken place via intracellular, with minor or no interference of many biological species including: α-CT, trypsin, bovine serum albumin, CES2, lysing enzymes, lipase, proteinase K, pepsase, D-beta-hydroxybutyrate (BHb), lysozyme, and AchE.

Furthermore, dimethoate and fenitrothion were also compared against chlorpyrifos showing a more remarkable turn-on behavior toward chlorpyrifos, estimating its detection limit as 1.6×10^{-7} M.

The authors also investigated kinetic parameters, and monitored the real-time activity of CES1 coexisting with chlorpyrifos in living cells, obtaining encouraging results headed for more complex and sophisticated designs in LMOFs as a sensing platform in their application toward toxic pollutants.

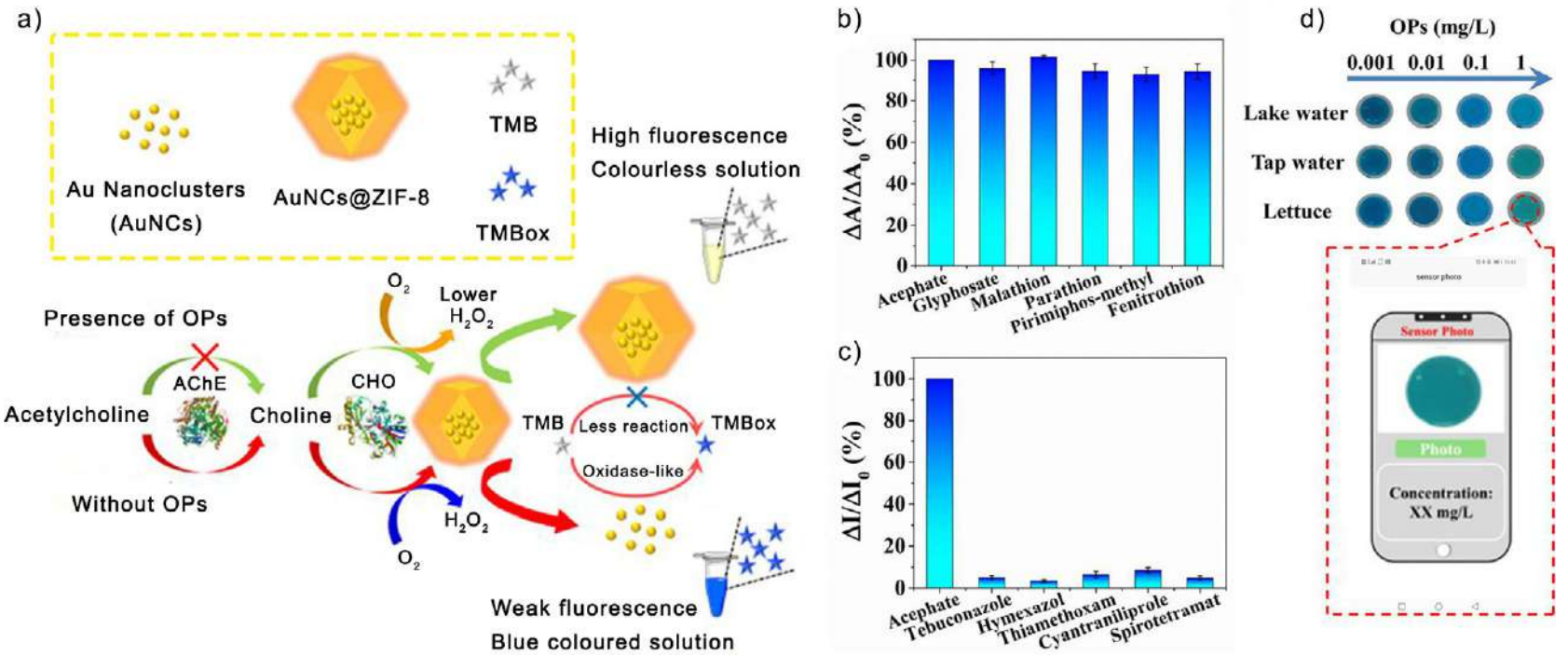

FIG. 6 (A) OPPs detection mechanism by AuNCs@ZIF-8. (B) Changes in the absorbance of AuNCs@ZIF-8 by the addition of different OPPs. (C) Selectivity toward OPPs by the sensor (acephate as an example). (D) Chromogenic sensing in real samples and the use of a smartphone to analyze the determination of OPPs in the problem solution. *(Adapted with permission from Cai Y, Zhu H, Zhou W, Qiu Z, Che, C, Qileng A, Li K, Liu Y. Capsulation of AuNCs with AIE effect into metal-organic framework for the marriage of a fluorescence and colorimetric biosensor to detect organophosphorus pesticides.* Anal Chem. *2021;93(19):7275–7282. https://doi.org/10.1021/acs.analchem.1c00616, ©2021, ACS.)*

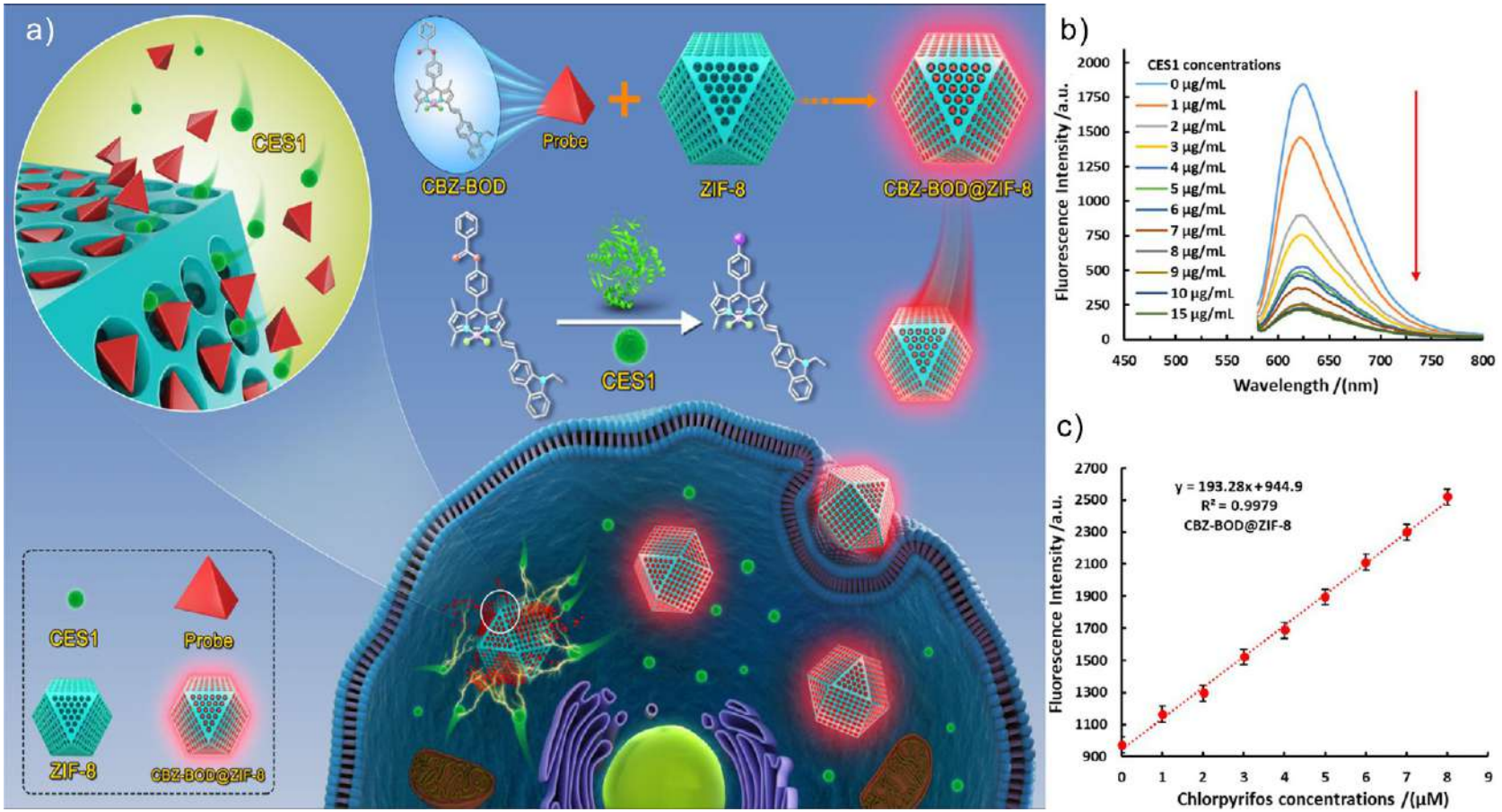

FIG. 7 (A) Designing of the nanocomposite CBZ-BOD@ZIF-8 (**6**) and its applications in living cell sensing. (B) Fluorimetric titration experiment of CBZ-BOD@ZIF-8 (10 μM) among the presence of different concentrations of CES1. (C) Fluorescence changes of CBZ-BOD@ZIF-8 in the presence of increasing chlorpyrifos concentrations. *(Adapted with the permission from Shen B, Ma C, Ji Y, Dai J Li B, Zhang X, Huang H. Detection of carboxylesterase 1 and chlorpyrifos with ZIF-8 metal-organic frameworks using a red emission BODIPY-based probe.* ACS Appl Mater Interfaces. *2021;13(7):8718–8726. https://doi.org/10.1021/acsami.0c19811, ©2021, ACS.)*

4 Conclusions

The current global challenges caused by the indiscriminate use of pesticides are evident and urgently need to be addressed. There is an obvious need to develop functional chemosensors with synergy between their structural and luminescent properties to develop sensitive and selective luminescent probes to detect these toxic compounds.

Among optical sensory materials, luminescent MOFs containing d^{10} transition metals (mainly Zn(II) and Cd(II) ion) are at the forepart as chemosensors owing to their simple preparation. Their highly modifiable structures, which by simply chemical functionalization of their components can generate an extended range of photoluminescent mechanisms and structural properties effective in sensing/recognition of pesticides through supramolecular interactions. Under this approach, the selective and quantitative detection of target pesticides is achieved through the MOF-pesticide interaction process that can be transduced to a change in its emission properties. Thus, more elaborated systems can be achieved by using water-stable LMOFs as a cornerstone platform in which other molecules can be placed toward a specific recognition of notorious pollutants or by and indirect detection considering other relevant biological targets like enzymes.

In summary, the suitable design of chemosensor based on Zn(II)- and Cd(II)-LMOFs can generate new analytical methodologies toward efficient quantitative detection of industrially scale produced agro molecules such as pesticides. However, the luminescent MOF-based sensors for pesticides have the following challenges: (1) Improve water stability because water is the main component in environmental and biological media. High water stability can endow sensors with high recyclability and render them inexpensive. (2) The detection limit for the targeted pesticides needs to be further improved or well matched with the range of complex samples. (3) The sensors should operate in real samples, requiring the sensors to be studied under real conditions at various concentrations of both analytes and common interfering species.

References

1. Lustig WP, Mukherjee S, Rudd ND, Desai AV, Li J, Ghosh SK. Metal-organic frameworks: functional luminescent and photonic materials for sensing applications. *Chem Soc Rev*. 2017;46(11):3242–3285. https://doi.org/10.1039/c6cs00930a.
2. Vikrant K, Tsang DCW, Raza N, Giri BS, Kukkar D, Kim KH. Potential utility of metal-organic framework-based platform for sensing pesticides. *ACS Appl Mater Interfaces*. 2018;10(10):8797–8817. https://doi.org/10.1021/acsami.8b00664.
3. Karri RR, Ravindran G, Dehghani MH. Wastewater—sources, toxicity, and their consequences to human health. In: *Soft Computing Techniques in Solid Waste and Wastewater Management*. Elsevier; 2021:3–33.
4. Zulkifli SN, Rahim HA, Lau WJ. Detection of contaminants in water supply: a review on state-of-the-art monitoring technologies and their applications. *Sens Actuators B Chem*. 2018;255:2657–2689. https://doi.org/10.1016/j.snb.2017.09.078.
5. Vasylevskyi SI, Bassani DM, Fromm KM. Anion-induced structural diversity of Zn and cd coordination polymers based on bis-9,10-(pyridine-4-yl)-anthracene, their luminescent properties, and highly efficient sensing of nitro derivatives and herbicides. *Inorg Chem*. 2019;58(9):5646–5653. https://doi.org/10.1021/acs.inorgchem.8b03628.
6. Di L, Xia Z, Li J, et al. Selective sensing and visualization of pesticides by ABW-type metal-organic framework based luminescent sensors. *RSC Adv*. 2019;9(66):38469–38476. https://doi.org/10.1039/c9ra08940c.
7. Yu CX, Hu FL, Song JG, et al. Ma LF ultrathin two-dimensional metal-organic framework nanosheets decorated with tetra-pyridyl calix[4]arene: design, synthesis and application in pesticide detection. *Sens Actuators B Chem*. 2020;310(January):127819. https://doi.org/10.1016/j.snb.2020.127819.
8. Zhao Y, Xu X, Qiu L, Kang X, Wen L, Zhang B. Metal-organic frameworks constructed from a new thiophene-functionalized dicarboxylate: luminescence sensing and pesticide removal. *ACS Appl Mater Interfaces*. 2017;9(17):15164–15175. https://doi.org/10.1021/acsami.6b11797.
9. Saito-Shida S, Nemoto S, Akiyama H. Multiresidue method for determining multiclass acidic pesticides in agricultural foods by liquid chromatography-tandem mass spectrometry. *Anal Methods*. 2021;13(7):894–902. https://doi.org/10.1039/d0ay02101f.
10. Vargas-Pérez M, Domínguez I, González FJE, Frenich AG. Application of full scan gas chromatography high resolution mass spectrometry data to quantify targeted-pesticide residues and to screen for additional substances of concern in fresh-food commodities. *J Chromatogr A*. 2020;1622:461118. https://doi.org/10.1016/j.chroma.2020.461118.
11. Beneito-Cambra M, Gilbert-López B, Moreno-González D, et al. Ambient (desorption/ionization) mass spectrometry methods for pesticide testing in food: a review. *Anal Methods*. 2020;12(40):4831–4852. https://doi.org/10.1039/d0ay01474e.
12. Li HY, Zhao SN, Zang SQ, Li J. Functional metal-organic frameworks as effective sensors of gases and volatile compounds. *Chem Soc Rev*. 2020;49(17):6364–6401. https://doi.org/10.1039/c9cs00778d.
13. Dong J, Zhao D, Lu Y, Sun WY. Photoluminescent metal-organic frameworks and their application for sensing biomolecules. *J Mater Chem A*. 2019;7(40):22744–22767. https://doi.org/10.1039/c9ta07022b.
14. Parmar B, Bisht KK, Rachuri Y, Suresh E. Zn(II)/Cd(II) based mixed ligand coordination polymers as fluorosensors for aqueous phase detection of hazardous pollutants. *Inorg Chem Front*. 2020;7(5):1082–1107. https://doi.org/10.1039/c9qi01549c.
15. Allendorf MD, Bauer CA, Bhakta RK, Houk RJT. Luminescent metal-organic frameworks. *Chem Soc Rev*. 2009;38(5):1330–1352. https://doi.org/10.1039/b802352m.

16. Heine J, Müller-Buschbaum K. Engineering metal-based luminescence in coordination polymers and metal-organic frameworks. *Chem Soc Rev*. 2013;42(24):9232–9242. https://doi.org/10.1039/c3cs60232j.
17. Karmakar A, Samanta P, Dutta S, Ghosh SK. Fluorescent "turn-on" sensing based on metal–organic frameworks (MOFs). *Chem Asian J*. 2019;14 (24):4506–4519. https://doi.org/10.1002/asia.201901168.
18. Yang L, Song Y, Wang L. Multi-emission metal-organic framework composites for multicomponent ratiometric fluorescence sensing: recent developments and future challenges. *J Mater Chem B*. 2020;8(16):3292–3315. https://doi.org/10.1039/c9tb01931f.
19. Guo XY, Dong ZP, Zhao F, Liu ZL, Wang YQ. Zinc(II)-organic framework as a multi-responsive photoluminescence sensor for efficient and recyclable detection of pesticide 2,6-dichloro-4-nitroaniline, Fe(III) and Cr(VI). *New J Chem*. 2019;43(5):2353–2361. https://doi.org/10.1039/c8nj05647a.
20. Pamei M, Puzari A. Luminescent transition metal–organic frameworks: an emerging sensor for detecting biologically essential metal ions. *Nano-Struct Nano-Objects*. 2019;19:100364. https://doi.org/10.1016/j.nanoso.2019.100364.
21. Li Y, Ma D, Chen C, et al. A hydrostable and bromine-functionalized manganese-organic framework with luminescence sensing of $Hg^{2+}$and antiferromagnetic properties. *J Solid State Chem*. 2019;269(July 2018):257–263. https://doi.org/10.1016/j.jssc.2018.09.034.
22. Kumar P, Deep A, Kim K-H. Metal organic frameworks for sensing applications. *TrAC Trends Anal Chem*. 2015;73:39–53. https://doi.org/10.1016/j.trac.2015.04.009.
23. Gu TY, Dai M, Young DJ, Ren ZG, Lang JP. Luminescent Zn(II) coordination polymers for highly selective sensing of Cr(III) and Cr(VI) in water. *Inorg Chem*. 2017;56(8):4668–4678. https://doi.org/10.1021/acs.inorgchem.7b00311.
24. Zhang L, Kang Z, Xin X, Sun D. Metal–organic frameworks based luminescent materials for nitroaromatics sensing. *CrstEngComm*. 2016;18(2):193–206. https://doi.org/10.1039/C5CE01917F.
25. Qin JH, Huang YD, Shi MY, et al. Aqueous-phase detection of antibiotics and nitroaromatic explosives by an alkali-resistant Zn-MOF directed by an ionic liquid. *RSC Adv*. 2020;10(3):1439–1446. https://doi.org/10.1039/c9ra08733h.
26. Dalapati R, Biswas S. Post-synthetic modification of a metal-organic framework with fluorescent-tag for dual naked-eye sensing in aqueous medium. *Sens Actuators B Chem*. 2017;239:759–767. https://doi.org/10.1016/j.snb.2016.08.045.
27. Jackson SL, Rananaware A, Rix C, Bhosale SV, Latham K. Highly fluorescent metal-organic framework for the sensing of volatile organic compounds. *Cryst Growth Des*. 2016;16(6):3067–3071. https://doi.org/10.1021/acs.cgd.6b00428.
28. Zhang J, Zhang X, Chen J, et al. Highly selective luminescent sensing of xylene isomers by a water stable Zn-organic framework. *Inorg Chem Commun*. 2016;69:1–3. https://doi.org/10.1016/j.inoche.2016.04.013.
29. Liu G, Li Y, Chi J, et al. Various Cd(II) coordination polymers induced by carboxylates: multi-functional detection of Fe3+, anions, aspartic acids and bovine serum albumin. *Dalton Trans*. 2020;49(3):737–749. https://doi.org/10.1039/c9dt04103f.
30. Chandrasekhar P, Mukhopadhyay A, Savitha G, Moorthy JN. Remarkably selective and enantiodifferentiating sensing of histidine by a fluorescent homochiral Zn-MOF based on pyrene-tetralactic acid. *Chem Sci*. 2016;7(5):3085–3091. https://doi.org/10.1039/c5sc03839a.
31. Qiu L-G, Li Z-Q, Wu Y, Wang W, Xu T, Jiang X. Facile synthesis of nanocrystals of a microporous metal–organic framework by an ultrasonic method and selective sensing of organoamines. *Chem Commun*. 2008;31:3642. https://doi.org/10.1039/b804126a.
32. Wu S, Min H, Shi W, Cheng P. Multicenter metal–organic framework-based ratiometric fluorescent sensors. *Adv Mater*. 2020;32(3):1–14. https://doi.org/10.1002/adma.201805871.
33. Li C, Yang W, Zhang X, et al. A 3D hierarchical dual-metal-organic framework heterostructure up-regulating the pre-concentration effect for ultrasensitive fluorescence detection of tetracycline antibiotics. *J Mater Chem C*. 2020;8(6):2054–2064. https://doi.org/10.1039/c9tc05941e.
34. Yao XQ, Xiao GB, Xie H, et al. Solvent-inducted structural diversity of two luminescent metal-organic frameworks as dual-functional sensor for the detection of nitroaromatic compounds and highly selective detection of ofloxacin antibiotics. *CrstEngComm*. 2019;21(15):2559–2570. https://doi.org/10.1039/C8CE02122H.
35. Ying YM, Tao CL, Yu M, et al. In situ encapsulation of pyridine-substituted tetraphenylethene cations in metal-organic framework for the detection of antibiotics in aqueous medium. *J Mater Chem C*. 2019;7(27):8383–8388. https://doi.org/10.1039/c9tc02229e.
36. Wang L, He K, Quan H, Wang X, Wang Q, Xu X. A luminescent method for detection of parathion based on zinc incorporated metal-organic framework. *Microchem J*. 2020;153:104441. https://doi.org/10.1016/j.microc.2019.104441.
37. Singha DK, Majee P, Mandal S, Mondal SK, Mahata P. Detection of pesticides in aqueous medium and in fruit extracts using a three-dimensional metal-organic framework: experimental and computational study. *Inorg Chem*. 2018;57(19):12155–12165. https://doi.org/10.1021/acs.inorgchem.8b01767.
38. Singha DK, Majee P, Mondal SK, Mahata P. Highly selective aqueous phase detection of azinphos-methyl pesticide in ppb level using a cage-connected 3D MOF. *ChemistrySelect*. 2017;2(20):5760–5768. https://doi.org/10.1002/slct.201700963.
39. Wang XQ, Feng DD, Tang J, et al. A water-stable zinc(II)-organic framework as a multiresponsive luminescent sensor for toxic heavy metal cations, oxyanions and organochlorine pesticides in aqueous solution. *Dalton Trans*. 2019;48(44):16776–16785. https://doi.org/10.1039/c9dt03195b.
40. Li J, Weng Y, Shen C, Luo J, Yu D, Cao Z. Sensitive fluorescence and visual detection of organophosphorus pesticides with a $Ru(bpy)_3^{2+}$-ZIF-90-MnO_2 sensing platform. *Anal Methods*. 2021;13(26):2981–2988. https://doi.org/10.1039/d1ay00841b.
41. Xu X, Guo Y, Wang X, et al. Sensitive detection of pesticides by a highly luminescent metal-organic framework. *Sens Actuators B Chem*. 2018;260:339–345. https://doi.org/10.1016/j.snb.2018.01.075.
42. Cai Y, Zhu H, Zhou W, et al. Capsulation of AuNCs with AIE effect into metal-organic framework for the marriage of a fluorescence and colorimetric biosensor to detect organophosphorus pesticides. *Anal Chem*. 2021;93(19):7275–7282. https://doi.org/10.1021/acs.analchem.1c00616.
43. Shen B, Ma C, Ji Y, et al. Detection of carboxylesterase 1 and chlorpyrifos with ZIF-8 metal-organic frameworks using a red emission BODIPY-based probe. *ACS Appl Mater Interfaces*. 2021;13(7):8718–8726. https://doi.org/10.1021/acsami.0c19811.

44. Burtch NC, Jasuja H, Walton KS. Water stability and adsorption in metal-organic frameworks. *Chem Rev*. 2014;114(20):10575–10612. https://doi.org/10.1021/cr5002589.
45. Rosales-Vázquez LD, Dorazco-González A, Sánchez-Mendieta V. Efficient chemosensors for toxic pollutants based on photoluminescent Zn(II) and Cd(II) metal-organic networks. *Dalton Trans*. 2021;50(13):4470–4485. https://doi.org/10.1039/d0dt04403b.
46. Kepp KP. Free energies of hydration for metal ions from heats of vaporization. *J Phys Chem A*. 2019;123(30):6536–6546. https://doi.org/10.1021/acs.jpca.9b05140.
47. Rosales-Vázquez LD, Valdes-García J, Bazany-Rodríguez IJ, et al. A sensitive photoluminescent chemosensor for cyanide in water based on a zinc coordination polymer bearing ditert-butyl-bipyridine. *Dalton Trans*. 2019;48(33):12407–12420. https://doi.org/10.1039/c9dt01861a.
48. Sidhu GK, Singh S, Kumar V, Dhanjal DS, Datta S, Singh J. Toxicity, monitoring and biodegradation of organophosphate pesticides: a review. *Crit Rev Environ Sci Technol*. 2019;49(13):1135–1187. https://doi.org/10.1080/10643389.2019.1565554.
49. Kumar T, Venkateswarulu M, Das B, Halder A, Koner RR. Zn(ii)-based coordination polymer: an emissive signaling platform for the recognition of an explosive and a pesticide in an aqueous system. *Dalton Trans*. 2019;48(33):12382–12385. https://doi.org/10.1039/c9dt02224d.
50. Amirzehni M, Hassanzadeh J, Vahid B. Surface imprinted CoZn-bimetalic MOFs as selective colorimetric probe: application for detection of dimethoate. *Sens Actuators B Chem*. 2020;325(July):128768. https://doi.org/10.1016/j.snb.2020.128768.
51. Kukkar P, Kukkar D, Younis SA, et al. Colorimetric biosensing of organophosphate pesticides using enzymatic nanoreactor built on zeolitic imdiazolate-8. *Microchem J*. 2021;166(December 2020):106242. https://doi.org/10.1016/j.microc.2021.106242.

crystals

MDPI

Article

Structure of a Luminescent MOF-2 Derivative with a Core of Zn(II)-Terephthalate-Isoquinoline and Its Application in Sensing of Xylenes

Luis D. Rosales-Vázquez [1], Iván J. Bazany Rodríguez [1], Simón Hernández-Ortega [1], Víctor Sánchez-Mendieta [2,*], Alfredo R. Vilchis-Nestor [2], José de Jesús Cázares-Marinero [3] and Alejandro Dorazco-González [1,*]

1 Instituto de Química, Universidad Nacional Autónoma de México, Circuito Exterior, Ciudad Universitaria, Ciudad de México 04510, Mexico; ld_222@hotmail.com (L.D.R.-V.); ivanbazany@comunidad.unam.mx (I.J.B.R.); simonho@unam.mx (S.H.-O.)

2 Centro Conjunto de Investigación en Química Sustentable UAEM-UNAM, Carretera Toluca-Ixtlahuaca Km. 14.5, Tlachaloya, Toluca, Estado de México 50200, Mexico; arvilchisn@uaemex.mx

3 Departamento de Investigación y Desarrollo, Polioles S.A. de C.V. Km. 52.5 Parque Industrial Lerma, Estado de México 52000, Mexico; jose.cazares@polioles.com.mx

* Correspondence: vsanchezm@aemex.mx (V.S.M.); adg@unam.mx (A.D.G.)

Received: 9 April 2020; Accepted: 24 April 2020; Published: 27 April 2020

Abstract: A new blue photoluminescent 2D metal–organic framework, **1**, with formula $\{[Zn_2(\mu_2\text{-BDC})_2(iQ)_2]\}_\infty$ has been synthesized in a high yield under solvothermal conditions by reacting Zn(II) ions with 1,4-benzenedicarboxylic acid (H_2BDC) and isoquinoline (*i*Q) in DMF. Compound **1** was thoroughly characterized by single-crystal X-ray diffraction, solid-state cross-polarization magic-angle spinning ^{13}C NMR, X-ray powder diffraction, scanning electron microscopy (SEM) with energy dispersive X-ray spectroscopy (EDS), and thermoanalysis. The crystal structure of **1** showed interpenetrated 2D frameworks consisting of dinuclear paddle-wheel cores Zn_2; moreover, this material possessed thermostability up to 310 °C. The CPMAS ^{13}C-NMR spectrum of **1** is consistent with the symmetry of the crystal structure. Luminescence studies showed that **1** strongly enhances its fluorescence emission in the presence of xylene isomers with a pronounced selectivity to p-xylene.

Keywords: MOF-2 derivative; fluorescent sensing; xylene isomers

1. Introduction

There is a growing interest in the development of photoluminescent metal–organic materials (MOMs) [1–4], where the color emission upon excitation is a significant feature of these materials that has been recently used in several applications such as emitting devices/materials [5,6], optical sensing of vapor phase analytes [3,7], detection of ions [8,9], bioanalytes [10], explosives [11,12], and detection of volatile organic solvents (VOCs) [8,13,14]. Most known MOMs-based chemosensors for organic solvents act in a "turn-off" response where the fluorescence intensity of the compound is quenched upon addition of the analyte [7,15,16]. The photoluminescent properties of MOMs are basically dependent on the used metal center, its coordination environment, the presence of aromatic ligands, as well as the supramolecular interactions such as π–π stacking in the final arrangement [1]. From a synthetic point view, the combination of divalent d^{10} transition metal ions with rigid aromatic dicarboxylic acids and auxiliary *N*-donor ligands such as pyridines [17], imidazole groups [18], and isoquinline rings [19] can be used to obtain crystalline metal–organic structures with adjustable emission properties. In this context, the planar symmetric 1,4-benzenedicarboxylate (BDC) anion is a very common bridging

ligand to achieve microporous MOF-2 derivatives [20] with rigid dinuclear cores, owing to this dianion generating paddle-wheel secondary building units (SBUs) of type [M_2(–COO)$_4$], particularly with Zn(II) ions [20–25]. In the area of optical sensing, MOMs with polynuclear d^{10} metal cores containing coordinated fluorescent ligands are very attractive because they exhibit striking crystal structures and outstanding photoluminescence properties mainly caused by charge transfer mechanisms [1,2,17,18,26].

On the other hand, methyl-substituted aromatic VOCs such as the xylene isomers and toluene are usually used as organic solvents in the industrial production of adhesives, rubber products, dyes, and paints [27]. Among these isomers, p-xylene is the most used in the industry mainly in the production of polyesters [28]. They are carcinogenic species and considered as some of the most hazardous pollutants among VOCs [29]. Acute exposure to xylene isomers and toluene, typically found in gasoline, has been associated with skin, eye irritation, and effects on the respiratory system [30]. The constant and chronic exposure to small amounts of these solvents (200 ppm or greater) in the ambient or at home with common products such as adhesives and solvents for paints is associated with various adverse health effects [27,31]. Data on the xylene isomers concentration in these products used at home or work are usually incomplete. While the need for rapid quantitative detection is vital for chemical industry and environmental monitoring for their toxic effects, so far, very few luminescent sensory systems have been described [14]. The optical sensing of xylenes is possible using Zn(II)-organic frameworks containing fluorescent aromatic moieties such as tetrapyridine tetraphenylethene [14], triazole derivatives [32–34], and tetrakis(4-carboxyphenyl)porphyrin (NUS-40 Zn) [35].

The usage of luminescent MOMs to sense VOCs is promising due to their high stability and ease of preparation, in addition to advantages inherent of the fluorescence technique such as high sensitivity [3,32,36].

Taking this into account, this work is based on the idea that a new metal–organic compound with photoluminescence can be achieved in a single step and in high yield by the straightforward combination of Zn(II) ions with 1,4-benzenedicarboxylic acid and a commercial benzopyridine ligand, which can act as a luminescent unit when coordinated to the metal center. X-ray crystal structures, thermogravimetry, CPMAS ^{13}C-NMR spectroscopy, morphological studies with SEM-EDS, and fluorescent sensing properties obtained for a novel blue luminescent 2D MOF based on Zn-terephthalate with an isoquinoline core are herein discussed.

2. Materials and Methods

2.1. Physical Measurements

All chemicals are commercially available (H_2BDC, 98%; isoquinoline, 98%; and $Zn(NO_3)_2{\cdot}4(H_2O)$, 98% from Sigma-Aldrich (St. Louis, Missouri, United States)) and were used as received. The FT-IR spectrum was recorded in the range of 4000–600 cm^{-1} by using the standard Pike ATR cell on a Bruker Tensor 27 FT-IR spectrophotometer (Bruker Optik GmbH, Ettlingen, Germany). Elemental analysis for C, H, and N were carried out by standard methods using a Vario Micro-Cube analyzer.

Powder X-ray diffraction (PXRD) was conducted using a Bruker D8 ADVANCE X-ray powder diffractometer (Cu-Kα, λ = 1.5418 Å) (Bruker AXS GmbH, Karlsruhe, Germany) with the 2θ range of 5–50°.

Thermogravimetric analyses were performed using TA Instruments equipment, under a dinitrogen atmosphere, at a heating rate of 10 °C min^{-1}, and from 25 to 475 °C.

The CPMAS ^{13}C NMR experiment was recorded with a Bruker Advance II 300 spectrometer (Bruker BioSpin GmbH, Rheinstetten, Germany) (operating at 75 MHz for ^{13}C) on a 4 mm rotor double resonance. The CPMAS experiment was recorded with a contact time of 2 ms and a delay of 5 s at a 7 kHz spinning rate at ambient temperature.

The shape and size of the crystals of compound **1** were examined with scanning electron microscopy (SEM) using a JSM-6510LV microscope from JEOL (JEOL, Ltd, Akishima, Tokyo, Japan) equipped with a Bruker QUANTAX 200 energy-dispersive X-ray spectrometer (EDS) (Bruker Nano GmbH, Adlershof,

Berlin, Germany) for elemental characterization. The crystals were let to dry at room-temperature conditions and fixed on Al stubs with carbon tape and finally coated with a thin layer of gold using a Denton IV sputtering chamber before SEM imaging acquisition.

Luminescence spectra in suspensions of **1** were recorded on an Agilent Cary Eclipse equipped with a crystal holder and a thermostated holder for quartz cuvettes. In all sensing studies, as-synthesized single-crystalline samples of **1** were used. Suspensions of **1** were prepared by stirring for 20 min at 25 °C in spectrophotometric-grade solvents with a final concentration of 25 μM. For the titration experiment of xylenes, a stock suspension of **1** (1 mg mL^{-1}) in acetonitrile was prepared by ultrasonic treatment by 20 min at r.t., and subsequently, 45 μL of this suspension was diluted with 2500 uL of acetonitrile, to give a final concentration of 25 μM, and the emission spectra (λ_{ex} = 330) of the suspension were recorded after adding aliquots of xylenes.

2.2. Synthesis of $\{[Zn_2(\mu_2\text{-}BDC)_2(iQ)_2]\}_\infty$, **1**

Initially, in a 4 mL vial, 32.6 mg of $Zn(NO_3)_2{\cdot}4H_2O$ (0.10 mmol) and 15.0 mg of BDC (0.09 mmol) were dissolved with 3 mL of DMF. After two and a half hours, 24 μL (0.20 mmol) of isoquinoline was added using a high-precision micropipette. The solution was stirred for 15 min at 75 °C and was then placed in a Parr bomb and heated at 115 °C for 16 h. After cooling the mixture, colorless crystals were obtained, which were filtered out and washed with DMF. Yield: 82%, based on the metal precursor.

Elemental analysis (%), $C_{34}H_{24}N_2O_8Zn_2$, cal.: C, 56.77; H, 3.36, N, 3.89; found: C, 56.72; H, 3.39; N, 3.80. IR (ATR): $\tilde{\nu}$ 3058 (w), 2087 (w), 1634 (m), 1596 (m), 1586 (m), 1410 (s), 1164 (w), 1041 (w), 1013 (w), 953 (w), 1085 (w), 1051, 861 (w), 823 (s), 732 (s).

2.3. Crystallographic Investigations

The relevant details of the crystal, data collection, and structural refinement can be found in Table 1. Crystallographic data for **1** were collected on a Bruker APEX II CCD diffractometer at 296 K using Mo-K_α radiation (k = 0.71073 Å), from an Incoatec IμS source and Helios optic monochromator [37]. Suitable crystals were coated with hydrocarbon oil (Parabar), and the specimen was collected with a glass fiber and fixed with glue. The structure was solved using intrinsic phasing (SHELXT) [38] and refined by full-matrix least-squares on F2 using the shelXle GUI [39]. The hydrogen atoms of the C–H bonds were placed in idealized positions and their position was refined with U_{iso} linked to the parent atom with distance restraints. Crystallographic data for **1** have been deposited at the Cambridge Crystallographic Data Center (CCDC) with the number 1994765.

Table 1. Crystal data and structure refinement for **1**.

Empirical formula	$C_{34}\ H_{24}\ N_2\ O_8\ Zn_2$
Formula weight	719.29
Temperature	296(2) K
Wavelength	0.71073 Å
Crystal system	Monoclinic
Space group	P 2/n
Unit cell dimensions	a = 10.9454(4) Å, α = 90°.
	b = 10.9146(4) Å, β = 112.457(2)°.
	c = 13.5283(5) Å, γ = 90°.
Volume	1493.59(10) $Å^3$
Z	2
Density (calculated)	1.599 mg/m^3
Absorption coefficient	1.664 mm^{-1}
F(000)	732
Crystal size	0.207 x 0.170 x 0.156 mm^3
Theta range for data collection	2.477° to 25.359°.
Index ranges	–13 <= h <= 12, –13 <= k <= 13, –14 <= l <= 16

Table 1. *Cont.*

Reflections collected	12,174
Independent reflections	2730 [R(int) = 0.0264]
Completeness to theta = 25.242°	99.4%
Absorption correction	Analytical
Max. and min. transmission	0.8479 and 0.7915
Refinement method	Full-matrix least-squares on F^2
Data / restraints / parameters	2730 / 216 / 268
Goodness-of-fit on F^2	1.173
Final R indices [I > 2 sigma(I)]	R1 = 0.0529, wR2 = 0.1239
R indices (all data)	R1 = 0.0554, wR2 = 0.1251
Largest diff. peak and hole	1.239 and −1.152 e.Å^{-3}

3. Results and Discussion

3.1. Crystal Structure of {[$Zn_2(\mu_2$-BDC)$_2$(iQ)$_2$]}$_\infty$, 1

The X-ray crystallographic analysis shows that **1** crystalizes in the monoclinic space group P 2/n, and the asymmetric unit consists of one Zn(II) ion, one BDC dianion, and one isoquinoline molecule (Figure 1). Each Zn(II) ion is five-coordinated in a slightly distorted square pyramidal geometry, coordinated by four carboxyl oxygen atoms of BDC and the nitrogen atom from the isoquinoline molecule. The basal plane is defined by O1, O2, O3, and O4 from four BDC ligands. The apical position is occupied by the nitrogen atom from the coordinated isoquinoline molecule. Toward the apical ligating atom, the metal ion is deviated from the corresponding basal plane by 0.378 Å. The basal planes are found to be very little tetrahedrally distorted with a τ value of 0.012 [τ = (159.01 − 158.29)/60 = 0.012] [40]. The Zn–O bond lengths vary from 2.003(3) to 2.065(4) Å, and the O–Zn–O bond angles range from 88.55(17) to 158.99(17) (Table 2); these values are representative of different coordination geometries of Zn(II) ions in coordination polymers with dicarboxylate-bridging ligands [41–43].

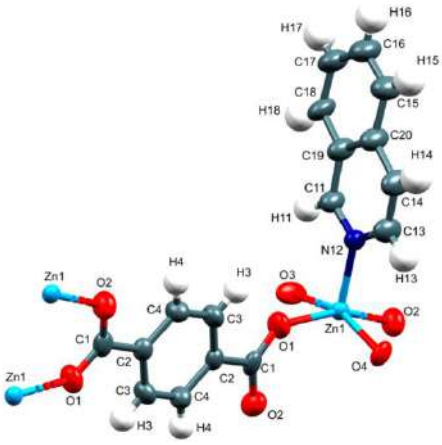

Figure 1. Asymmetric unit of **1**.

In **1**, each BDC ligand bridges four Zn(II) ions, with the two carboxylate moieties assuming a tetrakis(monodentate) coordination mode. As a consequence, pairs of Zn(II) ions are bridged by four carboxylates to form dinuclear secondary building units (SBUs) (Figure 2), which generate a 2D coordination network parallel to the ab plane, enclosing virtually a square grid with a size of 10.945 × 10.915 Å^2. In the SBU, the Zn···Zn distance of 2.9740(11) Å is in the characteristic range of BDC-bridged dinuclear Zn(II) complexes [20,42,44]. Furthermore, a 3D supramolecular network is formed by interpenetrated layers with π–π stacking interactions between the BDC and the secondary ring in the isoquinoline (Figure 3), with a centroid–centroid displacement angle of 7.62° and a distance equal to 3.47(8) Å. Although the presence of the isoquinoline ligand directly attached to the SBU could

contribute to avoiding interpenetration in a similar approach as in the isoreticular series of MOF-2 derivates [45], this phenomenon does not occur in **1**, as the layers along the crystallographic a axis are stabilized by the mentioned π–π interactions.

Table 2. The selected bond lengths (Å) and angles (°) for compound **1**.

Zn(1)-O(4)	2.003(3)	O(4)-Zn(1)-N(12)	102.83(17)
Zn(1)-N(12)	2.033(4)	O(4)-Zn(1)-O(2)#1	88.55(17)
Zn(1)-O(2)#1	2.042(4)	N(12)-Zn(1)-O(2)#1	103.56(17)
Zn(1)-O(3)#2	2.059(4)	O(4)-Zn(1)-O(3)#2	158.30(15)
Zn(1)-O(1)	2.065(4)	O(4)-Zn(1)-O(1)	87.57(17)
Zn(1)-Zn(1)#1	2.9740(11)	N(12)-Zn(1)-O(1)	97.43(17)
		N(12)-Zn(1)-O(3)#2	98.87(17)
		O(2)#1-Zn(1)-O(3)#2	86.9(2)

Symmetry transformations used to generate equivalent atoms: #1 –x + 1/2, y, –z + 5/2; #2 x, y + 1, z.

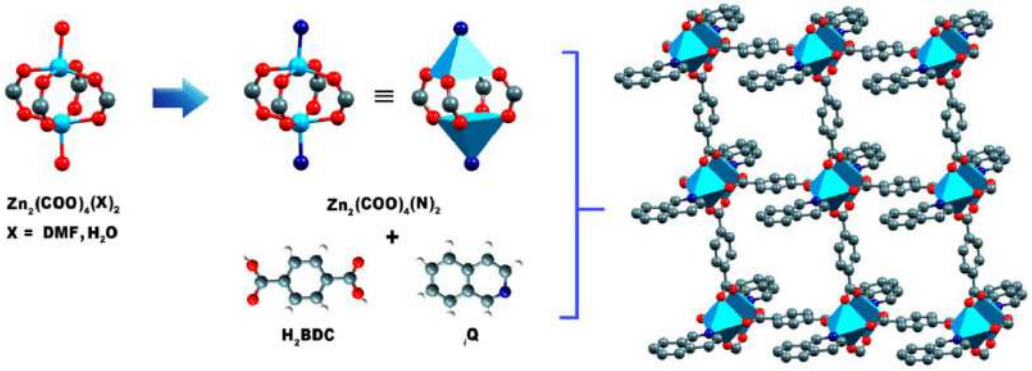

Figure 2. Dinuclear secondary building unit (SBU) and the 2D coordination array in **1**.

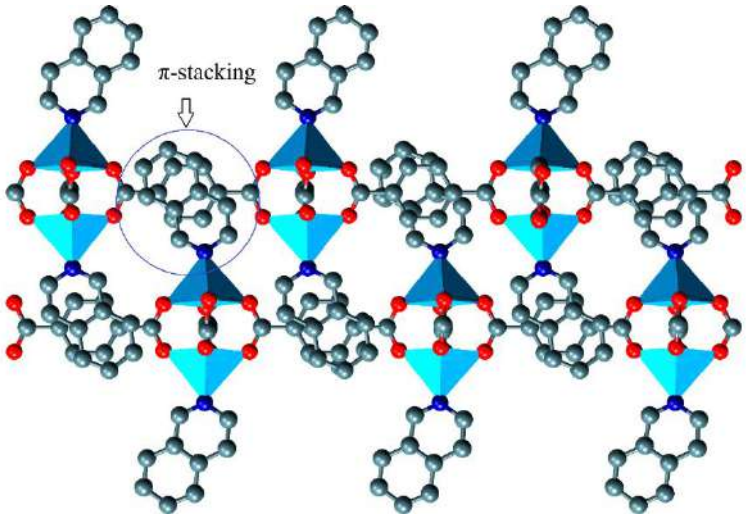

Figure 3. The 3D packing diagram of **1** constructed by π–π stacking interactions.

3.2. PXRD, Thermal Stability, IR-Correlation, and Solid-State Structure-CPMAS ^{13}C NMR Correlation

The purity of the crystalline as-synthesized bulk sample of **1** was examined by powder X-ray diffraction (PXRD) measurements at room temperature (Figure 4). The PXRD patterns of the synthesized sample is consistent with those simulated from single-crystal X-ray data, indicating high phase purity; thus, we used this sample for further solvent sensing studies. The thermal stability of **1** was tested

by thermogravimetric analysis (TGA) under a dinitrogen atmosphere (Figure 5A). Due to the lack of guest solvent molecules, compound **1** presents high stability up to 310 °C. The TGA curve of **1** shows a weight loss of 36.20% from 312 to 411 °C, corresponding to the removal of two coordinated *iQ* molecules (calcd 35.88%). The differential scanning calorimetry curve (DSC) shows a single endotherm peak at 375 °C with ΔH = 307 J/g, which can be attributed to the release of the aromatic N-donor ligand (Figure 5B) [19].

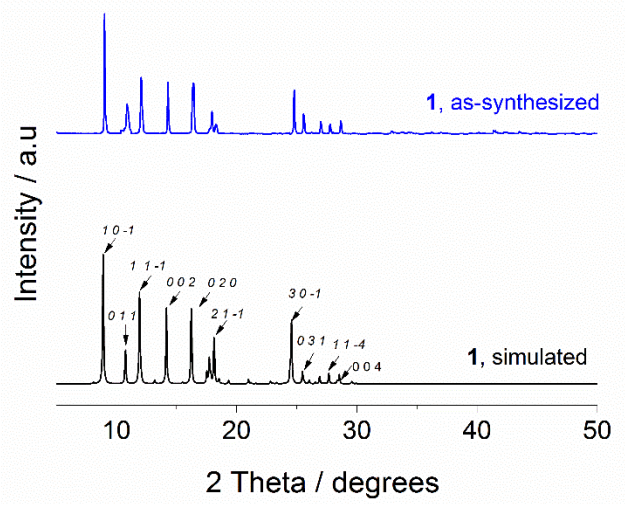

Figure 4. Indexed PXRD simulated pattern and measured pattern of **1** at room temperature.

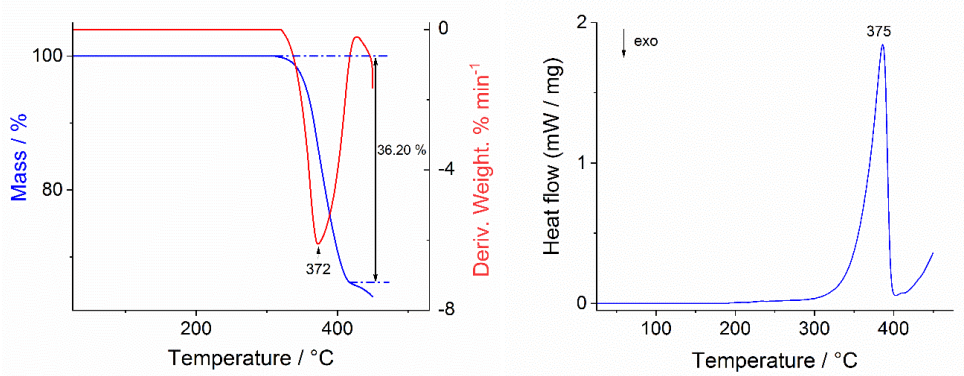

Figure 5. TGA and DTGA curves (**A**) and DSC (**B**) of **1**.

The IR spectrum shows the common bands expected for coordinated carboxylate ligands to atoms Zn(II) along with the corresponding bands to isoquinoline. Two bands of asymmetric and symmetric stretches for the $-CO_2^-$ groups at 1586 and 1410 cm^{-1} and the difference ($\Delta\nu$ = 176 cm^{-1}) can be assigned to the tetrakis(monodentate) coordination mode of the BDC^{2-} ligand, which is in agreement with the crystal structure [46].

The solid-state CPMAS ^{13}C NMR spectrum of **1** (Figure 6) shows three expected signals (red rectangles) for the BDC ligand at 129 and 136 ppm for aromatic carbon atoms (C3 and C4) and the ipso-carbon (C2), respectively, whereas the peak at 171 ppm can be ascribed to the carboxylate (C1) group. All of those assignments are in agreement with the ^{13}C CPMAS NMR spectra of related MOFs such as the zirconio-based MOFs UiO-66 [$Zr_6O_4(OH)_4(BDC)_6$] [47] and MIL-140C [ZrO(BDC)] [47], and zinc-based MOF [$Zn_2(\mu_2$-DBC$)_2(\mu_4$-btre)] (btre = 1,2-bis(1,2,4-triazol-4-yl)ethane) [48]. The blue rectangles denote the methine signals from the isoquinoline ligand, and, as can be seen, some of those peaks are superimposed along with the BDC signals, especially the ^{13}CH atoms C15, C17, C18, and C19, which are in the range of 127–129 ppm. The two downfield signals at 154 and 141 ppm can be ascribed

to methine groups C11 and C13, respectively. In general, the ^{13}C CPMAS spectrum of **1** is consistent with its crystalline structure.

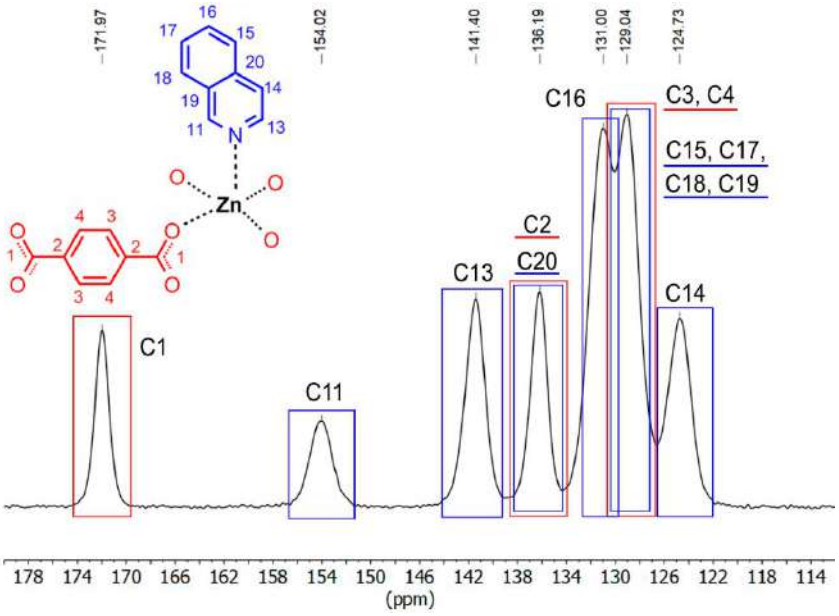

Figure 6. ^{13}C CPMAS NMR spectrum for **1** and numbering scheme of the building unit. Regions with rotation side bands at 8 (16) kHz = 64 (128) ppm from the signal are covered in the NMR spectrum.

3.3. SEM-EDS Analysis

Figure 7 shows SEM micrographs of crystalline compound **1**. Micrometric bars are observed with a well-defined plane facing along the transversal direction. The inset in 7A displays the edge of a bar with the typical cleavage for monoclinic structures (inset 7B), which confirms the crystal system obtained with X-ray diffraction studies. Even though different crystal sizes are shown, the morphology is homogenous, and this could be associated with the presence of only one phase based in the monoclinic unit-cell. EDS elemental mapping of compound **1** is shown in Figure 8. EDS analysis confirms the presence of C, O, and N as part of the chemical composition of the sample; furthermore, it can be observed that the signal of Zn atoms was detected all over the crystals, which can be related to a homogeneous distribution of the Zn in compound **1**.

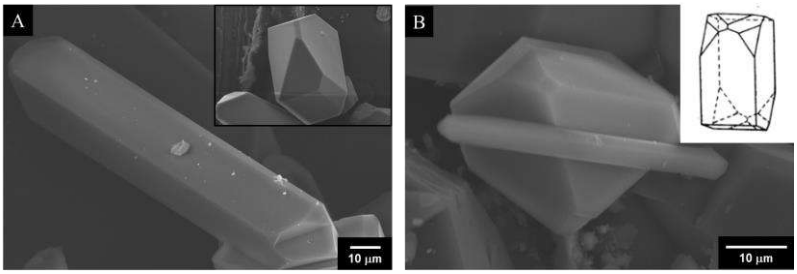

Figure 7. Representative SEM images of compound **1** showing its typical crystal sizes (**A** and **B**, respectively).

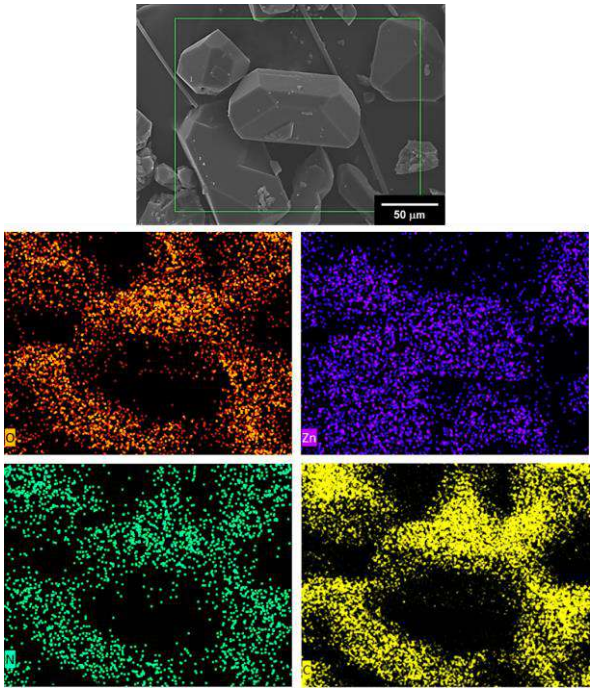

Figure 8. EDS mapping of compound **1**; oxygen (orange), zinc (purple), nitrogen (green), and carbon (yellow).

3.4. Photoluminescent Properties

Currently, luminescent MOMs have been widely studied for sensing different types of small-molecule volatile organic compounds and nitroaromatic compounds [7]; however, the sensing of BTX aromatic solvents (benzene, toluene, xylene isomers) still remains largely unexplored. In order to investigate the potential chemosensing properties of **1**, its photoluminescence spectra of liquid suspensions in several organic solvents including the BTX aromatics, with constant stirring, were analyzed. Figure 9A shows the family of the spectra (λ_{ex} = 330 nm) of **1** (~25 µM). In general, a fluorescence enhancement was observed in the presence of aromatic compounds containing electron-donating groups. Among the studied solvents, p-xylene displays the highest intensity (λ_{em} = 409 nm), followed by m-xylene and o-xylene (λ_{em} = 407 nm). Suspensions in toluene and benzene showed modest emissions at 409 nm, which are significantly lower than that observed for p-xylene. By contrast, alcohols (CH_3OH and EtOH) and aprotic solvents (acetone, $CHCl_3$, CH_3CN, DMF, and THF) practically do not present fluorescent emission. Considering that the acetonitrile suspension does not display emission and this solvent is highly miscible with BTX aromatics, we used an acetonitrile suspension medium of **1** to carry out a solvent sensing experiment due to its potential ability to turn-on fluorescence by addition of xylene isomers, toluene, and benzene. Due to the environmental, chemical, and industrial relevance of xylene isomers, which are anthropogenic polluting solvents, there is growing interest in the development of new luminescent MOF-based sensors in which the analytical responses are based on an increase in fluorescence intensity, rather than quenching, because this limits their practical applications. In this line, the literature features only a few examples for xylene isomer sensing [14,34,35].

Next, the solvent selectivity of an acetonitrile suspension of **1** (~25 µM) was examined by addition of 40 equiv. of BTX, and an emission intensity increase at 409 nm was recorded. Benzene and toluene gave low responses (Figure 9B). Interestingly, **1** showed sensitivity to xylene isomers, especially p-xylene with a considerable increase in its blue emission (I_F/I_0 = 27.2), as shown in Figure 9B. The differing "turn-on" response of the methyl-substituted aromatic VOCs versus the polar aprotic solvents demonstrates the potential of this material to act as a selective and sensitive sensor, and a

potential π–π interaction may arise as a mechanism of interaction between **1** and BTX, which depends on the electro-donating ability of the substituents, as shown in Figure 9B. This fluorescent enhancement may be related to the different interactions between compound **1** and xylene isomers, which have different shapes and volumes; thus, p-xylene is linear and can easily present π–π interactions with the isoquinoline fragments groups. A PLATON program analysis shows that there is about 5% of the crystal volume accessible to solvents [49], which is very limited.

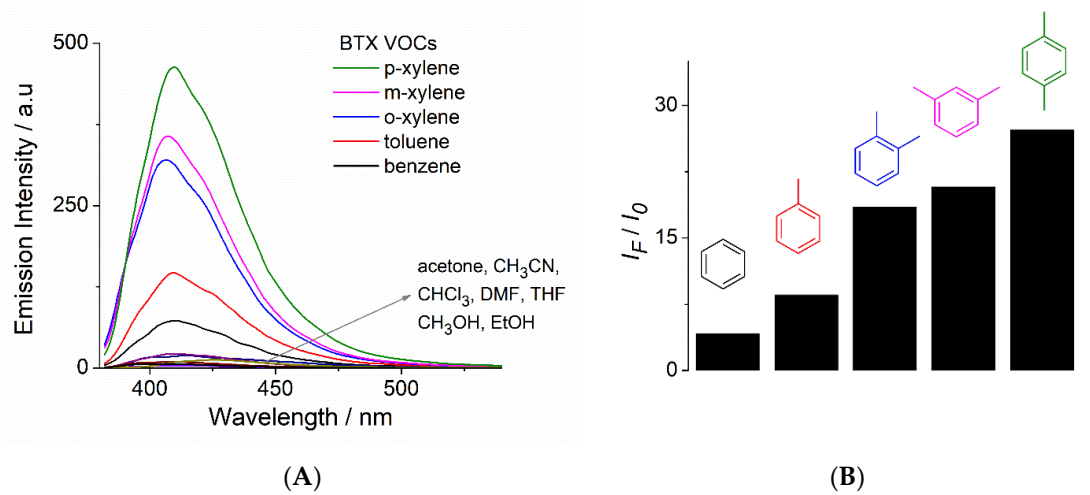

Figure 9. (**A**) Emission spectra of **1** (λ_{ex} = 330 nm) at room temperature in different pure organic solvents and (**B**) fluorescence intensity changes at 409 nm (λ_{ex} = 330 nm) of acetonitrile suspension of **1** upon addition of 40.0 equiv. of benzene, toluene, xylene isomers (BTX).

It is well-known that the fluorescent emission of MOFs is strongly dependent on their chemical environment such as solvation, which can change the relative contributions of charge transfers and intraligand luminescence [2,7]. The weak fluorescence or null of **1** in suspensions of polar solvents such as water, alcohols, and DMF is not unexpected, because these solvents are among the most efficient vibrational quenchers [7]. On the other hand, solvation with hydrophobic aromatic molecules can favor charge transfer processes, which results in an increase in fluorescence.

A similar "turn-on" response has been reported for some MOF-based sensors, and this has been ascribed to an aggregation-enhanced emission [14].

In order to estimate the sensitivity of **1** to p-xylene, a fluorescence titration experiment was carried out by addition of increasing amounts of this solvent to an acetonitrile suspension of **1**. The addition of p-xylene (0–40 equiv.) induced a turn-on fluorescence response (Figure 10). For the concentration range of [p-xylene] <200 μM, the emission shows a linear dependence, as shown in Figure 10 (inset). The detection limit (LOD) of p-xylene for **1**, defined as LOD = 3σ/s, where σ is the standard deviation of the blank signals and s is the slope of the calibration curve with the linear fit (inset, Figure 10), is 10 ± 0.3 μM.

Finally, in order to explore the chemical stability of **1** and potential guest introduction inside the layers, we compared PXRD patterns and FTIR spectra of the as-synthesized compound **1** and a sample of this MOF treated with p-xylene by stirring (30 min) at r.t. In general, the patterns and IR spectra are very similar to each other (Figure 11), before and after treatment, indicating that its crystal structure remains intact in the presence of p-xylene. This chemical stability can be favored by very limited access to solvents. In this sense, the enhancement of fluorescence can be mainly attributed to the solvation phenomenon.

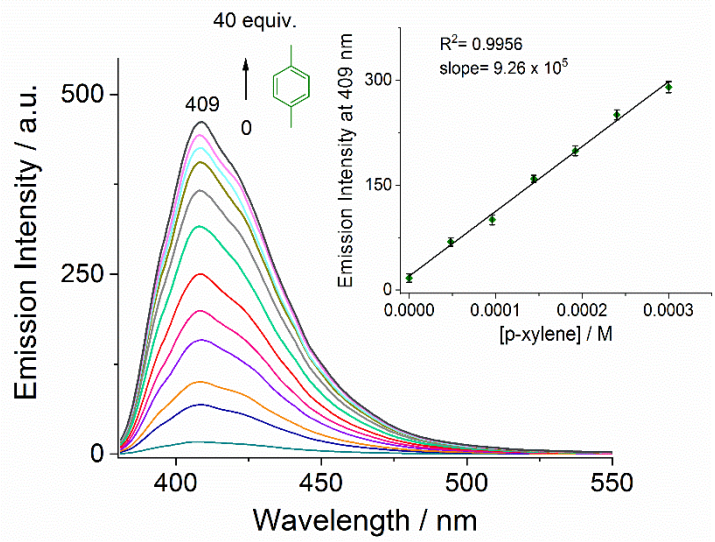

Figure 10. Changes in the emission spectra (λ_{ex} = 330 nm) of acetonitrile suspension of **1** upon addition of increasing amounts of p-xylene (0–300 μM). The inset shows the calibration curve with a linear fit at λ_{em} = 409 nm (average of triplicate experiments).

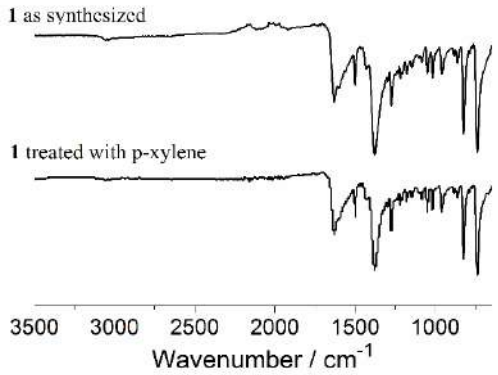

Figure 11. IR-ATR (attenuated total reflection) of as-synthesized **1** and treated with p-xylene isomer.

4. Conclusions

A new Zn(II)-based metal−organic framework, **1**, has been designed and synthesized by solvothermal synthesis combining terephthalic acid and isoquinoline in DMF. X-ray crystallographic studies revealed interpenetrated 2D networks containing a dinuclear Zn_2 paddle-wheel core. Photoluminescence properties of **1** in suspensions of xylene isomers show that **1** possesses a strong blue emission with a maximum at 409 nm. Compound **1**, suspended in acetonitrile, can be used as a luminescent material for the sensing of p-xylene in the micromolar concentration range based on an increase in its fluorescent emission.

The strong emission of **1** in combination with the straightforward synthesis and its high thermal stability up to 310 °C makes it a promising candidate for the design of more sophisticated blue-light-emitting materials with potential application in sensing of methyl-substituted aromatic VOCs.

Author Contributions: L.D.R.-V. and I.J.B.R. Synthesized and performed the experiments; S.H.-O. Single-crystal X-ray diffraction; A.R.V.-N. SEM-EDS analysis; J.d.J.C.-M. Contributed reagents and analysis of data; A.D.-G. and V.S.-M. wrote the paper. All authors have read and agreed to the published version of the manuscript.

Funding: This research was funded by Universidad Autónoma del Estado de México (Project 4995/2020CIB) and CONACyT (CB239648, ID-179 "Fronteras de la Ciencia"). L.D.R.-V., and I.J.B.R. are grateful to CONACyT for Ph.D. scholarships 713164 and 577221, respectively.

Acknowledgments: We thank María de la Nieves Zavala Segovia (NMR), Alejandra Núñez Pineda (thermal analysis), L.I.A María Citlalit Martínez Soto (computing assitance). María del Roció Patiño Maya (IR-ATR), María de la Paz Orta Pérez (elemental analysis) and Adriana Tejeda-Cruz (PXRD). The authors thank UNAM´s BGSI node.

Conflicts of Interest: The authors declare no competing financial interests.

References

1. Lei, J.; Qian, R.; Ling, P.; Cui, L.; Ju, H. Design and sensing applications of metal-organic framework composites. *Trends. Anal. Chem.* **2014**, *58*, 71–78. [CrossRef]
2. Allendorf, M.D.; Bauer, C.A.; Bhakta, R.K.; Houk, R.J.T. Luminescent metal-organic frameworks. *Chem. Soc. Rev.* **2009**, *38*, 1330–1352. [CrossRef] [PubMed]
3. Kreno, L.E.; Leong, K.; Farha, O.K.; Allendorf, M.D.; Van Duyne, R.P.; Hupp, J.T. Metal-organic framework materials as chemical sensors. *Chem. Rev.* **2012**, *112*, 1105–1125. [CrossRef] [PubMed]
4. Liao, Z.; Xia, T.; Yu, E.; Cui, Y. Luminescent metal–organic framework thin films: From preparation to biomedical sensing applications. *Crystals.* **2018**, *8*, 338. [CrossRef]
5. Zhang, X.; Wang, W.; Hu, Z.; Wang, G.; Uvdal, K. Coordination polymers for energy transfer: Preparations, properties, sensing applications, and perspectives. *Coord. Chem. Rev.* **2015**, *284*, 206–235. [CrossRef]
6. Zhang, N.; Guan, Q.L.; Liu, C.H.; Sun, Y.; Li, B.; Xing, Y.H.; Bai, F.Y. A rht-Type Luminescent Zn (II)-MOF Constructed by Triazine Hexacarboxylate Ligand: Tunable Luminescent Performance and White-light Emission Regulation through doping Eu^{3+}/Tb^{3+}. *Appl. Organometal Chem.* **2020**, *34*, 1–10. [CrossRef]
7. Müller-Buschbaum, K.; Beuerle, F.; Feldmann, C. MOF based luminescence tuning and chemical/physical sensing. *Microporous Mesoporous Mater.* **2014**, *216*, 171–199. [CrossRef]
8. Kumar, P.; Deep, A.; Kim, K.; Brown, R.J.C. Progress in Polymer Science Coordination polymers: Opportunities and challenges for monitoring volatile organic compounds. *Prog. Polym. Sci.* **2015**, *45*, 102–118. [CrossRef]
9. Rosales-Vázquez, L.D.; Valdes-García, J.; Bazany-Rodríguez, I.J.; Germán-Acacio, J.M.; Martínez-Otero, D.; Vilchis-Néstor, A.R.; Morales-Luckie, R.; Sánchez-Mendieta, V.; Dorazco-González, A. A sensitive photoluminescent chemosensor for cyanide in water based on a zinc coordination polymer bearing ditert-butyl-bipyridine. *Dalt. Trans.* **2019**, *48*, 12407–12420. [CrossRef]
10. Wu, S.; Lin, Y.; Liu, J.; Shi, W.; Yang, G.; Cheng, P. Rapid Detection of the Biomarkers for Carcinoid Tumors by a Water Stable Luminescent Lanthanide Metal–Organic Framework Sensor. *Adv. Funct. Mater.* **2018**, *28*, 1–10. [CrossRef]
11. Pramanik, S.; Zheng, C.; Zhang, X.; Emge, T.J.; Li, J. New Microporous Metal–Organic Framework Demonstrating Unique. *J. Am. Chem. Soc.* **2011**, *133*, 4153–4155. [CrossRef] [PubMed]
12. Zhang, L.; Kang, Z.; Xin, X.; Sun, D. Metal–Organic frameworks based luminescent materials for nitroaromatics sensing. *CrystEngComm* **2015**, *18*, 193–206. [CrossRef]
13. Rosales-Vázquez, L.D.; Sánchez-Mendieta, V.; Dorazco-González, A.; Martínez-Otero, D.; García-Orozco, I.; Morales-Luckie, R. Cadmium-1,4-cyclohexanedicarboxylato coordination polymers bearing different di-alkyl-2,2′-bipyridines: Syntheses, crystal structures and photoluminescence studies. *Dalt. Trans.* **2017**, *46*, 12516–12526. [CrossRef] [PubMed]
14. Jackson, S.L.; Rananaware, A.; Rix, C.; Bhosale, S.V.; Latham, K. Highly Fluorescent Metal-Organic Framework for the Sensing of Volatile Organic Compounds. *Cryst. Growth Des.* **2016**, *16*, 3067–3071. [CrossRef]
15. Kumar, P.; Deep, A.; Kim, K.-H. Metal organic frameworks for sensing applications. *Trends. Anal. Chem.* **2015**, *73*, 39–53. [CrossRef]
16. Zhou, J.M.; Shi, W.; Xu, N.; Cheng, P. Highly selective luminescent sensing of fluoride and organic small-molecule pollutants based on novel lanthanide metal-organic frameworks. *Inorg. Chem.* **2013**, *52*, 8082–8090. [CrossRef] [PubMed]
17. Wang, X.; Qin, C.; Wang, E.; Li, Y.; Hao, N.; Hu, C.; Xu, L. Syntheses, structures, and photoluminescence of a novel class of d^{10} metal complexes constructed from pyridine-3,4-dicarboxylic acid with different coordination architectures. *Inorg. Chem.* **2004**, *43*, 1850–1856. [CrossRef]
18. Liu, G.X.; Zhu, K.; Chen, H.; Huang, R.Y.; Xu, H.; Ren, X.M. Two novel three-dimensional coordination polymers based on metal clusters: Hydrothermal syntheses, crystal structures and luminescence. *Inorg. Chim. Acta* **2009**, *362*, 1605–1610. [CrossRef]

19. Rendón-Balboa, J.C.; Villanueva-Sánchez, L.; Rosales-Vázquez, L.D.; Valdes-García, J.; Vilchis-Nestor, A.R.; Martínez-Otero, D.; Martínez-Vargas, S.; Dorazco-González, A. Structure of a luminescent 3D coordination polymer constructed with a trinuclear core of cadmium-trimesate and isoquinoline. *Inorg. Chim. Acta* **2018**, *483*, 235–240. [CrossRef]
20. Ma, B.Q.; Mulfort, K.L.; Hupp, J.T. Microporous pillared paddle-wheel frameworks based on mixed-ligand coordination of zinc ions. *Inorg. Chem.* **2005**, *44*, 4912–4914. [CrossRef] [PubMed]
21. Li, M.; Li, D.; O'Keeffe, M.; Yaghi, O.M. Topological analysis of metal-organic frameworks with polytopic linkers and/or multiple building units and the minimal transitivity principle. *Chem. Rev.* **2014**, *114*, 1343–1370. [CrossRef]
22. Munn, A.S.; Amabilino, S.; Stevens, T.W.; Daniels, L.M.; Clarkson, G.J.; Millange, F.; Lennox, M.J.; Düren, T.; Bourelly, S.; Llewellyn, P.L.; et al. Metal-organic frameworks from divalent metals and 1,4-benzenedicarboxylate with bidentate pyridine-N-oxide co-ligands. *Cryst. Growth Des.* **2015**, *15*, 891–899. [CrossRef]
23. Hawxwell, S.M.; Brammer, L. Two-dimensional metal-organic frameworks containing linear dicarboxylates. *Acta Cryst. Sect. B Struct. Sci.* **2006**, *3*, 808–814. [CrossRef]
24. Luisi, B.S.; Ma, E.Z.; Moulton, E.B. Tri-metal Secondary Building Units: Toward the Design of Thermally Robust Crystalline Coordination Polymers. *J. Chem. Crystallogr.* **2007**, *37*, 743–747. [CrossRef]
25. Hailian, L.; Eddaoudi, M.; Groy, T.L.; Yaghi, O.M. Establishing Microporosity in Open Metal–Organic Frameworks: Gas Sorption Isotherms for Zn (BDC). *J. Am Chem Soc.* **1998**, *120*, 8571–8572.
26. Tao, J.; Tong, M.-L.; Shi, J.-X.; Chen, X.-M.; Ng, S.W. Blue photoluminescent Zinc coordination polymers with supertetranuclear cores. *Chem. Commun.* **2000**, *20*, 2043–2044. [CrossRef]
27. Mirzaei, A.; Kim, J.H.; Kim, H.W.; Kim, S.S. Resistive-based gas sensors for detection of benzene, toluene and xylene (BTX) gases: A review. *J. Mater. Chem. C.* **2018**, *6*, 4342. [CrossRef]
28. Martins, V.D.; Granato, M.A.; Rodrigues, A.E. Isobaric Vapor-Liquid Equilibrium for Binary Systems 2,2,4-Trimethylpentane with o-Xylene, m-Xylene, p-Xylene, and Ethylbenzene at 250 kPa. *J. Chem. Eng. Data* **2014**, *59*, 1499. [CrossRef]
29. Rushi, A.D.; Datta, K.P.; Ghosh, P.S.; Mulchandani, A.; Shirsat, M.D. Selective Discrimination among Benzene, Toluene, and Xylene: Probing Metalloporphyrin-Functionalized Single-Walled Carbon Nanotube-Based Field Effect Transistors. *J. Phys. Chem. C.* **2014**, *118*, 24034. [CrossRef]
30. Liu, F.F.; Escher, B.I.; Were, S.; Duffy, L.; Ng, J.C. Mixture effects of benzene, toluene, ethylbenzene, and xylenes (BTEX) on lung carcinoma cells via a hanging drop air exposure system. *Chem. Res. Toxicol.* **2014**, *27*, 952–959. [CrossRef]
31. WHO (1993) Benzene, in Environmental Health Criteria 150, World Health Organization, International. Program on Chemical Safety. Available online: http://www.inchem.org/documents/ehc/ehc/ehc150.htm (accessed on 6 April 2020).
32. Pamei, M.; Puzari, A. Luminescent transition metal–organic frameworks: An emerging sensor for detecting biologically essential metal ions. *Nano-Struct. Nano-Objects.* **2019**, *19*, 100364. [CrossRef]
33. Zhang, J.; Zhang, X.; Chen, J.; Deng, C.; Xu, N.; Shi, W.; Chen, P. Highly selective luminescent sensing of xylene isomers by a water stable Zn-organic framework. *Inorg. Chem. Commun.* **2016**, *69*, 1–3. [CrossRef]
34. Semitut, E.Y.; Sukhikh, T.S.; Filatov, E.Y.; Anosova, G.A.; Ryadun, A.A.; Kovalenko, K.A.; Potapov, A.S. Synthesis, crystal structure, and luminescent properties of novel zinc metal-organic frameworks based on 1,3-Bis(1,2,4-triazol-1-yl)propane. *Cryst. Growth Des.* **2017**, *17*, 5559–5567. [CrossRef]
35. Zhang, J.; Wang, J.; Long, S.; Peh, B.; Dong, J.; Wang, Y.; Karmakar, A.; Yuan, Y.D.; Cheng, Y.; Zhao, D. Luminescent Metal-Organic Frameworks for the Detection and Discrimination of o-Xylene from Xylene Isomers. *Inorg. Chem.* **2018**, *57*, 13631–13639. [CrossRef] [PubMed]
36. Zhang, H.; Ma, J.; Chen, D.; Zhou, J.; Zhang, S.; Shia, W.; Cheng, P. Microporous heterometal-organic framework as a sensor for BTEX with high selectivity. *J. Mater. Chem. A.* **2014**, *2*, 20450–20453. [CrossRef]
37. *APEX 2 Software Suite*; Bruker AXS Inc.: Madison, WI, USA, 2010.
38. Sheldrick, M.G. SHELXT−Integrated space-group and crystal-structure determination . *Acta Crystallogr. Sect. A Found. Adv.* **2015**, *A71*, 3. [CrossRef]
39. Hübschle, B.C.; Sheldrick, G.M.; Dittrich, B. ShelXle: A Qt graphical user interface for SHELXL. *J. Appl. Crystallogr.* **2011**, *44*, 1281. [CrossRef]

40. Addison, A.W.; Rao, T.N.; Reedijk, J.; van Rijn, J.; Verschoor, G.C. Synthesis, Structure, and Spectroscopic Properties of copper(II) compounds containing nitrogen–sulphur donor ligands; the crystal and molecular structure of aqua[1,7-bis(N-methylbenzimidazol-2′-yl)-2,6-dithiaheptane]copper(II) perchlorate. *J. Chem. Soc. Dalton. Trans.* **1984**, *1*, 1349–1356. [CrossRef]
41. Chisca, D.; Croitor, L.; Petuhov, O.; Kulikova, O.V.; Galina, F.; Volodina, G.F.; Coropceanu, E.B.; Masunov, A.E.; Fonari, M.S. Tuning structures and emissive properties in a series of Zn(II) and Cd(II) coordination polymers containing dicarboxylic acids and nicotinamide pillars. *CrystEngComm* **2018**, *20*, 432–447. [CrossRef]
42. Cui, K.; Ma, J.; Huo, X.K.; Qu, Z.; Zhang, J.X. A new 2D Zinc(II)-organic framework with dinuclear units based on iodinated terephthalate: Synthesis, crystal structure and luminescence behavior. *Z. Fur Nat. Sect. B. J. Chem. Sci.* **2014**, *69*, 859–863. [CrossRef]
43. Shi, Z.; Pan, Z.; Jia, H.; Chen, S.; Qin, L.; Zheng, H. Zn(II)/Cd(II) terephthalate coordination polymers incorporating Bi-, Tri-, and tetratopic phenylamine derivatives: Crystal structures and photoluminescent properties. *Cryst. Growth Des.* **2016**, *16*, 2747–2755. [CrossRef]
44. Wang, F.K.; Yang, S.Y.; Huang, R.B.; Zheng, L.S.; Batten, S.R. Control of the topologies and packing modes of three 2D coordination polymers through variation of the solvent ratio of a binary solvent mixture. *CrystEngComm* **2008**, *10*, 1211–1215. [CrossRef]
45. Schoedel, A.; Yaghi, O.M. Porosity in Metal–Organic Compounds. In *Macrocyclic and Supramolecular Chemistry How Izatt–Christensen Award Winners Shaped the Field*; Reed, M.I., Ed.; John Wiley & Sons Inc: Chichester, West Sussex, UK, 2016; Volume 1, pp. 210–212.
46. Dorazco-González, A.; Martinez-Vargas, S.; Hernández-Ortega, S.; Valdés-Martínez, J. Directed self-assembly of mono and dinuclear copper(II) isophthalates into 1D polymeric structures. Design and an unusual cocrystallization. *CrystEngComm* **2013**, *15*, 5961–5968.
47. Bennett, T.D.; Todorova, T.K.; Baxter, E.F.; Reid, D.G.; Gervais, C.; Bueken, B.; Van de Voorde, B.; De Vos, D.; Keenf, D.A.; Mellot-Draznieks, C. Connecting defects and amorphization in UiO-66 and MIL-140 metal-organic frameworks: A combined experimental and computational study. *Phys. Chem. Chem. Phys.* **2016**, *18*, 2192–2201. [CrossRef] [PubMed]
48. Habib, H.A.; Hoffmann, A.; Höppe, H.A.; Janiak, C. Crystal structures and solid-state CPMAS ^{13}C NMR correlations in luminescent zinc(II) and cadmium(II) mixed-ligand coordination polymers constructed from 1,2-bis(1,2,4-triazol-4-yl)ethane and benzenedicarboxylate. *Dalt. Trans.* **2009**, *10*, 1742–1751. [CrossRef] [PubMed]
49. Spek, A.J. Single-crystal structure validation with the program. *PLATON J. Appl. Crystallogr.* **2003**, *36*, 7. [CrossRef]

NJC

ROYAL SOCIETY OF CHEMISTRY

PAPER

View Article Online
View Journal | View Issue

Cite this: *New J. Chem.*, 2020, 44, 10317

Dinuclear complexes of Mn, Co, Zn and Cd assembled with 1,4-cyclohexanedicarboxylate: synthesis, crystal structures and acetonitrile fluorescence sensing properties†

Luis D. Rosales-Vázquez, [a] Diego Martínez-Otero,[b] Víctor Sánchez-Mendieta, *[b] Jonathan Jaramillo-García,[b] Antonio Téllez-López,[b] Roberto Escudero, [c] Francisco Morales, [c] Josue Valdes-García[a] and Alejandro Dorazco-González *[a]

Received 22nd March 2020,
Accepted 17th May 2020

DOI: 10.1039/d0nj01410a

rsc.li/njc

Four dinuclear complexes: $[Mn_2(H_2O)_2(chdc)_2(bipy)_2]$, **1**; $[Co_2(H_2O)_2(chdc)_2(bipy)_2]\cdot H_2O$, **2**; $[Zn_2(H_2O)_2(chdc)_2(bipy)_2]\cdot H_2O$, **3**; and $[Cd_2(H_2O)_2(chdc)_2(bipy)_2]\cdot H_2O$, **4**; chdc = *e*,*a*-*cis*-1,4,cyclohexanedicarboxylate and bipy = 2,2′-bipyridine, were attained as single crystals under ambient conditions. Crystallographic studies show that complexes **1**, **2** and **3** are isostructural and crystallize in the monoclinic system with the $P2_1/c$ space group. The metal centers in these complexes are hexa-coordinated with a distorted octahedral coordination sphere. Complex **4** crystallizes in the triclinic system with the $P\bar{1}$ space group; in this compound, the metal centers are hepta-coordinated and their coordination sphere is distorted-capped trigonal prismatic. Magnetic property measurements reveal that complexes **1** and **2** exhibit weak antiferromagnetic ordering. Complex **4** displays solid-state blue emission properties and a highly sensitive response to acetonitrile in water based on turn-on fluorescence with a low detection limit of 1.1 μM and selectivity over common polar organic solvents.

1. Introduction

Dinuclear and polynuclear coordination complexes have been synthesized extensively throughout, at least, the past sixty years, primarily as a subject of chemical structure studies and its relationship to properties, such as, magnetism, optics, electronics, *etc.*[1] However, in the last three decades, these types of compounds have been pursued further as functional materials, with novel applications according to their chemical, morphological and textural properties, among others. These applications range from sensing[2] and molecular recognition[3] to catalysis[4] and anticancer.[5] Thus, nowadays, the search for new coordination complexes with fascinating structures but, most importantly, with relevant properties and applications continues to be a hot topic. Among the possible properties that can be incorporated into a coordination compound, luminescence is a very treasured one, since it provides the possibility of using the complex as a fluorescent probe for chemosensing hazardous substances,[6] amid other technological applications. Dinuclear complexes assembled with 1,4-cyclohexanedicarboxylate are, to some extent, rare. To our knowledge, dinuclear complexes of Cu,[7] Mo,[8] Sn,[9] Pb,[10] Eu[11] and Tb[11] have been reported. In most of these complexes the chdc bridging ligand assumes the most common *e*,*a*-*cis* conformation of the carboxylate moieties. The *e*,*e*-*trans* conformation of the chdc ligand is somewhat uncommon, it has been reported only in coordination polymers made with Fe,[12] La,[13] Nd,[14] and Sm[14] and in our work with a 3-D Cd polymer.[15] The rarest conformation is *a*,*a*-*trans*, which has been found only once in a Sm coordination polymer, in combination with the *e*,*e*-*trans* conformation.[16] In most of the literature related to dinuclear complexes using the chdc bridging ligand, structural studies and solid-state fluorescence properties have mainly been investigated, but no further potential applications have been explored.

On the other hand, the development of fluorescent sensors based on d^{10} metal complexes that can detect small-molecule organic solvents with chemical and environmental relevance,

[a] *Instituto de Química, Universidad Nacional Autónoma de México, Circuito Exterior, Ciudad Universitaria, Ciudad de México, 04510, Mexico. E-mail: adg@unam.mx*
[b] *Centro Conjunto de Investigación en Química Sustentable UAEM-UNAM, Carretera Toluca-Ixtlahuaca Km. 14.5, Tlachaloya, Toluca, Estado de México, 50200, Mexico. E-mail: vsanchezm@uaemex.mx*
[c] *Instituto de Investigaciones en Materiales, Universidad Nacional Autónoma de México, Apartado Postal 70-360, Ciudad de México, 04510, Mexico*

† Electronic supplementary information (ESI) available: CCDC 1907858–1907861 (**1**–**4**). For ESI and crystallographic data in CIF or other electronic format see DOI: 10.1039/d0nj01410a

such as DMF, alcohols, aromatic solvents, acetone and CH_3CN, has become an active area in research within supramolecular chemistry and materials science.[17–19] It is well known that the interplay between d^{10} metal centers and organic aromatic ligands such as 2,2′-bipy derivatives with flexible multi-carboxylate acids offers structural diversity and versatile photoluminescence processes.[20–23] In this context, Zn(II)/Cd(II) complexes containing one available coordination site occupied by a labile solvent molecule are potential molecular sensors for coordinating solvents with higher affinity for the metal center, by a solvent exchange reaction.[15]

Herein, we provide the crystallographic and structural studies of four novel dinuclear complexes made up of Mn, Co, Zn and Cd with 1,4-cyclohexanedicarboxylate as a bridging ligand and 2,2′-bipyridine as an ancillary ligand. Magnetic properties of Mn and Co complexes are presented. Moreover, the Zn and Cd complexes exhibit strong blue photoluminescence in the solid state; remarkably, the Cd dinuclear complex is an efficient fluorescence sensor of acetonitrile in water.

2. Experimental section

2.1 Materials and methods

All chemicals were of analytical grade, purchased commercially (Aldrich) and used without further purification. All syntheses were carried out under aerobic and ambient conditions. Elemental analyses for C, H, and N were obtained by standard methods using a Vario Micro-Cube analyzer. IR spectra of the complexes were obtained using a FT-IR Shimadzu spectrophotometer, IR Prestige-21, from 4000 to 500 cm^{-1}. Magnetic characteristics of the complexes were determined using a MPMS Quantum Design magnetometer, with measurements performed at zero field cooling (ZFC) and field cooling (FC) from 2 to 300 K and *vice versa*. The applied magnetic field was 1000 Oe, and diamagnetic corrections were estimated using Pascal's constants as -250×10^{-6} cm^3 mol^{-1}.

2.2 Synthetic procedures

$[Mn_2(H_2O)_2(chdc)_2(bipy)_2]$ (1). Firstly, disodium 1,4-cyclohexanedicarboxylate was prepared by adding an aqueous solution of NaOH (5 ml; 0.16 M) to a methanol solution (5 ml) of 1,4-cyclohexanedicarboxylic acid (0.0688 g; 0.4 mmol). A solution of 2,2′-bipyridine (0.0624 g; 0.4 mmol) in DMF (5 ml) was added to the solution of sodium 1,4-cyclohexanedicarboxylate while stirring. Then, a deionized water solution (25 ml) of $MnCl_2{\cdot}4H_2O$ (0.07916 g; 0.4 mmol) was added. A yellow translucent solution was obtained. After two weeks, yellow crystals formed; these were filtered out and washed with deionized water. Yield: 79% based on the metal precursor. Elemental analysis (%), $C_{36}H_{40}Mn_2N_4O_{10}$, cal.: 54.14% C, 5.05% H, 7.02% N; found: 53.76% C, 5.16% H 7.06% N.

$[Co_2(H_2O)_2(chdc)_2(bipy)_2]{\cdot}H_2O$ (2). Analogous conditions to the synthesis of **1** were used, except that in this case, a solution of 2,2′-bipyridine (0.0624 g; 0.4 mmol) in methanol (5 ml) was added to the solution of sodium 1,4-cyclohexanedicarboxylate while stirring. Then, a deionized water solution (10 ml) of $Co(NO_3)_2{\cdot}6H_2O$ (0.1164 g; 0.4 mmol) was added. A red-brown translucent solution was obtained. After five days, red crystals were deposited; these were filtered out and washed with deionized water. Yield: 73% based on the metal precursor. Elemental analysis (%), $C_{36}H_{44}Co_2N_4O_{12}$, cal.: 51.31% C, 5.26% H, 6.65% N; found: 51.69% C, 5.17% H 6.68% N.

$[Zn_2(H_2O)_2(chdc)_2(bipy)_2]{\cdot}H_2O$ (3). Similar conditions to the synthesis of **1** were used, except that a deionized water solution (25 ml) of $Zn(NO_3)_2{\cdot}6H_2O$ (0.09413 g; 0.4 mmol) was added. After five days, white crystals were deposited; these were filtered out and washed with deionized water. Yield: 79% based on the metal precursor. Elemental analysis (%), $C_{36}H_{44}N_4O_{12}Zn_2$, cal.: 50.54% C, 5.18% H, 6.55% N; found: 50.71% C, 5.10% H, 6.77% N.

$[Cd_2(H_2O)_2(chdc)_2(bipy)_2]{\cdot}H_2O$ (4). Comparable conditions to the synthesis of **1** were used, except that a deionized water solution (10 ml) of $Cd(NO_3)_2{\cdot}4H_2O$ (0.1233 g; 0.4 mmol) was added. After three days, white crystals formed; these were filtered out and washed with deionized water. Yield: 82% based on the metal precursor. Elemental analysis (%), $C_{36}H_{44}Cd_2N_4O_{12}$, cal.: 45.53% C, 4.67% H, 5.90% N; found: 45.44% C, 4.61% H, 5.89% N.

2.3 X-ray crystallography

Crystallographic data for **1–4** were collected using a Bruker APEX II CCD diffractometer, at 100 K, using Mo-Kα radiation (k = 0.71073 Å) from an Incoatec IμS source and Helios optic monochromator.[24] Suitable crystals were coated with hydrocarbon oil (Parabar), picked up with a nylon loop, and mounted in the cold nitrogen stream of the diffractometer. The structures were solved using intrinsic phasing (SHELXT)[25] and refined by full-matrix least-squares on F^2 [25] using the shelXle GUI.[26] The hydrogen atoms of the C–H bonds were placed in idealized positions whereas the hydrogen atoms from water molecules were localized from the difference electron density map, and their position was refined with U_{iso} tied to the parent atom with distance restraints. In compound **4**, the hydrogens from water molecules present positional disorder in two positions, the occupation was set at 50% and their positions were localized from the difference electron density map and refined using DFIX instruction. In compound **4**, one carboxylate moiety presented positional disorder that was solved using SIMU, RIGU and SADI instructions and the occupancy was refined using a free variable.

Crystallographic data for **1–4** have been deposited at the Cambridge Crystallographic Data Center (CCDC) with the numbers 1907858–1907861,† respectively.

The crystallographic data and refinement details for the complexes are summarized in Table S1 (ESI†). Selected bond lengths, angles, and hydrogen bond interactions for **1–4** are listed in Tables S2–S5, respectively, ESI.†

2.4 Photoluminescence properties

Luminescence spectra in the solid state and those of suspensions of **3** and **4** were recorded using a Fluorometer Agilent Cary

Eclipse system equipped with a crystal holder or a thermostated cell holder with a quartz cuvette. In all cases, single crystalline samples of as synthesized **3** and **4** were used. The suspensions of **4** were prepared by stirring for 10 min at 25 °C using spectrophotometric grade solvents and double distilled water with a concentration of 50.0 μM. Luminescence quantum yields were determined using an aqueous solution of quinine sulfate containing H_2SO_4 (0.5 M) as standard (Φ = 0.546; excited at 360 nm). For the determination of the quantum yield, the excitation wavelength was chosen so that $A < 0.05$[27,28] using the following equation: $\Phi_s = \Phi_r(A_rF_s/A_sF_r)(n_s^2/n_r^2)$, where, s and r denote sample and reference, respectively, A is the absorbance, F is the relative integrated fluorescence intensity, and n is the refractive index of the solvent or solvent mixture. The solid state quantum yield was measured according to the procedure reported by Pålsson,[29] using an integrating sphere previously mounted onto a Jobin Yvon Horiba Fluoromax-3 spectrofluorometer.[29]

3. Results and discussion

3.1 Crystal structures

The dinuclear complex **1** consists of two Mn(II) ions, and two aqua, two chdc and two bipy ligands, as shown in Fig. 1. The Mn(II) ions are hexa-coordinated in a distorted octahedral geometry, each coordinated by three carboxyl oxygen atoms of chdc, two nitrogen atoms from bipy and one oxygen atom from the aqua molecule. The Mn–O bond lengths range from 2.0937(10) to 2.2818(10) Å, while the Mn–N distances are 2.2612(12) and 2.2969(12) Å, which are similar values to those reported for related compounds.[30–32]

Compounds **1**, **2** and **3** are isostructural (Fig. 1 and Fig. S1, S2, ESI†). Therefore, only a few differences are emphasized here, such as bond lengths. In **2**, the Co–O bond lengths range from 2.0638(10) to 2.1974(10) Å, while the Co–N distances are 2.0808(12) and 2.1356(12) Å, which are values that are close to the ones reported for related compounds.[33–35] For **3**, the Zn–O bond lengths range from 2.0549(11) to 2.3105(12) Å, and the Zn–N distances are 2.0894(13) and 2.1765(13) Å, which are like those values reported for associated complexes.[36–38] These dinuclear complexes are formed due to the presence of both monodentate and chelate bidentate coordination modes of chdc ligands, and the *equatorial* and *axial cis* configurations of their carboxylate moieties bridging the two metal ions. We have previously found similar coordination modes of this bridging ligand in 1-D Co(II) coordination polymers.[39] It is worthwhile mentioning that by varying the solvent–water mixtures in the synthesis, we have been able to obtain coordination polymers[15] or complexes with the chdc bridging ligand, using CH_3OH or DMF, respectively. Although these findings require more investigation, it seems that depending on the co-solvent used, there are subtle changes in the solubility of the polymeric *vs* dimeric compounds, leading to the crystallization of different products. This opens an alternative route for trying to control the dimensionality of coordination complexes.[40]

The crystal packing of complexes **1**, **2** and **3** is further stabilized by hydrogen bonds. Adjacent complex units of **1** are connected by hydrogen bonds formed between non-coordinated (O2) and coordinated (O3) carboxyl-oxygen atoms of the two chdc and the oxygen (O5) of the coordinated water. This supramolecular assembly leads to a zigzag 1-D array (Fig. 2). Similar to **1**, molecules of **2** and **3** are bridged by hydrogen bonds, including the ones formed by the corresponding crystallization water molecules, creating also zig-zag 1-D chains (Fig. S3 and S4, ESI†).

The dinuclear complex **4** exhibits a distorted-monocapped trigonal prismatic coordination environment in its hepta-coordinated metal centers, coming from two chdc, two bipy and one coordinated water molecule (Fig. 3). Unlike complexes **1–3**, in **4**, the chdc ligand coordination mode is chelate bidentate at both carboxylate groups. The metal to nitrogen distances are 2.3537(13) and 2.3574(13) Å. The metal to oxygen distances for chcd range from 2.3467(11) to 2.580(3) Å. The M–O bond for the coordinated water molecule is 2.3085(11) Å. The reported Cd(II) hepta-coordinated complexes exhibit similar bond length values.[41–43]

Due to the noticeable differences in distances and the corresponding angles that give form to the trapezoid and triangular faces, in the distorted-monocapped trigonal prismatic geometry of Cd(II) in **4**, the two triangular faces are not parallel (Fig. S5, ESI†). Thus, the planes defined by O1–N1–O3 and O5–N2–O4 make an angle of 22.3°, known as the Bailar twist angle.[44] Intermolecular hydrogen-bonding interactions assemble complex **4** into a 2-D supramolecular array. These interactions are promoted by the presence of both the aqua ligand and the crystallization

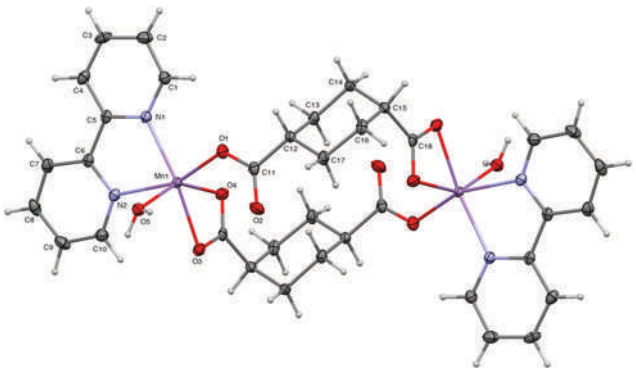

Fig. 1 Molecular structure of **1** (ellipsoids shown at 60% probability).

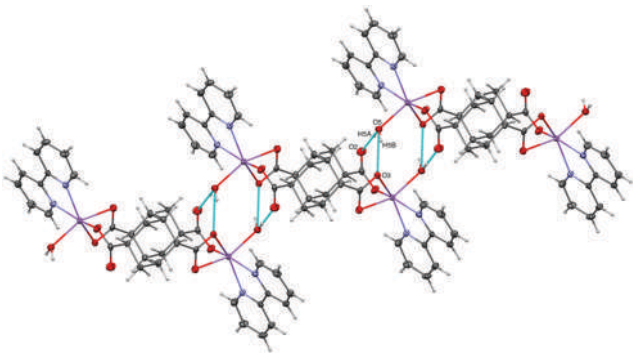

Fig. 2 Supramolecular 1-D zig-zag chain of **1** formed by hydrogen-bonding interactions (ellipsoids shown at 60% probability).

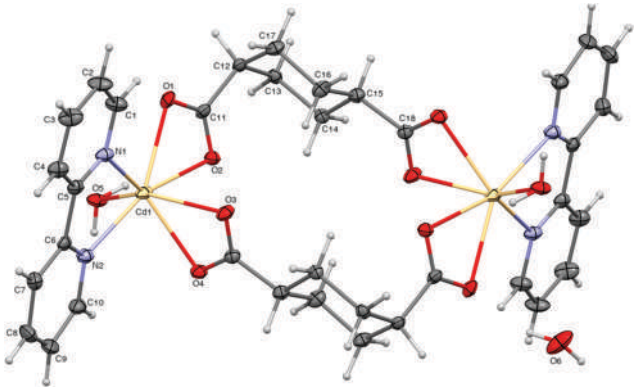

Fig. 3 Molecular structure of **4** (ellipsoids shown at 50% probability).

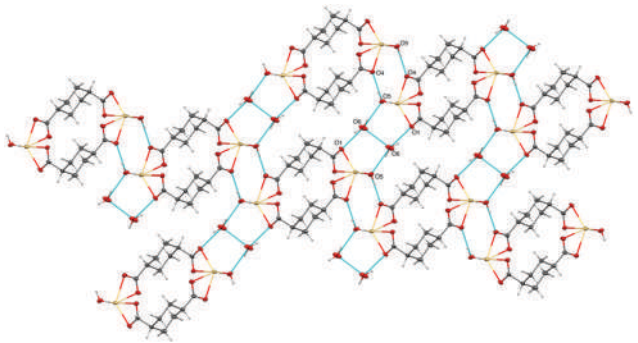

Fig. 4 Supramolecular 2-D array of **4** formed by hydrogen-bonding interactions (chdc ligands are omitted for clarity. Ellipsoids shown at 60% probability).

water molecule. This is shown in Fig. 4, where the main O–H···O interactions involve the O–H moiety (O5) of the aqua ligand with an oxygen atom (O4) of the chdc ligand in an intermolecular hydrogen bond. Furthermore, each water ligand (O5) generates a double hydrogen bridge; the one described above, and another with the oxygen atom (O6) of non-coordinated water, which also forms a hydrogen bond with the oxygen atom (O1) of a neighboring chdc ligand (another intermolecular hydrogen bond), yielding thus the 2-D supramolecular arrangement.

3.2 Magnetic properties of 1 and 2

DC magnetic susceptibility, χ, was determined for **1** and **2**, in zero field cooling (ZFC) and field cooling (FC) modes, from 2–300 K and *vice versa*, in an applied field of 1000 Oe. χT values at room temperature are 13.4 and 5.6 $cm^3\ mol^{-1}$ K for **1** and **2**, respectively, which are higher than the value expected for two magnetically isolated Mn^{2+} (S = 5/2) (8.7 $cm^3\ mol^{-1}$ K) and close to the value of two magnetically isolated Co^{2+} (S = 3/2) (5.2 $cm^3\ mol^{-1}$ K), respectively. Particularly for compound **1**, the χT at 300 K is close to a value when three Mn^{2+} ions would be interacting (~13.0 $cm^3\ mol^{-1}$ K).[45] The calculated magnetic susceptibility (χ_M) *vs.* temperature plots for **1** and **2** can be seen in Fig. 5 and 6, respectively.

Even though no maximum is detected in the magnetic susceptibility plots, the observed increase of χ_M and the decrease in χT (Fig. S6 and S7, ESI†), with decreasing temperature, suggest

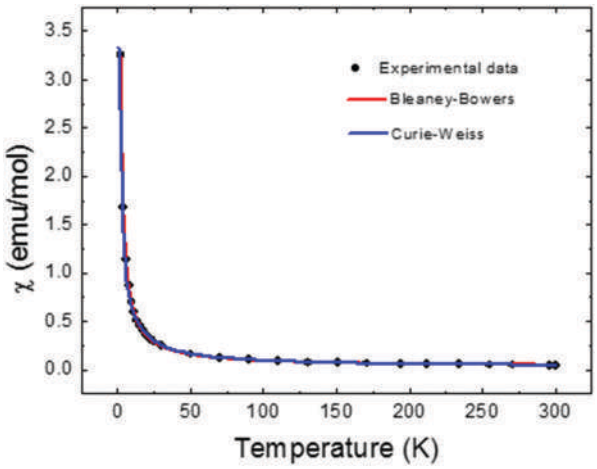

Fig. 5 χ_M *vs.* T plot for **1**.

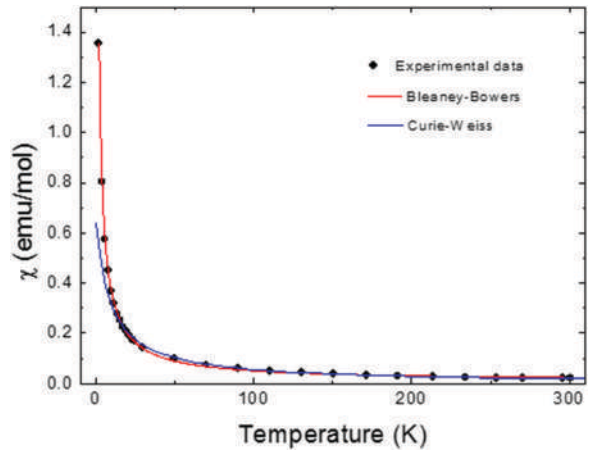

Fig. 6 χ_M *vs.* T plot for **2**.

weak antiferromagnetic coupling in both compounds. Once fitting the obtained data to the Curie–Weiss model:

$$\chi_M = C/(T - \Theta) \quad (1)$$

the Curie constants were determined to be C = 7.4 and 6.0 emu·K mol^{-1} for **1** and **2**, respectively; for S = 5/2 and S = 3/2, respectively, with a small orbital contribution, not totally quenched, which leads to an orbital angular contribution value of less than one. The Curie–Weiss temperatures were determined to be $\Theta_{(C-W)}$ = −1.93 and −9.45 K for **1** and **2**, respectively, both indicative of a weak antiferromagnetic ordering. Frequently, the effects of spin–orbit coupling occur in combination with the effects of a symmetry-lowering structural distortion, away from O_h symmetry,[46] as in these complexes.

Due to the dinuclear nature of complexes **1** and **2**, and to the difficulty of fitting the Curie–Weiss model to the χ *vs.* T plot, particularly below 25 K for compound **2** (Fig. 6), the experimental data were fit using the Bleaney–Bowers eqn (2)[47] for coupled S = 5/2 and S = 3/2 dimeric units, respectively.

$$\chi = (1-\rho)\frac{N_A g^2 \mu_B{}^2 \left(2e^{2J/k_B T}\right)}{k_B (T-\theta)(1+3e^{2J/k_B T})} + \rho\frac{N_A g^2 \mu_B{}^2}{2k_B T} \quad (2)$$

where Θ is the Curie–Weiss temperature and J is the magnetic spin exchange interaction according to the Hamiltonian interaction: $H = -2J\ (S_1 \cdot S_2)$, between two metal magnetic moments in the dimeric unit. The second term in eqn (2) refers to the noninteracting paramagnetic species, with the factor ρ as the molar fraction of these paramagnetic moments, k_B is the Boltzmann constant, N_A is the Avogadro number and μ_B is the Bohr magneton. The best fit of the experimental data was obtained with $J = 133\ cm^{-1}$, $g = 1.61$, and $\Theta = -0.3$ K for **1**, and $J = 97\ cm^{-1}$, $g = 1.34$, and $\Theta = -2.4$ K for **2**. Thus, even though the g values are low and the J values obtained are higher than expected for both complexes, the small and negative Θ values confirm the weak antiferromagnetic interaction between the metal centers in complexes **1** and **2**, as obtained by the Curie–Weiss approach. It is important to mention that the Bleaney–Bowers model has been applied for other complexes and coordination polymers having similar dinuclear units.[48,49] Attempts to fit the magnetic susceptibility data of **2** to the Rueff phenomenological approach,[50] in order to account for the spin–orbit coupling and the magnetic interaction, resulted in divergence of the refinement. So, the magnetic behavior of **1** and **2** agrees well with a weak antiferromagnetic intramolecular interaction between the metal centers, which has usually been found in the *syn–syn*, equatorial–equatorial arrangement in carboxylate bridges of metal ions in analogous dinuclear units.[51] The magnetic properties obtained are also in good accordance with the M···M distances found in **1** and **2**, because of their structural particularities. Complexes **1** and **2** exhibit the shortest distance between metal centers through their supramolecular structures (5.272 and 6.997 Å, respectively) (Fig. 2 and Fig. S3, ESI†); therefore, they display only weak magnetic interactions. We have found similar magnetic properties in complexes and coordination polymers with analogous structural characteristics, where the metal centers are separated by no more than 5 Å, while magnetic exchange was not found in compounds where the metal ion distances fluctuate from 7 to 10 Å.[52]

3.3 Photoluminescence properties of 3 and 4

In the solid-state, **4** exhibits a photoluminescence emission with a band centered at 370 nm, corresponding to a purplish blue color in the CIE-1931 chromaticity diagram, upon excitation at 290 nm, as shown in Fig. 7. In contrast, crystals of **3** display a modest emission intensity at 360 nm with a shoulder band at 369 nm under the same excitation conditions. The emission broad bands for complexes **3** and **4** can be assigned to effective coordination of the chelating N-aromatic ligands to the Zn(II) and Cd(II) ions with a blue-shift ($\Delta \sim$ 5–15 nm) by comparison to the weak fluorescence intensities and emission maxima of the free bipy (λ_{em} = 375 nm, and λ_{ex} = 290 nm) and chdc (λ_{em} = 339 and 431 nm, and λ_{ex} = 290 nm) ligands.[17,53] It is well known that increased fluorescence emission of bipy derivatives on complexation with d^{10} transition metals is due to the increase of the rigidity of the aromatic heterocyclic ligand in the final crystal arrangement, which reduces the loss of energy through non-radiative processes.[54–59] Typically, the emission located in the range of 380–440 nm for free aromatic N-donors is assigned to the intraligand charge transitions (ICTs) entailing the filled π(HOMO) and empty π*(LUMO) orbitals.[57,60,61]

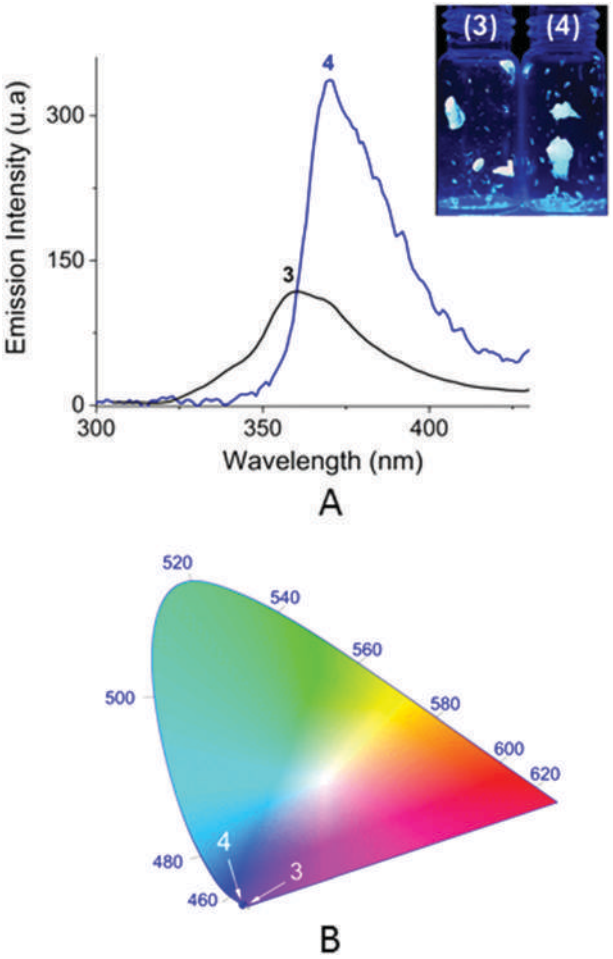

Fig. 7 (A) Solid-state emission spectra (λ_{ex} = 290 nm) of **3** and **4** at room temperature. The inset shows the photographs of crystals of **3** and **4** under UV light of 365 nm. (B) The corresponding color coordinate diagram of emission.

The photoluminescence quantum yield of **4** in the solid state is $\Phi_{ss} = 0.1$ at room temperature. Similar quantum efficiencies (<0.4) have been observed for a series of Cu(I) complexes bearing bipyridines in the solid state and these have been assigned to a ligand-to-metal charge transfer (LMCT)-excited state involving the coordinated bipy.[62]

We have reported previously several dinuclear Zn(II)/Cd(II) polymeric structures bearing di-alkyl-bipy ligands with emission bands in the range of 370–440 nm.[15,28,63] Furthermore, similar photophysical properties for several Zn(II)/Cd(II) polynuclear complexes and metal organic frameworks containing [*N*,*N*]-chelating ligands, such as 2,2′-bipy derivatives and multicarboxylate or arenesulfonate anions, have been reported; for recent examples, see: $[Cd_2(L^1)_2(2,2'\text{-bipy})_2]$,[20] $\{[Cd_5(L^2)_2(2,2'\text{-bipy})_4(H_2O)_4]\text{-bpy}\cdot(NO_3)_2\cdot(H_2O)_8\}_n$,[18,53] $\{[Zn_2(L^3)(2,2'\text{-bipy})(H_2O)_2]\cdot 3H_2O\}_n$.[59,64] $\{[Zn_3(2,2'\text{-bipy})_2(L^4)_2\ (H_2O)_2]\cdot 4H_2O\}_n$,60[56,65] $[Cd_2(\textit{trans}\text{-chdc})(\textit{cis}\text{-chdc})(2,2'\text{-bpp})_2]_n$,[22,53] and $[Cd_{1.5}(L^5)(2,2'\text{-bipy})]$, where: L^1 = 2-hydroxy-5-chloro-1,3-benzenedisulfonic acid, L^2 = (ethylene-bis(oxyethylenenitrilo) tetraacetic acid), L^3 = 4-((3,5-dicarboxyphenyl)carbamoyl)phthalic acid, L^4 = 1*H*-1,2,3-triazole-4,5-dicarboxylic acid, bpp = (1,3-bis(4-pyridyl)propane) and

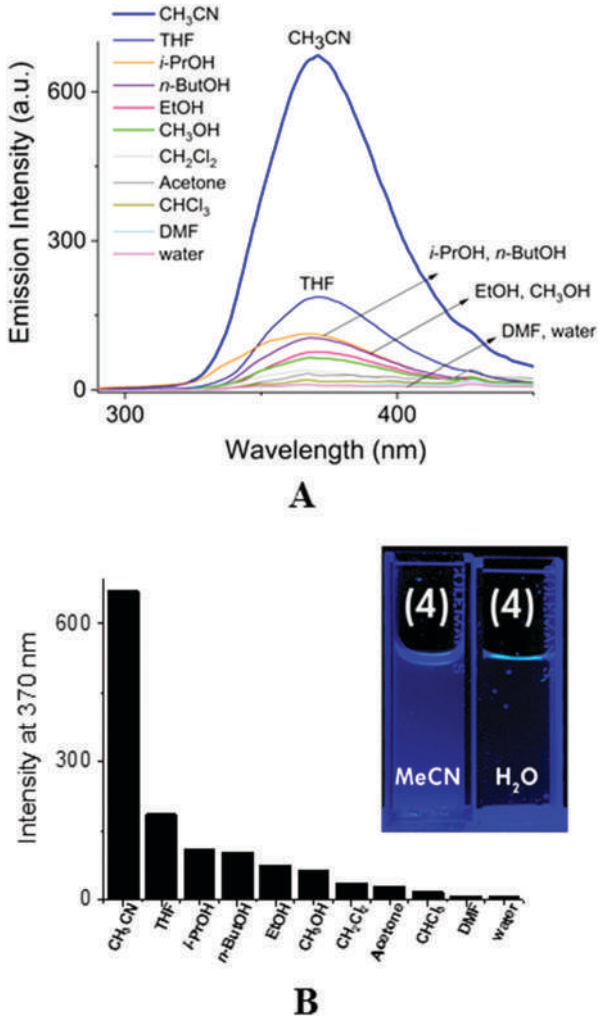

Fig. 8 (A) Emission spectra of **4** (50 μM) dispersed in different organic solvents and water. (B) Fluorescence intensity ratio histograms of **4** in different solvents. The inset shows acetonitrile and water suspensions of **4** under irradiation of 365 nm UV-light.

L^5 = 3-(2′,3′-dicarboxylphenoxy) benzoic acid. The photoluminescence of these kinds of d^{10} metal complexes is assigned to ligand-to-metal charge transfer (LMCT)[17,61] in combination with perturbed π–π and π–n* transitions.[22,57]

To explore the potential sensing properties of **4**, photoluminescence spectra of its liquid suspensions in several pure organic solvents and water were measured. Fig. 8 shows the family of spectra (λ_{ex} = 290 nm) of **4** (~50 μM). In general, the emission intensity is strongly dependent on the solvent molecules. Specifically, in the case of acetonitrile and water, it displayed the highest emission intensity and the most significant quenching effect, respectively (Fig. 10B).

All alcohols (CH_3OH, EtOH, i-PrOH, and *n*-ButOH), chlorinated solvents and THF showed a modest but significantly lower emission than that observed for acetonitrile. In contrast, suspensions in DMF, acetone and water practically do not present photoluminescence. Particularly in water, this fact is not unexpected, because water molecules in the first coordination sphere are among the most efficient vibrational quenchers.[17] Taking the above results and the chemical, environmental and industrial relevance of acetonitrile into account,[66] we used a pure aqueous suspension to sense this solvent by "turn-on" fluorescence. As mentioned before, compound **3** emits weaker light compared to **4**, and for this reason, only the photoluminescence sensing properties of **4** were studied, and this fact may be ascribed to the presence of the dinuclear core, [{Cd(1)N_2O_5}^{Cd(2)N_2O_5}], involving multiple μ-CO_2 ligands, which may rigidify the whole cluster, thus resulting in much weaker vibrations.[58] Nowadays, most luminescent transition-metal-based sensors used for quantification of volatile organic solvents operate under quenching processes and, interestingly, the literature features very few examples for the optical sensing of acetonitrile.[17,67,68]

Next, a fluorescence titration experiment was carried out by addition of increasing amounts of CH_3CN to a suspension of **4** (50 μM) in pure water, as shown in Fig. 9. Notably, there was a linear dependence of the fluorescence intensity on the acetonitrile concentration in the range of 0–0.8 mM (R^2 = 0.993) with a detection limit of 1.1×10^{-6} M. The detection limit is defined as LOD = $3\sigma/s$, where σ is the standard deviation of the blank and s is the slope of the calibration curve (s = 9.06(±0.08) × 10^5). The enhancement of the photoluminescence intensity upon the addition of acetonitrile (I_F/I_o = 67) could be attributed to a dehydration process through an efficient dynamic exchange of coordinated water molecules by acetonitrile molecules. Reversible water-exchange by polar organic solvents has been reported recently for metal-based luminescent sensors.[15,17,69]

We further examined the quantum fluorescence yield (Φ) of **4** in mixtures of water–acetonitrile with different ratios (25%, 50% and 75%, v/v) and pure acetonitrile at room temperature. The quantum yields in these solvent mixtures ($\Phi_{25\%}$ = 0.035, $\Phi_{50\%}$ = 0.048, and $\Phi_{75\%}$ = 0.062) increased depending on the concentration of CH_3CN up to a maximum value of Φ_{CH_3CN} = 0.083 in acetonitrile. This enhanced quantum yield may result from the decreased hydration,[17] both in the number of the

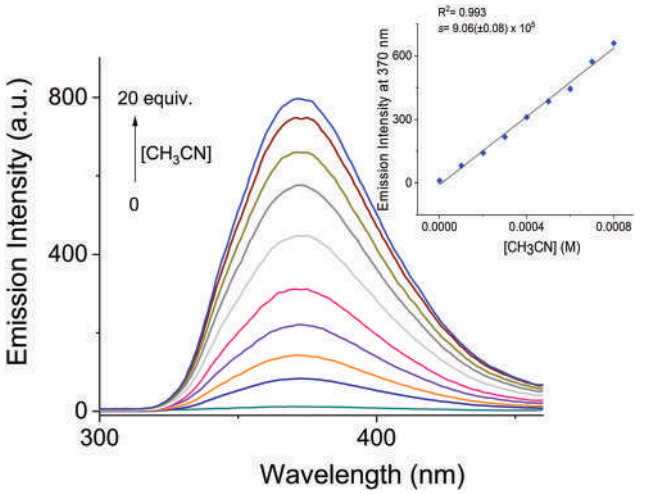

Fig. 9 Changes of the emission spectra (λ_{ex} = 290 nm) of a pure aqueous suspension of **4** upon addition of increasing amounts of CH_3CN (0–0.8 mM). The inset shows the calibration curve with a linear fit at λ_{em} = 370 nm.

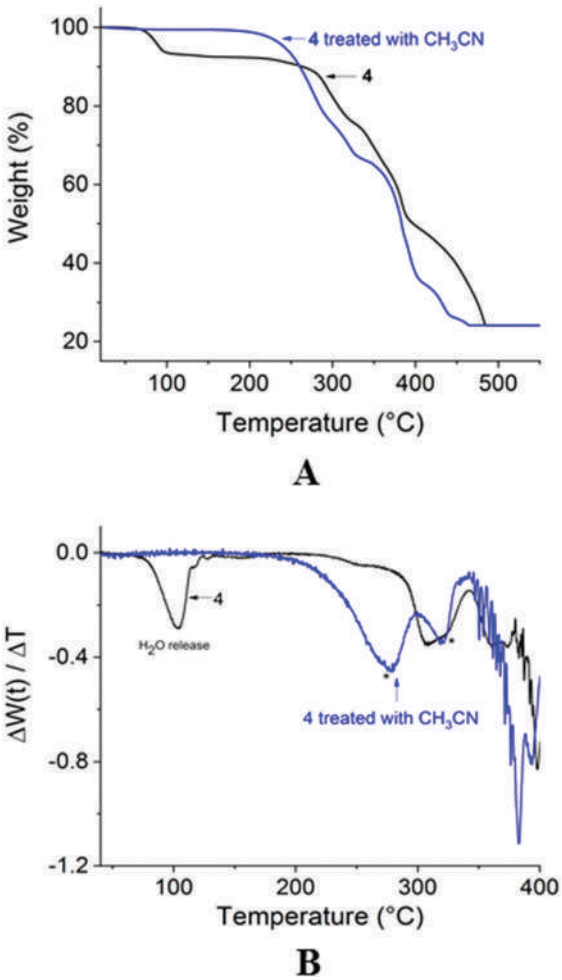

Fig. 10 (A) TGA of the aqua complex **4** (black) and after treatment with CH_3CN by stirring at r.t. (blue). (B) First-derivative TGA plots of solvent exchange. * Decomposition of the complexes.

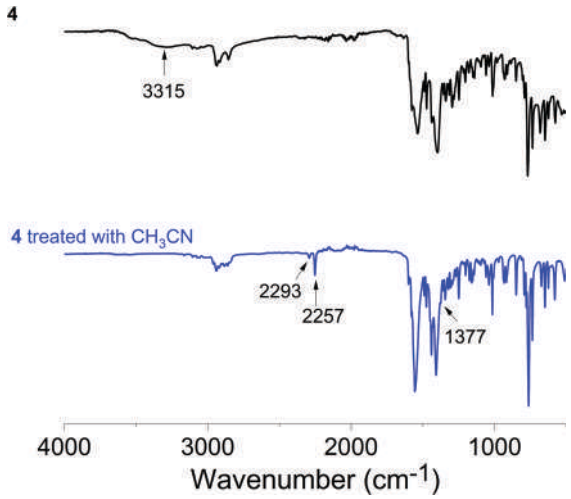

Fig. 11 FT-IR spectra of **4** before (black) and after treatment with CH_3CN (blue).

coordinated water molecules and the crystallization water molecules, with a possible contribution of the aggregation-induced emission (AIE) mechanism.[70]

In order to confirm this solvent-exchange with fluorescence enhancement in **4**, thermogravimetric analysis (TGA) and FT-spectra of aqua complex **4** and a sample of this dinuclear complex treated with CH_3CN, by stirring at r.t., filtering and drying under vacuum, were measured and compared. The TGA curve of **4** (Fig. 10A) shows a continuous weight loss of 7.47% from 80 to 130 °C, corresponding to the removal of two crystallization water molecules and two coordinated water molecules (calcd 7.58%), and no further mass loss was observed until 220 °C. The decomposition process of **4** was observed up to 280 °C. In contrast, the treated dinuclear Cd(II) complex with acetonitrile, shows a different thermal curve with a loss of mass of 40% at a higher temperature range of 170–337 °C in comparison with that observed in the aqua complex **4**, which can be ascribed to the removal of two CH_3CN molecules and two bypi ligands (calcd 41.1%). Finally, the FTIR spectrum of the treated sample **4** (Fig. 11) shows typical bands (cm^{-1}) for CH_3CN at 2293 (stretch, CH_3), 2257 (stretch, CN) and 1377 (*s*-deformation, CH_3) and the characteristic water band at 3315 cm^{-1} was not observed. This fact clearly supports a dynamic solvent-exchange and it is consistent with the IR spectra. For practical applications, sensors are required to have not only a good optical response and affinity but also recyclability. Thus, we studied the reversibility of this water–CH_3CN exchange and the successive fluorescence sensing ability for acetonitrile, considering that it can be easily monitored by IR spectroscopy. Complex **4** can be straightforwardly reactivated by heat desolvation (~70 °C) under vacuum for 2 h with subsequent hydration and reused for four cycles of CH_3CN detection–activation without the loss of sensing ability and retaining the original intensity (~84%), as shown in Fig. S8 (ESI†). Overall, these results highlight the potential utility of simple cadmium-based complexes for efficient sensing of small-molecule solvents.

4. Conclusions

Four dinuclear complexes of Mn (**1**), Co (**2**), Zn (**3**) and Cd (**4**) were obtained under ambient conditions, using 1,4-cyclohexanedicarboxylate and 2,2′-bipyridine as bridging and ancillary ligands, respectively. Complexes **1–3** are isostructural with a pseudo-octahedral coordination sphere and 1D supramolecular assembly formed by hydrogen bonding. Complex **4** exhibits an unusual distorted capped trigonal prismatic coordination sphere, with a 2D supramolecular array formed *via* hydrogen bonding. Complexes **1** and **2** show very weak antiferromagnetic coupling according to Curie–Weiss law fitting. Complex **3** displays only moderate blue photoluminescence emission, unlike complex **4**, which exhibits very strong blue photoluminescence emission in the solid state and is capable of sensing acetonitrile selectively and reversibly in water with the very low detection limit of 1.1×10^{-6} M, and selectivity over alcohols, acetone and DMF. The outstanding sensing ability of **4** for acetonitrile, in combination with its high-yielding synthesis and photophysical properties, makes it a promising candidate for the design of more sophisticated materials with application in the sensing of small molecule solvents.

Conflicts of interest

There are no conflicts to declare.

Acknowledgements

The authors are thankful to M. en C. Alejandra Nuñez Pineda and L. I. A. María Citlalit Martínez Soto (CCIQS UAEM-UNAM) for elemental analysis and computing assistance, respectively. Funding for this work was provided by the Universidad Autónoma del Estado de México (project 4995/2020CIB). We thank UNAM (PAPIIT-UNAM IN216220) and CONACyT for PhD scholarships 713164 and 848787 to L. D. R.-V. and J. V.-G, respectively. R. Escudero acknowledges DGAPA-UNAM, project 1T100217; the authors thank M. C. Ana Bobadilla for the liquid He, Carlos Reyes Damian for technical support, A. López and A. Pompa-Garcia for help with the graphs and figures.

Notes and references

1 E. Berti, A. Caneschi, C. Daiguebonne, P. Dapporto, M. Formica, V. Fusi, L. Giorgi, A. Guerri, M. Micheloni, P. Paoli, R. Pontellini and P. Rossi, *Inorg. Chem.*, 2003, **42**(2), 348.
2 G. Li, D. Zhu, X. Wang, Z. Su and M. R. Bryce, *Chem. Soc. Rev.*, 2020, **49**, 765.
3 M. M. Rhaman, M. H. Hasan, A. Alamgir, L. Xu, D. R. Powell, B. M. Wong, R. Tandon and M. A. Hossain, *Sci. Rep.*, 2018, **8**, 286.
4 A. E. Martell, J. Perutka and D. Kong, *Coord. Chem. Rev.*, 2001, **216–217**, 55.
5 R. W.-Y. Sun, M. Zhang, D. Li, Z.-F. Zhang, H. Cai, M. Li, Y.-J. Xian, S. W. Ng and A. S.-T. Wong, *Chem. – Eur. J.*, 2015, **21**, 18534.
6 N. Kwon, Y. Hu and J. Yoon, *ACS Omega*, 2018, **3**(10), 13731.
7 V. F. Shul'gin, Y. V. Trush, O. V. Konnik, E. B. Rusanov, V. Y. Zub and V. V. Minin, *Russ. J. Inorg. Chem.*, 2011, **56**(5), 707.
8 S. Takamizawa, W. Moil, M. Furihata, S. Takeda and K. Yamaguchi, *Inorg. Chim. Acta*, 1998, **283**, 268.
9 C. Ma, Y. Wang and R. Zhang, *Inorg. Chim. Acta*, 2009, **362**, 4137.
10 J. Yang, J.-F. Ma, Y.-Y. Liu, J.-C. Ma and S. R. Batten, *Cryst Growth Des*, 2009, **9**(4), 1894.
11 L.-N. Dong, Y. Tian, X. Li and Y. Jiang, *J. Coord. Chem.*, 2010, **63**(12), 2088.
12 Y.-Z. Zheng, W. Xue, W.-X. Zhang, M.-L. Tong, X.-M. Chen, F. Grandjean, G. J. Long, S.-W. Ng, P. Panissod and M. Drillon, *Inorg. Chem.*, 2009, **48**, 2028.
13 G. Tian, G. Zhu, B.-L. Su and S. Qiu, *J. Mater. Sci.*, 2009, **44**, 6576.
14 J. Lü, W.-H. Bi, F.-X. Xiao, S. R. Batten and R. Cao, *Chem. – Asian J.*, 2008, **3**, 542.
15 L. D. Rosales-Vázquez, V. Sánchez-Mendieta, A. Dorazco-González, D. Martínez-Otero, I. García-Orozco, R. A. Morales-Luckie, J. Jaramillo-García and A. Téllez-López, *Dalton Trans.*, 2017, **46**, 12516.
16 J. Lü, W.-H. Bi and R. Cao, *CrystEngComm*, 2009, **11**, 2248.
17 J. Heine and K. Müller-Buschbaum, *Chem. Soc. Rev.*, 2013, **42**, 9232.
18 X.-N. Li, L. Li, H.-Y. Wang, C. Fu, J.-W. Fu, Y.-N. Sun and H. Zhang, *Dalton Trans.*, 2019, **48**, 6558.
19 F. Klongdee, S. Youngme and J. A. Boonmak, *Polyhedron*, 2020, **180**, 114437.
20 Y.-Z. Yu, Y.-N. Li, Z.-D. Deng, Z.-B. Zhu and S. Gao, *Polyhedron*, 2015, **90**, 77.
21 G. Yuan, K.-Z. Shao, D.-Y. Du, X.-L. Wang and Z.-M. Su, *Solid State Sci.*, 2011, **13**, 1083.
22 X.-D. Zhu, Y. Li, W.-X. Zhou, R.-M. Liu, Y.-J. Ding, J. Lu and D. M. Proserpio, *CrystEngComm*, 2016, **18**, 4530.
23 S. Zhang, W. Shi and O. Cheng, *Coord. Chem. Rev.*, 2017, **352**, 108.
24 *APEX 2 software suite*. Bruker AXS Inc., Madison, Wisconsin, USA.
25 G. M. Sheldrick, *Acta Crystallogr.*, 2015, **A71**, 3.
26 C. B. Hübschle, G. M. Sheldrick and B. Dittrich, shelXle, *Appl. Cryst.*, 2011, **44**, 1281.
27 W. A. A. Arafa, M. D. Kärkäs, B.-L. Lee, T. Åkermark, R.-Z. Liao, H.-M. Berends, J. Messinger, P. E. M. Siegbahn and B. Åkermark, *Phys. Chem. Chem. Phys.*, 2014, **16**, 11950.
28 A. Dorazco-González, *Organometallics*, 2014, **33**, 868.
29 L.-O. Pålsson and A. P. Monkman, *Adv. Mater.*, 2002, **14**, 757.
30 A. Koval, M. Huisman, A. F. Stassen, P. Gamez, M. Lutz, A. L. Spek, D. Pursche, B. Krebs and J. Reedijk, *Inorg. Chim. Acta*, 2004, **357**, 294.
31 X. Jiang, H. Liu, B. Zheng and J. Zhang, *Dalton Trans.*, 2009, 8714.
32 N. Kotsakis, C. P. Raptopoulou, V. Tangoulis, A. Terzis, J. Giapintzakis, T. Jakusch, T. Kiss and A. Salifoglou, *Inorg. Chem.*, 2003, **42**(1), 22.
33 M. Tabatabaeea, B.-M. Kukovec and V. Razavimahmoudabadia, *Z. Naturforsch.*, 2011, **66b**, 813.
34 M. Bera, A. B. S. Curtiss, G. T. Musie and D. R. Powell, *Inorg. Chem.*, 2012, **51**(22), 12093.
35 X.-M. Chen, Y.-X. Tong and T. C. W. Mak, *Inorg. Chem.*, 1994, **33**(20), 4586.
36 K. Naskar, S. Maity, S. Jana, B. Dutta, S. Tanaka, D. Mallick, T. Akitsu and C. Sinha, *Cryst. Growth Des.*, 2018, **18**(5), 2986.
37 S.-Q. Zhang, F.-L. Jiang, M.-Y. Wu, J. Ma, Y. Bu and M.-C. Hong, *Cryst. Growth Des.*, 2012, **12**(3), 1452.
38 N. Dutta, A. Majumder, A. Das, A. Chatterjee, M. Tarafder, B. Datta and M. Bera, *J. Mol. Struct.*, 2020, **1206**, 127708.
39 L. D. Rosales-Vázquez, V. Sánchez-Mendieta, I. García-Orozco, S. Hernández-López, D. Martínez-Otero, R. A. Morales-Luckie, R. Escudero and F. Morales, *Inorg. Chim. Acta*, 2018, **471**, 674.
40 R. Seetharaj, P. V. Vandana, P. Arya and S. Mathew, *Arabian J. Chem.*, 2019, **12**, 295.
41 F.-Y. Ge, X. Ma, D.-D. Guo, L.-N. Zhu, Z.-P. Deng, L.-H. Huo and S. Gao, *Cryst. Growth Des.*, 2017, **17**(5), 2667.
42 S. Banerjee, P.-G. Lassahn, C. Janiak and A. Ghosh, *Polyhedron*, 2005, **24**, 2963.
43 J. Granifo, S. Suarez and R. Baggio, *Acta Crystallogr.*, 2015, **E71**, 890.

44 S. Alvarez, *Chem. Rev.*, 2015, **115**, 13447.
45 S. G. Baca, Y. Sevryugina, R. Clérac, I. Malaestean, N. Gerbeleu and M. A. Petrukhina, *Inorg. Chem. Commun.*, 2005, **8**, 474.
46 O. Kahn, *Molecular Magnetism*, VCH Publishers, New York, 1993.
47 B. Bleaney and K. D. Bowers, *Proc. R. Soc. London, Ser. A*, 1952, **214**, 451.
48 S. K. Dey, M. Hazra, L. K. Thompson and A. Patra, *Inorg. Chim. Acta*, 2016, **443**, 224.
49 Y. Lou, J. Wang, Y. Tao, J. Chen, A. Mishimab and M. Ohba, *Dalton Trans.*, 2014, **43**, 8508.
50 J. M. Rueff, N. Masciocchi, P. Rabu, A. Sironi and A. Skoulios, *Eur. J. Inorg. Chem.*, 2001, 2843.
51 C. C. Wang, F. Gao, X. X. Guo, H.-P. Jing, P. Wang and S. J. Gao, *Transition Met. Chem. (N. Y.)*, 2016, **41**, 375.
52 A. Téllez-López, V. Sánchez-Mendieta, J. Jaramillo-García, L. D. Rosales-Vázquez, I. García-Orozco, R. A. Morales-Luckie, R. Escudero and F. Morales-Leal, *Transition Met. Chem. (N. Y.)*, 2016, **41**, 879.
53 R. Gaur, *Inorg. Chem. Front.*, 2019, **6**, 278.
54 T. Lu, J.-Y. Wang, D. Tu, Z.-N. Chen, X.-T. Chen and Z.-L. Xue, *Inorg. Chem.*, 2018, **57**, 13618.
55 Y. Ren, S. Zhou, Z. Wang, M. Zhang, J. Wang and J. Cao, *J. Mol. Struct.*, 2017, **1147**, 292.
56 L.-Y. Zhang, J.-P. Zhang, Y.-Y. Lin and X. M. Chen, *Cryst. Growth Des.*, 2006, **6**, 1684.
57 X. Wang, C. Qin, E. Wang, Y. Li, N. Hao, C. Hu and L. Xu, *Inorg. Chem.*, 2004, **43**, 1850.
58 J. Tao, M.-L. Tong, J.-X. Shi, X.-M. Chen and S.-W. Ng, *Chem. Commun.*, 2000, 2043.
59 P. Suresh and G. Prabusankar, *J. Chem. Sci.*, 2014, **126**, 1409.
60 X.-D. Zhu, Y. Li, W.-X. Zhou, R.-M. Liu, Y.-J. Ding, J. Lü and D.-M. Proserpio, *CrystEngComm*, 2016, **18**, 4530.
61 L. Ma, N. Yu, S. Chen and H. Deng, *CrystEngComm*, 2013, **15**, 1352.
62 L. D. Rosales-Vázquez, J. Valdes-García, I. J. Bazany-Rodríguez, J. M. Germán-Acacio, D. Martínez-Otero, A. R. Vilchis-Néstor, R. Morales-Luckie, V. Sánchez-Mendieta and A. Dorazco-González, *Dalton Trans.*, 2019, **48**, 12407.
63 J. C. Rendón-Balboa, L. Villanueva-Sánchez, L. D. Rosales-Vázquez, J. Valdes-García, A. R. Vilchis-Nestor, D. Martínez-Otero, S. Martínez-Vargas and A. Dorazco-González, *Inorg. Chim. Acta*, 2018, **483**, 235.
64 X.-J. Deng, W. Gu, X. Liu, H.-D. Ju, H.-X. He, B.-L. Wang and Z.-H. Weng, *J. Mol. Struct.*, 2020, **1202**, 127212.
65 G. Yuan, K.-Z. Shao, D.-Y. Du, X.-L. Wang and Z.-M. Su, *Solid State Sci.*, 2011, **13**, 1083.
66 X. Yang, S. Wang, G. Li, F. Zhao, Z. Feng, X. Chen, Z. Zhu, Y. Wang and J. Gao, *Ind. Eng. Chem. Res.*, 2020, **59**(11), 5047.
67 J.-L. Du, X. Lu, T.-L. Shen, C.-P. Li, Y.-J. Mu and L.-J. Li, *Mater. Lett.*, 2015, **158**, 225.
68 J.-M. Zhou, W. Shi, N. Xu and P. Cheng, *Inorg. Chem.*, 2013, **52**, 8082.
69 J.-H. Wang, M. Li and D. Li, *Chem. Sci.*, 2013, **4**, 1793.
70 X. Li, Y. Sun, J. Chen, Z. Wu, P. Cheng, Q. Li, J. Fang and D. Chen, *Polym. Chem.*, 2019, **10**, 1575.

Referencias

1 O. M. Yaghi, M. J. Kalmutzki and C. S. Diercks, *Introduction to Reticular Chemistry*, 2019.
2 S. R. Batten, S. M. Neville and D. R. Turner, *Design , Analysis and Application*, .
3 X. Zhang, W. Wang, Z. Hu, G. Wang and K. Uvdal, *Coord. Chem. Rev.*, 2015, **284**, 206–235.
4 A. Erxleben, *Coord. Chem. Rev.*, 2003, **246**, 203–228.
5 M. Eddaoudi, J. Kim, N. Rosi, D. Vodak, J. Wachter, M. O'Keeffe and O. M. Yaghi, *Science (80-.).*, 2002, **295**, 469–472.
6 M. Li, D. Li, M. O'Keeffe and O. M. Yaghi, *Chem. Rev.*, 2014, **114**, 1343–1370.
7 A. Schoedel, M. Li, D. Li, M. O'Keeffe and O. M. Yaghi, *Chem. Rev.*, 2016, **116**, 12466–12535.
8 D. J. Tranchemontagne, J. L. Tranchemontagne, M. O'keeffe and O. M. Yaghi, *Chem. Soc. Rev.*, 2009, **38**, 1257–1283.
9 C. S. Diercks, M. J. Kalmutzki, N. J. Diercks and O. M. Yaghi, *ACS Cent. Sci.*, 2018, **4**, 1457–1464.
10 S. Abednatanzi, P. Gohari Derakhshandeh, H. Depauw, F. X. Coudert, H. Vrielinck, P. Van Der Voort and K. Leus, *Chem. Soc. Rev.*, 2019, **48**, 2535–2565.
11 Y. B. Zhang, H. Furukawa, N. Ko, W. Nie, H. J. Park, S. Okajima, K. E. Cordova, H. Deng, J. Kim and O. M. Yaghi, *J. Am. Chem. Soc.*, 2015, **137**, 2641–2650.
12 Q. Liu, H. Cong and H. Deng, *J. Am. Chem. Soc.*, 2016, **138**, 13822–13825.
13 L. J. Wang, H. Deng, H. Furukawa, F. Gándara, K. E. Cordova, D. Peri and O. M. Yaghi, *Inorg. Chem.*, 2014, **53**, 5881–5883.
14 R. Ma, H. Jiang, C. Wang, C. Zhao and H. Deng, *Chem. Commun.*, 2020, **56**, 2715–2718.
15 C. Hon Lau, R. Babarao and M. R. Hill, *Chem. Commun.*, 2013, **49**, 3634–3636.
16 R. Seetharaj, P. V. Vandana, P. Arya and S. Mathew, *Arab. J. Chem.*, 2019, **12**, 295–315.
17 L. Schweighauser, K. Harano and E. Nakamura, *Inorg. Chem. Commun.*, 2017, **84**, 1–4.
18 D. Frahm, F. Hoffmann and M. Fröba, *Cryst. Growth Des.*, 2014, **14**, 1719–1725.
19 S. L. Yao, S. J. Liu, C. Cao, X. M. Tian, M. N. Bao and T. F. Zheng, *J. Solid State Chem.*, 2019, **269**, 195–202.
20 M. Köppen, V. Meyer, J. Ångström, A. K. Inge and N. Stock, *Cryst. Growth Des.*, 2018, **18**, 4060–4067.
21 C. Gropp, S. Canossa, S. Wuttke, F. Gándara, Q. Li, L. Gagliardi and O. M. Yaghi, *ACS Cent. Sci.*, 2020, **6**, 1255–1273.
22 G. Schmid, *Mind Screen*, 2016, **336**, 1018–1024.
23 A. Dutta, Y. Pan, J. Q. Liu and A. Kumar, *Coord. Chem. Rev.*, 2021, **445**, 214074.
24 M. Lammert, H. Reinsch, C. A. Murray, M. T. Wharmby, H. Terraschke and N. Stock, *Dalt. Trans.*, 2016, **45**, 18822–18826.
25 Z. Li, X. Xu, Y. Fu, Y. Guo, Q. Zhang, Q. Zhang, H. Yang and Y. Li, *RSC Adv.*, 2019, **9**, 620–625.
26 J. Lyu, X. Zhang, K. I. Otake, X. Wang, P. Li, Z. Li, Z. Chen, Y. Zhang, M. C. Wasson, Y. Yang, P. Bai, X. Guo, T. Islamoglu and O. K. Farha, *Chem. Sci.*, 2019, **10**, 1186–1192.
27 F. N. Al-Rowaili, U. Zahid, S. Onaizi, M. Khaled, A. Jamal and E. M. AL-Mutairi, *J. CO2 Util.*, 2021, **53**, 101715.
28 M. Fakhraei Ghazvini, M. Vahedi, S. Najafi Nobar and F. Sabouri, *J. Environ. Chem. Eng.*, 2021, **9**, 104790.
29 Q. Wang and D. Astruc, *Chem. Rev.*, 2020, **120**, 1438–1511.
30 Y. Xue, G. Zhao, R. Yang, F. Chu, J. Chen, L. Wang and X. Huang, *Nanoscale*, 2021, **13**, 3911–3936.
31 C. Pettinari, R. Pettinari, C. Di Nicola, A. Tombesi, S. Scuri and F. Marchetti, *Coord. Chem. Rev.*, 2021, **446**, 214121.
32 N. Rabiee, M. Atarod, M. Tavakolizadeh, S. Asgari, M. Rezaei, O. Akhavan, A. Pourjavadi, M. Jouyandeh, E. C. Lima, A. H. Mashhadzadeh, A. Ehsani, S. Ahmadi, M. Shokouhimehr and M. R. Saeb, *Microporous Mesoporous Mater.*, 2022, 111670.
33 S. Mallakpour, E. Nikkhoo and C. M. Hussain, *Coord. Chem. Rev.*, 2022, **451**, 214262.
34 M. A. Shamim, H. Zia, M. Zeeshan, M. Y. Khan and M. Shahid, *J. Environ. Chem. Eng.*, 2022,

10, 106991.
35 M. Mon, R. Bruno, J. Ferrando-Soria, D. Armentano and E. Pardo, *J. Mater. Chem. A*, 2018, **6**, 4912–4947.
36 M. D. Allendorf, C. A. Bauer, R. K. Bhakta and R. J. T. Houk, *Chem. Soc. Rev.*, 2009, **38**, 1330–1352.
37 Y. Zhang, S. Yuan, G. Day, X. Wang, X. Yang and H. C. Zhou, *Coord. Chem. Rev.*, 2018, **354**, 28–45.
38 L. Chen, D. Liu, J. Peng, Q. Du and H. He, *Coord. Chem. Rev.*, 2020, **404**, 213113.
39 Y. Cui, Y. Yue, G. Qian and B. Chen, *Chem. Rev.*, 2012, **112**, 1126–1162.
40 J. Dong, D. Zhao, Y. Lu and W. Y. Sun, *J. Mater. Chem. A*, 2019, **7**, 22744–22767.
41 M. Pamei and A. Puzari, *Nano-Structures and Nano-Objects*, 2019, **19**, 100364.
42 J. R. Lakowicz, *Principles of Fluorescence Spectroscopy*, Springer, 2006.
43 J. Heine and K. Müller-Buschbaum, *Chem. Soc. Rev.*, 2013, **42**, 9232–9242.
44 B. Valeur, *Molecular Fluorescence*, 2001.
45 J. R. Lakowicz, *Principles of Fluorescence Spectroscopy*, 2006.
46 Y. Du, X. Li, X. Lv and Q. Jia, *ACS Appl. Mater. Interfaces*, 2017, **9**, 30925–30932.
47 Y. Liu, X. Y. Xie, C. Cheng, Z. S. Shao and H. S. Wang, *J. Mater. Chem. C*, 2019, **7**, 10743–10763.
48 J. A. Broussard and K. J. Green, *J. Invest. Dermatol.*, 2017, **137**, e185–e191.
49 L. Yang, Y. L. Liu, C. G. Liu, F. Ye and Y. Fu, *J. Hazard. Mater.*, 2020, **381**, 120966.
50 Y. B. Hao, Z. S. Shao, C. Cheng, X. Y. Xie, J. Zhang, W. J. Song and H. S. Wang, *ACS Appl. Mater. Interfaces*, 2019, **11**, 31755–31762.
51 C. Wang, L. Tian, W. Zhu, S. Wang, P. Wang, Y. Liang, W. Zhang, H. Zhao and G. Li, *ACS Appl. Mater. Interfaces*, 2017, **9**, 20076–20085.
52 Z. Xiaoxiong, Z. Wenjun, L. Cuiliu, Q. Xiaohong and Z. Chengyu, *Inorg. Chem.*, , DOI:10.1021/acs.inorgchem.8b03555.
53 Y. Li, C. Jiang, X. Chen, Y. Jiang and C. Yao, *ACS Appl. Mater. Interfaces*, , DOI:10.1021/acsami.2c00160.
54 N. Bagheri, A. Khataee, B. Habibi and J. Hassanzadeh, *Talanta*, 2018, **179**, 710–718.
55 Y. Cai, H. Zhu, W. Zhou, Z. Qiu, C. Chen, A. Qileng, K. Li and Y. Liu, *Anal. Chem.*, 2021, **93**, 7275–7282.
56 M. Amirzehni, J. Hassanzadeh and B. Vahid, *Sensors Actuators, B Chem.*, 2020, **325**, 128768.
57 L. D. Rosales-Vázquez, V. Sánchez-Mendieta, A. Dorazco-González, D. Martínez-Otero, I. García-Orozco, R. A. Morales-Luckie, J. Jaramillo-Garcia and A. Téllez-López, *Dalt. Trans.*, 2017, **46**, 12516–12526.
58 E. Moradi, R. Rahimi, Y. D. Farahani and V. Safarifard, *J. Solid State Chem.*, 2020, **282**, 121103.
59 H. Chai, Y. Ren, H. He, Z. Wang, Y. Zhang and L. Gao, *J. Solid State Chem.*, 2019, **271**, 162–167.
60 B. L. Li, H. N. Wang, L. Zhao, G. Z. Li and Z. M. Su, *Inorg. Chem. Commun.*, 2016, **66**, 87–89.
61 E. Moradi, R. Rahimi and V. Safarifard, *J. Solid State Chem.*, 2020, **286**, 121277.
62 Z. Li, Z. Zhan, Y. Jia, Z. Li and M. Hu, *J. Ind. Eng. Chem.*, 2021, **97**, 180–187.
63 Z. Long Ma, M. Chen Wang, L. Tian and L. Cheng, *Inorganica Chim. Acta*, 2021, **526**, 120513.
64 X. L. Chen, L. Shang, L. Liu, H. Yang, H. L. Cui and J. J. Wang, *Dye. Pigment.*, 2021, **196**, 109809.
65 B. Parmar, K. K. Bisht, Y. Rachuri and E. Suresh, *Inorg. Chem. Front.*, 2020, **7**, 1082–1107.
66 T. Rasheed and F. Nabeel, *Coord. Chem. Rev.*, 2019, 401, 213065.
67 A. Karmakar, P. Samanta, S. Dutta and S. K. Ghosh, *Chem. - An Asian J.*, 2019, **14**, 4506–4519.
68 H. Y. Li, S. N. Zhao, S. Q. Zang and J. Li, *Chem. Soc. Rev.*, 2020, **49**, 6364–6401.
69 J. de J. C.-M. and A. D.-G. Luis D. Rosales-Vázquez, Iván J. Bazany Rodríguez, Simón Hernández-Ortega, Víctor Sánchez-Mendieta, Alfredo R. Vilchis-Nestor, *Crystals*, 2020, 1–13.
70 L. Zhang, Z. Kang, X. Xin and D. Sun, *CrystEngComm*, 2015, **18**, 193–206.
71 X. Q. Yao, G. Bin Xiao, H. Xie, D. D. Qin, H. C. Ma, J. C. Liu and P. J. Yan, *CrystEngComm*, 2019, **21**, 2559–2570.

72 T. Kumar, M. Venkateswarulu, B. Das, A. Halder and R. R. Koner, *Dalt. Trans.*, 2019, **48**, 12382–12385.
73 L. Zhang, Z. Kang, X. Xin and D. Sun, *CrystEngComm*, 2015, **18**, 193–206.
74 J. H. Qin, Y. D. Huang, M. Y. Shi, H. R. Wang, M. Le Han, X. G. Yang, F. F. Li and L. F. Ma, *RSC Adv.*, 2020, **10**, 1439–1446.
75 C. S. Wang, Q. Huang, X. Wang, Y. T. Zhang, D. S. Ma, Y. H. Yu and J. S. Gao, *RSC Adv.*, 2019, **9**, 42272–42283.
76 D. Feng, J. Tang, J. Yang, X. Ma, C. Fan and X. Wang, *J. Mol. Struct.*, 2020, **1221**, 128841.
77 L. Di, Z. Xia, J. Li, Z. Geng, C. Li, Y. Xing and Z. Yang, *RSC Adv.*, 2019, **9**, 38469–38476.
78 C. S. Wang, Q. Huang, X. Wang, Y. T. Zhang, D. S. Ma, Y. H. Yu and J. S. Gao, *RSC Adv.*, 2019, **9**, 42272–42283.
79 L. Q. Zhang, X. W. Wang, L. Gu, Y. H. Yu and J. S. Gao, *RSC Adv.*, 2020, **10**, 9476–9485.
80 T. Kumar, M. Venkateswarulu, B. Das, A. Halder and R. R. Koner, *Dalt. Trans.*, 2019, **48**, 12382–12385.
81 L. Fan, F. Wang, D. Zhao, Y. Peng, Y. Deng, Y. Luo and X. Zhang, *Appl. Organomet. Chem.*, 2020, **34**, 1–10.
82 L. Di, Z. Xia, J. Li, Z. Geng, C. Li, Y. Xing and Z. Yang, *RSC Adv.*, 2019, **9**, 38469–38476.
83 D. Banerjee, Z. Hu and J. Li, *Dalt. Trans.*, 2014, **43**, 10668–10685.
84 M. L. Hu, S. A. A. Razavi, M. Piroozzadeh and A. Morsali, *Sensing organic analytes by metal-organic frameworks: A new way of considering the topic*, Royal Society of Chemistry, 2020, vol. 7.
85 D. W. Sun, L. Huang, H. Pu and J. Ma, *Chem. Soc. Rev.*, 2021, **50**, 1070–1110.
86 J. Tang, X. Ma, J. Yang, D. D. Feng and X. Q. Wang, *Dalt. Trans.*, 2020, **49**, 14361–14372.
87 Y. Li, D. Ma, C. Chen, M. Chen, Z. Li, Y. Wu, S. Zhu and G. Peng, *J. Solid State Chem.*, 2019, **269**, 257–263.
88 E. Moradi, R. Rahimi and V. Safarifard, *J. Solid State Chem.*, 2020, **288**, 121397.
89 M. Bagheri and M. Y. Masoomi, *ACS Appl. Mater. Interfaces*, 2020, **12**, 4625–4631.
90 X. Y. Guo, Z. P. Dong, F. Zhao, Z. L. Liu and Y. Q. Wang, *New J. Chem.*, 2019, **43**, 2353–2361.
91 H. Chen, P. Fan, X. Tu, H. Min, X. Yu, X. Li, J. L. Zeng, S. Zhang and P. Cheng, *Chem. - An Asian J.*, 2019, **14**, 3611–3619.
92 J. Dong, D. Zhao, Y. Lu and W. Y. Sun, *J. Mater. Chem. A*, 2019, **7**, 22744–22767.
93 X. Q. Wang, D. D. Feng, J. Tang, Y. Di Zhao, J. Li, J. Yang, C. K. Kim and F. Su, *Dalt. Trans.*, 2019, **48**, 16776–16785.
94 W. P. Lustig, S. Mukherjee, N. D. Rudd, A. V. Desai, J. Li and S. K. Ghosh, *Chem. Soc. Rev.*, 2017, **46**, 3242–3285.
95 T. Y. Gu, M. Dai, D. J. Young, Z. G. Ren and J. P. Lang, *Inorg. Chem.*, 2017, **56**, 4668–4678.
96 Y. Q. Zhang, V. A. Blatov, X. X. Lv, C. H. Yang, L. L. Qian, K. Li, B. L. Li and B. Wu, *Polyhedron*, 2018, **155**, 223–231.
97 X. Zhuang, X. Zhang, N. Zhang, Y. Wang, L. Zhao and Q. Yang, *Cryst. Growth Des.*, 2019, **19**, 5729–5736.
98 H. T. Ngo, X. Liu and K. A. Jolliffe, *Chem. Soc. Rev.*, 2012, **41**, 4928–4965.
99 Y. J. Ding, T. Li, X. J. Hong, L. C. Zhu, Y. P. Cai, S. M. Zhu and S. J. Yu, *CrystEngComm*, 2015, **17**, 3945–3952.
100 B. Parmar, Y. Rachuri, K. K. Bisht, R. Laiya and E. Suresh, *Inorg. Chem.*, 2017, **56**, 2627–2638.
101 X. Du Zhang, Y. Zhao, K. Chen, Y. F. Jiang and W. Y. Sun, *Chem. - An Asian J.*, 2019, **14**, 3620–3626.
102 P. Xing, D. Wu, J. Chen, J. Song, C. Mao, Y. Gao and H. Niu, *Analyst*, 2019, **144**, 2656–2661.
103 D. K. Singha, P. Majee, S. K. Mondal and P. Mahata, *J. Photochem. Photobiol. A Chem.*, 2018, **356**, 389–396.
104 Z. Li, D. Zhan, A. Saeed, N. Zhao, J. Wang, W. Xu and J. Liu, *Dalt. Trans.*, 2021, **50**, 8540–8548.
105 J. H. Qin, Y. D. Huang, M. Y. Shi, H. R. Wang, M. Le Han, X. G. Yang, F. F. Li and L. F. Ma, *RSC Adv.*, 2020, **10**, 1439–1446.
106 X. G. Liu, C. L. Tao, H. Q. Yu, B. Chen, Z. Liu, G. P. Zhu, Z. Zhao, L. Shen and B. Z. Tang, *J.*

Mater. Chem. C, 2018, **6**, 2983–2988.
107 P. Xing, D. Wu, J. Chen, J. Song, C. Mao, Y. Gao and H. Niu, *Analyst*, 2019, **144**, 2656–2661.
108 C. Li, W. Yang, X. Zhang, Y. Han, W. Tang, T. Yue and Z. Li, *J. Mater. Chem. C*, 2020, **8**, 2054–2064.
109 K. Xing, R. Q. Fan, X. Y. Liu, S. Gai, W. Chen, Y. L. Yang and J. Li, *Chem. Commun.*, 2020, **56**, 631–634.
110 K. Ren, S. H. Wu, X. F. Guo and H. Wang, *Inorg. Chem.*, 2019, **58**, 4223–4229.
111 B. Wang and B. Yan, *Talanta*, 2020, **208**, 120438.
112 M. Marimuthu, S. S. Arumugam, D. Sabarinathan, H. Li and Q. Chen, *Trends Food Sci. Technol.*, 2021, **116**, 1002–1028.
113 M. Zhang, C. Chen, Z. Shi, K. Huang, W. Fu and W. Zhou, *Inorg. Chem.*, 2019, 8–13.
114 Z. P. Qi, Y. S. Kang, F. Guo and W. Y. Sun, *Microporous Mesoporous Mater.*, 2019, **273**, 60–66.
115 Y. Ji, L. Ding, Y. Cheng, H. Zhou, S. Yang, F. Li and Y. Li, *J. Phys. Chem. C*, 2017, **121**, 24104–24113.
116 X. Q. Wu, D. D. Huang, Y. P. Wu, J. Zhao, X. Liu, W. W. Dong, S. Li, D. S. Li and J. R. Li, *ACS Appl. Energy Mater.*, 2019, **2**, 5698–5706.
117 J. Yang, L. Zhang, X. Wang, R. Wang, F. Dai and D. Sun, *RSC Adv.*, 2015, **5**, 62982–62988.
118 J. C. Jin, J. Wu, Y. X. He, B. H. Li, J. Q. Liu, R. Prasad, A. Kumar and S. R. Batten, *CrystEngComm*, 2017, **19**, 6464–6472.
119 X. Lin, J. Jia, X. Zhao, K. M. Thomas, A. J. Blake, G. S. Walker, N. R. Champness, P. Hubberstey and M. Schröder, *Angew. Chemie - Int. Ed.*, 2006, **45**, 7358–7364.
120 H. Wu, M. Li, C. Sun, X. Wang and Z. Su, *Dalt. Trans.*, 2020, **49**, 5087–5091.
121 X. C. Lu, H. L. Wang, X. Wang, Q. Z. Li and L. Liao, *J. Clust. Sci.*, 2019, **30**, 1673–1681.
122 X. Liu, B. Fu, L. Li, Y. F. Jian and S. Shu, *Acta Crystallogr. Sect. C Struct. Chem.*, 2019, **75**, 277–282.
123 J. An, S. J. Geib and N. L. Rosi, *J. Am. Chem. Soc.*, 2009, **131**, 8376–8377.
124 A. Karmakar, B. Joarder, A. Mallick, P. Samanta, A. V. Desai, S. Basu and S. K. Ghosh, *Chem. Commun.*, 2017, **53**, 1253–1256.
125 A. Karmakar, N. Kumar, P. Samanta, A. V. Desai and S. K. Ghosh, *Chem. - A Eur. J.*, 2016, **22**, 864–868.
126 W. Morris, C. J. Doonan, H. Furukawa, R. Banerjee and O. M. Yaghi, *J. Am. Chem. Soc.*, 2008, **130**, 12626–12627.
127 R. Dalapati, S. Nandi and S. Biswas, *Dalt. Trans.*, 2020, **49**, 8684–8692.
128 S. Yuan, W. Lu, Y. P. Chen, Q. Zhang, T. F. Liu, D. Feng, X. Wang, J. Qin and H. C. Zhou, *J. Am. Chem. Soc.*, 2015, **137**, 3177–3180.
129 A. Schaate, P. Roy, T. Preuße, S. J. Lohmeier, A. Godt and P. Behrens, *Chem. - A Eur. J.*, 2011, **17**, 9320–9325.
130 J. Ren, M. Ledwaba, N. M. Musyoka, H. W. Langmi, M. Mathe, S. Liao and W. Pang, *Coord. Chem. Rev.*, 2017, **349**, 169–197.
131 A. Rana, C. Gogoi, S. Ghosh, S. Nandi, S. Kumar, U. Manna and S. Biswas, *New J. Chem.*, 2021, **45**, 20193–20200.
132 C. Gogoi, N. Nagarjun, S. Roy, S. K. Mostakim, D. Volkmer, A. Dhakshinamoorthy and S. Biswas, *Inorg. Chem.*, 2021, **60**, 4539–4550.
133 https://ncdrisc.org/cholesterol-non-hdl-map.html, https://ncdrisc.org/cholesterol-non-hdl-map.html.
134 F. Farhadi Abkanar, A. Eslami and M. Kubicki, *J. Therm. Anal. Calorim.*, 2020, **140**, 1779–1789.
135 J. Bernstein, R. E. Davis, L. Shimoni and N. -L Chang, *Angew. Chemie Int. Ed. English*, 1995, **34**, 1555–1573.
136 M. C. Etter, *Acc. Chem. Res.*, 1990, **23**, 120–126.
137 M. C. Etter, J. C. MacDonald and J. Bernstein, *Acta Crystallogr. Sect. B*, 1990, **46**, 256–262.
138 C. R. Martinez and B. L. Iverson, *Chem. Sci.*, 2012, **3**, 2191–2201.
139 L. D. Rosales-Vázquez, J. Valdes-García, I. J. Bazany-Rodríguez, J. M. Germán-Acacio, D. Martínez-Otero, A. R. Vilchis-Néstor, R. Morales-Luckie, V. Sánchez-Mendieta and A. Dorazco-

González, *Dalt. Trans.*, 2019, **48**, 12407–12420.
140 V. Zeleňák, Z. Vargová and K. Györyová, *Spectrochim. Acta - Part A Mol. Biomol. Spectrosc.*, 2007, **66**, 262–272.
141 T. Ishioka, Y. Shibata, M. Takahashi, I. Kanesaka, Y. Kitagawa and K. T. Nakamura, *Spectrochim. Acta - Part A Mol. Biomol. Spectrosc.*, 1998, **54**, 1827–1835.
142 3 Zlatko Meić Mladen Žini ć Snežzana Miljanić, Leo Frkanec, Tomislav Biljan, *J. Raman Spectrosc.*, 2007, **38**, 1538–1553.
143 V. A. Blatov, A. P. Shevchenko and D. M. Proserpio, *Cryst. Growth Des.*, 2014, **14**, 3576–3586.
144 V. Amendola, L. Fabbrizzi and E. Monzanita, *Chem. - A Eur. J.*, 2004, **10**, 76–82.
145 R. O. Gunache (Roșca), A. V. Bounegru and C. Apetrei, *Inventions*, 2021, **6**, 57.
146 A. Tavousi, E. Ahmadi, L. Mohammadi-Behzad, V. Riahifar and F. Maghemi, *Microchem. J.*, 2020, **158**, 105159.
147 O. Fazlolahzadeh, A. Rouhollahi and M. Hadi, *Anal. Bioanal. Electrochem.*, 2016, **8**, 566–577.
148 Z. Kamalzadeh and S. Shahrokhian, *Bioelectrochemistry*, 2014, **98**, 1–10.
149 S. D. Bukkitgar, N. P. Shetti and R. M. Kulkarni, *Sensors Actuators, B Chem.*, 2018, **255**, 1462–1470.
150 T. A. Silva, H. Zanin, F. C. Vicentini, E. J. Corat and O. Fatibello-Filho, *Analyst*, 2014, **139**, 2832–2841.
151 L. D. Rosales-Vazquez, J. Valdes-García, J. M. German-Acacio, J. C. Páez-Franco, D. Martínez-Otero, A. R. Vilchis-Néstor, J. Barroso-Flores, V. Sanchez-Mendieta and A. Dorazco-González, *J. Mater. Chem. C*, 2022, 32–35.
152 T. J. Offerdahl, J. S. Salsbury, Z. Dong, D. J. W. Grant, S. A. Schroeder, I. Prakash, E. M. Gorman, D. H. Barich and E. J. Munson, *J. Pharm. Sci.*, 2005, **94**, 2591–2605.
153 R. Yao, X. Cui, X. Jia, F. Zhang and X. Zhang, 2016, 2–7.
154 J. Peng, H. Tian, Q. Du, X. Hui and H. He, *Microchim. Acta*, 2018, **185,** 2-9..